
Sea Level Static Calibration of a Compact Multimission Aircraft Propulsion Simulator With Inlet Flow Distortion

Mark J. Won, Ames Research Center, Moffett Field, California

ORIGINAL CONTAINS
COLLATERAL INFORMATION

November 1990



National Aeronautics and
Space Administration

Ames Research Center
Moffett Field, California 94035-1000

NOMENCLATURE

$\frac{N}{N_{des} \sqrt{\theta_2}}$	sea level-corrected rotor speed, %
$\frac{P_{s2}}{P_{s1}}$	inlet wall static pressure loss
$\frac{P_{s2,i}}{P_{s2}}$	mass-averaged compressor static pressure ratio
$\frac{P_{s57}}{\delta_2}$	sea level-corrected, compressor-referenced mixer pressure
$\frac{P_{s2max} - P_{s2min}}{\bar{P}_{s2}}$	compressor inlet wall static pressure distortion, %
$\frac{P_{s7max} - P_{s7min}}{\bar{P}_{s7}}$	nozzle entrance wall static pressure distortion, %
$\frac{P_{s15max} - P_{s15min}}{\bar{P}_{s15}}$	compressor discharge wall static pressure distortion, %
$\frac{\bar{P}_{t2}}{P_{t1}}$	inlet total pressure recovery
$\frac{P_{t2max} - P_{t2min}}{\bar{P}_{t2}}$	compressor inlet total pressure distortion, %
$\frac{\bar{P}_{t7}}{\bar{P}_{t2}}$	engine pressure ratio
$\frac{P_{t7}}{P_{\infty}}$	nozzle pressure ratio
$\frac{\bar{P}_{t15}}{\bar{P}_{t2}}$	compressor pressure ratio
$\frac{P_{t15max} - P_{t15min}}{\bar{P}_{t15}}$	compressor discharge total pressure distortion, %
$\frac{T_{t7max} - T_{t7min}}{\bar{T}_{t7}}$	nozzle entrance total temperature distortion, %
$\frac{\dot{w}_1 \sqrt{\theta_1}}{\delta_1}$	sea level-corrected bellmouth airflow
$\frac{\dot{w}_2 \sqrt{\theta_2}}{\delta_2}$	sea level-corrected compressor airflow
$\frac{\dot{w}_7 \sqrt{\theta_2}}{\delta_2}$	sea level-corrected, compressor-referenced nozzle airflow
A	flow area, in ²
C_f	flow coefficient
F	Mach number iteration function
g	gravitational constant, 32.17 ft/sec ²
M	Mach number
N	rotor speed, rpm
N_{des}	CMAPS design rotor speed, 75185 rpm
P	pressure, psia
r	rake probe radial position, in.

R	universal gas constant, 53.35 lbf-ft/lbf-°R
Re_I	Reynolds number index: $\frac{\delta}{\phi\sqrt{\theta}}$
t	time, sec
T	temperature, °F, °R
V	vibration, g rms
\dot{w}	airflow, lbm/sec
γ	ratio of specific heats (1.4)
δ	sea level-referenced pressure ratio: $\frac{P}{14.69}$
θ	sea level-referenced temperature ratio: $\frac{T}{518.67}$
ϕ	sea level-referenced viscosity ratio: $\frac{718.2\theta^{3/2}}{T + 199.5}$

Subscripts

a	averaged value
b	reference to bleed flow measurement
ba	reference to aft bearing
bf	reference to forward bearing
c	calibrated value
d	reference to drive flow measurement
$db8$	reference to drive, bleed, and nozzle flow measurements
i	ideal value
m	measured value
max	maximum value
min	minimum value
o	initial iteration value
par	parasitic term
ref	referenced value
s	static value
sl	reference to sea level conditions
t	total or stagnation value
∞	reference to ambient conditions
1	reference to bellmouth instrument plane
2	reference to compressor inlet instrument plane
4	reference to turbine inlet
5	reference to turbine exit
7	reference to nozzle entrance instrument plane
8	reference to nozzle throat
15	reference to compressor discharge instrument plane
57	reference to mixer injector slot

SUMMARY

Wind tunnel tests of propulsion-integrated aircraft models have identified inlet flow distortion as a major source of compressor airflow measurement error in turbine-powered propulsion simulators. Consequently, two Compact Multimission Aircraft Propulsion Simulator (CMAPS) units were statically tested at sea level ambient conditions to establish simulator operating performance characteristics and to calibrate the compressor airflow against an accurate bellmouth flowmeter in the presence of inlet flow distortions. The distortions were generated using various-shaped wire mesh screens placed upstream of the compressor. CMAPS operating maps and performance envelopes were obtained for inlet total pressure distortions (ratio of the difference between the maximum and minimum total pressures to the average total pressure) up to 35%, and were compared to baseline simulator operating characteristics for a uniform inlet. Deviations from CMAPS baseline performance were attributed to the coupled variation of both compressor inlet-flow distortion and Reynolds number index throughout the simulator operating envelope for each screen configuration. Four independent methods were used to determine CMAPS compressor airflow: direct compressor inlet and discharge measurements, an entering/exiting flow-balance relationship, and a correlation between the mixer pressure and the corrected compressor airflow. Of the four methods, the last yielded the least scatter in the compressor flow coefficient, approximately $\pm 3\%$ over the range of flow distortions.

INTRODUCTION

Aircraft turbine-engine simulators are complex, turbomachines capable of simulating propulsion effects on wind tunnel aircraft models. During the 1970s, Multimission Aircraft Propulsion Simulators (MAPS) were developed and tested for wind tunnel test applications. Results from these MAPS development programs are discussed in references 1–3. As shown in figure 1, these simulators relied on an external high-pressure air source to power a single-stage turbine and drive a four-stage compressor. Engine parameters simulated by MAPS included corrected compressor airflow, $\dot{w}_2\sqrt{\theta_2}/\delta_2$; exhaust nozzle flow function, $\dot{w}_8\sqrt{T_{t8}}/P_{t8}$; and exhaust nozzle pressure ratio, P_{t8}/P_∞ . MAPS demonstrated favorable simulator control and performance capabilities. However, the simulator's relatively large size distorted the external contours and mold lines of wind tunnel aircraft models.

The development of a more compact simulator with improved operating capabilities resulted in the Compact Multimission Aircraft Propulsion Simulator (CMAPS). As shown in figure 2, CMAPS contains the same rotor hardware used in MAPS, but has a smaller external diameter and shorter overall length than its predecessor. CMAPS is capable of providing either dry power or reheat (afterburning) simulation. During the simulator's development, five CMAPS units were fabricated by Tech Development, Inc. (TDI) for testing at the Arnold Engineering Development Center (AEDC) and at Ames Research Center. As discussed in references 4–9, these tests generated a data base on CMAPS performance envelopes and operating characteristics to support wind tunnel tests involving propulsion-integrated aircraft models. A mathematical cycle deck (ref. 10) was developed from the accumulated CMAPS data to provide an analytical tool for estimating simulator performance at various inlet pressures for different exhaust nozzle configurations.

A wind tunnel test at Ames of a propulsion-integrated fighter aircraft model (discussed in references 7–9) identified inlet flow distortion as having a significant effect on CMAPS operating performance and on compressor airflow measurement accuracy. As much as a 15% total pressure distortion was measured at the aircraft model's simulated engine face at a 15° angle of attack. In general, the typical sources for flow distortion entering an inlet duct include the model's nacelle and duct walls, where large internal flow separation can occur at even moderate angles of attack. Another source is the aircraft model's forebody, which can shed vortices that enter the inlet as a form of swirling flow distortion. If these unsteady flow disturbances enter the CMAPS compressor over a prolonged period when operating under high-power simulator conditions, severe rotor and stator blade damage can occur.

Because of the three-dimensional, oftentimes dynamic, nature of these flow disturbances, steady, time-averaged pressure or temperature measurements can be difficult to quantify and analyze. Consequently, direct measurement of CMAPS compressor airflow cannot be accurately determined when inlet flow distortion is present. As discussed in reference 6, the need to reduce compressor-inlet pressure instrumentation owing to aircraft model size limits the survey of the distorted flow field entering the compressor and contributes to compressor airflow measurement uncertainty.

Static calibrations of CMAPS units at both AEDC and Ames measured compressor airflow using several practical methods. Accuracies to within $\pm 1.5\%$ of the actual airflow were obtained at Ames (ref. 6) based on an indirect compressor airflow correlation method over a specific range of inlet pressures using a reheat nozzle. However, extensive CMAPS calibration had not been performed at either research center to evaluate simulator performance and compressor airflow measurement methods with nominal compressor-inlet total pressure distortion greater than 5%.

This technical memorandum presents the results of the most recent sea-level static calibration test performed at Ames on two CMAPS engines with inlet flow distortion. These simulators were designated by the serial numbers 006/3 and 008/3 (SN/006/3 and SN/008/3, respectively, with the “3” designating the number of maintenance overhauls performed by TDI on each engine). The primary objectives for this test were as follows:

1. Verify CMAPS operation conformity with operating “norms” established during previous calibrations for a dry mixer/nozzle configuration with no inlet distortion
2. Investigate the effects of inlet flow distortion on CMAPS performance envelopes and operating characteristics
3. Assess current methods to accurately measure compressor airflow with inlet distortion present
4. Expand the existing CMAPS data base to include distortion effects for future simulator applications

The author is grateful for the experienced guidance on CMAPS testing provided by Rodney O. Bailey, and for the significant technical support provided by Donald E. Baker, Martin M. Rebholz, Alexander A. Te, Thomas K. Timbal, and Max W. Williams.

MODEL DESCRIPTION

CMAPS

As shown in figure 3, the CMAPS internal hardware is contained within a forward frame, main frame, and bleed frame, augmented by the drive and bleed manifolds and the nozzle assembly. CMAPS has a design rotor speed of 75,185 rpm, with a design corrected compressor airflow of 1.73 lbm/sec. A four-stage compressor driven by a single-stage, high-efficiency turbine within the CMAPS gas-generator section provides a nominal compressor pressure ratio of 3. The simulator is capable of producing engine pressure ratios near 5. Figure 3 also shows the numbering convention adopted for the simulator instrumentation planes: compressor inlet (Plane 2), compressor discharge (Plane 15); turbine inlet (Plane 4); turbine discharge (Plane 5); mixer injection slot (Plane 57); nozzle entrance (Plane 7); and nozzle throat (Plane 8). A detailed description of CMAPS components and functions is presented in reference 4.

The CMAPS rotor speed is controlled by varying the amount of drive air and bleed air flowing through the simulator's mainframe and bleedframe. Turbine discharge air that is not bled from CMAPS is allowed to mix with the compressor discharge air through a mixer. Combining turbine and compressor discharge air augments the nozzle and engine pressure ratios. Two different mixers, each matched to a corresponding nozzle, provide dry power or afterburning (reheat) exhaust flow simulation.

CMAPS has a full complement of internal and external instrumentation for pressure, temperature, rotor-thrust, vibration, and rotor-speed measurements; these instruments are used for monitoring simulator health and acquiring data. The simulator also has oil lubrication and scavenge systems which respectively supply and recover oil from the forward and aft rotor bearings.

Inlet Assembly

As shown in figure 4, the CMAPS inlet assembly consisted of a bellmouth flowmeter, distortion unit, and compressor inlet (Plane 2) instrument ring. The aluminum bellmouth was instrumented as an accurate flowmeter to measure CMAPS compressor airflow. Calibration of the bellmouth against a sonic-throat venturi flowmeter was conducted at the Colorado Engineering Experiment Station, Inc. (CEESI), and is reported in reference 11. Bellmouth instrumentation included four wall static pressure orifices and four, single-probed total pressure rakes.

The distortion unit consisted of a bellmouth adapter, an interchangeable screen set, and a flow-through duct, all with a 3-in. inside diameter. The distortion unit was located between the CMAPS Plane 2 instrument ring and the bellmouth. O-rings were used to seal all mating flanged surfaces within the unit. The screen set was compressed at the edges between two neoprene gaskets to secure the screens within the distortion unit. Figure 5 displays the components of the distortion unit.

The interchangeable screen set contained a backup and a primary screen which were silver-brazed together. The screen set was located about 5 in. upstream of the CMAPS compressor inlet. The backup screen was composed of medium, light weave, No. 2 mesh, 0.063-in.-diam stainless steel wire with 0.437-in. openings. The primary screen was constructed from a No. 8-1/2 mesh consisting of 0.063-in.-diam stainless steel wire with 0.187-in. openings. Ten interchangeable screen sets with different

primary screen patterns were used to generate various levels of flow distortion upstream of the CMAPS compressor. The geometry of each screen pattern is shown in figure 6. These patterns were derived from reference 12 in which similar screen profiles were used for full-scale turbojet inlet distortion tests. Table 1 lists the geometric properties of each screen pattern.

Figure 7 shows the Plane 2 instrument ring attached to the CMAPS compressor inlet. The ring contained eight equally spaced pressure rakes, each measuring a rake-base (wall static) pressure and five total pressures. The radial position of each pressure probe was designed to provide an area-weighted average total pressure measurement at the compressor inlet. A single orifice circumferentially positioned between each rake along the ring provided eight additional wall-static pressure measurements.

Control System

The CMAPS control system (controller) was configured by McDonnell Douglas Corp. for use at Ames. The controller could simultaneously control two CMAPS units and provide the necessary emergency shutdown routines for simulator protection. It could also collect data from CMAPS and transfer information to a data facility such as the Ames Standardized Wind Tunnel System (SWTS) (ref. 13). The CMAPS controller operated the drive- and bleed-air valves, providing both automatic and manual control of the simulators. The controller also had provisions for automatic shutdown of the airflow regulation system in the event of a CMAPS or a high-pressure air system malfunction. The CMAPS controller included the following major hardware items: control console, signal conditioning and CPU equipment racks, printer and keyboard, hydraulic cart, oil supply, and bearing oil scavenge system. Pressure transducers (semiconductor bridge type), air control valves, and cabling were among the controller's essential components. Detailed documentation of the CMAPS controller is provided in reference 14.

For multiplexing pressure measurements from CMAPS, two Pressure Systems Inc. (PSI) electronic pressure scanner modules were used. Each module provided up to 48 differential pressure measurements relative to a reference pressure (atmospheric for this test). Computer or manual operation of both modules was accomplished through two NASA-fabricated pressure control units (PCU's), a PSI 80-IFC interface module, and two electro-pneumatic solenoid valves. Computer operation of both modules was performed by the CMAPS controller via the Analogic AN5400 and two Pacific Precision data channels.

The CMAPS controller operated and monitored the hydraulic power supply, oil supply, and the oil scavenge system. The hydraulic power supply delivered hydraulic fluid to the CMAPS flow control valves. The oil supply delivered the prescribed flow rate of lubricating oil to the CMAPS forward and aft bearings, and contained wet/wet-type bidirectional differential pressure transducers, which the CMAPS controller used for monitoring oil delivery rates to the bearings. The scavenge system removed and collected oil from the CMAPS bearings for oil sediment analysis.

FACILITY DESCRIPTION

CMAPS testing was performed at the Ames Propulsion Simulator Calibration Laboratory (PSCL). As discussed in reference 15, the PSCL was developed to provide accurate thrust and airflow measurement and calibration capabilities for compact propulsion simulators and wind tunnel propulsion models.

The primary elements of the facility include a calibration tank, thrust measurement system, airflow measurement system, high-pressure air system, tank vacuum system, and data acquisition system. Elements not actively used during this CMAPS test included the thrust-measurement and tank vacuum systems. A schematic of the PSCL is shown in figure 8; a schematic of the high-pressure air system for dual CMAPS operation is shown in figure 9.

The calibration vacuum tank was about 25 ft long and 12 ft in diameter, and could be evacuated to 2 psia. An access door located on one end of the tank provided access for model installation and service of support systems. A built-in 2-ton trolley hoist, a support platform, metric frame, primary thrust measurement system, and drive/bleed airflow regulation systems were contained within the tank.

High-pressure (3000 psia) air was supplied to the PSCL by the Ames High-Pressure Air Distribution Network. A supply of filtered, heated air to the CMAPS turbine was provided by the Ames portable 1-MW high-pressure air heater which could supply 28 lbm/sec of 200°F air to the facility. The heated drive air was necessary to prevent ice formation within the CMAPS exhaust-air/bleed-air mixer passages.

An exhaust extractor duct assembly was attached to one of three ports leading to the vacuum system circuit at the rear of the calibration tank. Since CMAPS units normally eject oil into the exhaust, the duct captured the atomized lubricant and prevented the hot nozzle exhaust from recirculating back into the simulator's inlet.

As shown in figure 10, CMAPS was secured to a flow-through sting which was attached to an adapter and a sting extension mounted on the metric frame within the PSCL calibration tank. The attachment between the simulator and sting was made at the turbine drive and bleed manifolds by means of manifold crossovers, and at a mounting bracket located on the CMAPS forward frame. Two flexible air hoses linked the sting's drive and bleed lines to the PSCL high-pressure air system. Details of the sting and drive/bleed assemblies are described in reference 7. The drive and bleed airflows were measured by calibrated sonic-throat venturi flowmeters, which offered a high level of flow measurement accuracy.

INSTRUMENTATION

Complete summaries of CMAPS and facility instrumentation are given in tables 2 and 3, respectively. The summaries provide instrument descriptions, parameter names, sensor types, and expected ranges used by the CMAPS control console and facility data acquisition system (SWTS).

Pressures at the CMAPS inlet (Plane 2), compressor discharge (Plane 15), and exhaust nozzle entrance (Plane 7) were measured by the two PSI pressure scanner modules. The remaining simulator and facility pressures were measured by semiconductor-type, silicon diaphragm XTMS-series Kulite transducers, and Paroscientific digital quartz transducers with M600 computers. The Kulite and Paroscientific pressure transducers were installed within the Temperature Environment Control Module (TECM) located inside of the calibration tank. Because of transducer thermal sensitivity, the TECM's interior was insulated by heater blankets to maintain a constant temperature inside the module's cavity. The heater blankets were monitored by Watlow temperature controllers using iron-constantan (Type J) thermocouples. All CMAPS internal temperatures were measured with chromel-constantan (Type E)

thermocouples. For appropriate temperature referencing, the type E and J thermocouples respectively used a Celesco and a Pace Engineering thermocouple reference junction box.

CMAPS vibrations were measured with a HP-series Endevco accelerometer mounted to the simulator's forward frame. A CEL-series Kulite transducer was used to monitor compressor discharge dynamic pressure, and to indicate incipient compressor stall activity. Both accelerometer and dynamic pressure transducer were connected to appropriate CMAPS controller-excitation and signal-conditioning hardware.

The axisymmetric CMAPS nozzle extension duct was attached to the dry nozzle to minimize nozzle flow distortion. As shown in figure 11, the nozzle instrumentation rakes were oriented in the "C" position relative to the dry mixer struts for optimum total pressure and temperature measurements, which was demonstrated in reference 4. The dry nozzle and mixer hardware used for this test are shown in figure 12.

TEST PROGRAM

The test matrix followed throughout the CMAPS test is presented in the run schedule given in table 4. The matrix consisted of 11 desired run configurations, including a baseline (no distortion screens) and the 10 distortion screens.

The first configuration was the uniform baseline configuration with only the bellmouth and Plane 2 instrument ring attached to the CMAPS compressor inlet (fig. 13). The CMAPS controller was operated in either the manual or auto-rpm control mode. The first three data runs under this configuration provided the desired control constants for the CMAPS controller, allowed the adjustment of signal-conditioning equipment, verified simulator operating "norms" and automatic shutdown capabilities, and established the minimum operating (min-op) and stall lines for subsequent runs. The parameters that were measured during this verification/calibration phase included rotor speed, rotor acceleration, forward and aft bearing temperatures and temperature rates, mixer pressure, vibrations, compressor discharge dynamic pressure, and turbine pressure.

The min-op line consisted of data points taken at idle, 60, 70, 80, 90, 100, and 110% corrected speed with the bleed valve fully open. Complete compressor stall was initiated by slowly closing the bleed valve (while maintaining a constant corrected rotor speed) until the dynamic pressure display on the CMAPS control console responded to a stall-related signal from the compressor discharge dynamic pressure transducer. The stall line on the compressor operating map was obtained by recording data points at 60, 65, 70, 75, and 80% corrected speeds with the compressor stalled.

The next six data runs mapped the engine operating (flexibility) envelope under the baseline inlet configuration along 60, 70, 80, 90, 100, and 110% corrected speed lines. The final run for this configuration consisted of data points selected from the preceding six runs with the CMAPS controller operated in the full-auto-airflow/engine-pressure-ratio (AF/EPR) control mode. The purpose of this run was to analyze the controller's ability to seek and maintain an AF/EPR set point with a modified controller algorithm. This algorithm empirically determined the compressor corrected airflow as a function of corrected mixer (Plane 57) static pressure and percent corrected rotor speed from the min-op line

generated during the second data run. This mixer pressure-compressor airflow correlation method is described later.

The remaining run configurations in the test matrix mapped the entire CMAPS operating envelope for each distortion screen. As shown in figure 14, the bellmouth, distortion unit, and Plane 2 instrument ring were attached to the CMAPS compressor inlet for these configurations. The envelope-mapping runs included the min-op line, stall line, and the 60, 70, 80, 90, 100, and 110% corrected speed lines with the CMAPS controller operated in auto-rpm mode.

RESULTS AND DISCUSSION

Operation Description

Approximately 94 hr of combined simulator powered operation were accumulated throughout the test, 66 and 28 hours for CMAPS's SN/008/3 and SN/006/3, respectively. Initially, it was planned that SN/008/3 would operate for all runs outlined in the test matrix. However, after about two-thirds of the test matrix had been completed, SN/008/3 developed severe vibrations and excessive forward and aft bearing temperature rates for corrected speeds beyond 70%. These prompted the CMAPS controller to effect emergency shutdowns for higher operating speeds. Subsequently, SN/008/3 operation was discontinued. The simulator was removed from the flow-through sting and replaced by SN/006/3. SN/006/3 was initially tested under the baseline and screen No. 4 configuration (a repeat run series) before continuing with the remaining screen configurations in the test matrix. Tables 5 and 6 tabulate the completed run schedule and the history of powered operation, respectively, for CMAPS SN/006/3 and 008/3.

During CMAPS operation in the baseline configuration near the stall line, more controller-effected emergency shutdowns generally occurred than during near-stall simulator operation with the various distortion screens installed. These shutdowns were initiated by excessive rotor accelerations once the compressor became completely stalled during increased bleed valve closure. Under the screen No. 8 configuration, CMAPS SN/008/3 could not be operated beyond 105% corrected speed, a result of large increases in simulator vibration and bearing temperature. Hence, complete simulator operating characteristics and performance envelopes were not obtained for this screen configuration.

The accelerometer and rotor-thrust load cell outputs from both simulators were unstable, and exhibited extreme signal drifts while maintaining a steady CMAPS operating condition. Accurate vibration and rotor-thrust maps could not be generated for either simulator during baseline- and distortion-screen configuration testing and were excluded from simulator operating analysis.

CMAPS controller operation under the full-auto AF/EPR mode demonstrated satisfactory set-point convergence results. A desired compressor airflow and engine pressure ratio set-point was achieved typically within 4 min during any non-stall operating condition within the CMAPS performance envelope. The desired condition was effectively maintained within user-defined full-auto control mode limits without experiencing complete set-point divergence. Full-auto AF/EPR control limits prescribed by the CMAPS Controller Operation Manual (ref. 14) were often sufficient enough to achieve set-point convergence within 2 min.

Baseline Configuration

Compressor Operating Performance

The compressor operating maps for CMAPS SN/006/3 and SN/008/3 are shown in figure 15 for the baseline inlet configuration. The maps were generated from data points recorded along the min-op line, during stall, and at constant corrected speed lines of 60, 70, 80, 90, 100, and 110%. Figure 15(a) compares the calibration data to “norms” data from reference 16 for CMAPS SN/006 under dry power simulation at ambient compressor inlet pressure. Since past CMAPS SN/008 tests simulated reheat nozzle exhaust only, no comparable dry-nozzle norms data were available for this simulator in figure 15(b).

Dry Nozzle Flexibility Envelopes

The dry nozzle engine pressure ratio-compressor corrected airflow (flexibility) envelopes for CMAPS SN/006/3 and SN/008/3 are presented in figure 16 for the baseline inlet configuration. Norms data and CMAPS cycle-deck predictions (from reference 10) in figure 16(a) are compared with the baseline calibration data for SN/006/3. SN/008/3 baseline calibration data are compared with cycle-deck predictions in figure 16(b). Cycle-deck predictions were based on a dry mixer area of 0.11 in^2 , dry nozzle throat area of 3.0 in^2 , and a compressor inlet pressure of 13.0 psia.

Bearing Temperatures

The average of two separate temperatures measured at the forward bearing is shown in figure 17 for SN/006/3 and SN/008/3 as a function of percent corrected rotor speed. The forward bearing temperatures for SN/006/3 and SN/008/3 were within the general CMAPS forward bearing temperature operating envelope obtained from norms data. As discussed in reference 16, the CMAPS forward bearing temperature is primarily dependent on the rotor speed, compressor inlet total temperature, compressor inlet total pressure, and the bearing itself. The temperature variation observed in figure 17 at each constant corrected rotor speed particularly reflects the variations in compressor-inlet total temperature during SN/006/3 and SN/008/3 baseline operation. These variations were a result of temperature fluctuations within the PSCL calibration tank. The internal tank temperature was affected by the heat radiated from the high-pressure air drive-line and the venting of hot air by the drive-line dump valves within the tank during simulator emergency shutdowns. For both SN/006/3 and SN/008/3, the compressor inlet total temperature (measured at the bellmouth inlet) typically ranged between 80°F and 110°F throughout the simulator operating envelope, and generally increased with increasing rotor speed.

The average of two temperatures measured at the aft bearing is shown in figure 18 for CMAPS SN/006/3 and SN/008/3 as a function of the turbine inlet total pressure. The relationship between the aft bearing temperature and turbine inlet total temperature is presented in figure 19 for SN/006/3 and SN/008/3. Differences between each simulator’s aft bearing temperatures were due to varying turbine inlet pressure and temperature, and different bearing tolerances within the rotor hardware. Since SN/008/3 operated under higher turbine inlet total temperatures than did SN/006/3, the aft bearing temperature for SN/008/3 was generally higher than that for SN/006/3. SN/008/3’s relatively higher aft bearing temperatures might have been a precursor to the simulator’s eventual malfunction (which resulted in excessive aft bearing temperature rates and high vibrations).

Turbine Performance

Figure 20 compares the pressure drop across the turbine for CMAPS's SN/006/3 and SN/008/3, respectively, throughout their baseline operating envelope. Along the constant corrected speed line in figure 20(a), CMAPS SN/006/3 had a larger pressure drop across its turbine stage than does SN/008/3 in figure 20(b). Hence, less turbine airflow was required by SN/008/3 than by SN/006/3 in order to operate at the same condition on the compressor performance map. As shown in figure 21, the relationship between the turbine airflow and turbine inlet pressure agreed with the norms data for SN/006 and SN/008.

Compressor Inlet Distortion

Compressor inlet total pressure and wall static pressure distortion envelopes for the baseline inlet configuration are shown in figure 22 for both CMAPS's SN/006/3 and SN/008/3. Both pressure distortions were defined as the ratio of the difference between the maximum and minimum pressures to the average pressure. The compressor inlet total and static pressure distortions ranged as high as 5%, generally increasing with compressor airflow. These distortions were primarily caused by the wake generated upstream of the compressor face by the bellmouth's total pressure rakes.

Compressor Discharge Distortion

The compressor discharge total pressure and wall static pressure distortions are presented in figures 23 and 24, respectively, for both CMAPS's SN/006/3 and SN/008/3. Both pressure distortions were defined similarly to the compressor inlet pressure distortions. Compressor discharge total pressure and static pressure distortions were under 15% and 2%, respectively. The total pressure distortion generally increased with increasing compressor airflow along the min-op line, and decreased with increasing compressor pressure ratio at a constant corrected speed. The static pressure distortion did not display similar trends with compressor airflow or pressure ratio variations. This could be attributed to the few Plane 15 static pressure measurements available on CMAPS (three compressor discharge wall static pressure orifices). Since only one active thermocouple was used in the compressor discharge instrumentation plane, no thermal distortion data were obtained.

Nozzle Entrance Temperature Distortion

Baseline dry nozzle entrance total temperature distortions are shown in figure 25 for CMAPS's SN/006/3 and SN/008/3. The nozzle distortion was defined by the ratio of the difference between the maximum and minimum total temperatures to the average total temperature. The temperature distortion increased with increasing rotor speed, ranging as high as 80% (based on temperature measured in degrees Rankine). At a constant corrected speed, the nozzle temperature distortion generally remained steady with increasing nozzle flow (engine pressure ratio) relative to the temperature distortion variation along the min-op line.

The large thermal distortion can be explained by the non-uniform mixing of compressor discharge flow with the expanded, relatively cooler mixer flow discharged from the turbine. Because of the back-pressuring of the compressor by the mixer flow within the nozzle, the compressor discharge air undergoes little expansion (cooling) as it enters the nozzle entrance, remaining relatively hot (typically

between 150°F and 400°F) throughout the CMAPS operating envelope. High-pressure turbine discharge air entering the mixer slots is throttled by the mixer, expanding and cooling as it is ejected into the nozzle entrance. Once inside the nozzle duct, the flow plumes produced by the mixer orifices combine with the hotter, swirling compressor discharge flow. The mixed flow swirls about the duct's centerline, owing to the rotating upstream flow produced by the compressor. Depending on the relative positions of the nozzle temperature probes with respect to the mixer's ejector orifices and the compressor discharge chutes in the mixer, the nozzle's thermocouples can survey a wide range of temperatures.

For example, at 110% corrected speed along the min-op line, the compressor discharge total temperature was nominally 350°F for both SN/006/3 and SN/008/3 at an ambient compressor inlet temperature of 100°F. The corresponding turbine discharge total pressure and temperature were about 200 psia. and 60°F, respectively. Under these conditions, the surveyed nozzle entrance total temperatures ranged from -80°F to 270°F at an averaged nozzle entrance total pressure of 40 psia. The nozzle temperature variation is evident in figures 26–29 for CMAPS's SN/006/3 and SN/008/3. These figures present the radial temperature profiles measured by two rakes separated 144° apart (with reference to figure 11) at the nozzle entrance (Plane 7). The temperature distributions are shown for simulator operating conditions at 60, 80, and 110% corrected speeds on the min-op line, and at varying engine pressure ratios at 100% correct speed. In figures 26 and 27, the radial temperature distributions increasingly varied with increasing rotor speed, but the distributions remained relatively unchanged with increasing engine pressure ratio at a constant corrected speed, as shown in figures 28 and 29.

Nozzle Entrance Pressure Distortion

Nozzle entrance total pressure and wall static pressure distortions are presented in figures 30 and 31, respectively, for both CMAPS's SN/006/3 and SN/008/3. Both pressure distortions were defined similarly to the compressor inlet distortions. The nozzle-entrance-wall static pressure distortion was typically less than 2%, whereas the total pressure distortion was within 30%. The total pressure distortion generally remained constant along the min-op line, and increased with increasing nozzle flow and engine pressure ratio during speed-line excursions from the min-op line. The nozzle wall static pressure distortion did not exhibit a similar relationship with variations in nozzle flow or engine pressure ratio. As with the compressor discharge static pressure distortion, this behavior could be attributed to the low number of static pressure instruments contained within the nozzle (five wall static pressure orifices).

The radial total pressure profiles for the three dry nozzle pressure rakes (in the "C" position) are shown in figures 32–35 for CMAPS's SN/006/3 and SN/008/3. The pressure distributions were obtained for simulator operating conditions at 60, 80, and 110% corrected speeds on the min-op line, and at varying engine pressure ratios at 100% corrected speed. In figure 32, the min-op line pressure profiles were radially uniform for SN/006/3. But as shown in figure 33, the pressure increased radially outward at 60 and 80% corrected speeds, then increased radially inward at 110% corrected speed for all three nozzle pressure rakes in CMAPS SN/008/3. For both simulators, the latter radial pressure gradient is also displayed in figures 34 and 35 for the engine pressure ratio variations at 100% corrected speed. The higher pressure at the nozzle centerline resulted from airflow discharged from the thrust trim orifices within the mixer tie bolt. During engine pressure ratio excursions from the min-op line, the bleed valve was closed while maintaining a constant corrected rotor speed, causing more high-pressure turbine discharge air to leak into the cavities behind the aft bearing (shown in figure 3). The

high-pressure cavity air was then injected into the thrust trim orifices to be discharged into the nozzle. Hence, the total pressure in the nozzle flow along the nozzle centerline was greater than the pressure in the surrounding nozzle flow at high engine pressure ratios.

Distortion Screen Configurations

Distortion Screen Performance

In the presence of a distortion screen, the ratio of the compressor inlet (Plane 2) total pressure to the bellmouth (Plane 1) total pressure represents the total pressure recovery across the screen. Similarly, the ratio of the compressor inlet wall static pressure to the bellmouth wall static pressure is the static pressure loss across the screen (confined along the inlet duct wall). The total pressure recovery and wall static pressure loss for each screen configuration are shown in figures 36 and 37 as functions of the sea-level-corrected bellmouth airflow along the min-op line. Except for the hub-radial screen configurations (Nos. 6 and 7), the total pressure recovery and static pressure losses generally increased with screen blockage area. The wall static pressure losses for screens Nos. 6 and 7 were less sensitive to screen blockage since these screens did not extend radially outward to the inlet duct wall. Figure 38 shows the variation of compressor inlet Reynolds number index with the sea-level-corrected bellmouth airflow along the min-op line for all screen configurations tested on SN/006/3 and SN/008/3. For each screen configuration, the compressor Reynolds number index was strongly dependent on the inlet total pressure recovery, and decreased accordingly with increasing compressor airflow. The lowest Reynolds number index of 0.63 was obtained from screen No. 11.

Compressor inlet total pressure and wall static pressure distortion variations with the sea-level-corrected bellmouth airflow along the min-op line are shown in figures 39 and 40 for all distortion screen configurations. The highest total and static pressure distortions were approximately 35% and 15%, respectively. Figures 41–51 present color representations of the compressor inlet total pressure distribution at 60, 80, and 110% corrected speeds along the min-op line for all screen configurations. The color-generating scheme used to produce these images is described in appendix A. Figures 52–62 show the compressor inlet wall-static pressure profiles at 60, 80, and 110% corrected speeds along the min-op line for all screen configurations. The spatial pressure distortion at the compressor inlet relative to upstream screen position can be inferred from these figures.

The effect of circumferential screen location on the compressor inlet total pressure and wall static pressure measurements is evident by comparing, respectively, figures 43–44 and figures 54–55 for screen No. 4. On SN/006/3, the spatial pressure variation was measured with screen No. 4 centered circumferentially on a rake (at 180°), whereas the pressure variation on SN/008/3 was measured with the same screen centered between two consecutive rakes (at 135° and 180°). The circumferential position of screen No. 4 also affected the measured compressor inlet total pressure recovery and static pressure loss, which are evident in figures 36 and 37. For each simulator, screen No. 4 had a separate distribution of total pressure recovery and static pressure loss with increasing inlet airflow, which is especially noticeable at corrected speeds greater than 80%. The total pressure recovery and static pressure loss distributions for screen No. 4 differed by about 1% between CMAPS's SN/006/3 and SN/008/3 along the min-op line. This small but measurable difference reflects the sensitivity of the Plane 2 instrumentation to the spatial compressor inlet pressure variations at moderate inlet flow distortion levels.

Compressor Operating Performance

Comparisons between the baseline and distortion screen compressor operating maps for CMAPS's SN/006/3 and SN/008/3 are shown in figures 63–72. Compressor pressure ratio and corrected airflow deviations from the baseline compressor operating map at a constant operating condition could be attributed to the compressor-inlet Reynolds number index variations for each screen. The most evident deviations were obtained from screen No. 11 at 110% corrected speed (fig. 72). For all screen configurations, the compressor performance deviations generally increased with decreasing Reynolds number index. Since the compressor-inlet total pressure and distortion varied simultaneously with increasing compressor airflow, the coupling of both pressure distortion and Reynolds number index could have had a more predominant effect on CMAPS compressor performance than just the Reynolds number index alone. Because of the ambient conditions that existed at the bellmouth inlet (the compressor inlet total pressure could not be controlled), neither the total pressure distortion nor the Reynolds number index could be assessed independently of each other in this test.

Bearing Temperatures

The averaged forward bearing temperatures for CMAPS's SN/006/3 and SN/008/3 under each distortion screen configuration are compared with a representative norms envelope in figures 73–82. For each screen configuration, the bearing temperatures were within the norms envelope defined by the measured rotor speed, compressor inlet total pressure, and total temperature. The norms envelope was unique for each screen configuration, a result of the variations in compressor inlet total pressure and temperature. The total pressure variations were dependent on the total pressure recovery associated with the particular distortion screen being tested. As previously discussed for the baseline configuration, the CMAPS compressor inlet temperature variations were caused by temperature fluctuations within the PSCL calibration tank. Under distortion screen testing, the CMAPS compressor inlet total temperature (measured at the bellmouth inlet) typically ranged between 80°F and 120°F throughout a simulator operating envelope, and generally increased with increasing rotor speed (turbine airflow demand). Overall, the forward bearing temperature stayed within the norms-defined envelopes for all distortion screen configurations.

The aft bearing temperature for each distortion screen configuration is compared with the associated baseline envelope in figures 83–92 for CMAPS's SN/006/3 and SN/008/3. As discussed in reference 16, the aft bearing temperature is a function of the compressor inlet total pressure, turbine inlet temperature, and rotor speed for a fixed mixer configuration. Thus, aft bearing temperature excursions beyond the baseline envelope could be attributed to the combined variation of any one of these factors for a given distortion-screen configuration.

Turbine Performance

The influence of each distortion screen on turbine performance is presented on the turbine pressure loss maps shown in figures 93–102 for CMAPS's SN/006/3 and SN/008/3. As similarly demonstrated by the compressor operating maps under inlet distortion, differences between the baseline and distortion screen turbine performance maps could be related to the Reynolds number index (total pressure recovery) variations for each screen. For example, the screen configuration with the lowest compressor inlet Reynolds number index, screen No. 11, required the least amount of turbine inlet pressure to operate at

a given speed line. When comparing figures 93–102 to figure 38 by screen configuration, the turbine inlet total pressure deviation from the baseline at a given corrected rotor speed is seen to generally coincide with the Reynolds number index variation from unity at the same speed along the min-op line for a given screen.

Compressor Discharge and Nozzle Distortions

Compressor discharge total pressure and wall static pressure distortions for each screen configuration are compared with their respective simulator baseline envelopes in figures 103–113. The most significant compressor discharge total pressure distortion variations from the baseline distortion map were displayed by the circumferential screen configurations. This observation is evident in figure 103(a) and 104(a) for the circumferential distortion screens with high blockage areas, namely, screens Nos. 2 and 3. The compressor discharge-wall static pressure distortion remained relatively low (typically less than 3%), but displayed noticeable variations from the baseline distortion envelope for the circumferential distortion screens.

Dry nozzle entrance total temperature, wall static pressure, and total pressure distortion maps for each screen configuration are also compared with their respective simulator baseline envelopes in figures 114–135. The baseline temperature and total pressure distortion maps generally remained unaffected by the distortion screens. Similar to the compressor discharge distortion, the nozzle entrance-wall static pressure distortion remained low (less than 3%), and exhibited noticeable deviations from the baseline envelope for the circumferential screen configurations.

Simulator Malfunction

Figure 136 presents a time-history of vibration, aft bearing temperature, and physical rotor speed over a 45-sec time window at the time of the CMAPS SN/008/3 malfunction while testing the No. 7 screen configuration. At approximately 45 sec before the emergency shutdown (0 sec), the aft bearing temperature and vibration had begun to increase in normal response to the increasing rotor speed. At about 8 sec before shutdown, both aft bearing temperature and vibration briefly decreased for 1 sec, then continued to rise for another 3 sec. A rapid cooling of the aft bearing and a reduction in vibration followed for a period of 4 sec while the rotor speed continued to increase. At 1 sec before shutdown, the vibration peaked at about 18 g rms, which was detected by the CMAPS controller, effecting a subsequent simulator shutdown.

The large vibrations and aft bearing temperature rates were caused by the loss of a compressor blade in the fourth-stage rotor. After completing the CMAPS distortion test, the blade was found to be missing when the SN/008/3 compressor was inspected during disassembly. The compressor blade did not likely fail due to the particular distortion screen configuration being tested at the time of failure (No. 7), since the same screen was again tested on SN/006/3 without similar operating difficulties occurring. The blade apparently failed from cyclic fatiguing as a result of prolonged simulator operation under inlet flow distortion and repeated emergency shutdowns. In past CMAPS tests at AEDC, high cyclic fatigue caused compressor rotor blade failures. These tests showed that pressure perturbations produced upstream of the CMAPS compressor inlet were detrimental to the fatigue life of the compressor blades. Flow disturbances entering the compressor can excite the natural frequencies of the blades within a

stage into various flex modes, ultimately leading to a catastrophic blade failure. Blade failures have usually propagated from surface imperfections located near the blade root.

Compressor Airflow Calibration: Development of Methods

Four methods for calibrating the CMAPS compressor airflow were developed; they followed schemes similar to those introduced in references 4–6. The methods were based on direct compressor inlet and discharge measurements, the simulator entering/exiting flow balance relationship, and a correlation between the sea level-corrected airflow and mixer pressure. The results from each method were obtained in the form of a flow coefficient defined by the ratio of the method's calculated airflow to the calibrated bellmouth-measured airflow.

The calibrated bellmouth airflow $\dot{w}_{1,c}$ was used as the reference airflow for comparing the results from the different CMAPS compressor airflow calibration methods. This airflow was calculated from

$$\dot{w}_{1,c} = C_{f1} \dot{w}_{1,m} \quad (1)$$

where C_{f1} is the bellmouth flow coefficient and $\dot{w}_{1,m}$ is the measured (uncorrected) bellmouth airflow. From the calibration results reported in reference 11, C_{f1} was expressed as a polynomial function of the bellmouth Mach number M_1 , as determined from the measured bellmouth total and static pressures, P_{t1} and P_{s1} , respectively:

$$M_1 = \sqrt{\left(\frac{2}{\gamma - 1}\right) \left[\left(\frac{P_{t1}}{P_{s1}}\right)^{\frac{\gamma - 1}{\gamma}} - 1 \right]} \quad (2)$$

$$C_{f1} = a_0 + a_1 M_1 + a_2 M_1^2 + a_3 M_1^3 \quad (3)$$

where the values for the polynomial coefficients $a_0 \dots a_3$ are provided in appendix B. The $\dot{w}_{1,m}$ term was calculated from the one-dimensional, isentropic weight-flow expression,

$$\dot{w}_{1,m} = \sqrt{\frac{\gamma g}{RT_{t1}}} A_1 P_{t1} M_1 \left(\frac{P_{s1}}{P_{t1}}\right)^{\frac{\gamma + 1}{2\gamma}} \quad (4)$$

where γ , g , and R are constants; A_1 is the bellmouth throat (Plane 1) flow area; and T_{t1} is the bellmouth inlet total temperature.

Compressor Inlet

Two schemes were used to determine the CMAPS compressor airflow based on the Plane 2 pressure measurements: averaging the total and static pressures; and summing area-weighted flow elements determined from discrete pressure measurements.

The compressor inlet airflow $\dot{w}_{2,a}$, obtained from the averaged Plane 2 pressure measurements, was determined from

$$\dot{w}_{2,a} = \sqrt{\frac{\gamma g}{RT_{t1}}} A_2 \bar{P}_{t2} M_2 \left(\frac{\bar{P}_{s2}}{\bar{P}_{t2}}\right)^{\frac{\gamma + 1}{2\gamma}} \quad (5)$$

where A_2 is the compressor inlet flow area, M_2 is the compressor inlet Mach number given by

$$M_2 = \sqrt{\left(\frac{2}{\gamma - 1}\right) \left[\left(\frac{\bar{P}_{t2}}{\bar{P}_{s2}}\right)^{\frac{\gamma - 1}{\gamma}} - 1 \right]} \quad (6)$$

and \bar{P}_{t2} and \bar{P}_{s2} are the Plane 2 area-weighted average total pressure and average wall static pressure, respectively. Using equation (1), the compressor flow coefficient $C_{f2,a}$, calculated from the averaged Plane 2 pressures, was defined by

$$C_{f2,a} = \frac{\dot{w}_{2,a}}{\dot{w}_{1,c}} \quad (7)$$

The measured compressor inlet airflow obtained from the summation of discretized flow elements was based on the model depicted in figure 137. Each area-weighted flow element, $\dot{w}_2(k)$, was centered on a Plane 2 total pressure probe such that the composite airflow, $\dot{w}_{2,sum}$, could be expressed as

$$\dot{w}_{2,sum} = \sum_{k=1}^{40} \dot{w}_2(k) = \sqrt{\frac{\gamma g}{RT_{t1}}} \frac{A_2}{40} \sum_{i=1}^5 \sum_{j=1}^8 P_{t2}(i,j) M_2(i,j) \left[\frac{P_{s2}(j)}{P_{t2}(i,j)} \right]^{\frac{\gamma + 1}{2\gamma}} \quad (8)$$

where

$$M_2(i,j) = \sqrt{\left(\frac{2}{\gamma - 1}\right) \left[\left(\frac{P_{t2}(i,j)}{P_{s2}(j)}\right)^{\frac{\gamma - 1}{\gamma}} - 1 \right]} \quad (9)$$

and i and j are the radial and circumferential indices, respectively, based on figure 137. In equation (8) it was assumed that the compressor inlet static pressure varied circumferentially, only. Using equations (1) and (8), the compressor flow coefficient $C_{f2,sum}$, calculated from the composite airflow in equation (8), was expressed as

$$C_{f2,sum} = \frac{\dot{w}_{2,sum}}{\dot{w}_{1,c}} \quad (10)$$

Compressor Discharge

The measured compressor discharge (Plane 15) airflow $\dot{w}_{15,m}$ was determined from

$$\dot{w}_{15,m} = \sqrt{\frac{\gamma g}{RT_{t15}}} A_{15} \bar{P}_{t15} M_{15} \left(\frac{\bar{P}_{s15}}{\bar{P}_{t15}} \right)^{\frac{\gamma + 1}{2\gamma}} \quad (11)$$

where A_{15} is the compressor discharge flow area, T_{t15} is the compressor discharge total temperature, M_{15} is the compressor discharge Mach number given by

$$M_{15} = \sqrt{\left(\frac{2}{\gamma - 1}\right) \left[\left(\frac{\bar{P}_{t15}}{\bar{P}_{s15}}\right)^{\frac{\gamma - 1}{\gamma}} - 1 \right]} \quad (12)$$

and \bar{P}_{t15} and \bar{P}_{s15} are the averaged Plane 15 total and static pressures, respectively. The compressor inlet airflow $\dot{w}_{2,15}$, determined from the measured discharge airflow in equation (11), could be obtained from

$$\dot{w}_{2,15} = \dot{w}_{15,m} - \dot{w}_{par} \quad (13)$$

where \dot{w}_{par} is the parasitic airflow entering the compressor discharge from the turbine through the labyrinth of seals within the CMAPS rotor assembly. Since the parasitic flow was not accounted for in this test, the compressor flow coefficient $C_{f2,15}$, based on the compressor discharge, was calculated as

$$C_{f2,15} = \frac{\dot{w}_{15,m}}{\dot{w}_{1,c}} \quad (14)$$

Flow Balance

The compressor inlet, drive, bleed, and nozzle flow-balance relationship is graphically illustrated in figure 138. Based on this figure, the compressor inlet airflow $\dot{w}_{2,db8}$ could be expressed in terms of the remaining flows entering/exiting the simulator; namely, turbine drive flow, \dot{w}_d ; turbine bleed flow, \dot{w}_b ; and the calibrated nozzle flow, $\dot{w}_{8,c}$. The resulting expression was

$$\dot{w}_{2,db8} = \dot{w}_{8,c} + \dot{w}_b - \dot{w}_d \quad (15)$$

and the compressor flow coefficient $C_{f2,db8}$ was determined from

$$C_{f2,db8} = \frac{\dot{w}_{2,db8}}{\dot{w}_{1,c}} \quad (16)$$

The drive and bleed flow were each measured by sonic-throat venturi flowmeters. The calibrated nozzle flow was calculated from

$$\dot{w}_{8,c} = C_{f8} \dot{w}_{8,m} \quad (17)$$

where C_{f8} is the nozzle flow coefficient and $\dot{w}_{8,m}$ is the uncalibrated (measured) nozzle flow. The nozzle flow coefficient was determined by ratioing the uncalibrated nozzle flow ($\dot{w}_{8,m}$) to the actual nozzle flow, $\dot{w}_{8,ref}$:

$$C_{f8} = \frac{\dot{w}_{8,m}}{\dot{w}_{8,ref}} \quad (18)$$

The actual nozzle flow was calculated by considering the calibrated bellmouth flow in the CMAPS flow-balance relation:

$$\dot{w}_{8,ref} = \dot{w}_{1,c} + \dot{w}_d - \dot{w}_b \quad (19)$$

Unlike reference 6, in which choked and unchoked nozzle throat flow conditions were considered, the uncalibrated nozzle flow was determined by assuming sonic flow at the nozzle throat throughout the entire CMAPS operating envelope. By using this assumption, the nozzle-entrance-wall static pressure measurement uncertainty (due to nozzle flow distortion) was not introduced into the nozzle flow calculation. Hence, $\dot{w}_{8,m}$ was defined by the critical-flow function

$$\dot{w}_{8,m} = \left(\frac{\gamma + 1}{2} \right)^{\frac{\gamma + 1}{2(1 - \gamma)}} \sqrt{\frac{\gamma g}{RT_{t15}}} A_8 \bar{P}_{t7} \quad (20)$$

where A_8 is the nozzle throat flow area, T_{t15} is the compressor discharge total temperature, and \bar{P}_{t7} is the averaged nozzle entrance total pressure ($P_{t8} = \bar{P}_{t7}$ assumed). Since the Plane 7 instrumentation was sensitive to the compressor discharge flow, the stable Plane 15 total temperature was used in equation (20) as a substitute for the averaged Plane 7 total temperature. Ideally, the averaged Plane 7 total temperature should have been used in this equation, but the total temperature distortion within the nozzle (up to 80%, as previously mentioned) would have subjected the nozzle flow calculation to a large measurement uncertainty.

The result of using the averaged Plane 7 total temperature in place of the compressor discharge total temperature in the nozzle critical-flow function is shown in figure 139. This figure shows the nozzle flow coefficient distribution expressed as a function of the nozzle pressure ratio for both CMAPS's in the baseline configuration. The large nozzle flow coefficient dispersion reflects the total temperature distortion at the nozzle entrance caused by the inadequate mixing of turbine and compressor discharge flows emanating from the mixer. In contrast, figure 140 shows a more uniform nozzle flow coefficient distribution based on the compressor discharge total temperature in the nozzle critical-flow function.

From the nozzle flow coefficient distribution in figure 140, C_{f8} was determined as a polynomial function of the nozzle pressure ratio, \bar{P}_{t7}/P_∞ :

$$C_{f8} = b_0 + b_1 \left(\frac{\bar{P}_{t7}}{P_\infty} \right) + b_2 \left(\frac{\bar{P}_{t7}}{P_\infty} \right)^2 + b_3 \left(\frac{\bar{P}_{t7}}{P_\infty} \right)^3 \cdots + b_n \left(\frac{\bar{P}_{t7}}{P_\infty} \right)^n, n = 10 \quad (21)$$

The values for the polynomial coefficients $b_0 \dots b_{10}$ are provided in appendix B. By expressing the nozzle flow coefficient as a function the nozzle pressure ratio, the calibrated nozzle flow could be calculated to determine the compressor airflow (by means of the flow-balance relation in equation (15)).

Mixer Pressure Correlation

The correlation between the compressor airflow and mixer pressure was developed by a method similar to the one discussed in reference 6. The basis for this correlation depends on the indirect relationship between the compressor airflow and the mixer pressure. The addition of turbine discharge flow through the mixer into the nozzle back-pressures the compressor, affecting the amount of inlet airflow that can be pumped by the compressor. Since the mixer pressure indicates the amount of turbine flow that is discharged into the nozzle, the mixer pressure also indirectly measures the compressor airflow.

The correlation map for the sea level-corrected compressor airflow $\dot{w}_2 \sqrt{\theta_2} / \delta_2$ (as determined from the calibrated bellmouth flowmeter and averaged Plane 2 total pressure) and the corrected mixer pressure P_{s57} / δ_2 is shown in figure 141 for CMAPS's SN/006/3 and SN/008/3. The sea level-referenced pressure ratio δ_2 and temperature ratio θ_2 were calculated, respectively, from the area-weighted average Plane 2 total pressure and bellmouth inlet total temperature,

$$\delta_2 = \frac{\bar{P}_{t2}}{P_{sl}} \quad (22)$$

$$\theta_2 = \frac{T_{t1}}{T_{sl}} \quad (23)$$

where P_{sl} and T_{sl} are the referenced sea level standard pressure and temperature, respectively.

For corrected rotor speeds less than 100%, a polynomial regression was obtained for each curved speed line in the compressor airflow-mixer pressure correlation map to express the compressor inlet corrected airflow, $\dot{w}_2\sqrt{\theta_2}/\delta_2$, as a second-order polynomial function of P_{s57}/δ_2 :

$$\frac{\dot{w}_2\sqrt{\theta_2}}{\delta_2} = c_0 + c_1 \left(\frac{P_{s57}}{\delta_2} \right) + c_2 \left(\frac{P_{s57}}{\delta_2} \right)^2 \quad (24)$$

The coefficients in equation (24) were expressed as polynomial functions of the percent corrected rotor speed ($N/(N_{des}\sqrt{\theta_2})$) to model the speed-line curvatures of each simulator:

$$c_k = d_0 + d_1 \left(\frac{N}{N_{des}\sqrt{\theta_2}} \right) + d_2 \left(\frac{N}{N_{des}\sqrt{\theta_2}} \right)^2 + \dots + d_l \left(\frac{N}{N_{des}\sqrt{\theta_2}} \right)^l \quad (25)$$

where $l = 2, 6, 5$ for $k = 0, 1, 2$, respectively. The corrected airflow for corrected rotor speeds greater than or equal to 100% was determined from a polynomial regression of the corrected airflow-rotor speed relation along the min-op line shown in figure 142 for both CMAPS's SN/006/3 and SN/008/3:

$$\frac{\dot{w}_2\sqrt{\theta_2}}{\delta_2} = e_0 + e_1 \left(\frac{N}{N_{des}\sqrt{\theta_2}} \right) + e_2 \left(\frac{N}{N_{des}\sqrt{\theta_2}} \right)^2 + \dots + e_m \left(\frac{N}{N_{des}\sqrt{\theta_2}} \right)^m, m = 5 \quad (26)$$

Numerical values for the polynomial coefficients d_l and e_m are given in appendix B. By combining either equation (24) or (26) with equation (1), the corresponding compressor flow coefficient $C_{f2,57}$ was determined from

$$C_{f2,57} = \frac{\dot{w}_2}{\dot{w}_{1,c}} \quad (27)$$

Compressor Airflow Calibration: Evaluation of Methods

A dispersion about the mean compressor flow coefficient was obtained for each method over a range of CMAPS data. To determine the effect of compressor inlet flow distortion on a method's accuracy, two dispersions were obtained from combined CMAPS SN/006/3 and SN/008/3 data: one for the baseline configuration only, and the other for the baseline and distortion screen configurations. From each flow coefficient dispersion, the approximate dispersion range and the rms error (square-root of the statistical variance as a percentage of the mean) were obtained to evaluate the accuracy of each method.

Compressor Inlet

Figure 143 represents the compressor flow coefficient distribution for the baseline configuration as determined from averaged Plane 2 total and static pressures for CMAPS's SN/006/3 and SN/008/3. The corresponding dispersion shown in figure 144(a) has an approximate range of $\pm 9\%$ and a 2.61% rms error based on the mean flow coefficient of 1.024. However, the flow coefficient dispersion in figure 144(b) for all distortion screen configurations, combined with the baseline, yields a larger dispersion range and rms error of $\pm 11\%$ and 3.39%, respectively, based on the mean flow coefficient of 1.063. The broader

dispersion range is not due to random data scatter; rather, it is a result of a flow coefficient biasing (from the baseline coefficient distribution) obtained from the tip-radial distortion screen configurations.

An example of the compressor flow coefficient biasing for tip-radial distortion screens is shown in figure 145, in which the flow coefficient distribution for screen No. 8 and the baseline distribution are compared. The flow coefficient distribution for screen No. 8 was about 13% higher than the distribution for the baseline configuration. Further evidence of flow coefficient biasing is presented in figure 146, in which the mean compressor flow coefficient and the corresponding rms error of each screen configuration to the baseline configuration are compared. The flow coefficient bias for each screen was independent of the associated rms error magnitude (typically less than 3%). Distortion screens with a large, tip-radial circumferential extent (such as screens Nos. 2 and 8) exhibited the greatest flow coefficient bias from the baseline configuration (screen No. 1). The spoiled flow concentrated along the compressor inlet wall downstream from these screens affected the Plane 2 wall-static pressure measurements. Therefore, the measured static pressure was lower than what would have been measured near the compressor hub. Hence, the calculated compressor airflow based on the averaged Plane 2 wall static pressure was higher than the actual calibrated bellmouth airflow, yielding the flow coefficient biases observed for the tip-radial distortion screens.

The effect of the tip-radial distortion screens on the calculated compressor flow coefficient can be characterized by the ratio of the averaged compressor inlet-wall static pressure to the mass-averaged static pressure. This ratio indicates the sensitivity of the Plane 2 wall static pressure measurements to tip-radial flow distortion (flow spoilage locally concentrated at the compressor wall). The mass-averaged static pressure was determined by applying a Newton-Raphson numerical iteration (ref. 17) to an analytical function representing the difference between the uncorrected (ideal) compressor airflow and the calibrated bellmouth airflow. The method used to obtain the mass-averaged static pressure is described in appendix C. Figure 147 shows the flow coefficient as a function of the static pressure ratio. For a given screen configuration, the static pressure ratio increased with increasing compressor airflow. At a constant corrected rotor speed, the lowest mass-averaged static pressure ratios were obtained for tip-radial distortion screens with large circumferential extents, namely, screens Nos. 2, 8, and 9. These low static pressure ratios correspond to the large compressor flow coefficient biases observed in figure 146 for the above three distortion screens.

For a more precisely averaged compressor inlet total pressure, a two-dimensional, bivariate interpolation using Hardy's multiquadratic method (ref. 18) was applied to the 40 Plane 2 total pressures that were measured. The interpolation provided pressure values for 1160 discrete, area-weighted points at Plane 2. For most screen configurations, the averaged 1160-point total pressure differed by less than $\pm 0.2\%$ from the average of the 40 area-weighted total pressure measurements. The resulting changes in compressor flow coefficient were less than $\pm 1\%$ using the interpolated average total pressure relative to the averaged (measured) wall static pressure. Spatial interpolation of the measured Plane 2 total pressures had little effect on reducing the inlet flow coefficient biasing error.

The inlet flow coefficient distribution from summed compressor inlet flow elements is presented in figure 148 for CMAPS's SN/006/3 and SN/008/3 under the baseline inlet configuration. The corresponding dispersion shown in figure 149(a) has an approximate dispersion range of $\pm 6\%$ and a 2.49% rms error based on an average flow coefficient of 1.022. The flow coefficient dispersion in figure 149(b)

for all screen configurations (combined with the baseline) yields a respectively larger dispersion range and rms error of $\pm 9\%$ and 2.99% based on a mean flow coefficient of 1.045:

Since this method also relied on the measured Plane 2 wall static pressures, the biasing effect was present for tip-radial distortion screen configurations. Figure 150 compares the mean flow coefficient and rms error for each screen configuration with the baseline configuration. The flow coefficient bias per screen is similar to the bias distribution observed in figure 146.

Compressor Discharge

From the compressor discharge method, the compressor flow coefficient distribution for the baseline configuration is presented in figure 151 for CMAPS's SN/006/3 and SN/008/3. Based on the mean flow coefficient of 1.037, the associated dispersion in figure 152(a) has a respective range and rms error of $\pm 4\%$ and 1.88% . The dispersion for all distortion screens, including the baseline configuration, is shown in figure 152(b). This latter dispersion has a range and rms error of $\pm 7\%$ and 1.95% , respectively, based on the mean flow coefficient of 1.043. Unlike the direct compressor inlet measurement methods, no significant compressor flow coefficient bias was obtained from the compressor discharge flow method. The observed flow coefficient dispersion primarily reflects the effect of compressor discharge flow distortion on Plane 15 temperature and pressure measurements.

Because of the labyrinth of seals within the rotor hardware assembly, internal parasitic airflow from the turbine leaking through the aft bearing and entering the compressor discharge region was also measured by the Plane 15 instrumentation. This parasitic flow could be determined by subtracting the calibrated bellmouth flow from the measured compressor discharge flow. However, as recognized in references 4 and 6, the distortion in the compressor discharge flow would translate into a significant parasitic flow measurement uncertainty. Thus, the parasitic airflow was not considered in this test.

Flow Balance

The compressor flow coefficient distribution determined from the flow-balance relationship for the baseline configuration is presented in figure 153 for CMAPS's SN/006/3 and SN/008/3. The associated dispersion in figure 154(a) has a range and rms error of $\pm 5\%$ and 2.20% , respectively, based on the average compressor flow coefficient of 1.009. The overall dispersion for all distortion screens, including the baseline configuration, is shown in figure 154(b). This overall dispersion has a range and rms error of $\pm 6\%$ and 1.78% , respectively, based on the mean compressor flow coefficient of 1.000.

As discussed in reference 6, the errors from the flow-balance method result from the accumulation of drive, bleed, and nozzle flow measurement errors. The uncertainty of the Plane 7 total pressure measurements, a result of the flow distortion within the nozzle, contributed to the nozzle flow measurement error. Another contributor to the error was the airflow leakage from the turbine into the oil scavenge system. During oil scavenging, the scavenge system captured high-pressure air from the turbine through the seals leading to the aft bearing. From scavenge airflow measurements performed in reference 4, this parasitic flow was measured and found to be less than 0.002 lbm/sec. Despite its presence, the turbine flow leakage could be considered negligible, relative to the level of distortion-related flow-measurement error encountered within the nozzle.

Mixer Pressure Correlation

The baseline compressor flow coefficient distribution determined from the baseline corrected mixer pressure-compressor airflow correlation map is presented in figure 155 for CMAPS's SN/006/3 and SN/008/3. The associated dispersion in figure 156(a) based on the average flow coefficient of 0.999 has a range and rms error of $\pm 2\%$ and 0.74%, respectively. The overall dispersion for all distortion screens, including the baseline configuration, is shown in figure 156(b), which has a range and rms error of $\pm 3\%$ and 1.11%, respectively, based on the mean flow coefficient of 1.005.

Since the 40 total pressure measurements at the compressor inlet provided a reasonably accurate pressure field survey, this method was very stable. The flow coefficient errors from the mixer pressure-compressor airflow correlation method could have been caused by the coupled variation of both compressor inlet total pressure distortion and Reynolds number index. In reference 6, mixer pressure-compressor airflow correlation maps (obtained at constant inlet total pressures) were obtained for a reheat mixer/nozzle configuration. From these maps, corrections for Reynolds number index variations were applied to the correlation method. A similar Reynolds number index correction could not be applied to the compressor airflow-mixer pressure correlation for this distortion test since a constant compressor inlet total pressure could not be maintained in the presence of a distortion screen.

Method Summary

Of the four compressor airflow calibration methods presented, the compressor airflow-mixer pressure correlation method was the most accurate, yielding the least compressor flow coefficient dispersion and the smallest rms error for combined baseline and distortion screen configuration data. Conversely, the direct compressor airflow measurement method using the averaged Plane 2 pressures was the least accurate, producing the largest flow coefficient dispersion and rms error for combined baseline and distortion screen configuration data. A statistical summary of the flow coefficient dispersions and errors is presented in table 7 for all methods. The coupled flow distortion and varying Reynolds number index produced larger flow coefficient dispersions and errors for the distortion screen data than for the baseline configuration data. Because of the sea level static nature of this test, the CMAPS compressor inlet total pressure could not be controlled during simulator operation with distortion screens. Thus, the effect of compressor inlet distortion on the airflow calibration methods (and the CMAPS performance parameters) could not be clearly distinguished from the effect of distortion screen-related Reynolds number index variations.

From an instrumentation-requirement perspective, the compressor discharge flow calibration method required the fewest CMAPS-related measurements. A quantitative description of the measurements required to support each method is presented in table 8. In future CMAPS tests in which physical instrumentation interface limitations or model size restrictions exist, the number of measurements could be reduced by manifolding multiple-pressure hardware at each CMAPS instrument plane. Simulator calibration with the simplified hardware would be required to determine the effect of pressure-instrumentation reduction on measured CMAPS performance parameters and on compressor airflow calibration methods.

CONCLUSIONS

Two Compact Multimission Aircraft Propulsion Simulator (CMAPS) units in the dry power configuration were statically tested at sea level (ambient) conditions for uniform and distorted compressor inlet flow. Baseline operating characteristics and performance envelopes for each simulator generally conformed to previously demonstrated operating "norms." With distortion screens present, deviations from the baseline operating characteristics and performance envelopes could be mainly attributed to a varying compressor inlet Reynolds number index coupled with the total pressure distortion. Approximate compressor inlet Reynolds number index and total pressure distortion extremes were 0.63 and 35%, respectively, over the range of distortion screen configurations tested. The Plane 2 pressure measurements were affected by the relative position of the distortion screen with respect to the measurement location. Compressor inlet wall static pressure measurements were radially biased, especially in the presence of tip-radial pressure distortion. The average static pressure measured at the compressor inlet might be improved by including static pressure instrumentation near the compressor hub, perhaps using pitot-static tubes. The blade failure on CMAPS SN/008/3 indicates that prolonged simulator operation under distorted inlet flow conditions severely deteriorates the physical integrity of the overall compressor rotor/stator-blade assembly.

Four methods for determining the CMAPS compressor airflow were assessed against the airflow measured by a calibrated bellmouth flowmeter. The methods relied on direct compressor inlet and discharge measurements, a balance of flows entering/exiting the simulator, and a correlation between the corrected mixer pressure and the compressor corrected airflow. Of the four, the compressor airflow-mixer pressure correlation method produced the most promising results for determining the CMAPS compressor airflow with inlet flow distortion. This method yielded a flow coefficient of 1.005, accurate to within $\pm 3\%$ of the actual compressor airflow over the entire range of flow distortion to which both simulators were subjected.

The results obtained from this sea-level static CMAPS calibration demonstrate that further CMAPS testing with inlet flow distortion should be conducted to independently assess the effects of Reynolds number index and flow distortion on simulator performance. Such an investigation will require a flow-regulation and conditioning system at the inlet to control the compressor inlet total pressure. Future CMAPS tests could evaluate the effect of instrument hardware reduction on simulator measurements and compressor airflow calibration accuracy in the presence of inlet flow distortion. Accelerometer and aft bearing load cell operating difficulties experienced during this CMAPS test should be resolved to obtain accurate vibration and rotor-thrust maps when inlet flow distortion is present. Most important, continuous simulator operation with distorted inlet flow should be minimized to avoid catastrophic compressor blade failure.

APPENDIX A

COLOR IMAGING SCHEME

The compressor inlet total pressure distribution was interpolated based on the 40 pressure measurements at Plane 2. Each pressure was nondimensionalized by dividing it by the average compressor inlet total pressure and subtracting the quantity by one. This eliminated inlet total pressure recovery effects and preserved the spatial pressure caused by the distortion screens. Interpolation was performed by applying a Hardy's bivariate least squares fit (described in reference 18) to the pressure coefficients based on corresponding rake probe locations (described in a Cartesian coordinate frame centered on the compressor inlet hub). The fit was evaluated on a polar mesh grid containing 1160 area-weighted nodes (29 nodes radially, 40 nodes circumferentially) to obtain a finer pressure distribution. A color-contouring algorithm was applied to the mesh to view the Plane 2 total pressure distribution. The algorithm assigned a color panel to each node to create a network representing the compressor inlet. The colors corresponding to the maximum and minimum pressure coefficients were red and blue, respectively, with intermediate colors of yellow, green, and cyan.

APPENDIX B

NUMERICAL VALUES FOR POLYNOMIAL COEFFICIENTS

The following are numerical values for the various polynomial coefficients that were introduced by the CMAPS airflow calibration methods. Where applicable, two values are provided for each coefficient, one for CMAPS SN/006/3 and one for SN/008/3.

<u>Coefficients for equation (3)</u>	a_0 :	0.951053	
	a_1 :	0.144420	
	a_2 :	-0.322058	
	a_3 :	0.239397	
<u>Coefficients for equation (21)</u>		SN/006/3	SN/008/3
	b_0 :	1.090550E+02	1.008453E+02
	b_1 :	-3.509922E+02	-3.190921E+02
	b_2 :	4.680689E+02	4.160867E+02
	b_3 :	-3.180884E+02	-2.713101E+02
	b_4 :	1.015164E+02	7.573377E+01
	b_5 :	1.503457E+00	1.069618E+01
	b_6 :	-1.295843E+01	-1.518924E+01
	b_7 :	4.505725E+00	4.905617E+00
	b_8 :	-6.753313E-01	-7.329395E-01
	b_9 :	3.741917E-02	4.357061E-02
	b_{10} :	3.301665E-04	0.000000E+00
<u>Coefficients for equation (25)</u>		for c_0 :	
		SN/006/3	SN/008/3
	d_0 :	-3.791790E-01	-1.200455E-01
	d_1 :	2.523812E-02	1.907713E-02
	d_2 :	-4.870541E-05	-1.489661E-05

	for c_1 :	
	SN/006/3	SN/008/3
d_0 :	-2.074029E+00	-1.017266E+00
d_1 :	1.790309E-01	8.514333E-02
d_2 :	-6.406077E-03	-2.963753E-03
d_3 :	1.215981E-04	5.494517E-05
d_4 :	-1.2491058E-06	-5.723010E-07
d_5 :	7.268301E-09	3.175352E-09
d_6 :	-1.694689E-11	-7.329464E-12

	for c_2 :	
	SN/006/3	SN/008/3
d_0 :	-2.378614E-04	-1.647479E-04
d_1 :	1.790657E-05	1.159145E-05
d_2 :	-5.311305E-07	-3.319890E-07
d_3 :	7.714765E-09	4.767126E-09
d_4 :	-3.421451E-11	9.798667E-14
d_5 :	1.547967E-13	-5.504081E-11

	for e :	
	SN/006/3	SN/008/3
e_0 :	-1.274475E+01	-8.281046E+00
e_1 :	9.227213E-01	5.960059E-01
e_2 :	-2.500744E-02	-1.573174E-02
e_3 :	3.337527E-04	2.061619E-04
e_4 :	-2.151241E-06	-1.299952E-06
e_5 :	5.355603E-09	3.147718E-09

Coefficients for equation (26)

APPENDIX C

MASS-AVERAGED COMPRESSOR INLET STATIC PRESSURE

The mass-averaged compressor inlet static pressure $P_{s2,i}$ was calculated by applying the Newton-Raphson iteration method (ref. 17) to an analytical function that represented the difference between equations (1) and (5). The iteration was performed for an initially “guessed” Mach number, $M_{2,io}$, to arrive at a successive value, $M_{2,i}$, from which $P_{s2,i}$ could be obtained.

The Mach number used for the iteration is given by

$$M_{2,i} = M_{2,io} - \frac{F}{F'} \quad (C-1)$$

where F is the analytical function defined for a constant $\dot{w}_{1,c}$ as

$$F = \dot{w}_{2,i} - \dot{w}_{1,c} \quad (C-2)$$

and where $\dot{w}_{2,i}$ is the ideal compressor airflow given by

$$\dot{w}_{2,i} = \sqrt{\frac{\gamma g}{RT_{t1}}} A_2 \bar{P}_{t2} M_{2,io} \left(1 + \frac{\gamma - 1}{2} M_{2,io}^2\right)^{\frac{\gamma + 1}{2(1 - \gamma)}} \quad (C-3)$$

and where F' is the derivative of F with respect to $M_{2,io}$:

$$F' = \sqrt{\frac{\gamma g}{RT_{t1}}} A_2 \bar{P}_{t2} \left[\left(1 + \frac{\gamma - 1}{2} M_{2,io}^2\right)^{\frac{\gamma + 1}{2(1 - \gamma)}} - \frac{\gamma + 1}{2} M_{2,io}^2 \left(1 + \frac{\gamma - 1}{2} M_{2,io}^2\right)^{\frac{3\gamma - 1}{2(1 - \gamma)}} \right] \quad (C-4)$$

Iteration convergence was obtained by setting the Mach number iteration error $\Delta M_{2,i} = M_{2,i} - M_{2,io}$, to 0.00001. The $P_{s2,i}$ term was then obtained from $M_{2,i}$ and \bar{P}_{t2} , using the isentropic relation,

$$P_{s2,i} = \bar{P}_{t2} \left(1 + \frac{\gamma - 1}{2} M_{2,i}^2\right)^{\frac{\gamma}{1 - \gamma}} \quad (C-5)$$

REFERENCES

1. Darlington, C. R.; Brooksbank, R. M.; and Brooks, J. O.: Component Performance and Stability Characteristics of an Engine Propulsion Simulator with Uniform and Distorted Inlet Pressure Profiles at Reynolds Number Indices of 0.39, 0.78, and 0.91. AEDC-TR73-172, Mar. 1974.
2. Eigenmann, M. R.; and Bailey, R. O.: Development of the Propulsion Simulator: a Test Tool Applicable to V/STOL Configurations. SAE Paper 770984, Nov. 1977.
3. Bailey, R. O.; Harper, M.; and Jannetta, T.: Evaluation of Turbo-Propulsion Simulators as a Testing Technique for Fighter Aircraft. AIAA Paper 79-1149, 1979.
4. Hoff, G. E.; and Few, T. L.: Compact Multimission Aircraft Propulsion Simulator Aero/Mechanical Test Results and Evaluation. General Electric TM No. 81-797, Evandale, OH, Mar. 1982.
5. Wagenknecht, C. D.; and Hoff, G. E.: Performance Calibration Results for a Compact Multimission Aircraft Propulsion Simulator. AIAA Paper 82-0254, 1982.
6. Smith, S. C.: Determining Compressor Inlet Airflow in the Compact Multimission Aircraft Propulsion Simulators in Wind Tunnel Applications. AIAA Paper 83-1231, 1983.
7. Bailey, R.; Mraz, M.; and Hiley, P.: The Design of a Wind Tunnel VSTOL Fighter Model Incorporating Turbine Powered Engine Simulators. AIAA Paper 81-2635, 1981.
8. Bailey, R. O.; Smith, S. C.; and Gustie, J. B.: Propulsion Simulation Test Technique for V/STOL Configurations. SAE Paper 83-1427, Oct. 1983.
9. Zilz, D. E.; and Bailey, R. O.: The Investigation of Inlet/Nozzle Flowfield Coupling Using Compact Propulsion Simulators. NASA TM-84399, 1985.
10. Hoff, G. E.; Balan, C.; and Meade, R. J.: CMAPS Installed Performance Prediction Handbook (Task D Final Report). General Electric TM 86-535, Evandale, OH, Sept. 1986.
11. Smith, S. C.: Airflow Calibration of a Bellmouth Inlet for Measurements of Compressor Airflow in Turbine-Powered Propulsion Simulators. NASA TM-84399, 1985.
12. Calogeras, J. E.; Mehlic, C. M.; and Burstadt, P. L.: Experimental Investigation of the Effect of Screen-Induced Total-Pressure Distortion on Turbojet Stall Margin. NASA TM X-2239, 1971.
13. SWTS User's Manual and Operating Instructions (SWTS Version 4.3). Report 7103-102/103, No. 36, Sterling Software, Palo Alto, CA, Apr. 1986.
14. Isaacson, C. C.: NASA-CMAPS Control System, Vols. I-III. NASA Contract No. NAS2-10793, McDonnell Douglas Corp., St. Louis, MO, Dec. 1982.
15. Harper, M.: The Propulsion Simulator Calibration Laboratory at Ames Research Center. AIAA Paper 82-0574, 1982.
16. Meade, R. J.; and Hoff, G. E.: CMAPS Operating "Norms" and Performance Handbook (Task A Final Report). General Electric Report NCR 86-01, Evandale, OH, Sept. 1986.

17. Maron, M. J.: Numerical Analysis, A Practical Approach. Macmillan Publishing Co., Inc., New York, 1982, pp. 48-53.
18. Kennelly, R.; and Saunders, D.: Aerodynamics Division Software Library. Report 7104-307, No. 16, Sterling Federal Systems, Inc., Palo Alto, CA, Apr. 1987.

Table 1. Distortion screen geometric properties











SCREEN NO.	GEOMETRY	CIRCUMFERENTIAL EXTENT	% BLOCKAGE AREA	SHAPE
2	CIRCUMFERENTIAL	180°	50	
3		90°	25	
4		60°	17	
5		30°	8	
6	HUB RADIAL	360°	40	
7			20	
8	TIP RADIAL	360°	67	
9			30	
10	RADIAL/ CIRCUMFERENTIAL	HUB RADIAL 270° CIRCUM- FERENTIAL 90°	15 25	
11		HUB RADIAL 270° CIRCUM- FERENTIAL 90°	45 25	

Table 2. CMAPS instrumentation summary

Description	Parameter	Sensor type	Range
Plane 2 rake-base wall static pressure:			
Rake 1, 0°	PS2-1	PSI module No. 1	8–15 psia
Rake 2, 45°	PS2-2	PSI module No. 1	8–15 psia
Rake 3, 90°	PS2-3	PSI module No. 1	8–15 psia
Rake 4, 135°	PS2-4	PSI module No. 1	8–15 psia
Rake 5, 180°	PS2-5	PSI module No. 1	8–15 psia
Rake 6, 225°	PS2-6	PSI module No. 1	8–15 psia
Rake 7, 270°	PS2-7	PSI module No. 1	8–15 psia
Rake 8, 315°	PS2-8	PSI module No. 1	8–15 psia
Plane 2 total pressure:			
Rake 1, 0°	PT2-1-1	PSI module No. 1	10–15 psia
Rake 1, 0°	PT2-1-2	PSI module No. 1	10–15 psia
Rake 1, 0°	PT2-1-3	PSI module No. 1	10–15 psia
Rake 1, 0°	PT2-1-4	PSI module No. 1	10–15 psia
Rake 1, 0°	PT2-1-5	PSI module No. 1	10–15 psia
Rake 2, 45°	PT2-2-1	PSI module No. 1	10–15 psia
Rake 2, 45°	PT2-2-2	PSI module No. 1	10–15 psia
Rake 2, 45°	PT2-2-3	PSI module No. 1	10–15 psia
Rake 2, 45°	PT2-2-4	PSI module No. 1	10–15 psia
Rake 2, 45°	PT2-2-5	PSI module No. 1	10–15 psia
Rake 3, 90°	PT2-3-1	PSI module No. 1	10–15 psia
Rake 3, 90°	PT2-3-2	PSI module No. 1	10–15 psia
Rake 3, 90°	PT2-3-3	PSI module No. 1	10–15 psia
Rake 3, 90°	PT2-3-4	PSI module No. 1	10–15 psia
Rake 3, 90°	PT2-3-5	PSI module No. 1	10–15 psia
Rake 4, 135°	PT2-4-1	PSI module No. 1	10–15 psia
Rake 4, 135°	PT2-4-2	PSI module No. 1	10–15 psia
Rake 4, 135°	PT2-4-3	PSI module No. 1	10–15 psia
Rake 4, 135°	PT2-4-4	PSI module No. 1	10–15 psia
Rake 4, 135°	PT2-4-5	PSI module No. 1	10–15 psia

Table 2. Continued

Description	Parameter	Sensor type	Range
Plane 2 total pressure:			
Rake 5, 180°	PT2-5-1	PSI module No. 1	10–15 psia
Rake 5, 180°	PT2-5-2	PSI module No. 1	10–15 psia
Rake 5, 180°	PT2-5-3	PSI module No. 1	10–15 psia
Rake 5, 180°	PT2-5-4	PSI module No. 1	10–15 psia
Rake 5, 180°	PT2-5-5	PSI module No. 1	10–15 psia
Rake 6, 225°	PT2-6-1	PSI module No. 1	10–15 psia
Rake 6, 225°	PT2-6-2	PSI module No. 1	10–15 psia
Rake 6, 225°	PT2-6-3	PSI module No. 1	10–15 psia
Rake 6, 225°	PT2-6-4	PSI module No. 1	10–15 psia
Rake 6, 225°	PT2-6-5	PSI module No. 1	10–15 psia
Rake 7, 270°	PT2-7-1	PSI module No. 1	10–15 psia
Rake 7, 270°	PT2-7-2	PSI module No. 1	10–15 psia
Rake 7, 270°	PT2-7-3	PSI module No. 1	10–15 psia
Rake 7, 270°	PT2-7-4	PSI module No. 1	10–15 psia
Rake 7, 270°	PT2-7-5	PSI module No. 1	10–15 psia
Rake 8, 315°	PT2-8-1	PSI module No. 1	10–15 psia
Rake 8, 315°	PT2-8-2	PSI module No. 1	10–15 psia
Rake 8, 315°	PT2-8-3	PSI module No. 1	10–15 psia
Rake 8, 315°	PT2-8-4	PSI module No. 1	10–15 psia
Rake 8, 315°	PT2-8-5	PSI module No. 1	10–15 psia
Plane 2 wall static pressure:			
22.5°	PS2-0-1	Kulite	11–15 psia
67.5°	PS2-0-2	Kulite	11–15 psia
112.5°	PS2-0-3	Kulite	11–15 psia
157.5°	PS2-0-4	Kulite	11–15 psia
202.5°	PS2-0-5	Kulite	11–15 psia
247.5°	PS2-0-6	Kulite	11–15 psia
292.5°	PS2-0-7	Kulite	11–15 psia
337.5°	PS2-0-8	Kulite	11–15 psia

Table 2. Continued

Description	Parameter	Sensor type	Range
Plane 15 wall static pressure:			
Rake 1, 0°	PS15-1	PSI module No. 2	14–45 psia
Rake 3, 144°	PS15-3	PSI module No. 2	14–45 psia
Rake 5, 288°	PS15-5	PSI module No. 2	14–45 psia
Plane 15 total pressure:			
Rake 1, 0°	PT15-1-1	PSI module No. 2	14–50 psia
Rake 1, 0°	PT15-1-2	PSI module No. 2	14–50 psia
Rake 1, 0°	PT15-1-3	PSI module No. 2	14–50 psia
Rake 3, 144°	PT15-3-1	PSI module No. 2	14–50 psia
Rake 3, 144°	PT15-3-2	PSI module No. 2	14–50 psia
Rake 3, 144°	PT15-3-3	PSI module No. 2	14–50 psia
Rake 5, 288°	PT15-5-1	PSI module No. 2	14–50 psia
Rake 5, 288°	PT15-5-2	PSI module No. 2	14–50 psia
Rake 5, 288°	PT15-5-3	PSI module No. 2	14–50 psia
Plane 7 wall static pressure:			
36°	PS7-1	PSI module No. 2	14–55 psia
108°	PS7-2	PSI module No. 2	14–55 psia
180°	PS7-3	PSI module No. 2	14–55 psia
252°	PS7-4	PSI module No. 2	14–55 psia
324°	PS7-5	PSI module No. 2	14–55 psia
Plane 7 total pressure:			
Rake 1, 0°	PT7-1-1	PSI module No. 2	14–60 psia
Rake 1, 0°	PT7-1-2	PSI module No. 2	14–60 psia
Rake 1, 0°	PT7-1-3	PSI module No. 2	14–60 psia
Rake 1, 0°	PT7-1-4	PSI module No. 2	14–60 psia
Rake 1, 0°	PT7-1-5	PSI module No. 2	14–60 psia
Rake 1, 0°	PT7-1-6	PSI module No. 2	14–60 psia
Rake 1, 0°	PT7-1-7	PSI module No. 2	14–60 psia
Rake 1, 0°	PT7-1-8	PSI module No. 2	14–60 psia

Table 2. Continued

Description	Parameter	Sensor type	Range
Plane 7 total pressure:			
Rake 3, 144°	PT7-3-2	PSI module No. 2	14-60 psia
Rake 3, 144°	PT7-3-3	PSI module No. 2	14-60 psia
Rake 3, 144°	PT7-3-4	PSI module No. 2	14-60 psia
Rake 3, 144°	PT7-3-5	PSI module No. 2	14-60 psia
Rake 3, 144°	PT7-3-6	PSI module No. 2	14-60 psia
Rake 3, 144°	PT7-3-7	PSI module No. 2	14-60 psia
Rake 3, 144°	PT7-3-8	PSI module No. 2	14-60 psia
Rake 5, 288°	PT7-5-2	PSI module No. 2	14-60 psia
Rake 5, 288°	PT7-5-3	PSI module No. 2	14-60 psia
Rake 5, 288°	PT7-5-4	PSI module No. 2	14-60 psia
Rake 5, 288°	PT7-5-5	PSI module No. 2	14-60 psia
Rake 5, 288°	PT7-5-6	PSI module No. 2	14-60 psia
Rake 5, 288°	PT7-5-7	PSI module No. 2	14-60 psia
Rake 5, 288°	PT7-5-8	PSI module No. 2	14-60 psia
Turbine inlet total pressure	PT4	Kulite	0-1500 psia
Turbine exit total pressure	PT5	Kulite	0-1200 psia
Mixer slot static pressure	PS57A	Kulite	14-700 psia
Forward bearing oil differential pressure	OPF	Bell & Howell	±15 psid
Aft bearing oil differential pressure	OPA	Bell & Howell	±15 psid
Plane 15 dynamic pressure	PSK15	Kulite	0-5 RMS psid
Forward accelerometer	A1-2	Endevco	0-10 rms g

Table 2. Concluded

Description	Parameter	Sensor type	Range
Rotor thrust	RT	Load cell	+50 to -300 lbf
Rotor speed	NC1	Speed pickup	0-86,000 rpm
Plane 15 total temperature	TT15-2-3	Type E T/C	70-400°F
Turbine inlet total temperature	TT4	Type E T/C	70-200°F
Turbine exit total temperature	TT5	Type E T/C	-20 to +200°F
Forward bearing temperature	TB1M-1	Type E T/C	70-250°F
	TB1M-2	Type E T/C	70-250°F
Aft bearing temperature	TB2M-1	Type E T/C	70-250°F
	TB2M-2	Type E T/C	70-250°F
Plane 7 total temperature:			
Rake 2, 72°	TT7-2-2	Type E T/C	-30 to +300°F
Rake 2, 72°	TT7-2-3	Type E T/C	-30 to +300°F
Rake 2, 72°	TT7-2-4	Type E T/C	-30 to +300°F
Rake 2, 72°	TT7-2-5	Type E T/C	-30 to +300°F
Rake 2, 72°	TT7-2-6	Type E T/C	-30 to +300°F
Rake 2, 72°	TT7-2-7	Type E T/C	-30 to +300°F
Rake 2, 72°	TT7-2-8	Type E T/C	-30 to +300°F
Rake 4, 216°	TT7-4-2	Type E T/C	-30 to +300°F
Rake 4, 216°	TT7-4-3	Type E T/C	-30 to +300°F
Rake 4, 216°	TT7-4-4	Type E T/C	-30 to +300°F
Rake 4, 216°	TT7-4-5	Type E T/C	-30 to +300°F
Rake 4, 216°	TT7-4-6	Type E T/C	-30 to +300°F
Rake 4, 216°	TT7-4-7	Type E T/C	-30 to +300°F
Rake 4, 216°	TT7-4-8	Type E T/C	-30 to +300°F

Table 3. Facility instrumentation summary

Description	Parameter	Sensor type	Range
Tank total pressure	PT	Paroscientific	14–15 psia
	PTO	Kulite	14–15 psia
Ambient pressure	PAMB	Paroscientific	14–15 psia
Tank static pressure	PSO	Kulite	14–15 psia
Bellmouth total pressure	PT1	Paroscientific	14–15 psia
Bellmouth static pressure	PS1	Paroscientific	11–15 psia
Drive venturi static pressure	PDV	Paroscientific	14–2500 psia
Bleed venturi static pressure	PBV	Paroscientific	14–600 psia
Drive valve supply pressure	DVSP	Kulite	14–3000 psia
Tank total temperature	TTF	Type J T/C	70–120 °F
	TTO	Type J T/C	70–120 °F
Bellmouth total temperature	TT1	Type J T/C	70–120 °F

Table 4. Test matrix

Screen No.	Runs									
	Norms check	Min-op line	Stall line	Percent corrected speed						Full auto
				60	70	80	90	100	110	
1 ^a										
2	N/A									N/A
3	N/A									N/A
4	N/A									N/A
5	N/A									N/A
6	N/A									N/A
7	N/A									N/A
8	N/A									N/A
9	N/A									N/A
10	N/A									N/A
11	N/A									N/A

^aBaseline configuration (no screen).

Table 5. Completed run schedule

Screen No.	Runs										CMAPS S/N
	Norms check	Min-op line	Stall line	Percent corrected speed						Full auto	
				60	70	80	90	100	110		
1 ^a	2	2	4	5	6	7	8	9	10	11	008/3
	101	101	102	103	104	105	106	110	111	...	006/3
2	...	21	22	23	24	25	26	27	28	...	008/3
3	...	60	61	62	63	64	65	66	67	...	008/3
4	...	13	14	15	16	17	18	19	20	...	008/3
	...	112	113	114	115	116	117	118	119	...	006/3
5	...	52	53	54	55	56	57	58	59	...	008/3
6	...	29	30	31	32	33	34	35	36	...	008/3
7	...	68 ^b								...	008/3
	...	137	138	139	140	141	142	143	144	...	006/3
8	...	37	38	39	40	41	42	43		...	008/3
9	...	120	121-2	123	124	125	126	127	128	...	006/3
10	...	44	45	46	47	48	49	50	51	...	008/3
11	...	129	130	131	132	133	134	135	136	...	006/3

^aBaseline configuration (no screen).

^bCMAPS malfunction, operation discontinued.

Table 6. History of CMAPS powered operation

CMAPS S/N	Date	Clock at start	Clock at stop	Powered hours >35 krpm	Comments
008/3	8-26-88	2212	2321	0	Tach card adjustments at < 10 krpm
008/3	8-29-88	2038	2310	0	Tach card adjustments at < 10 krpm, controller limits adjustment
008/3	9-09-88	1708 2008	1855 2019	0	Tach card adjustments at < 15 krpm, controller limits adjustment, CMAPS hardware & instrument check
008/3	9-19-88	2226	2359	0	Tach card adjustments at < 30 krpm, controller limits adjustment, signal conditioning hardware adjustment
008/3	9-20-88	1640 2240	1925 2340	2.0 0.4	Baseline configuration: min-op line (F2:1T2:19), ^a norms check on TBA, TBF, RT, VIB
008/3	9-21-88	1646	2021	2.2	Baseline configuration: PSK15 limit adjustment, operation near stall, emergency shutdown from exceeding the set mixer pressure limit

Table 6. Continued

CMAPS S/N	Date	Clock at start	Clock at stop	Powered hours >35 krpm	Comments
008/3	9-22-88	1437 1721	1556 2045	0.2 2.3	Baseline configuration: begin stall line (F4:1T4:9), PSI module malfunction, rotor acceleration limit adjustment, emergency shutdown from exceeding aft bearing temperature and rate limits
008/3	9-23-88	1645	2250	3.8	Baseline configuration: finish stall line (F4:10T4:15), begin speed lines (F5:1T9:13)
008/3	9-26-88	1815	2345	2.1	Baseline configuration: finish speed lines (F10:1T10:19), large rotor thrust signal drift, emergency shutdown from: exceeding aft bearing temperature and rate limits; exceeding rotor speed limit; computer stall
008/3	9-27-88	1407	1550	0.9	Baseline configuration: full auto AF/EPR control mode check (F11:1T11:11)
008/3	9-28-88	1541 1848	1650 2254	0.6 2.6	Screen No. 4 configuration: min-op line (F13:1T13:18), stall line (F14:1T14:18), speed lines (F15:1T20:11), emergency shutdown from exceeding rotor speed and stall limits

Table 6. Continued

CMAFS S/N	Date	Clock at start	Clock at stop	Powered hours >35 krpm	Comments
008/3	9-29-88	1431	1920	2.6	Screen No. 2 configuration: min-op line (F21:1T21:17), stall line (F22:1T22:15), speed lines (F23:1T28:11)
	9-30-88	2112	0020	2.9	
					Screen No. 6 configuration: min-op line (F29:1T29:16), stall line (F30:1T30:), speed lines (F31:1T36:12)
					Emergency shutdown from: exceeding stall and aft bearing temperature limits; high-pressure air loss
008/3	9-30-88	1615	2015	2.5	Screen No. 8 configuration: min-op line (F27:1T37:17), stall line (F38:1T38:17), speed lines (F39:1T43:12), could not exceed 105% corrected speed due to high vibrations
		2159	2325	0.7	
					Screen No. 10 configuration: min-op line (F44:1T44:20), stall line (F45:1T45:13),
					Emergency shutdown from exceeding rotor acceleration and aft bearing temperature rate limits

Table 6. Continued

CMAPS S/N	Date	Clock at start	Clock at stop	Powered hours >35 krpm	Comments
008/3	10-3-88	1653 2145	2024 2351	2.1 1.35	Screen No. 10 configuration: speed lines (F46:1T51:12) Screen No. 5 configuration: min-op line (F52:1T52:18), stall line (F53:1T53:17), begin speed line (F54:1T54:14) Emergency shutdown from exceeding rotor acceleration limit
008/3	10-4-88	1601 1832	1730 2238	1.05 2.2	Screen No. 5 configuration: finish speed lines (F55:1T59:1) Screen No. 3 configuration: min-op line (F60:1T60:19), stall line (F61:T61:17), speed lines (F62:1T67:9), PSK15 malfunction Emergency shutdown from main electrical power failure
008/3	10-5-88	1619	2358	1.25	Screen No. 7 configuration: begin min-op line (F68:1T68:8), E.S. from high vibrations and aft bearing temperature rates, unable to run at high rpm's, terminate SN/008/3 use

Table 6. Continued

CMAPS S/N	Date	Clock at start	Clock at stop	Powered hours >35 krpm	Comments
006/3	10-17-88	1837	2335	1.6	Baseline configuration: min-op line (F101:1T101:18), stall line (F102:1T102:16), controller limit adjustment, norms check, emergency shutdown from exceeding forward bearing temperature and rotor acceleration rates; high- pressure air loss
006/3	10-18-88	1633	2211	1.85	Baseline configuration: begin speed lines (F103:1T106:10), Plane 7 instrument malfunction
006/3	10-19-88	1615 1947	1758 2216	0.9 2.0	Baseline configuration: finish speed lines (F110:1T111:16) Screen No. 4 configuration: min-op line (F112:1T112:18), stall line (F113:1T113:18), speed lines (F114:1T119:13) Screen No. 9 configuration: min-op line (F120:1T120:18), begin stall line (F121:1T121:10) Emergency shutdown from controller stall

Table 6. Concluded

CMAPS S/N	Date	Clock at start	Clock at stop	Powered hours >35 krpm	Comments
006/3	10-20-88	1604	1941	0.5	Screen No. 9 configuration:
		2113	2237	1.1	finish stall line
	10-21-88	2320	0121	1.6	(F122:1T122:13), speed
		0211	0247	0.3	lines (F123:1T128:13)
					Screen No. 11 configuration: min-op line (F129:1T129:16), stall line (F130:1T130:15), speed lines (F131:1T136:10)
					Screen No. 7 configuration: min-op line (F137:1T137:18), begin stall line (F138:1T138:9), emergency shutdown from exceeding rotor acceleration and forward bearing temperature limits
006/3	10-21-88	1543	2023	1.95	Screen No. 7 configuration: finish stall line (F138:10T138:22), speed lines (F139:T144:12), emergency shutdown from exceeding rotor acceleration limit, end of test

^aFrom run:sequence to run:sequence.

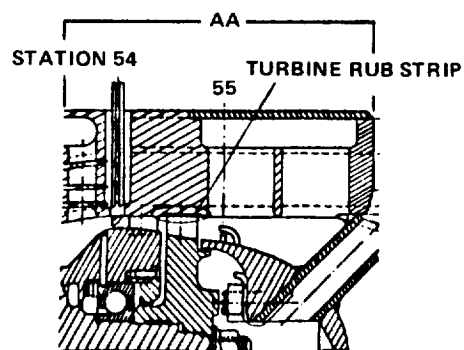
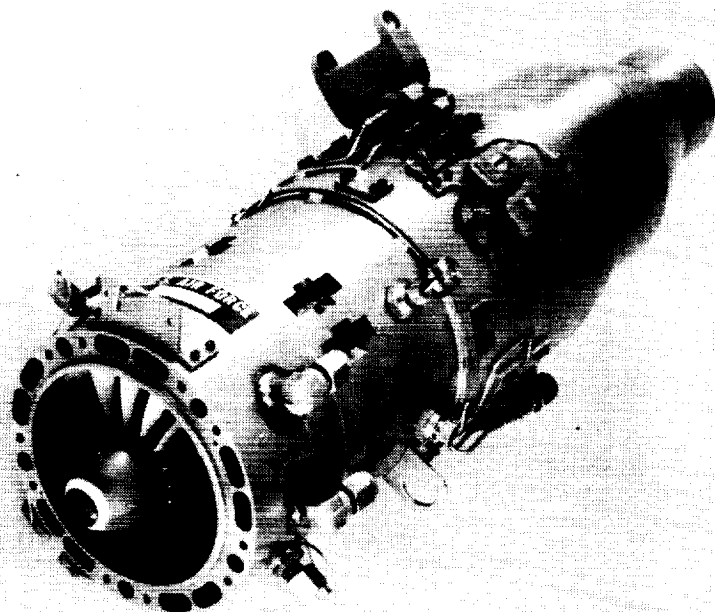
Table 7. Summary of compressor airflow calibration results

Method used	Flow coefficient name	Screen configuration	Mean flow coefficient	Dispersion range, % ^a	Rms error, % ^a
Compressor inlet: averaged Plane 2 pressure	$C_{f2,a}$	Baseline	1.024	±9	2.61
		All	1.063	±11	3.39
Summed flow elements	$C_{f2,sum}$	Baseline	1.022	±6	2.49
		All	1.045	±9	2.99
Compressor discharge	$C_{f2,15}$	Baseline	1.037	±4	1.88
		All	1.043	±7	1.95
Flow balance	$C_{f2,db8}$	Baseline	1.009	±5	2.20
		All	1.000	±6	1.78
Mixer pressure correlation	$C_{f2,57}$	Baseline	0.999	±2	0.74
		All	1.005	±3	1.11

^a% of mean flow coefficient.

Table 8. Required measurements for compressor airflow calibration methods

Method used	Pressures	Temperatures	Rotor speed	Total required
Compressor inlet: averaged Plane 2 pressure	48	1	0	49
Summed flow elements	48	1	0	49
Compressor discharge	18	1	0	19
Flow balance	25	3	1	29
Mixer pressure	41	1	1	43



DETAIL SECTION AA

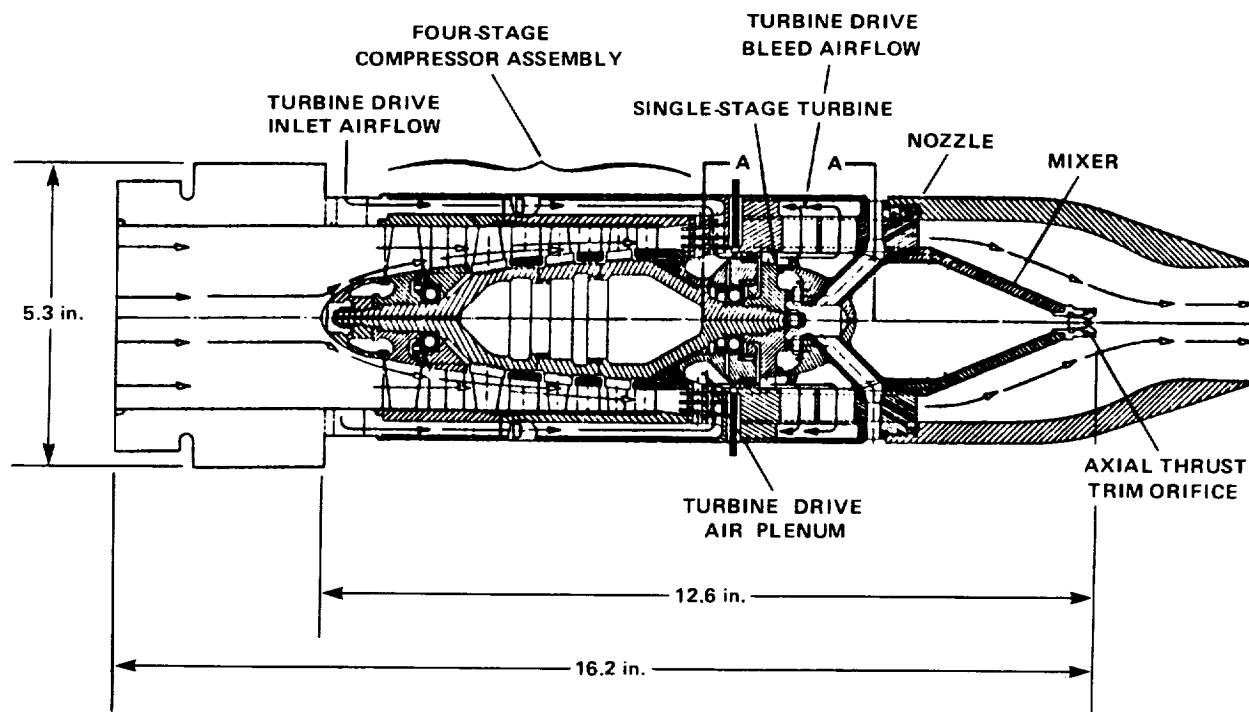


Figure 1. Multimission Aircraft Propulsion Simulator (MAPS).

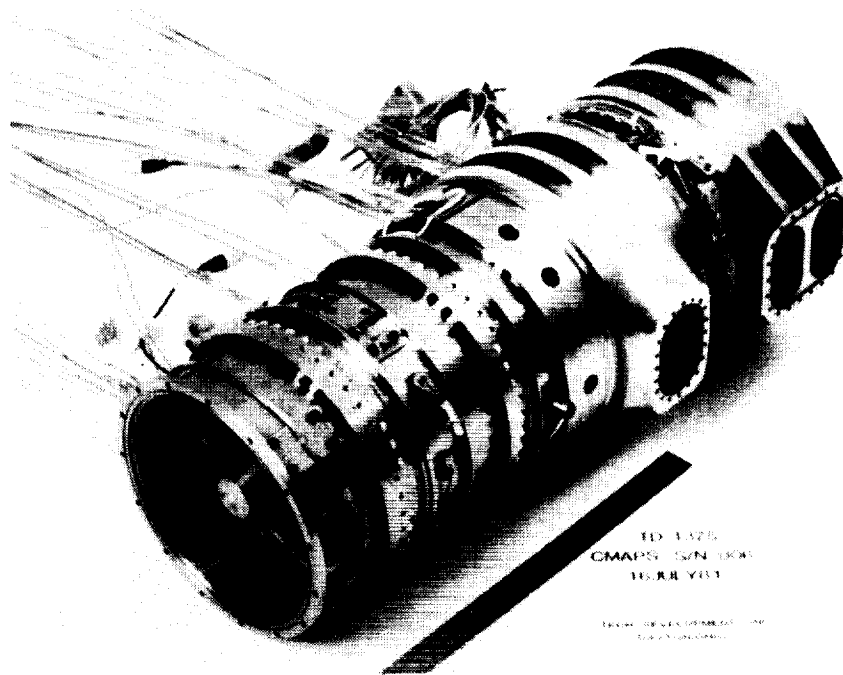
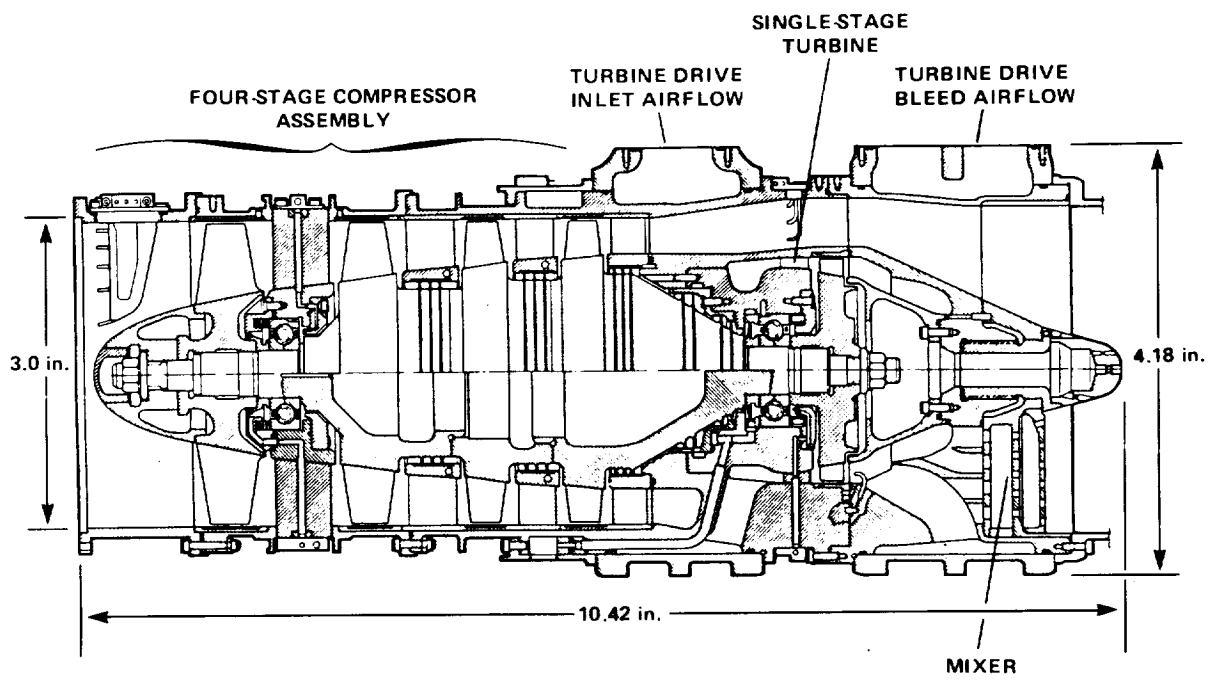


Figure 2. Compact Multimission Aircraft Propulsion Simulator (CMAPS).

ORIGINAL PAGE
BLACK AND WHITE PHOTOGRAPH

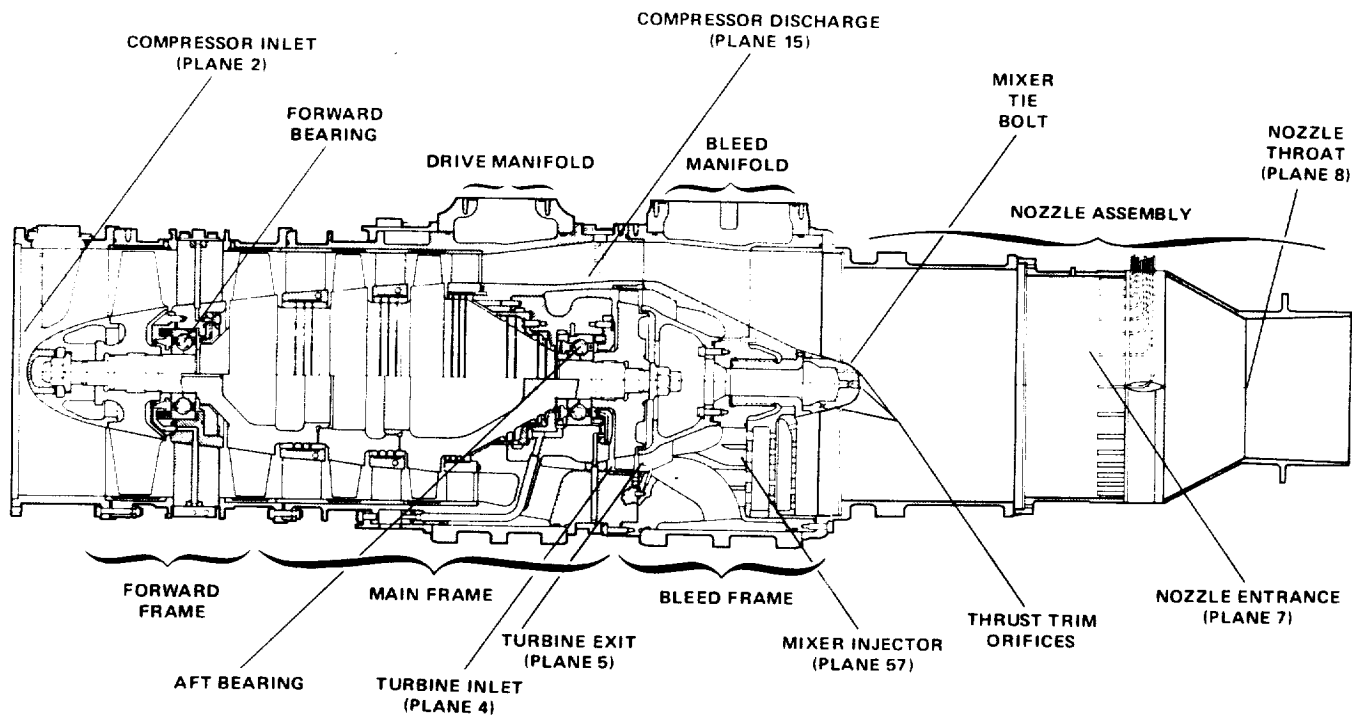


Figure 3. Detail of CMAPS internal hardware.

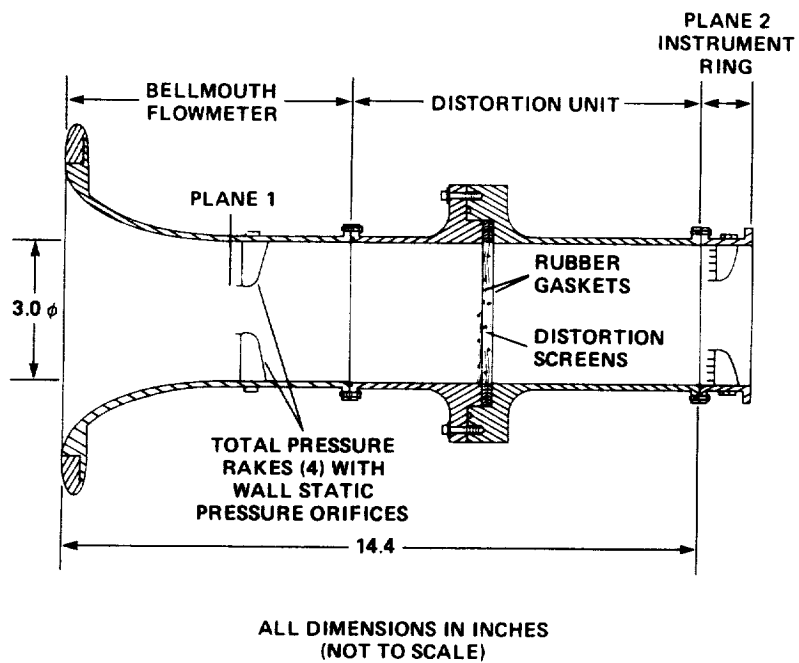


Figure 4. CMAPS inlet assembly.

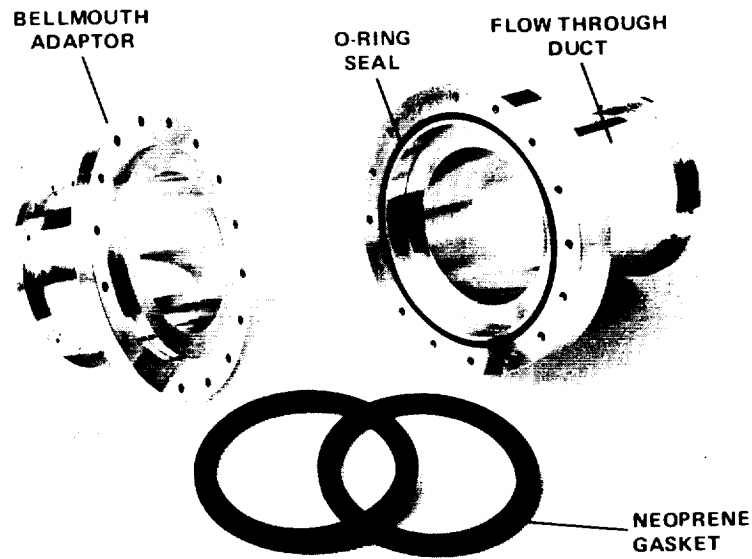


Figure 5. Distortion unit assembly.

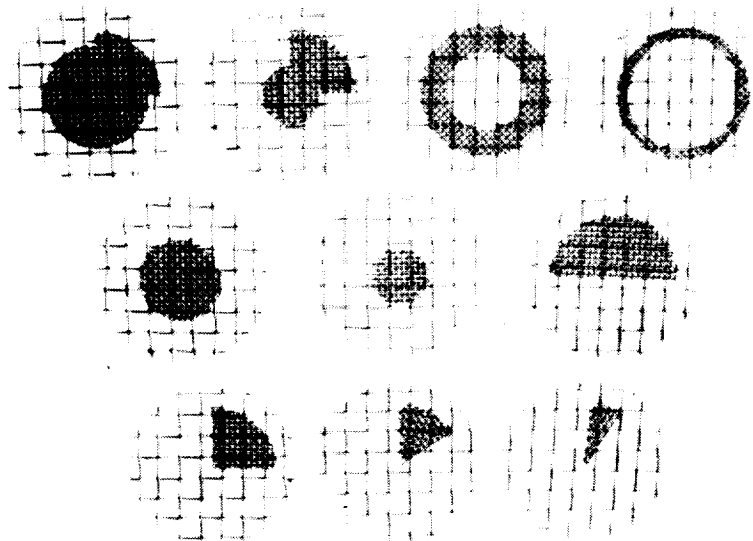


Figure 6. Primary distortion screen patterns.

ORIGINAL PAGE
BLACK AND WHITE PHOTOGRAPH

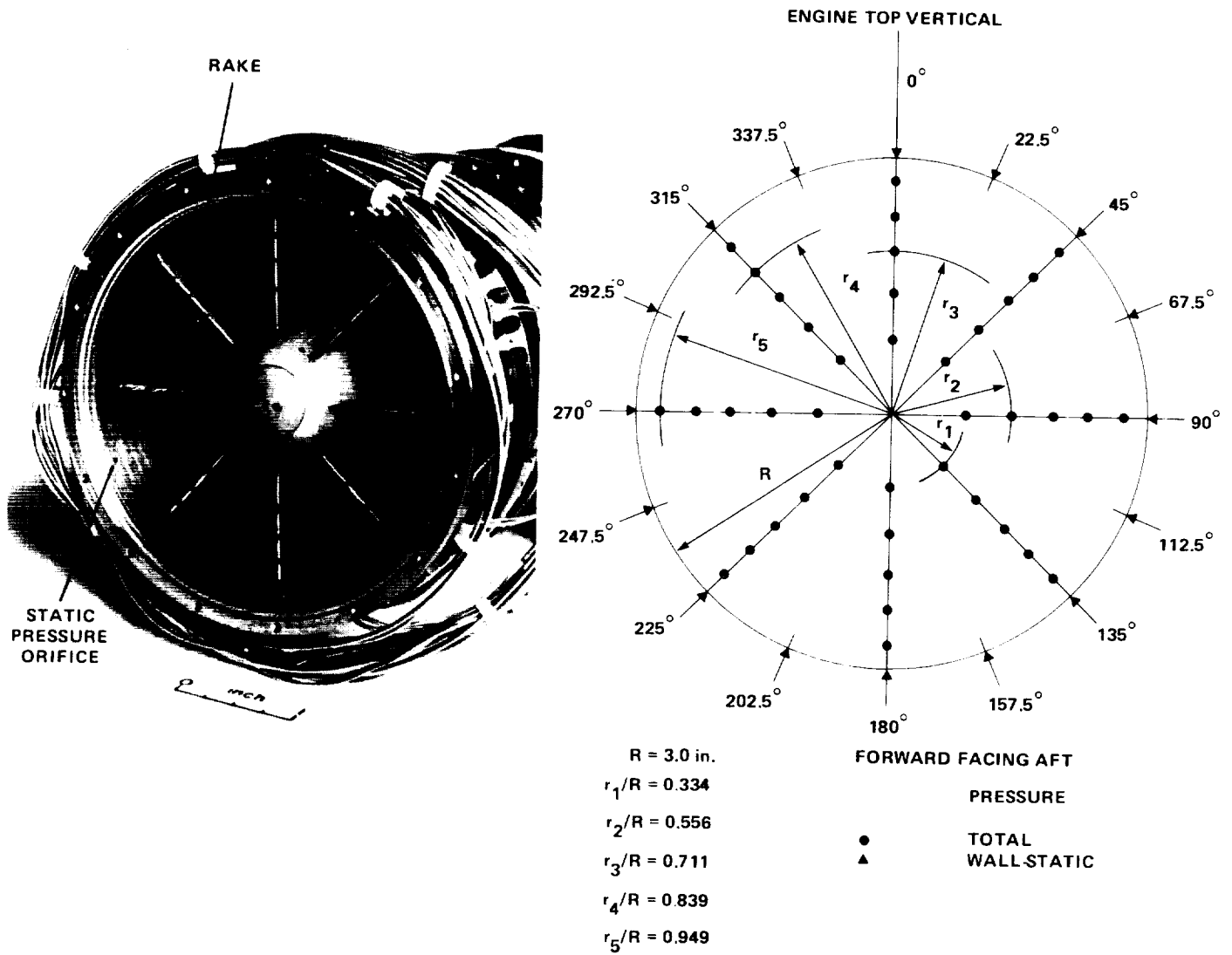


Figure 7. CMAPS Plane 2 instrument ring.

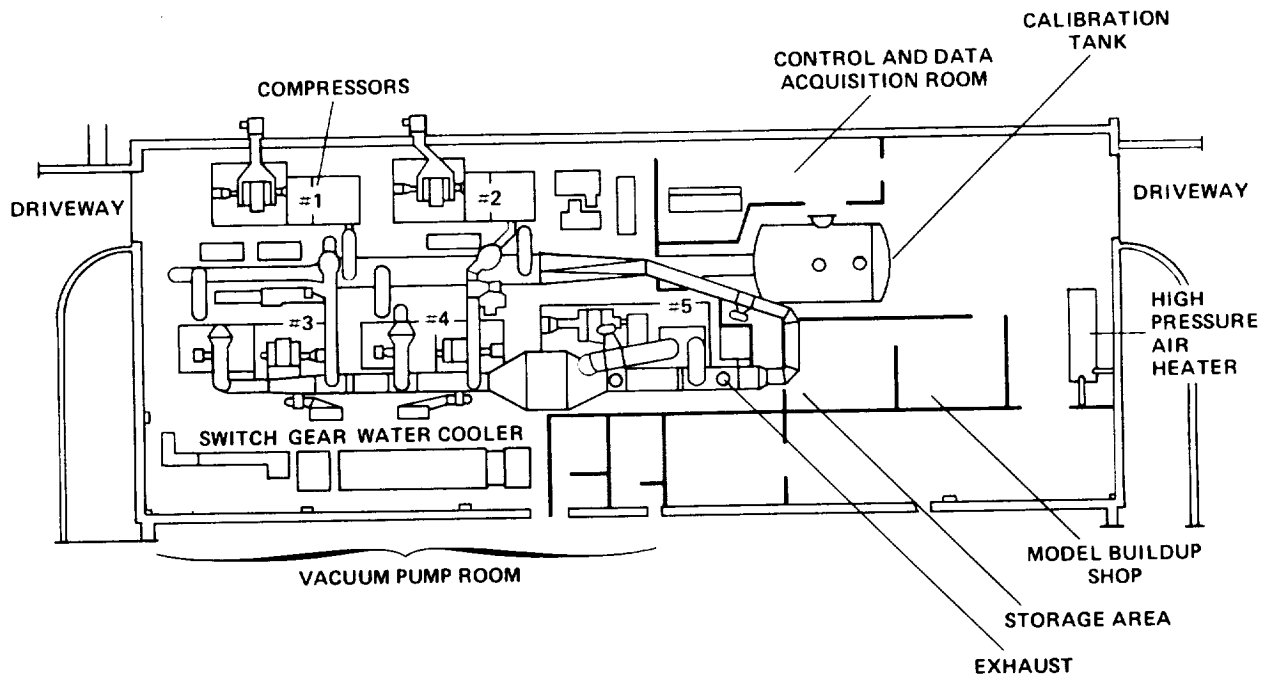


Figure 8. Ames Propulsion Simulator Calibration Laboratory (PSCL).

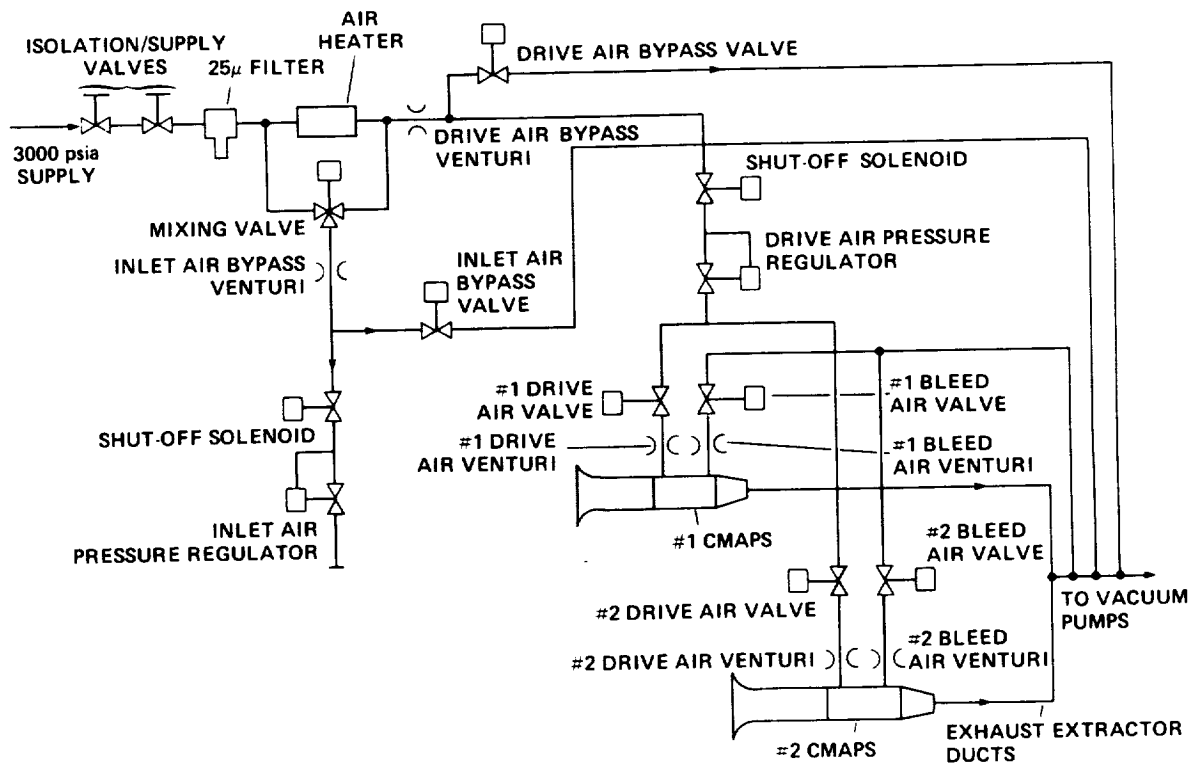


Figure 9. High-pressure air system for dual CMAPS operation.

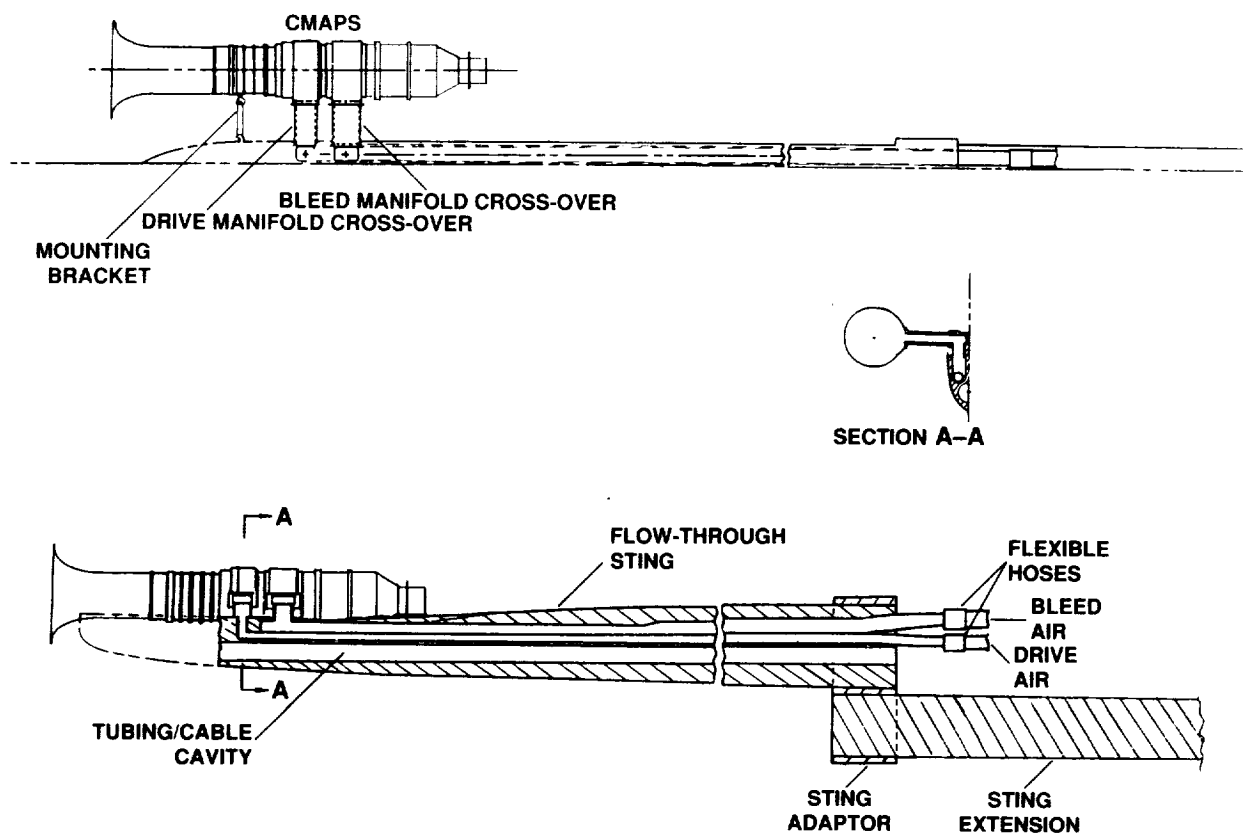


Figure 10. CMAPS attachment to flow-through sting.

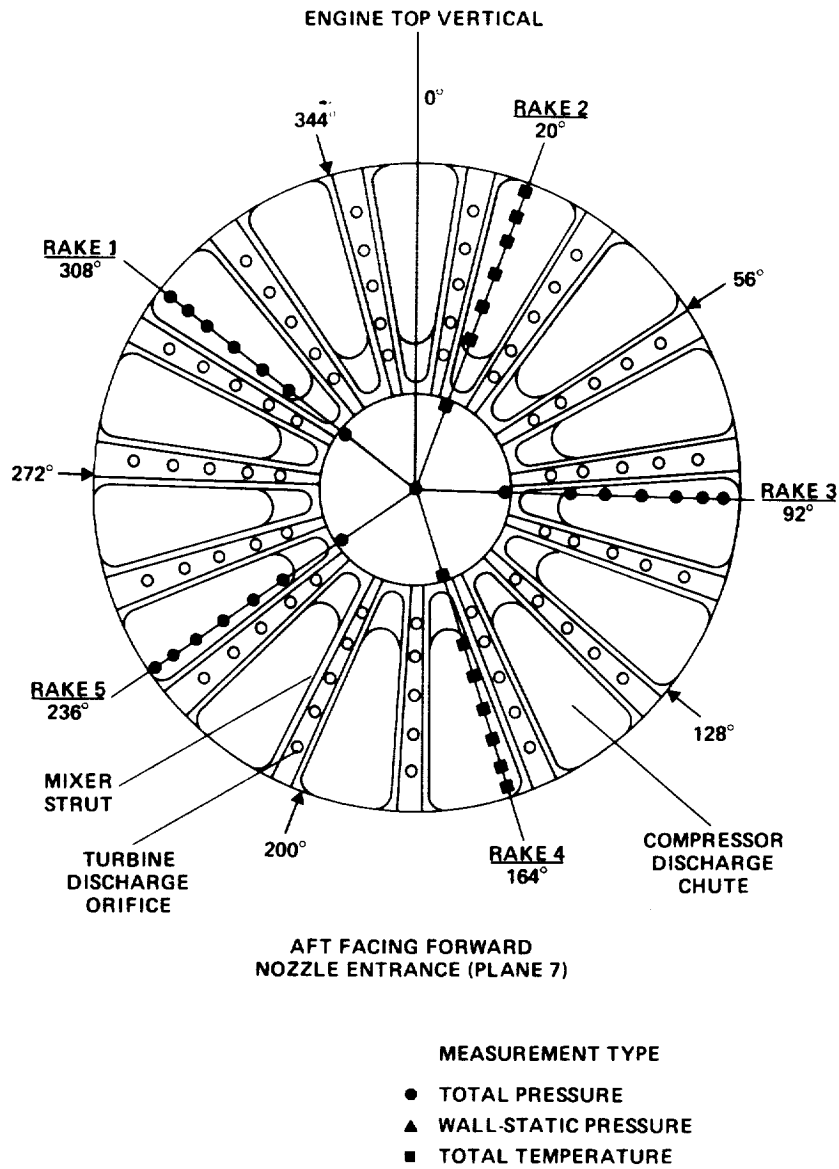


Figure 11. Dry nozzle instrument rakes in the "C" position oriented with respect to mixer struts.

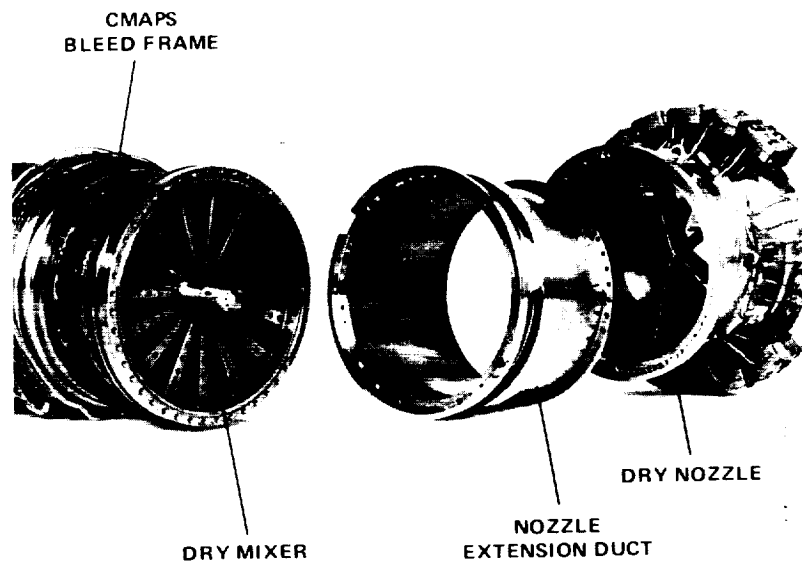


Figure 12. Nozzle hardware components.

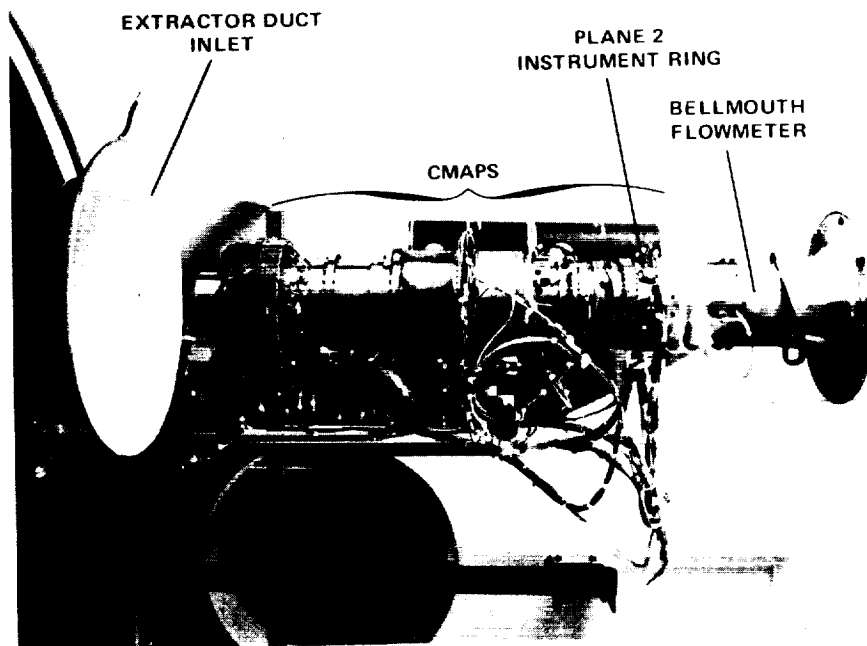


Figure 13. Bellmouth attachment to CMAPS SN/008/3 for baseline configuration testing.

ORIGINAL PAGE
BLACK AND WHITE PHOTOGRAPH

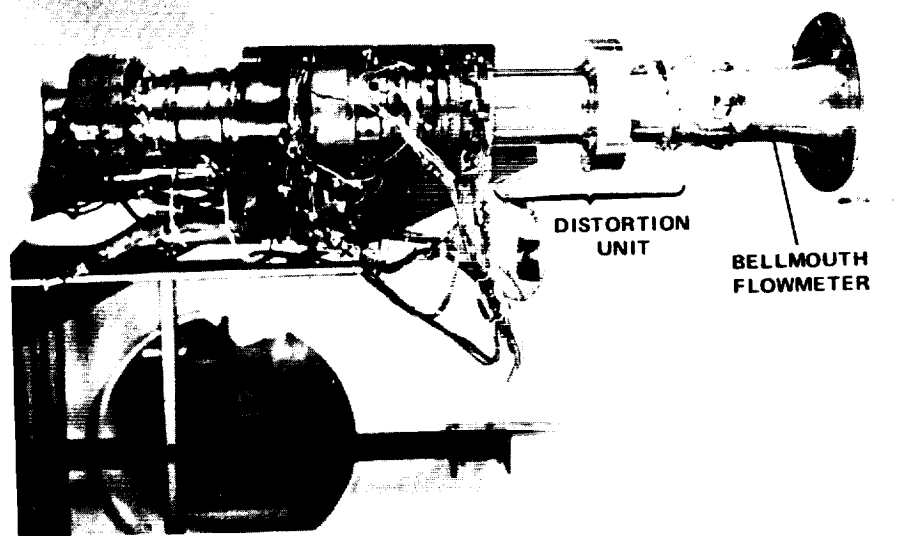


Figure 14. Distortion unit attachment to CMAPS SN/008/3 for distortion testing.

ORIGINAL PAGE
BLACK AND WHITE PHOTOGRAPH

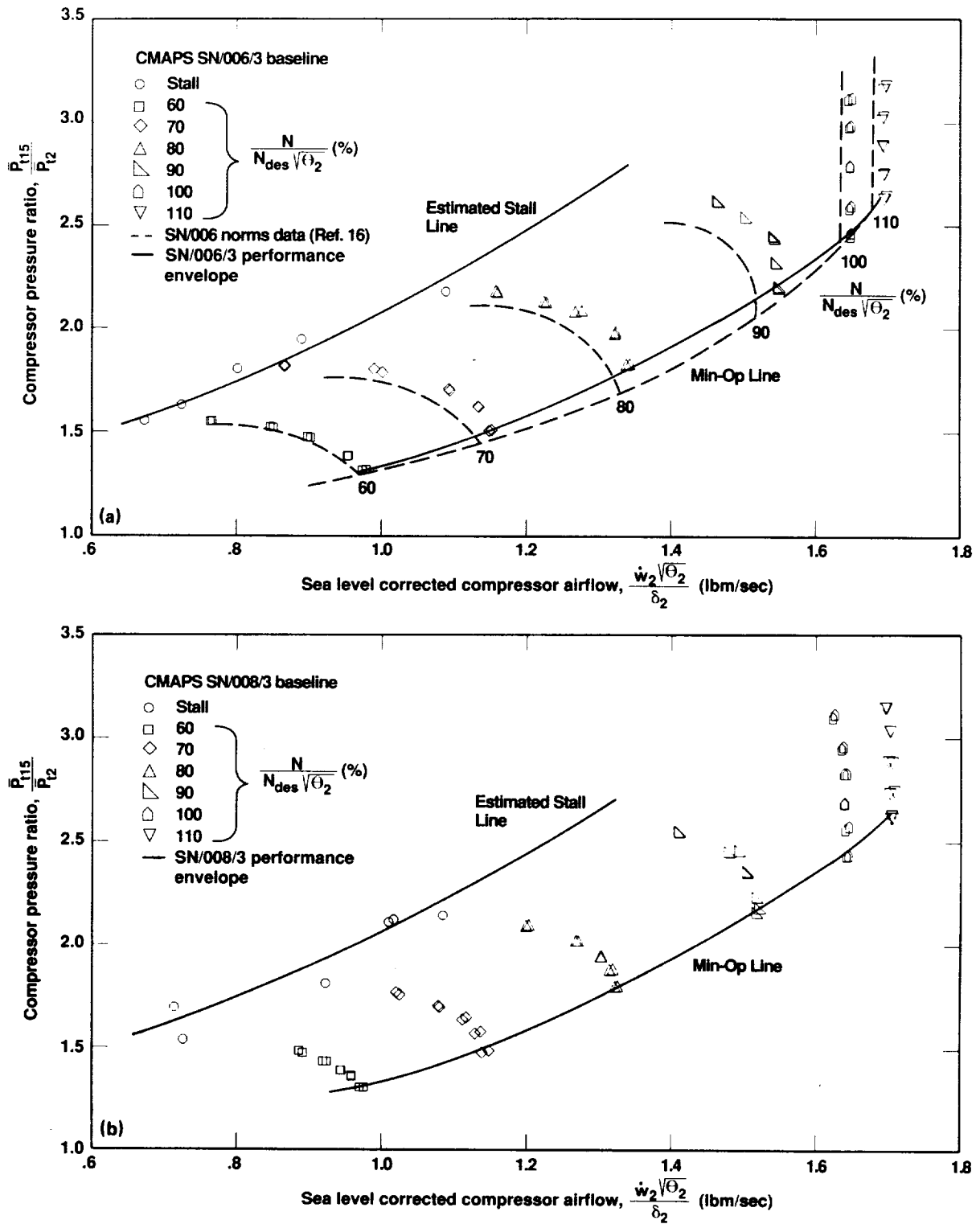


Figure 15. Baseline configuration compressor operating map. (a) CMAPS SN/006/3; (b) CMAPS SN/008/3.

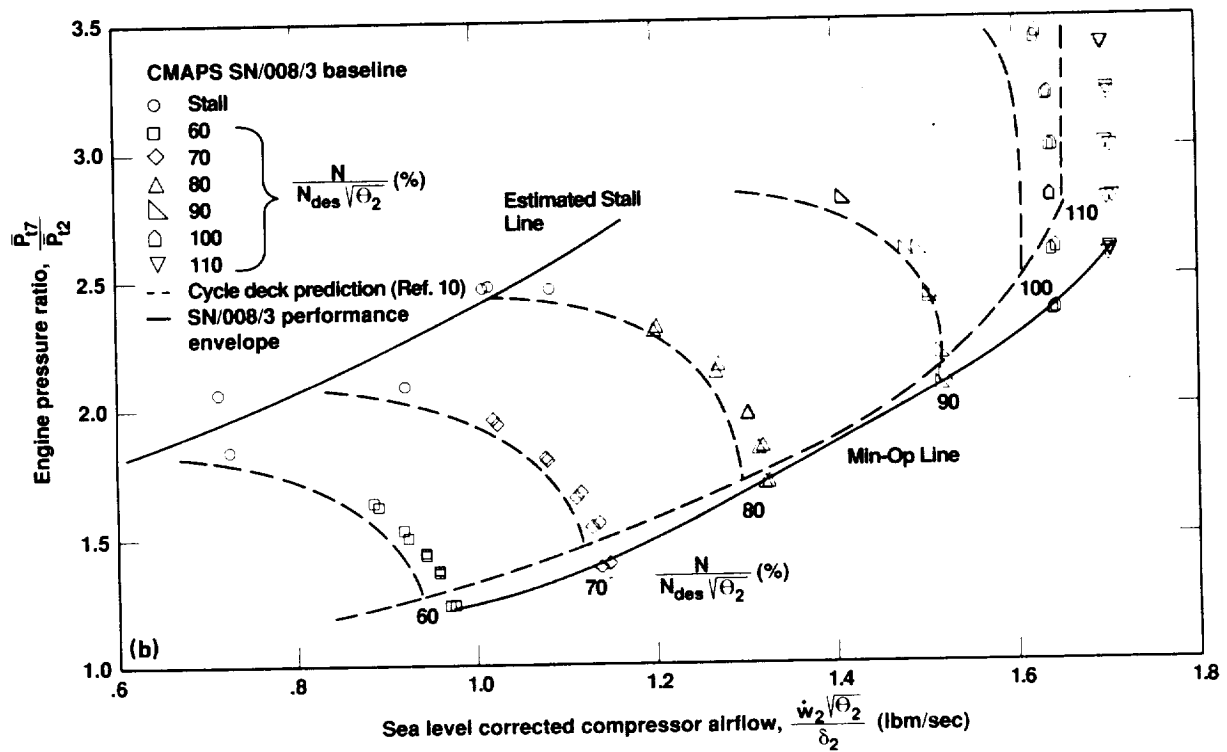
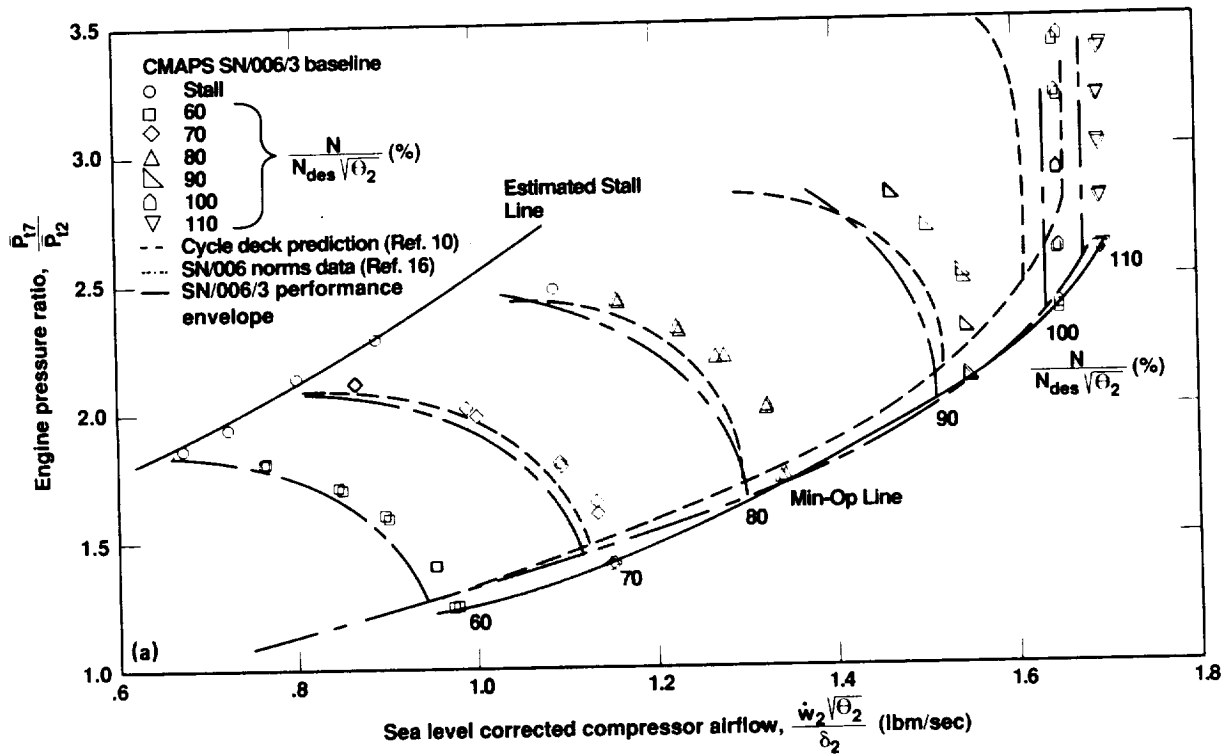


Figure 16. Baseline dry nozzle flexibility envelope. (a) CMAPS SN/006/3; (b) CMAPS SN/008/3.

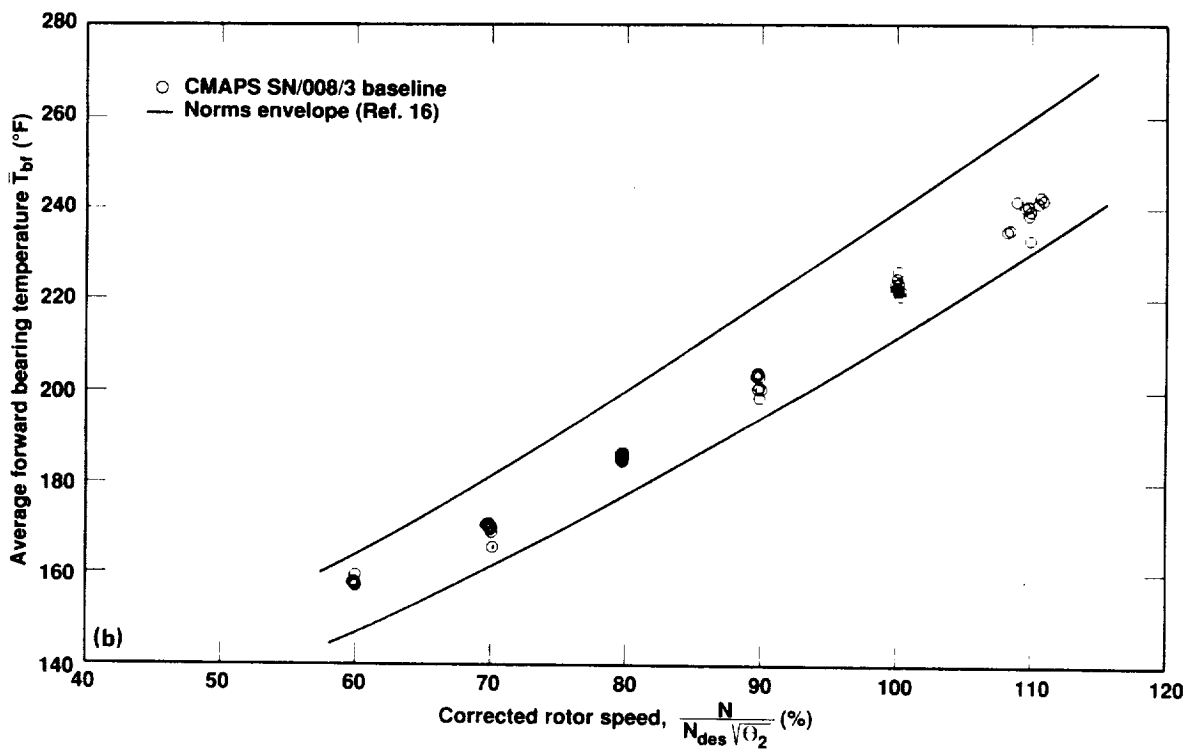
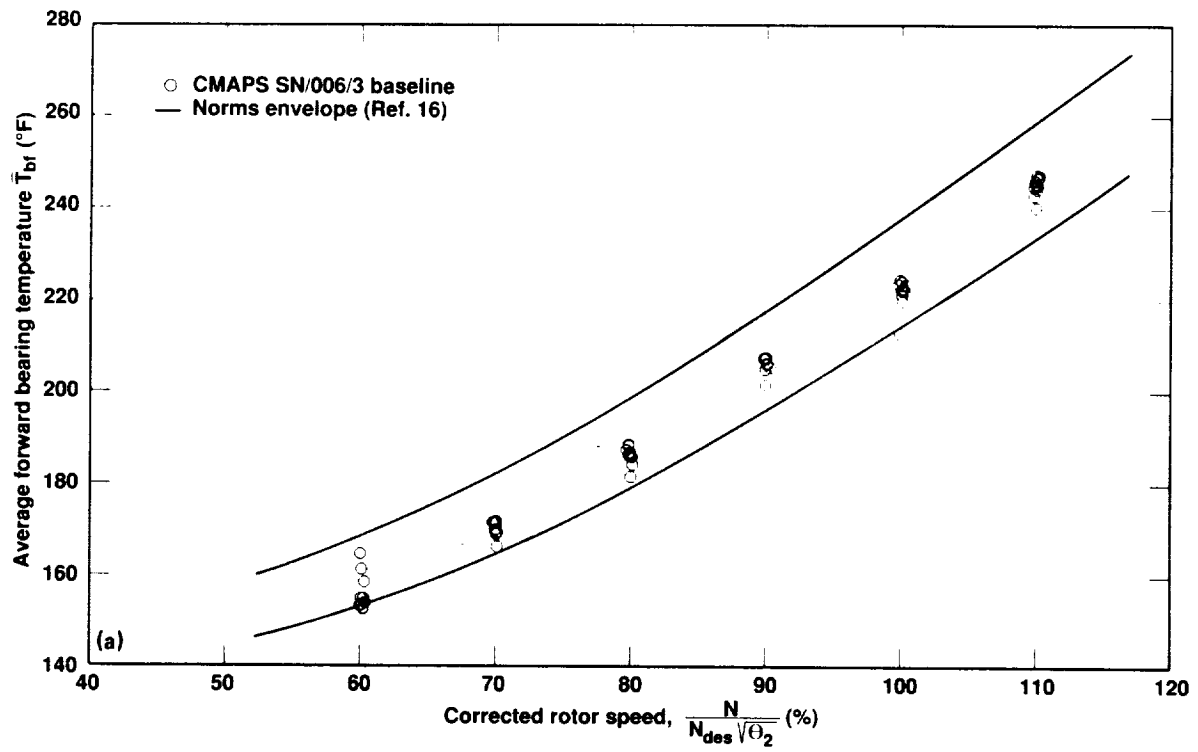


Figure 17. Baseline forward bearing temperature map. (a) CMAPS SN/006/3; (b) CMAPS SN/008/3.

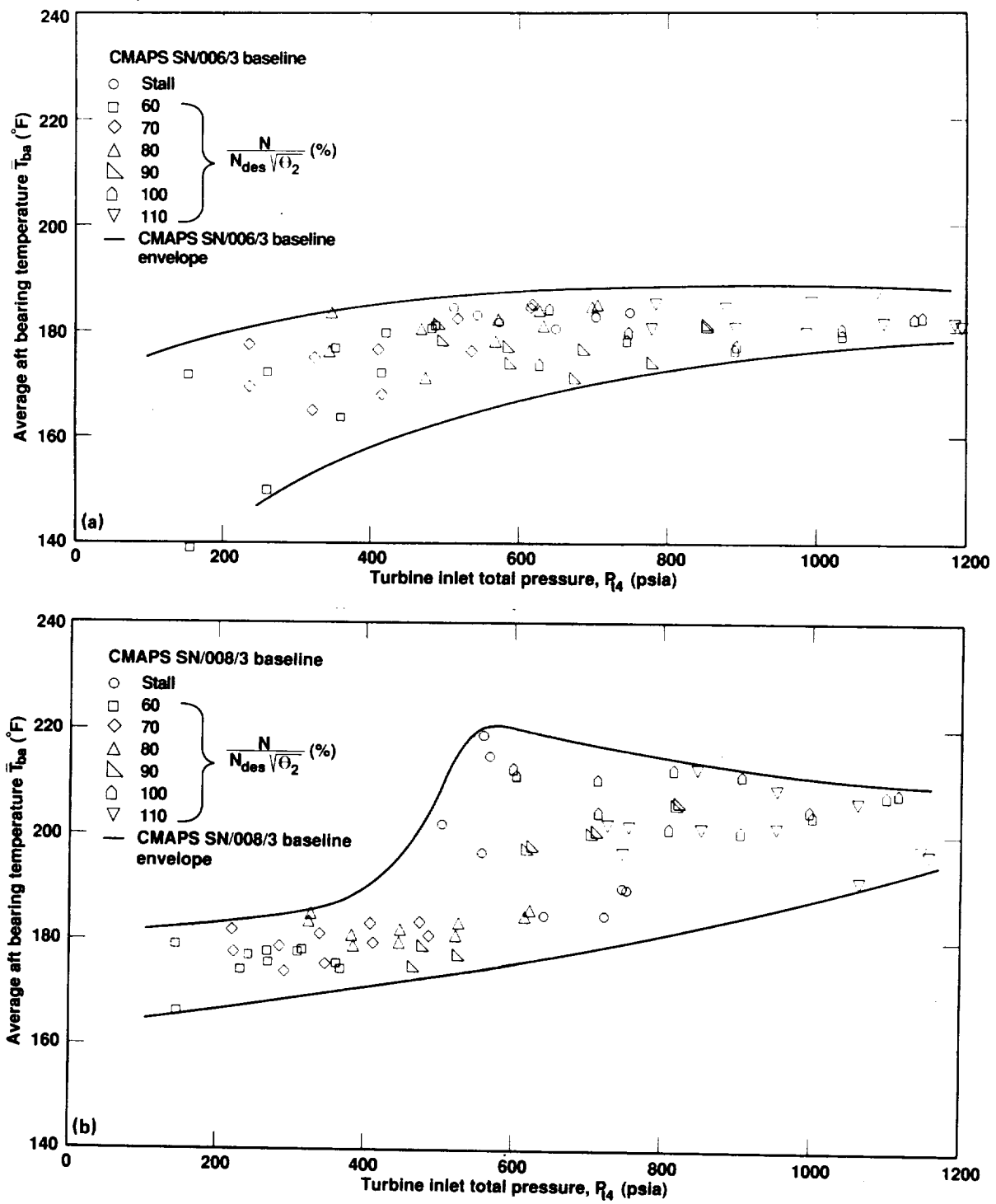


Figure 18. Baseline aft bearing temperature map. (a) CMAPS SN/006/3; (b) CMAPS SN/008/3.

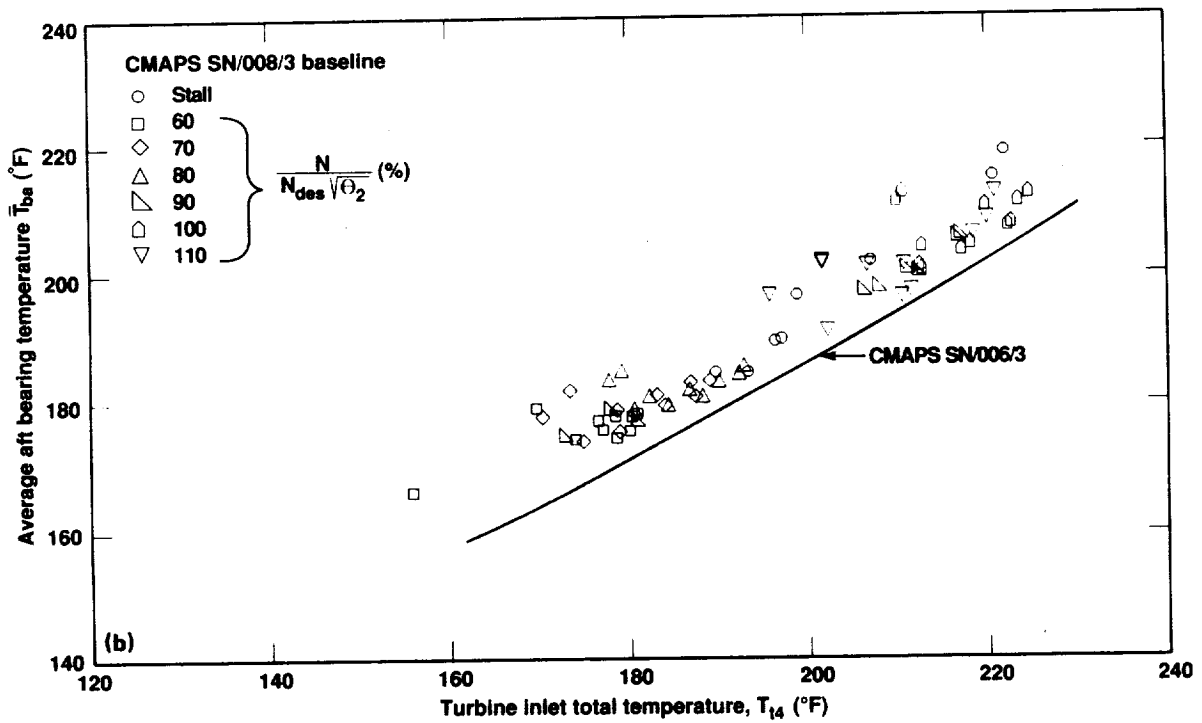
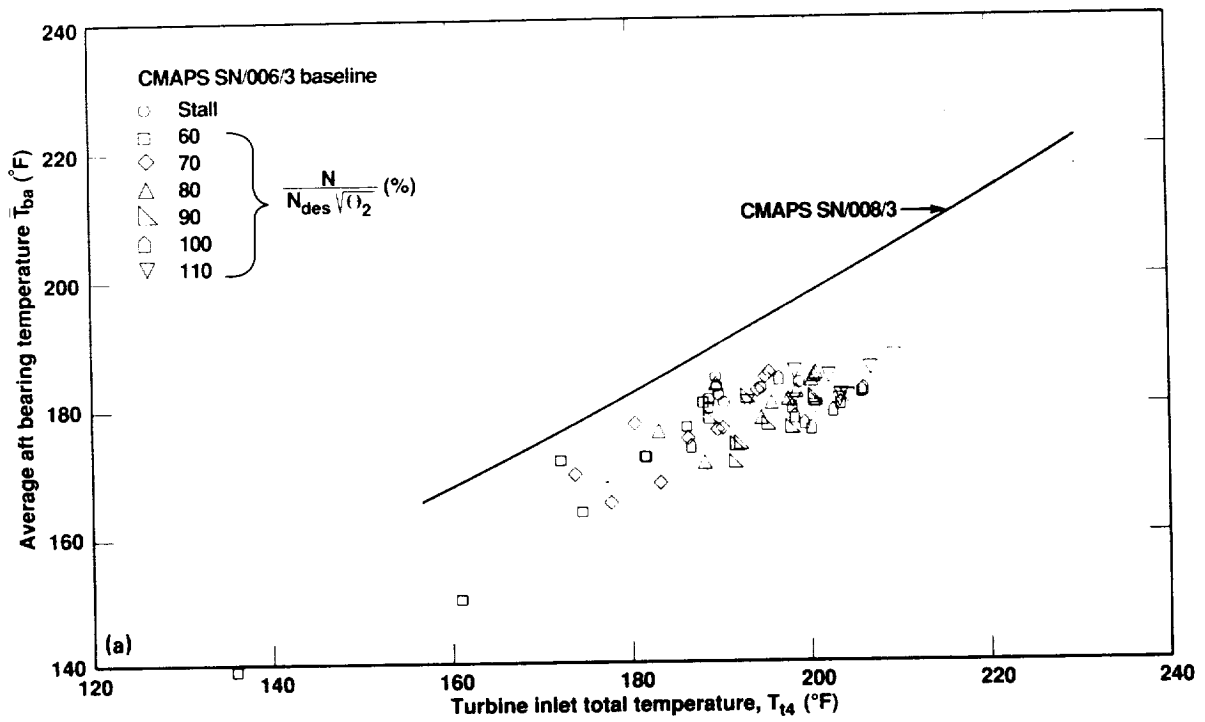


Figure 19. Baseline aft bearing temperature and turbine inlet temperature relation. (a) CMAPS SN/006/3; (b) CMAPS SN/008/3.

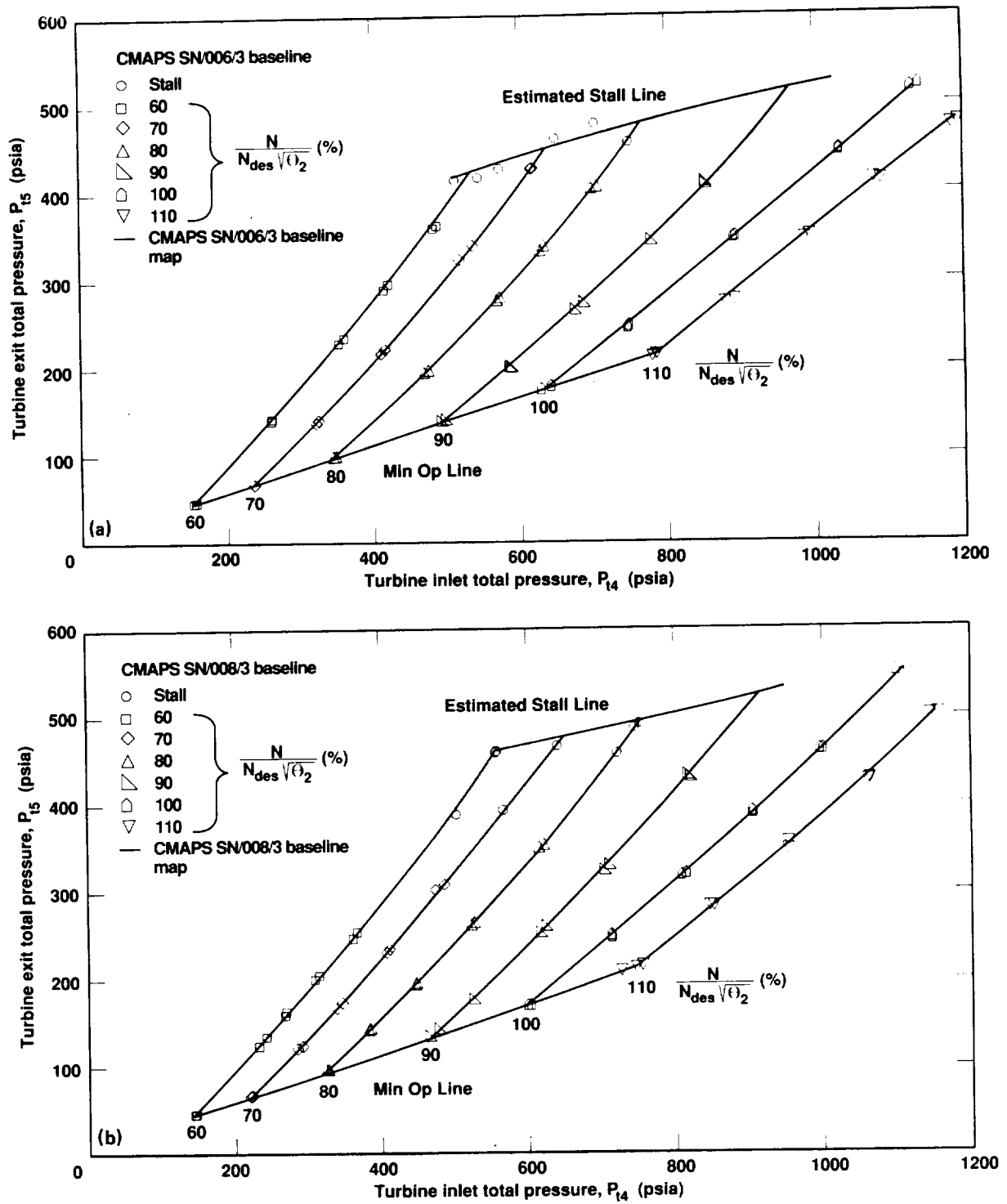


Figure 20. Baseline turbine pressure loss. (a) CMAPS SN/006/3; (b) CMAPS SN/008/3.

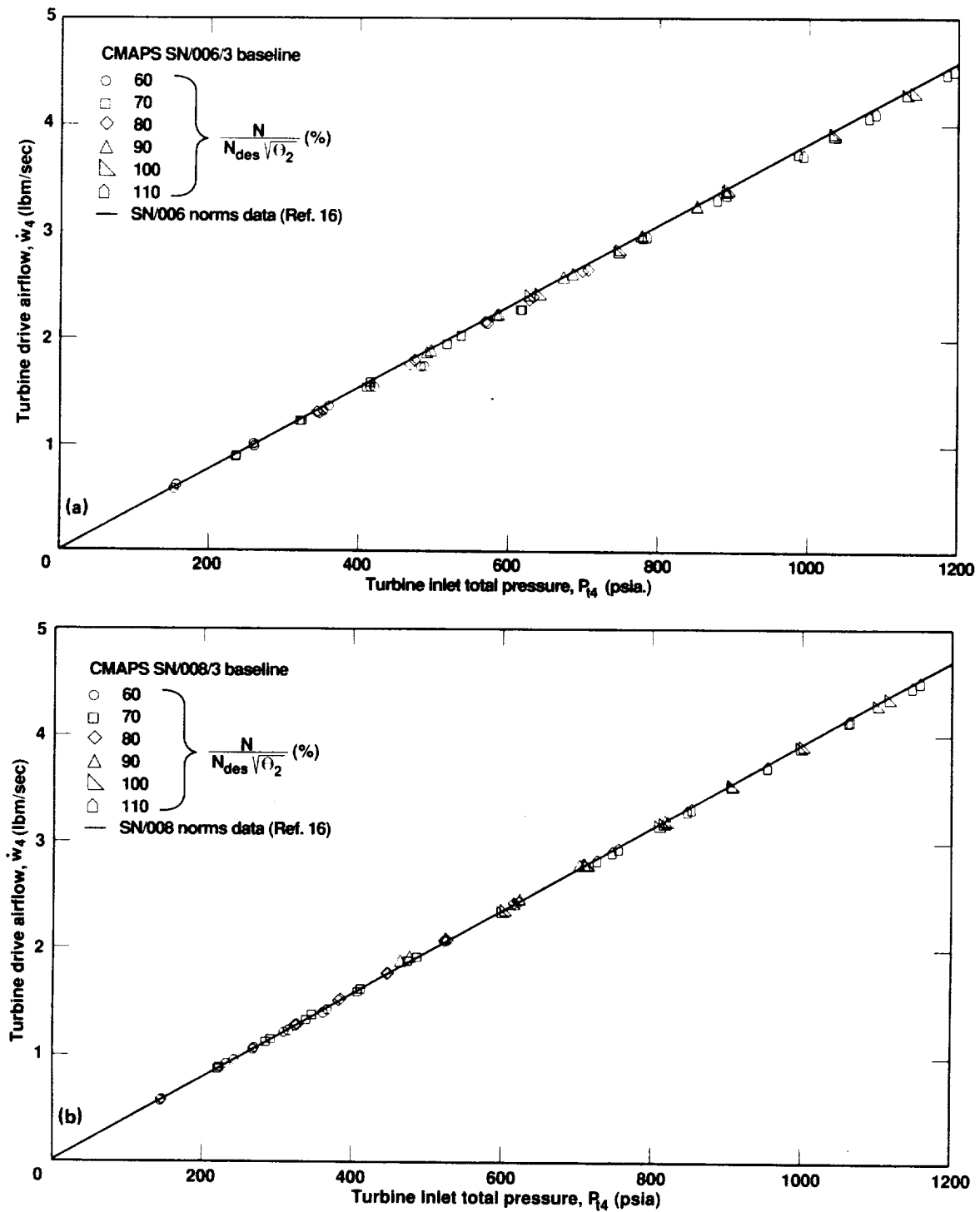


Figure 21. Turbine drive airflow and turbine inlet pressure relation. (a) CMAPS SN/006/3; (b) CMAPS SN/008/3.

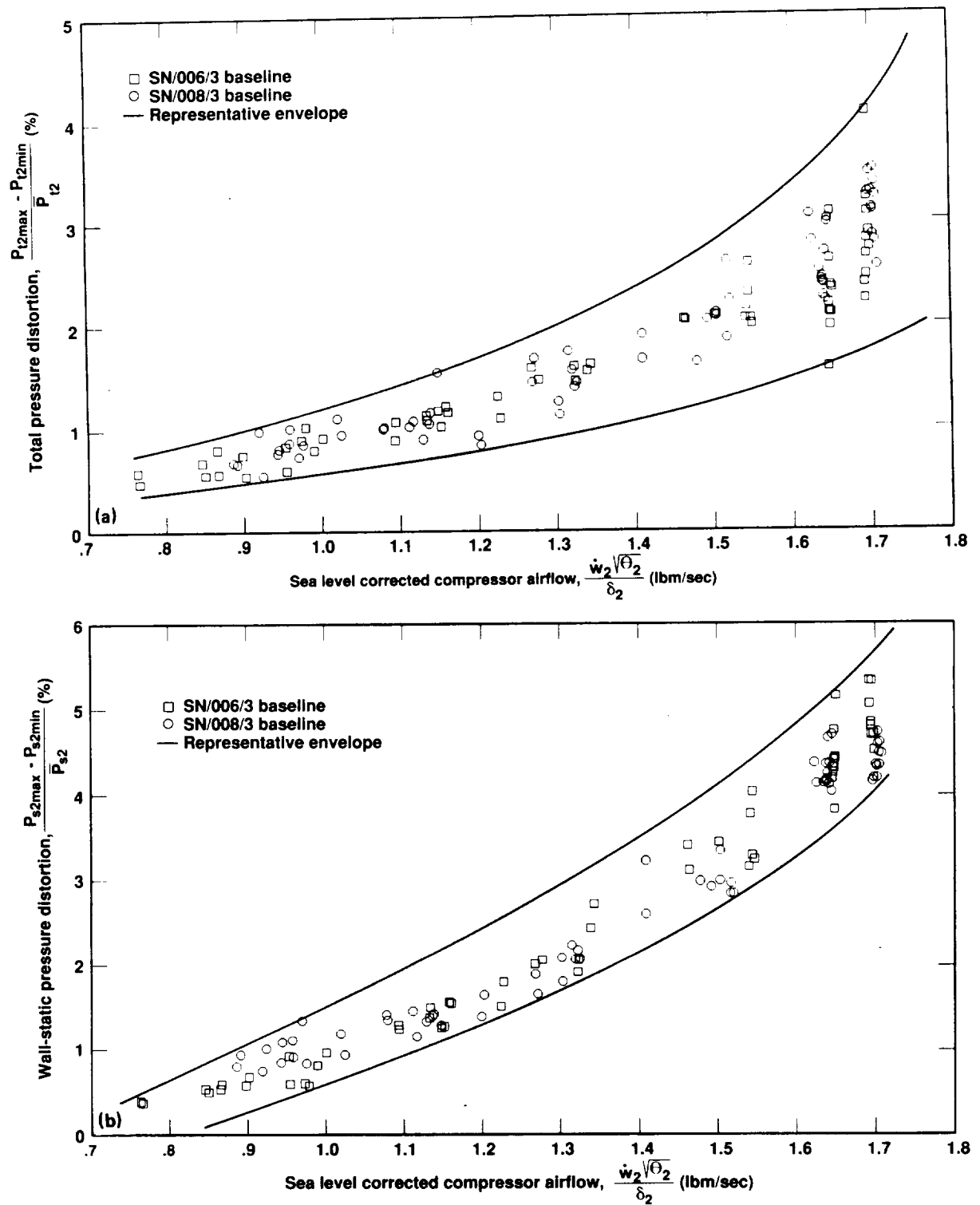


Figure 22. Baseline compressor inlet pressure distortion envelopes for CMAPS SN/006/3 and 008/3. (a) Total pressure; (b) wall static pressure.

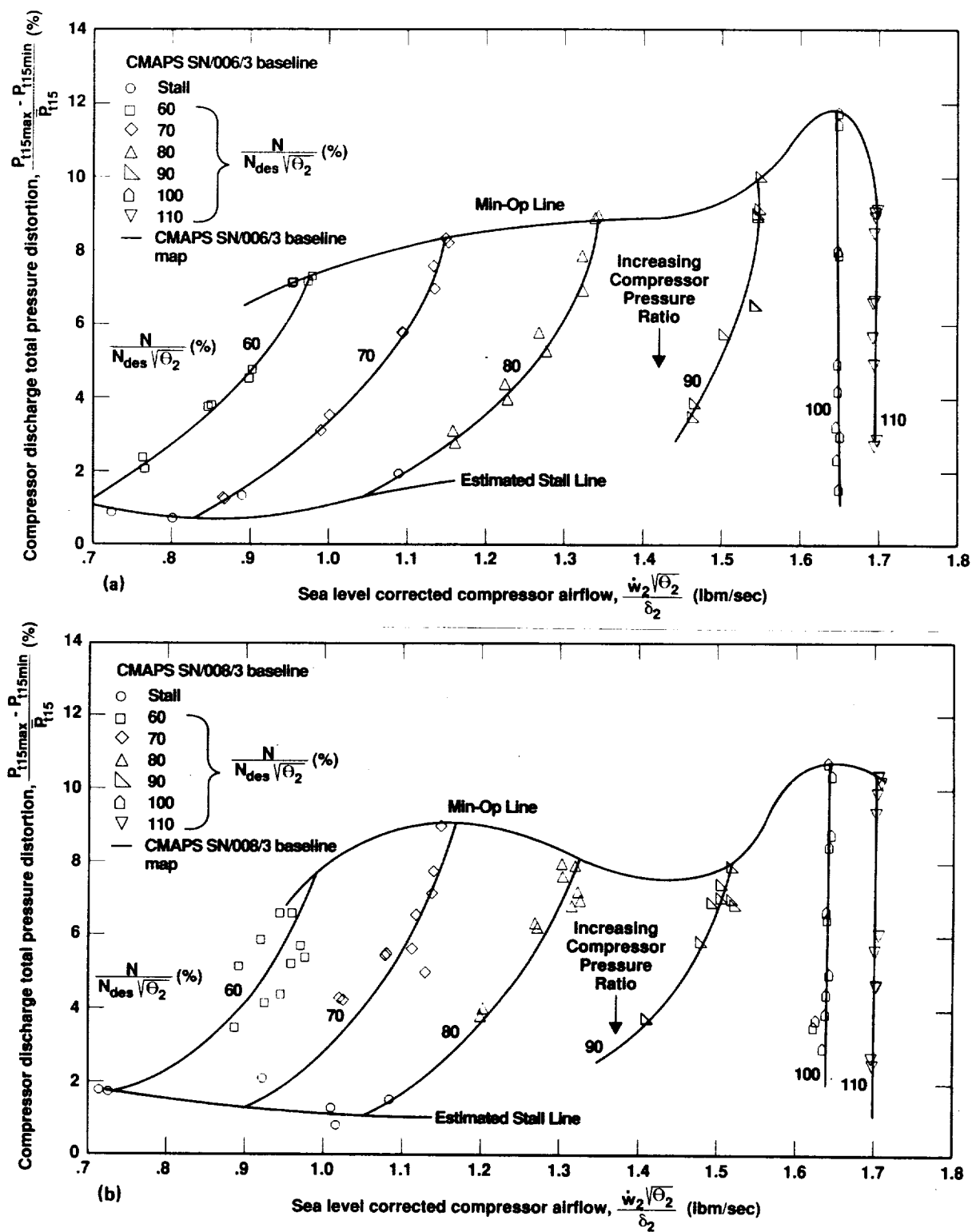


Figure 23. Baseline compressor discharge total pressure distortion. (a) CMAPS SN/006/3; (b) CMAPS SN/008/3.

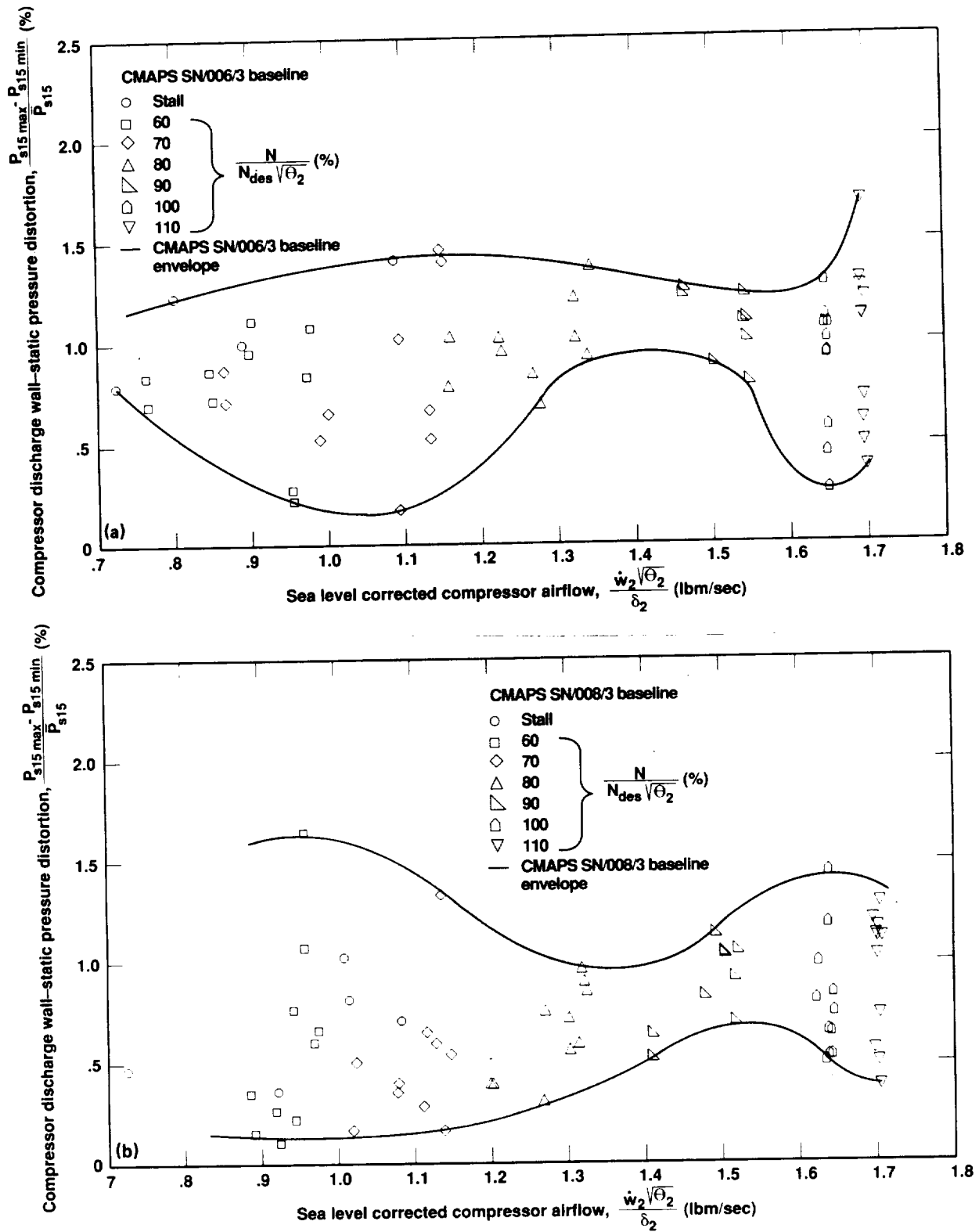


Figure 24. Baseline compressor discharge wall static pressure distortion. (a) CMAPS SN/006/3; (b) CMAPS SN/008/3.

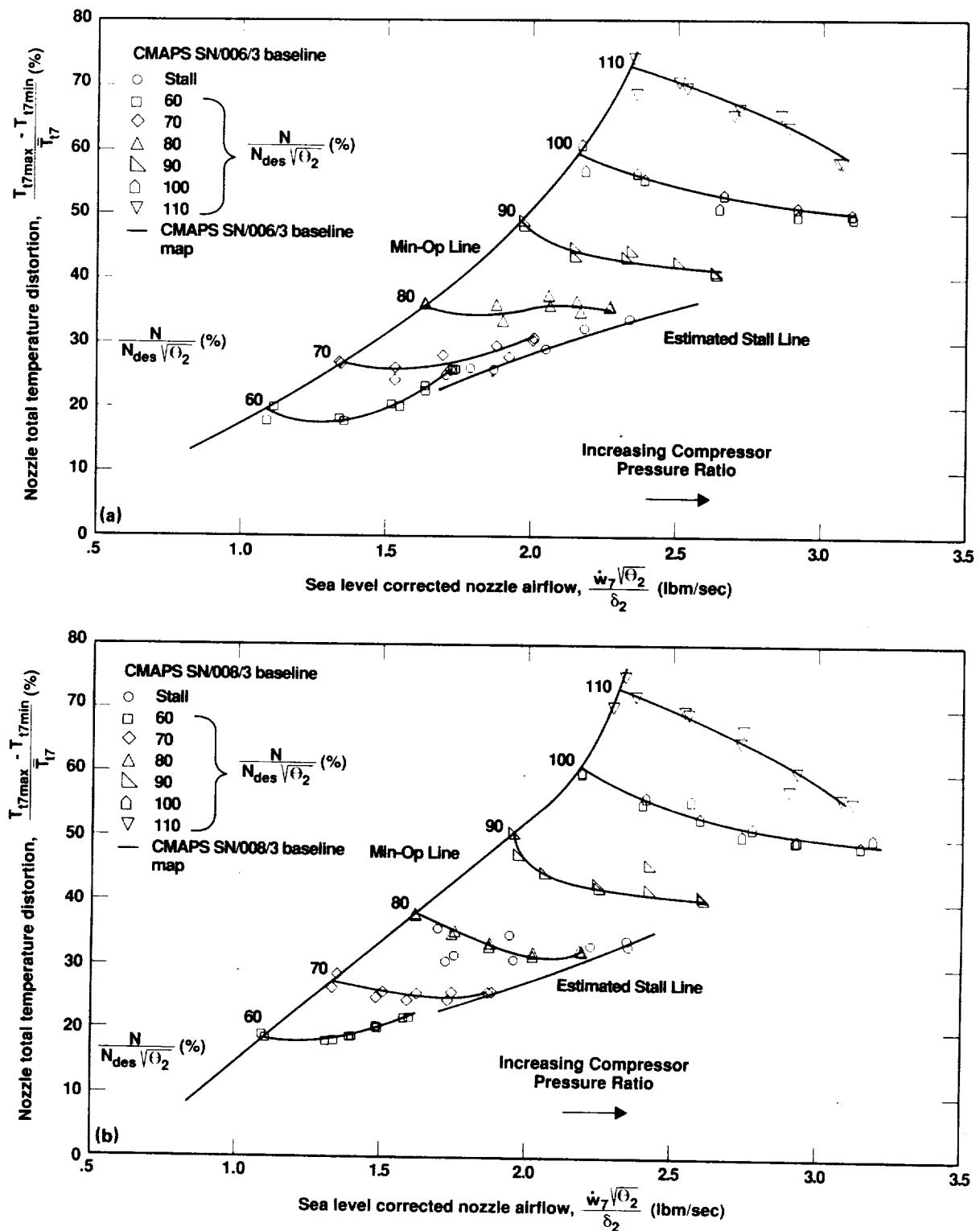


Figure 25. Baseline nozzle entrance total temperature distortion. (a) CMAPS SN/006/3; (b) CMAPS SN/008/3.

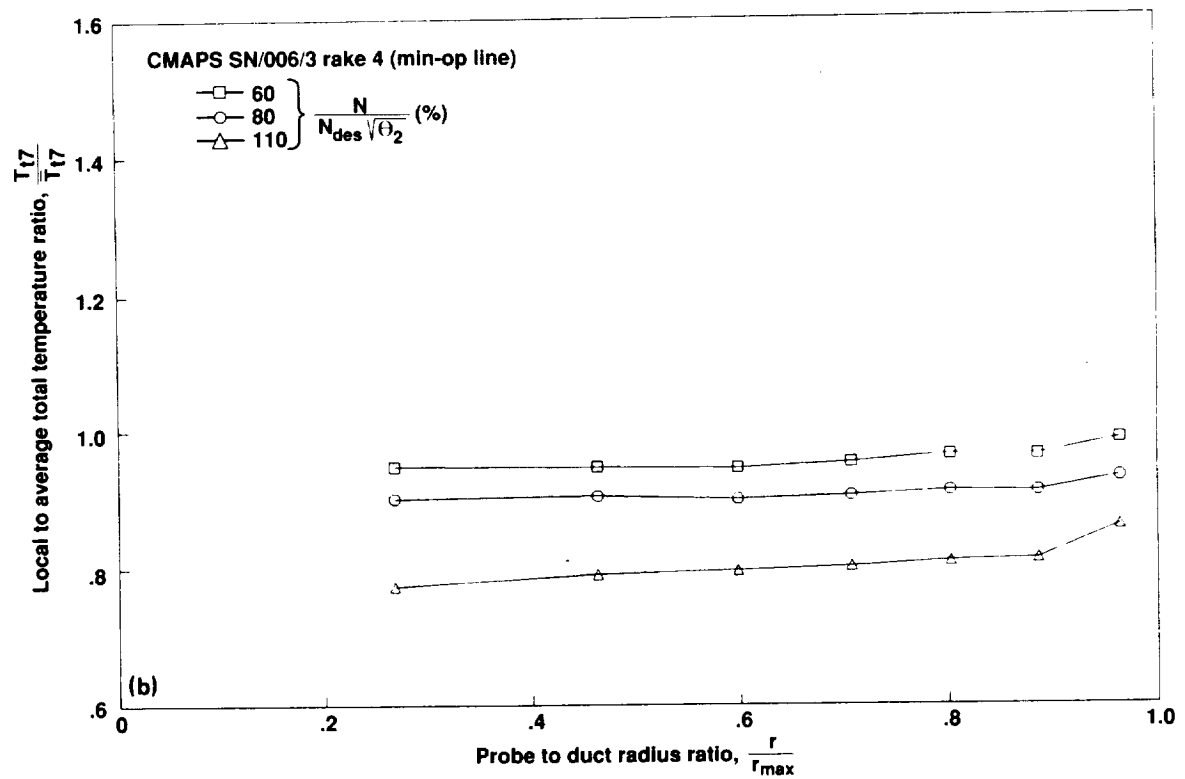
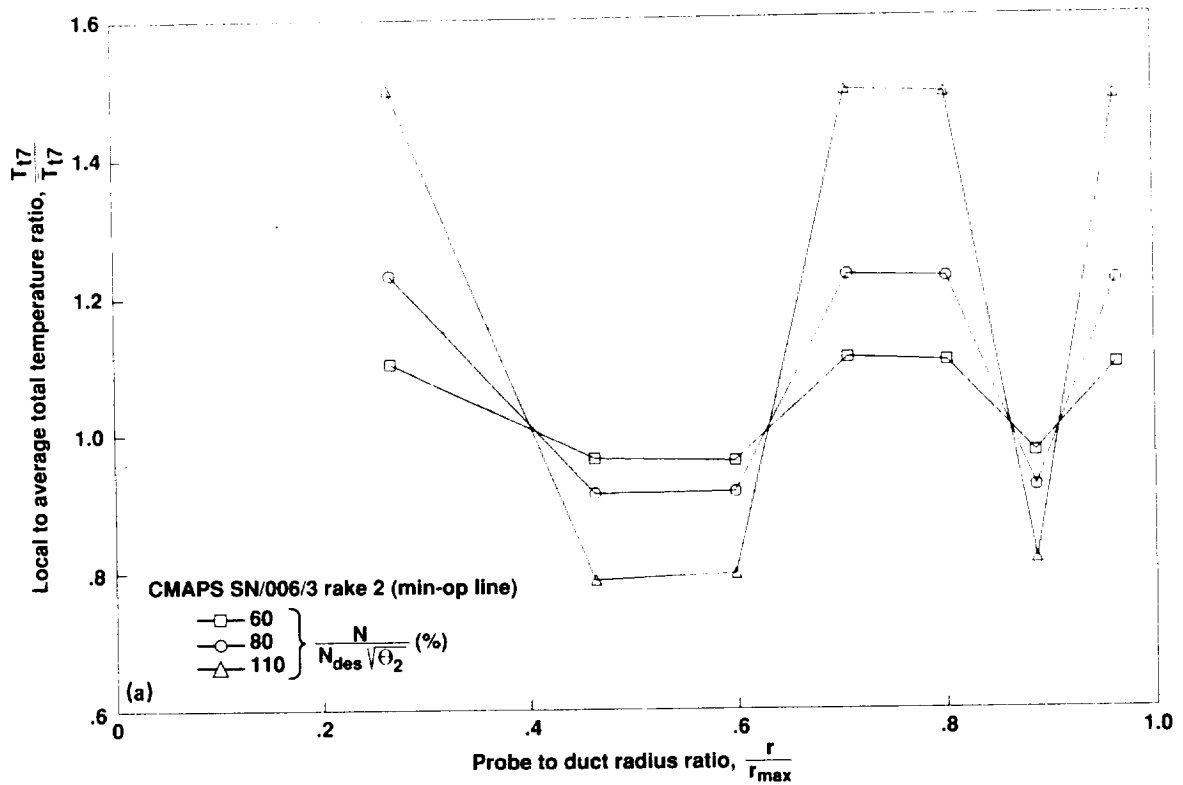


Figure 26. Baseline nozzle entrance radial temperature distribution for CMAPS SN/006/3 along the min-op line. (a) At 20°; (b) at 164°.

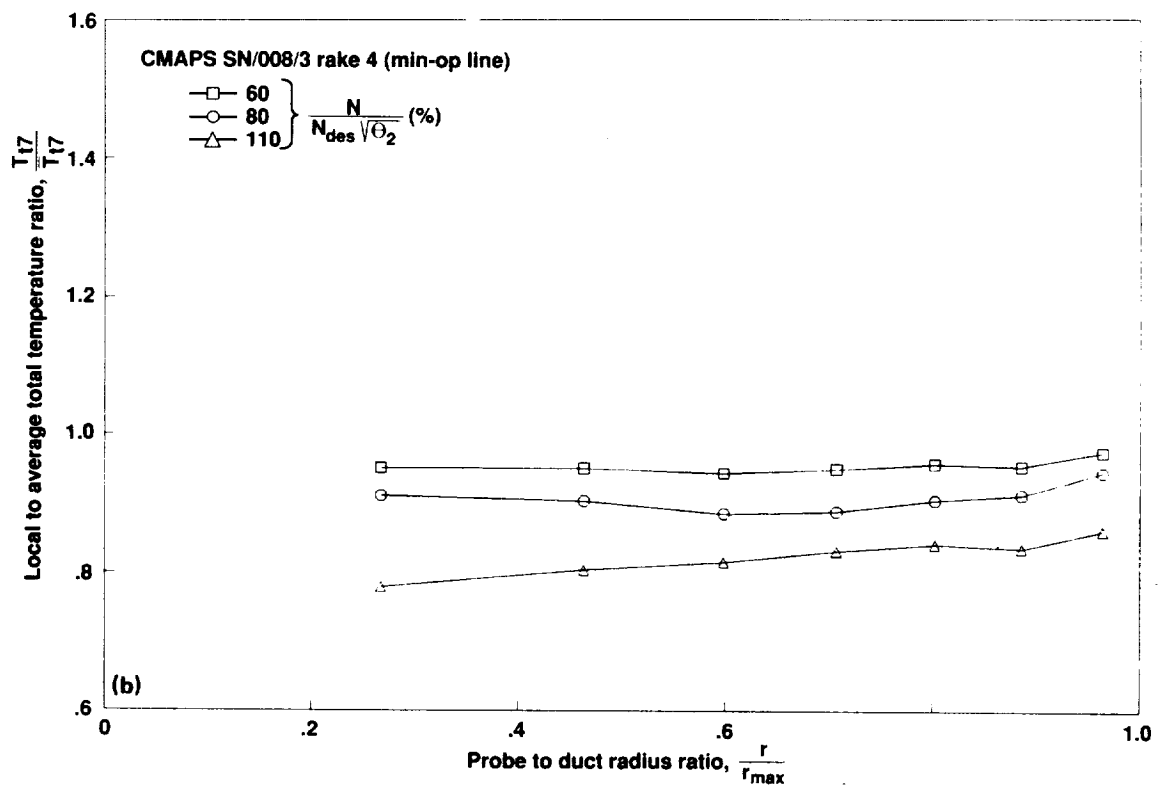
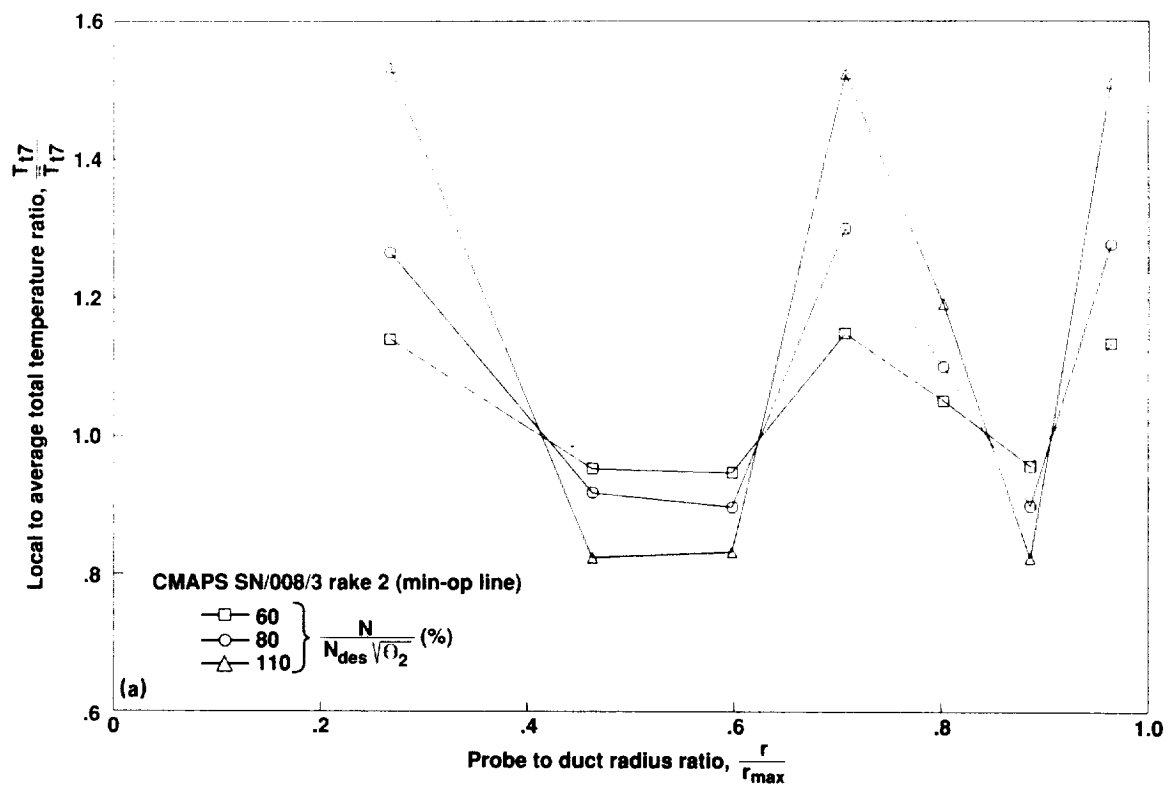


Figure 27. Baseline nozzle entrance radial temperature distribution for CMAPS SN/008/3 along the min-op line. (a) At 20°; (b) at 164°.

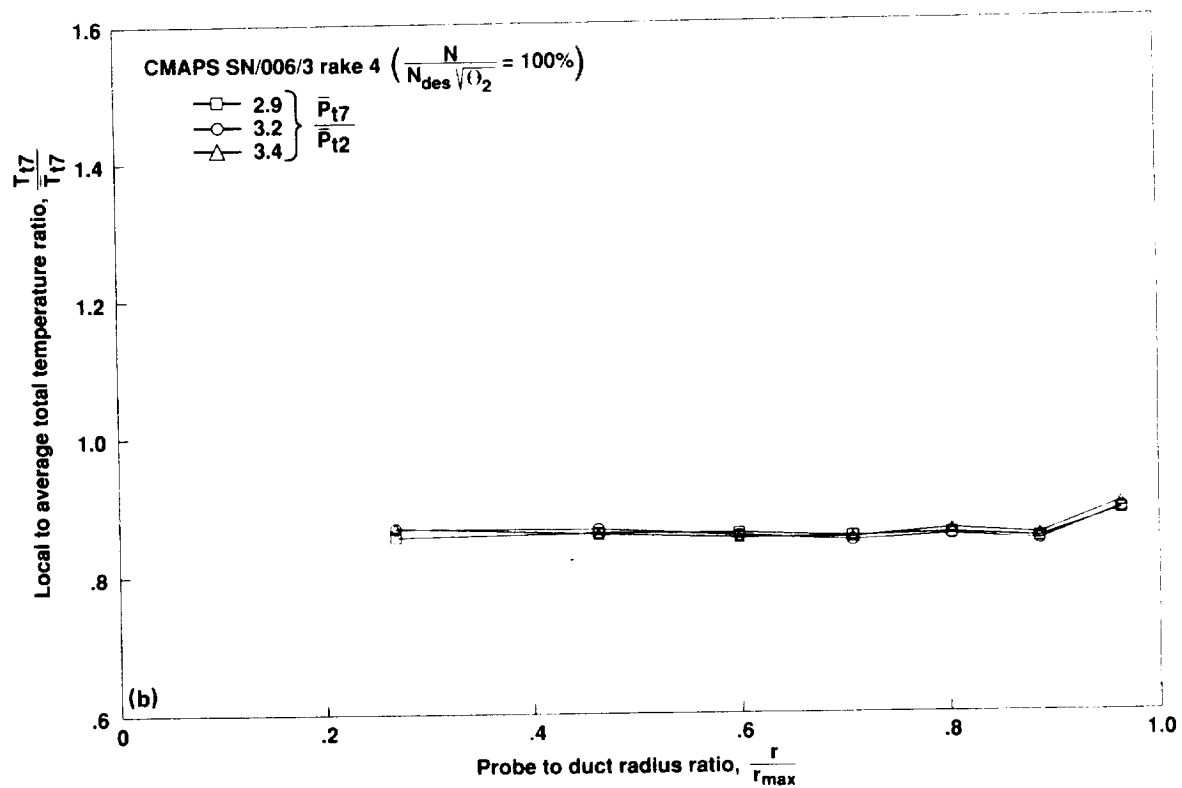
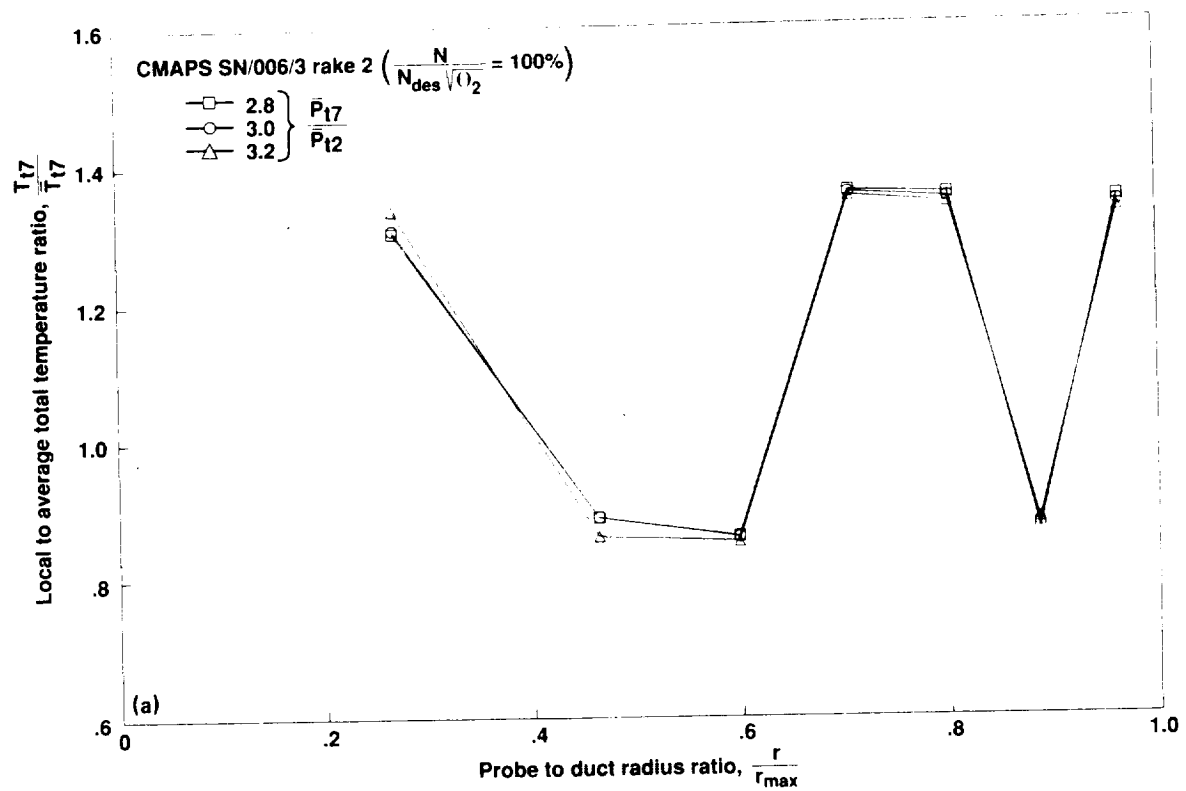


Figure 28. Baseline nozzle entrance radial temperature distribution for CMAPS SN/006/3 at 100% corrected speed. (a) At 20°; (b) at 164°.

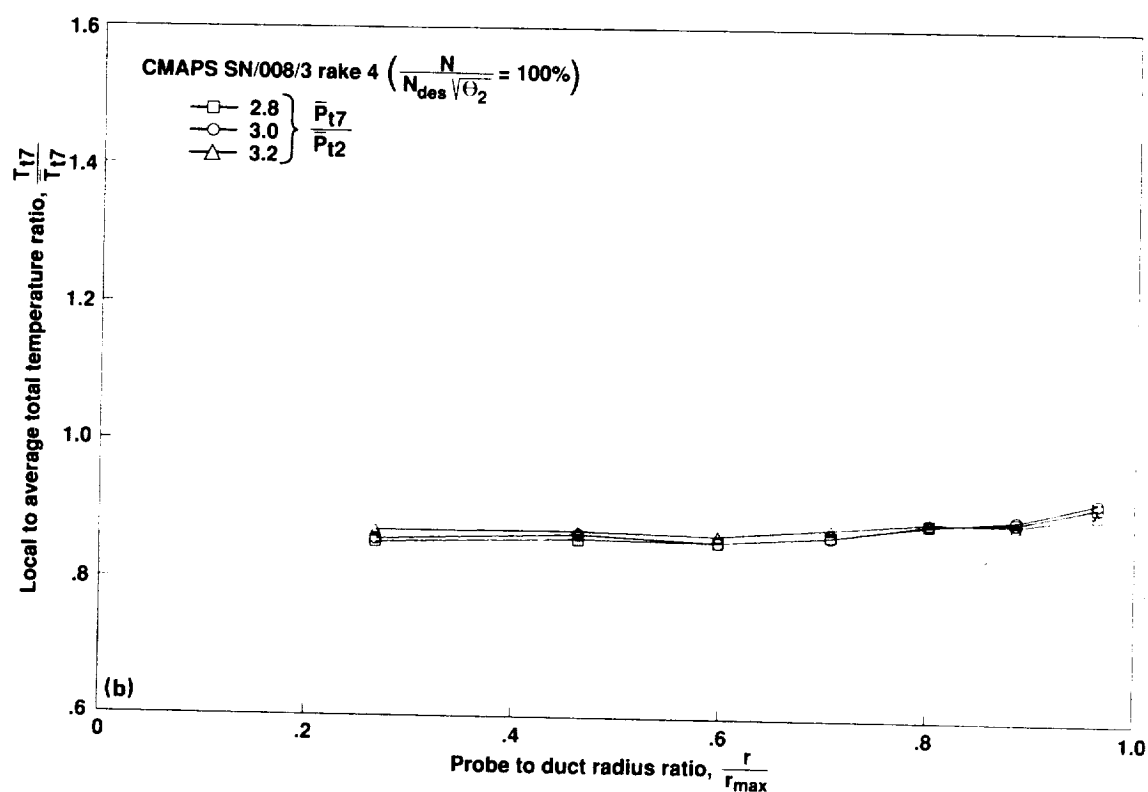
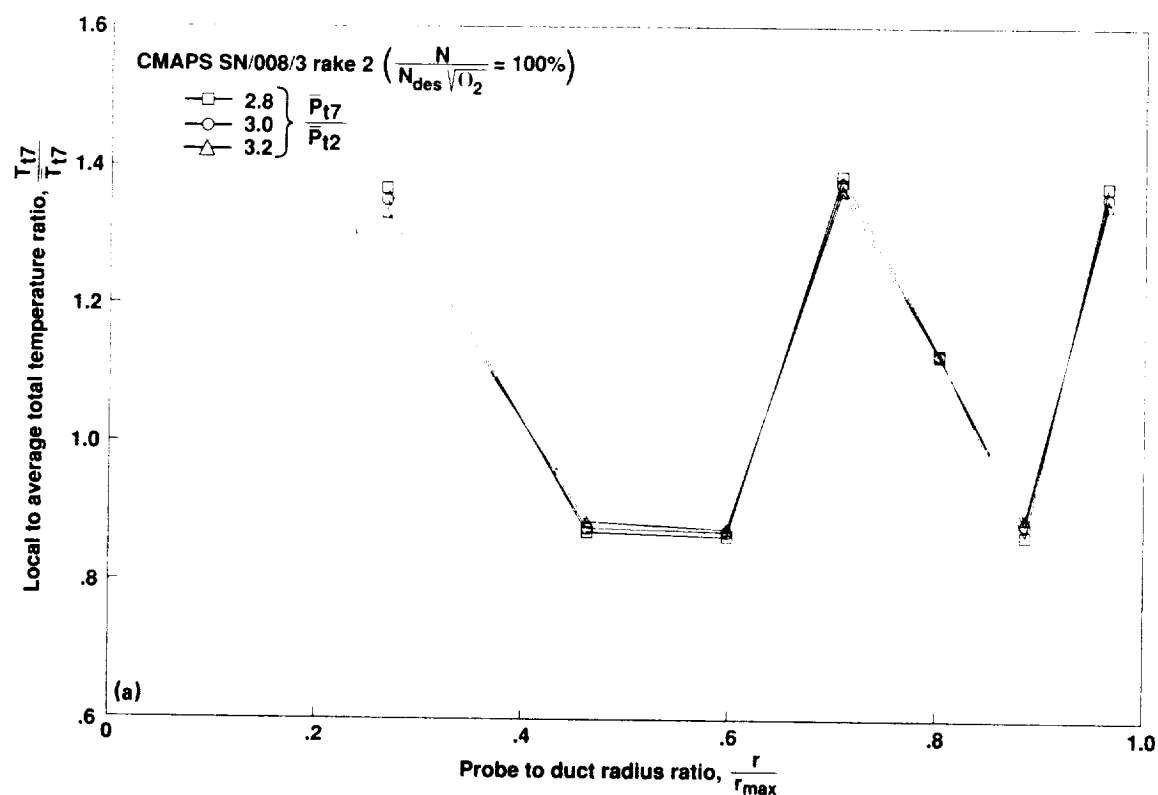


Figure 29. Baseline nozzle entrance radial temperature distribution for CMAPS SN/008/3 at 100% corrected speed. (a) At 20°; (b) at 164°.

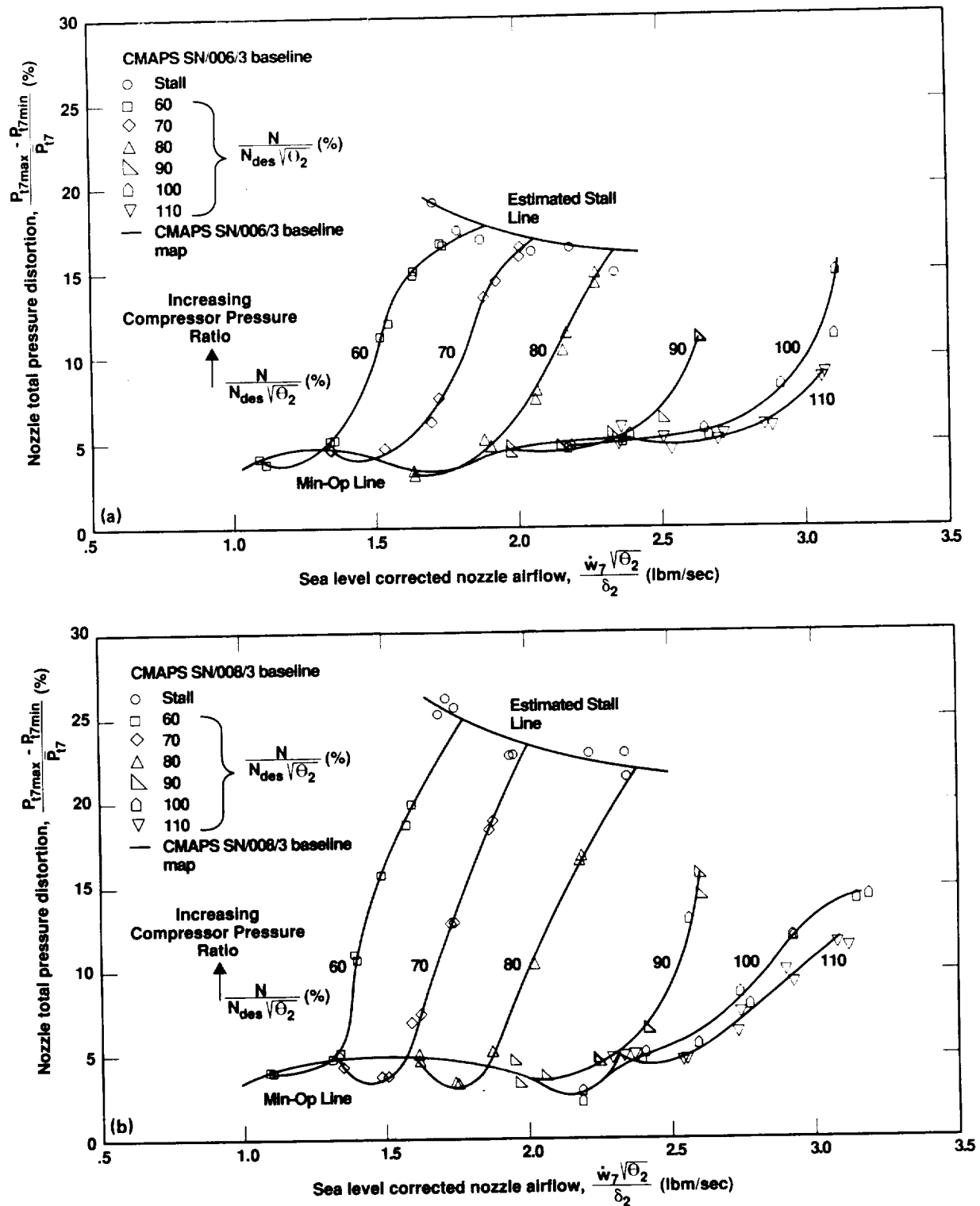


Figure 30. Baseline nozzle entrance total pressure distortion. (a) CMAPS SN/006/3; (b) CMAPS SN/008/3.

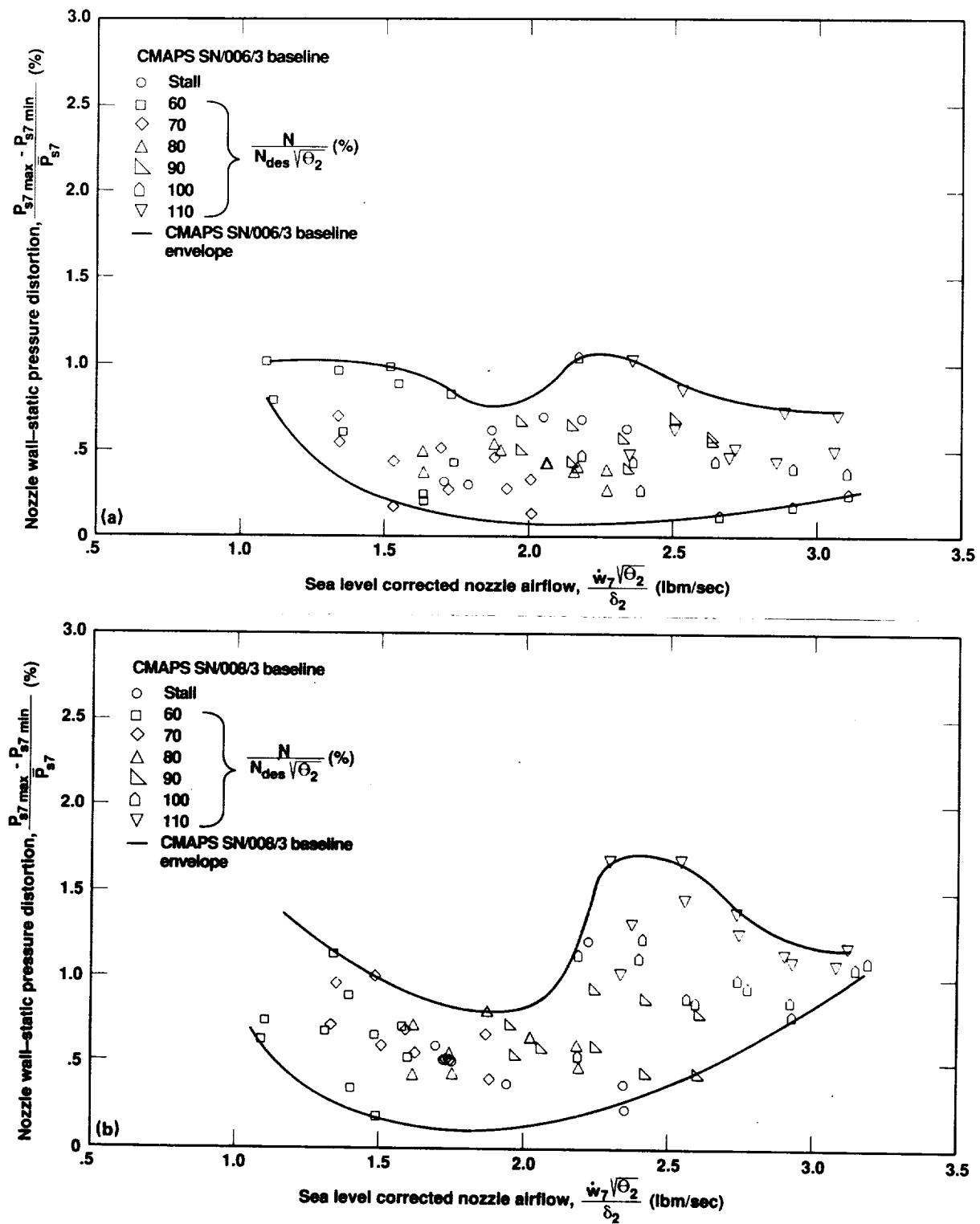


Figure 31. Baseline nozzle entrance wall static pressure distortion. (a) CMAPS SN/006/3; (b) CMAPS SN/008/3.

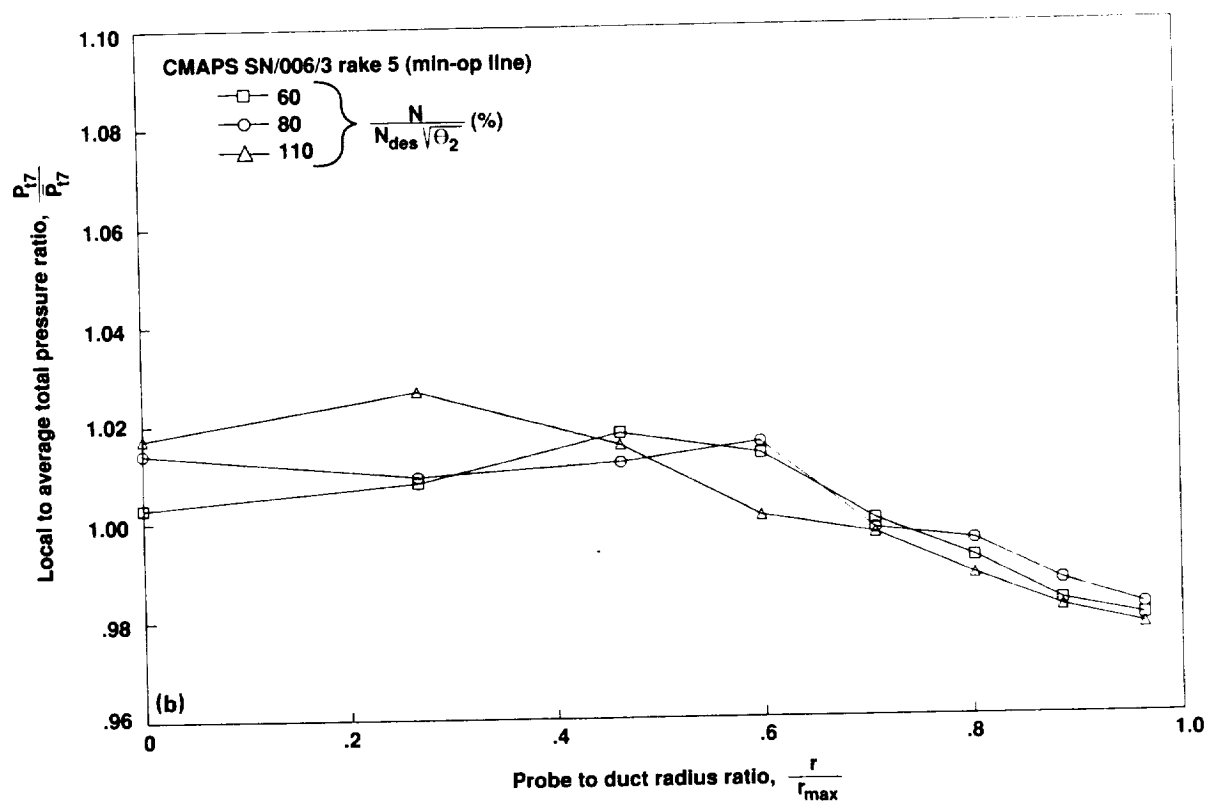
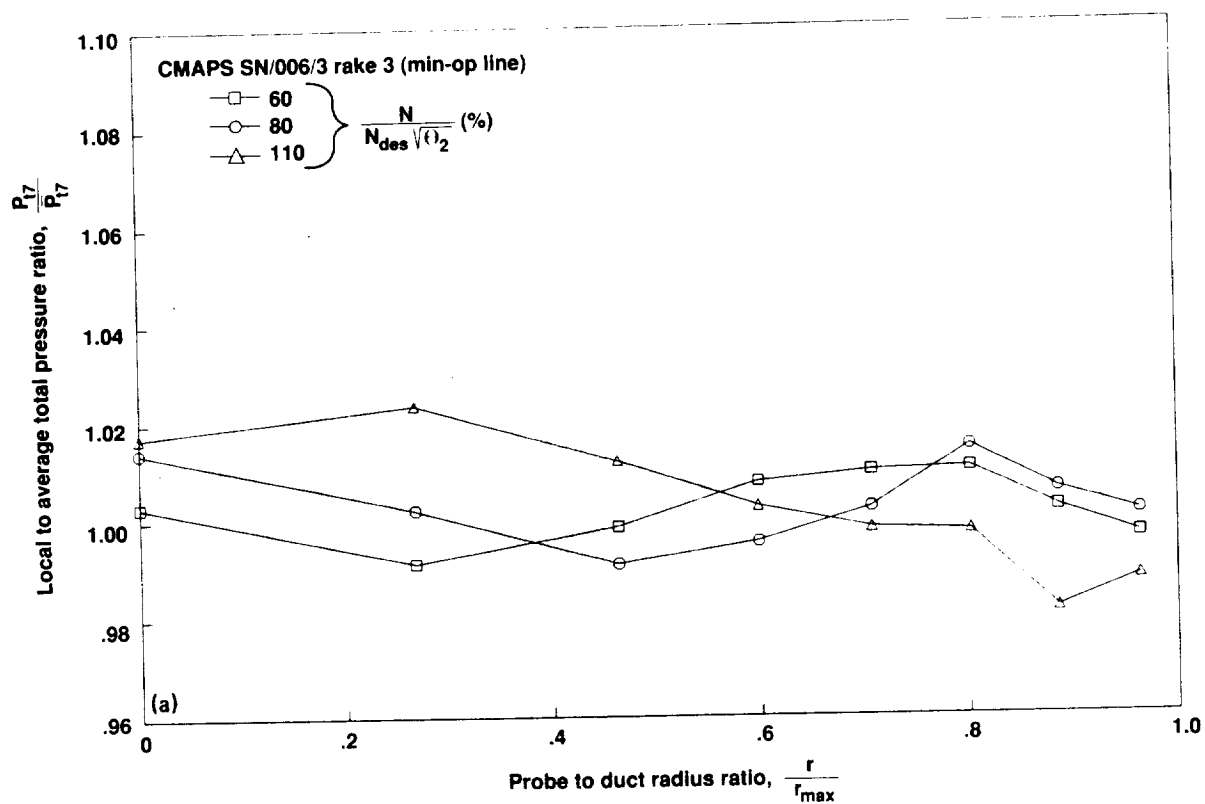


Figure 32. Baseline nozzle entrance radial pressure distribution for CMAPS SN/006/3 along the min-op line. (a) At 92° ; (b) at 236° .

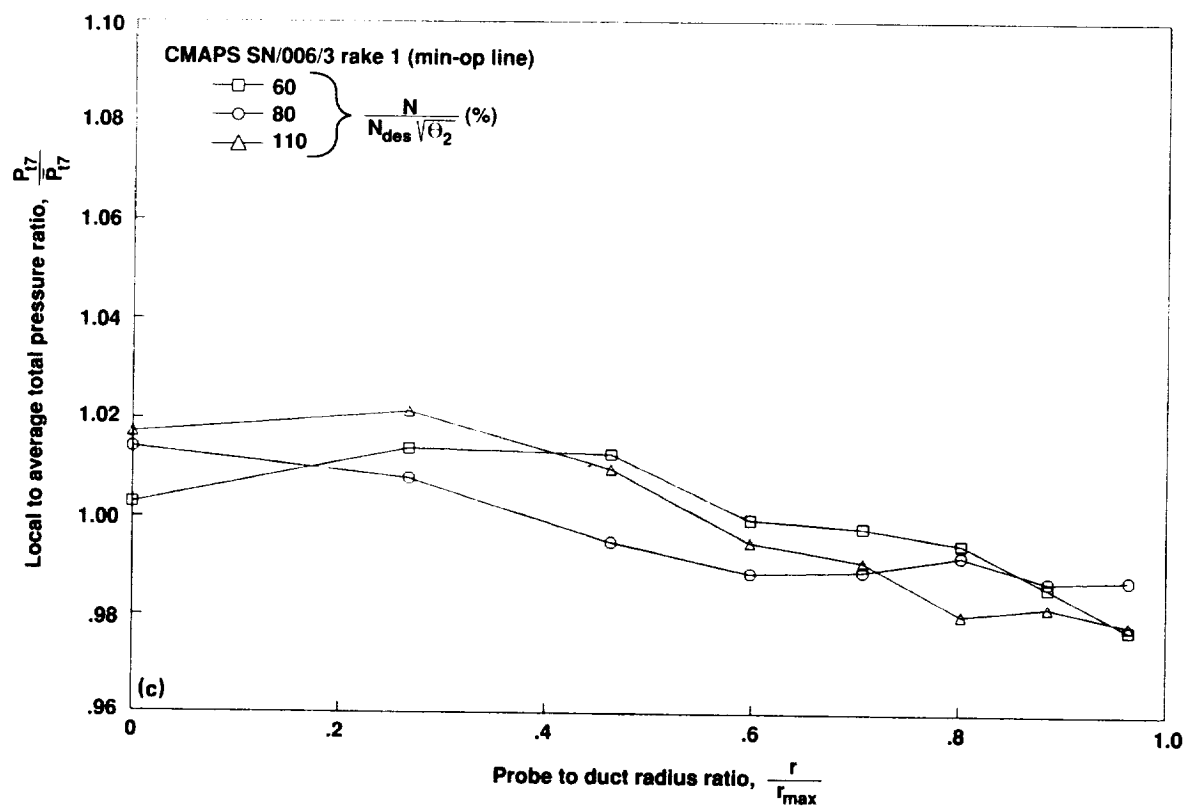


Figure 32. Concluded. (c) At 308°.

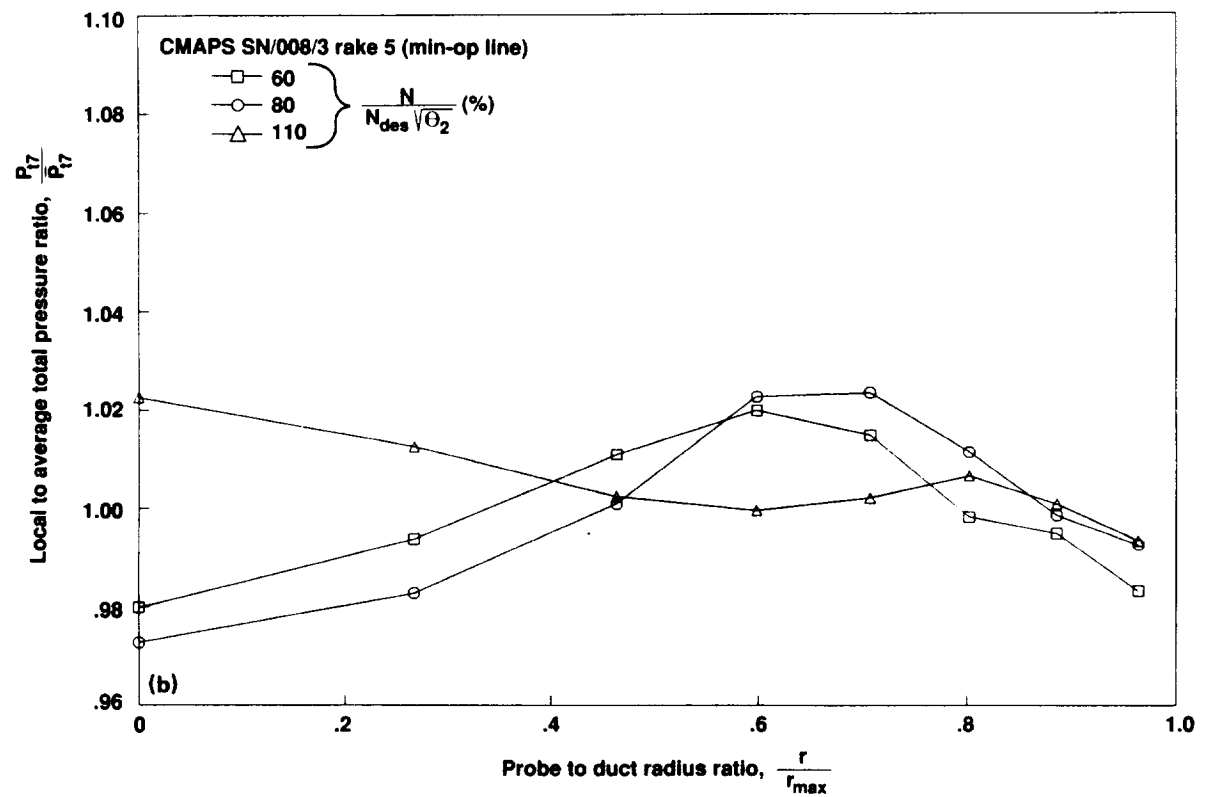
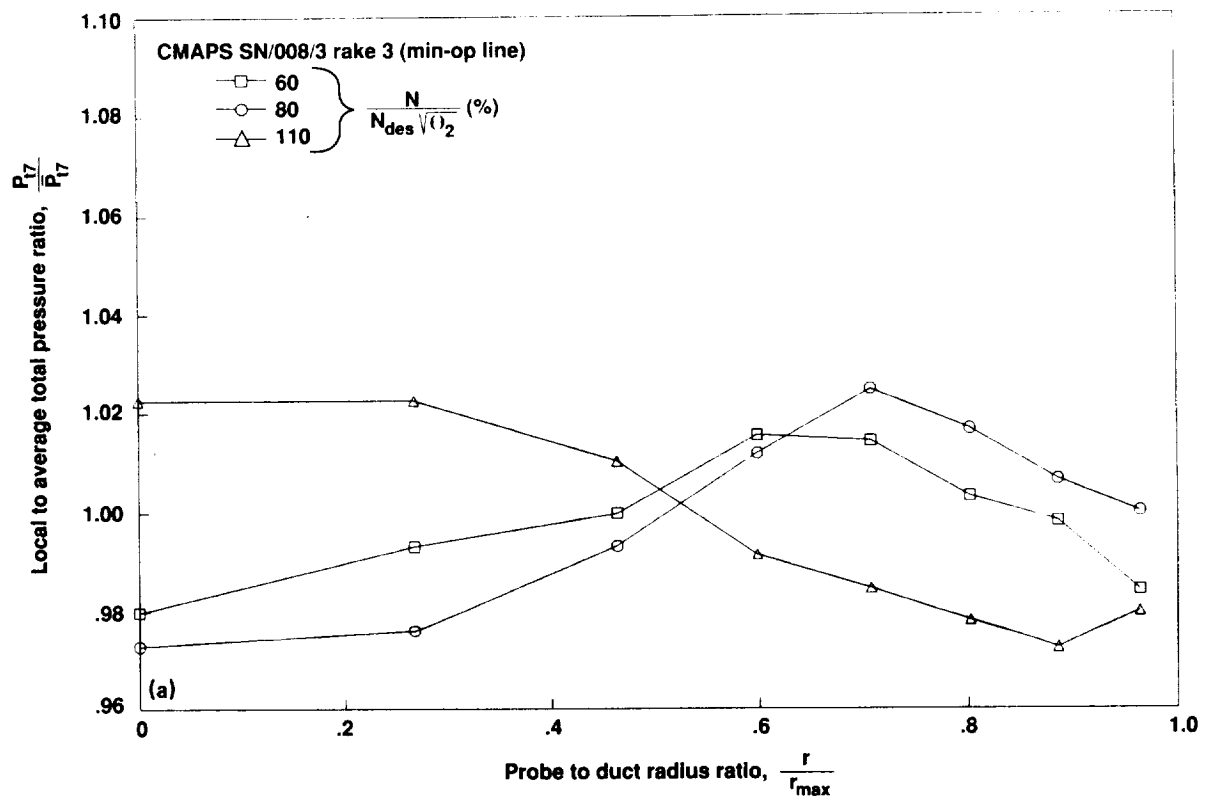


Figure 33. Baseline nozzle entrance radial pressure distribution for CMAPS SN/008/3 along the min-op line. (a) At 92°; (b) at 236°.

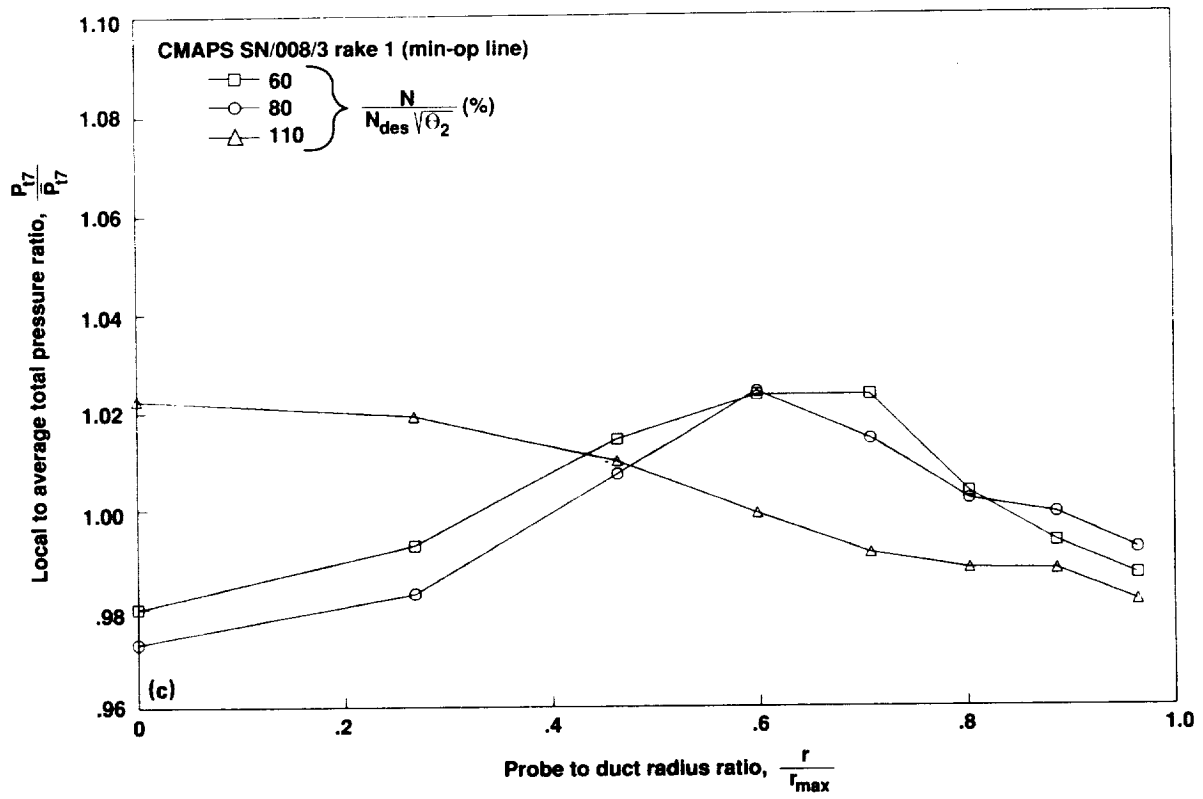


Figure 33. Concluded. (c) At 308°.

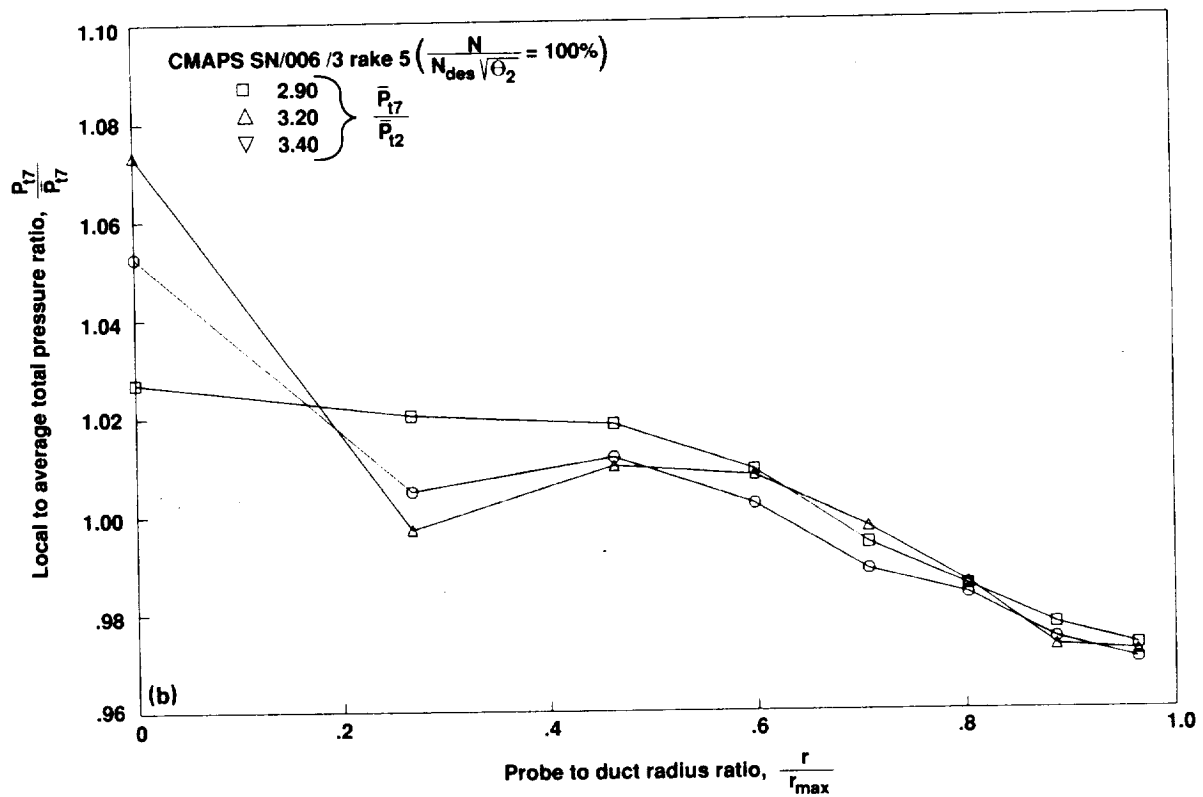
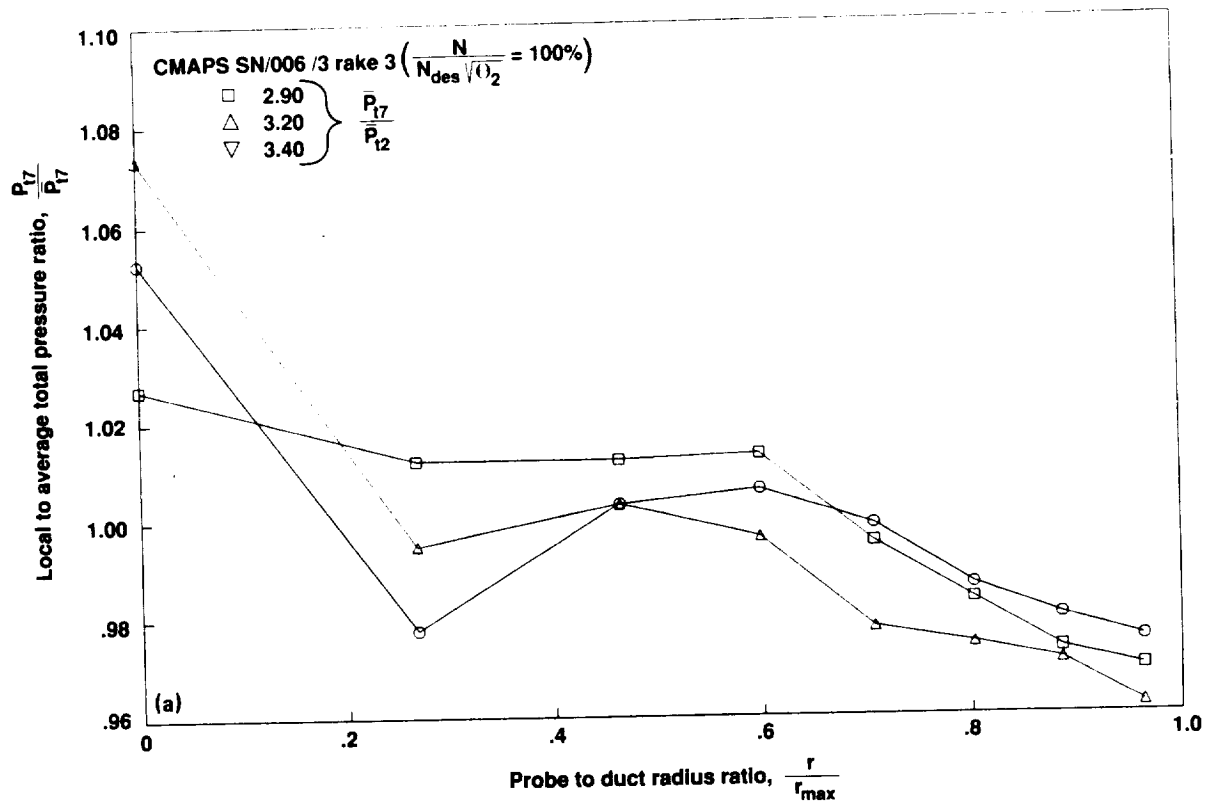


Figure 34. Baseline nozzle entrance radial pressure distribution for CMAPS SN/006/3 at 100% corrected speed. (a) At 92°; (b) at 236°.

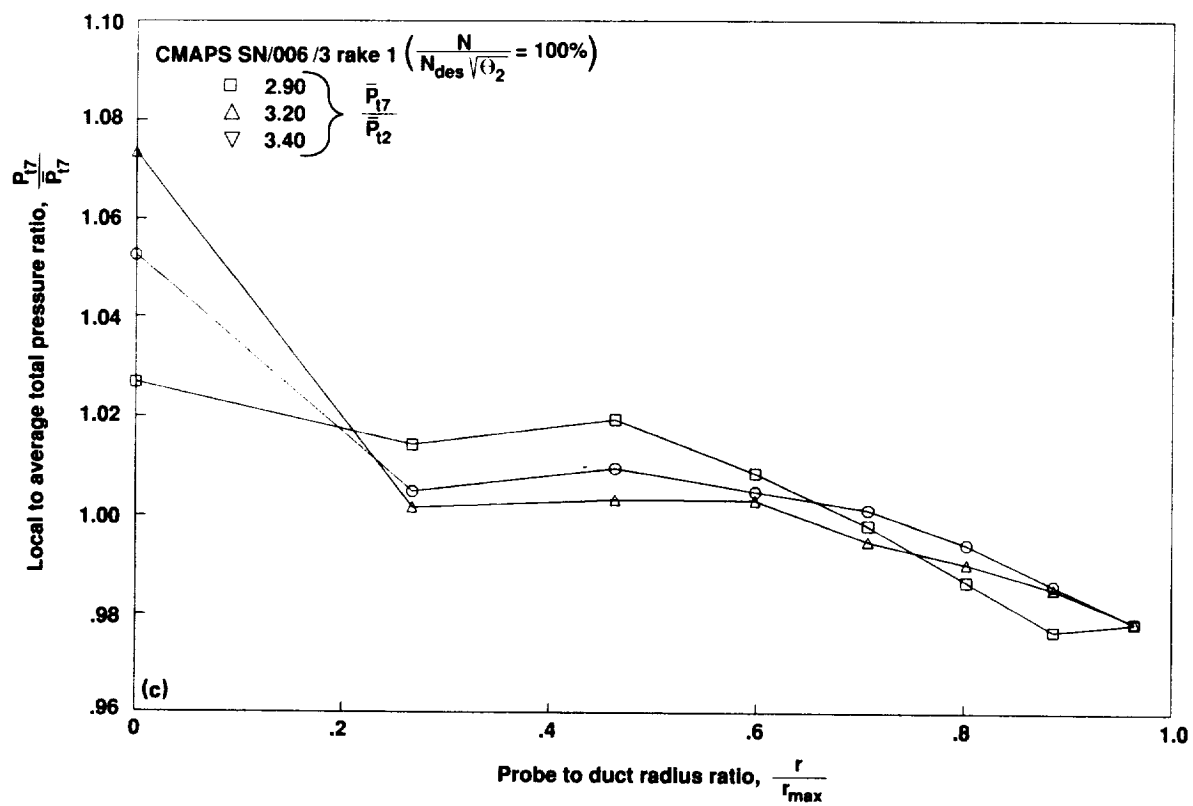


Figure 34. Concluded. (c) At 308°.

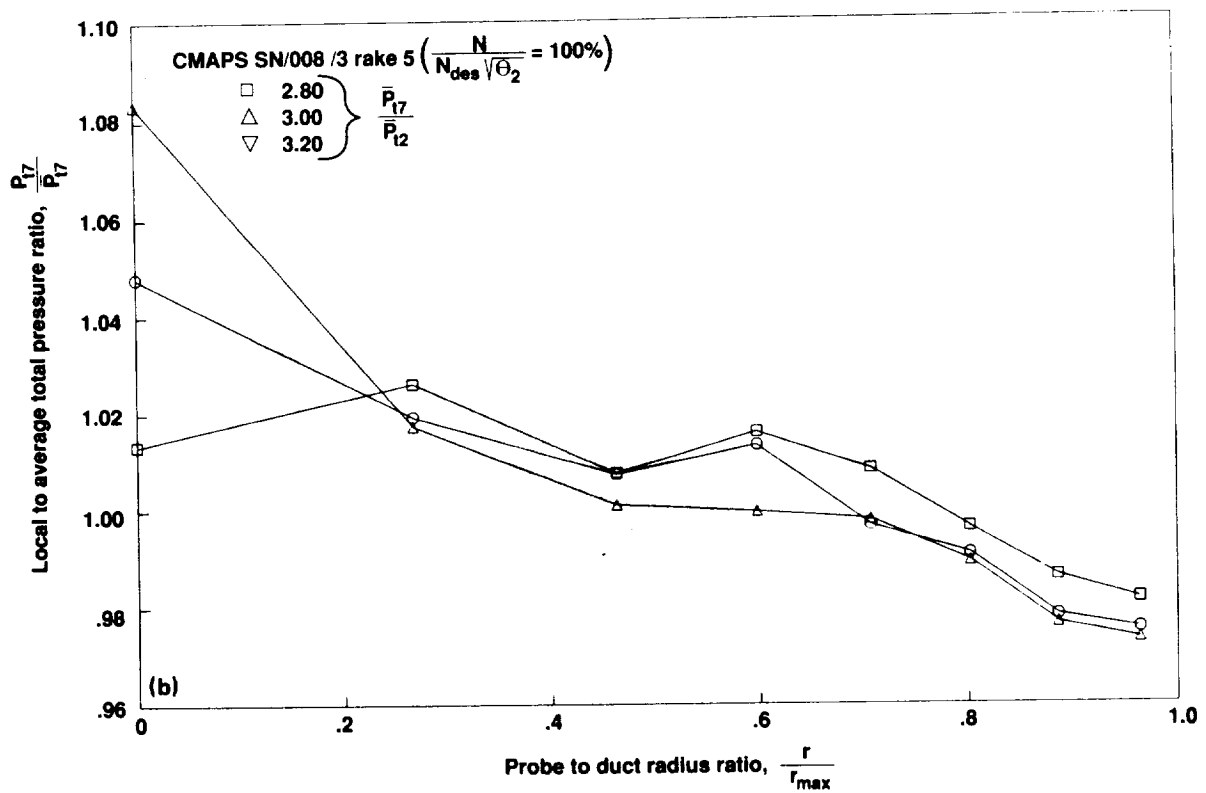
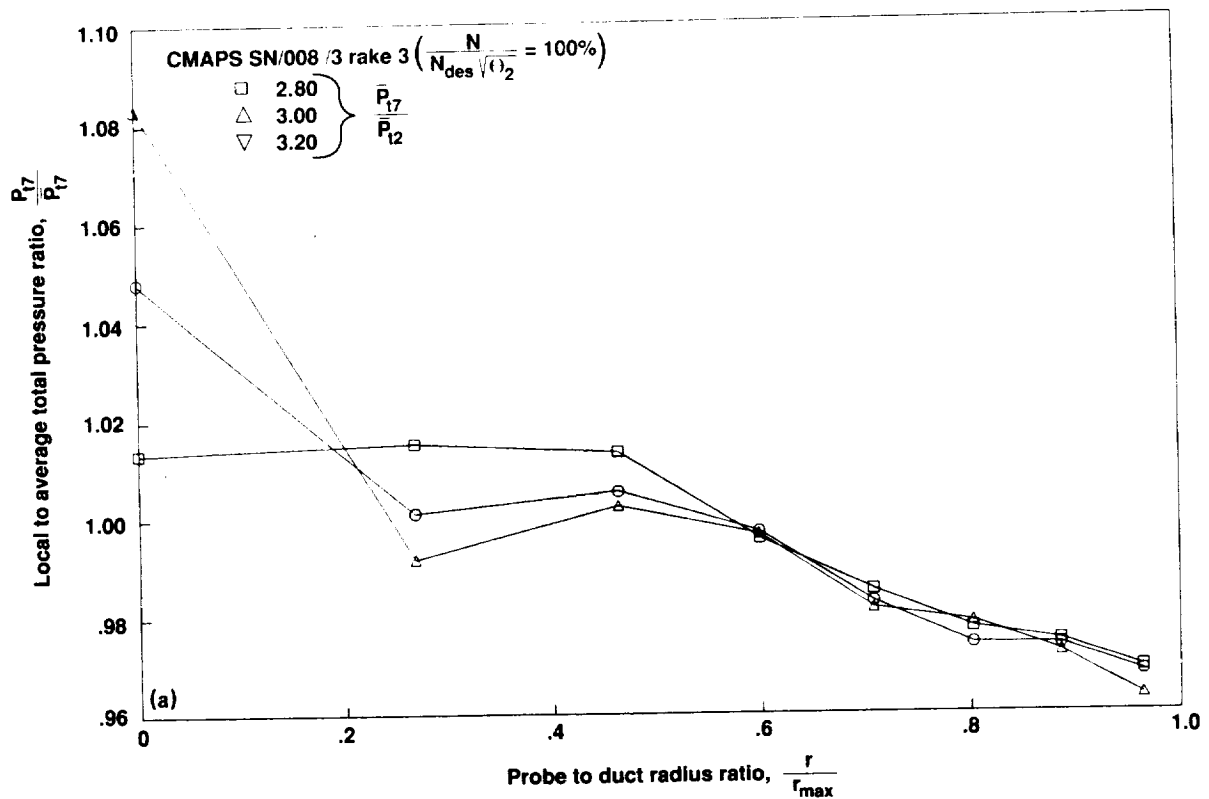


Figure 35. Baseline nozzle entrance radial pressure distribution for CMAPS SN/008/3 at 100% corrected speed. (a) At 92°; (b) at 236°.

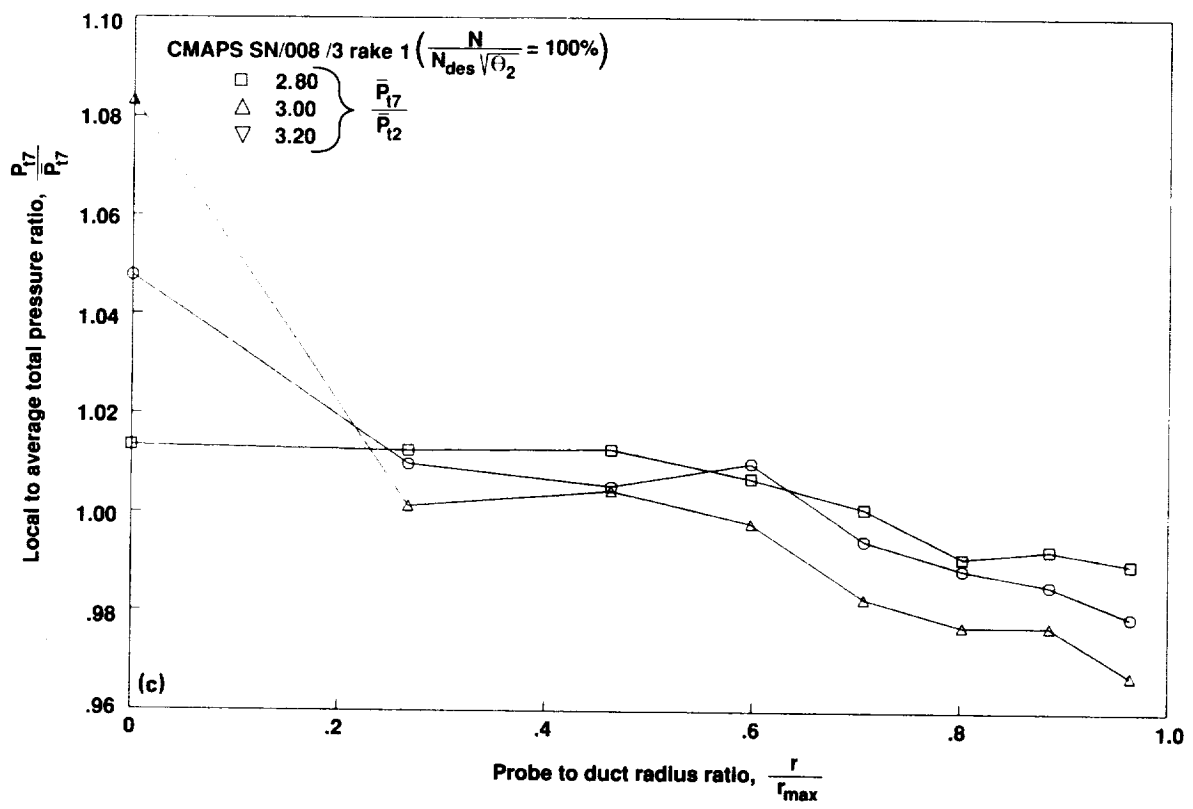


Figure 35. Concluded. (c) At 308°.

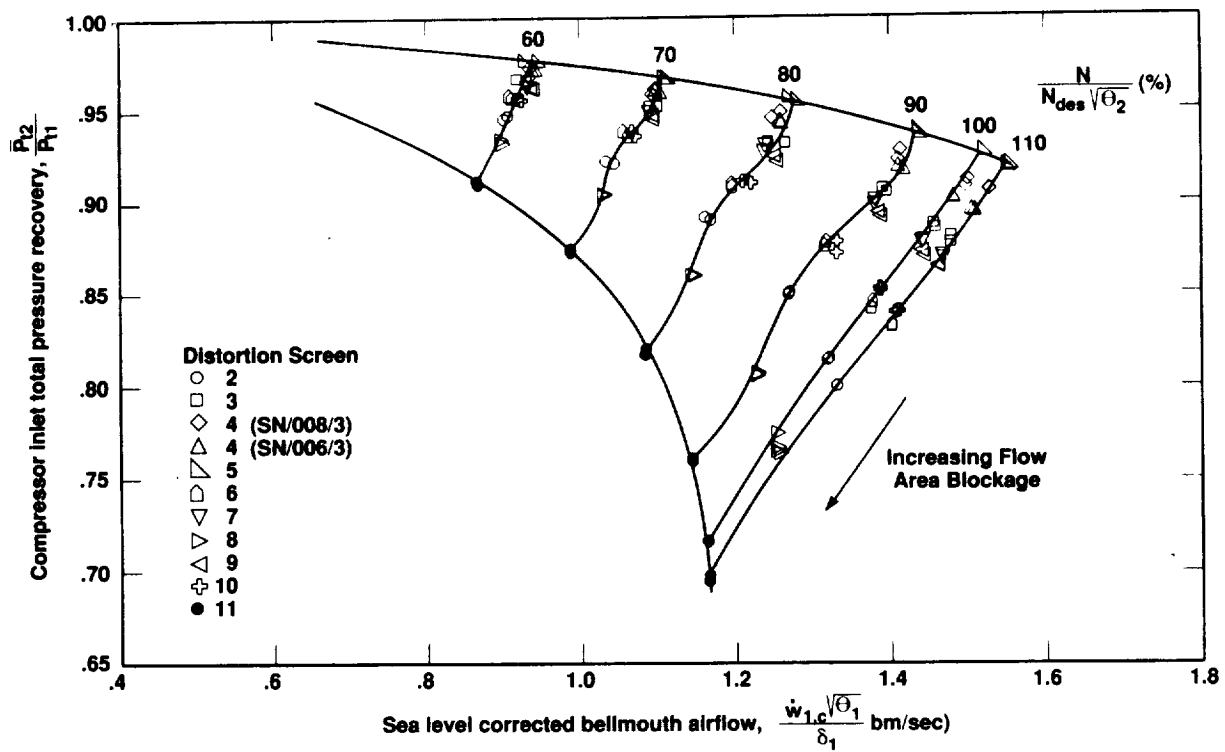


Figure 36. Compressor inlet total pressure recovery along the min-op line with distortion screens.

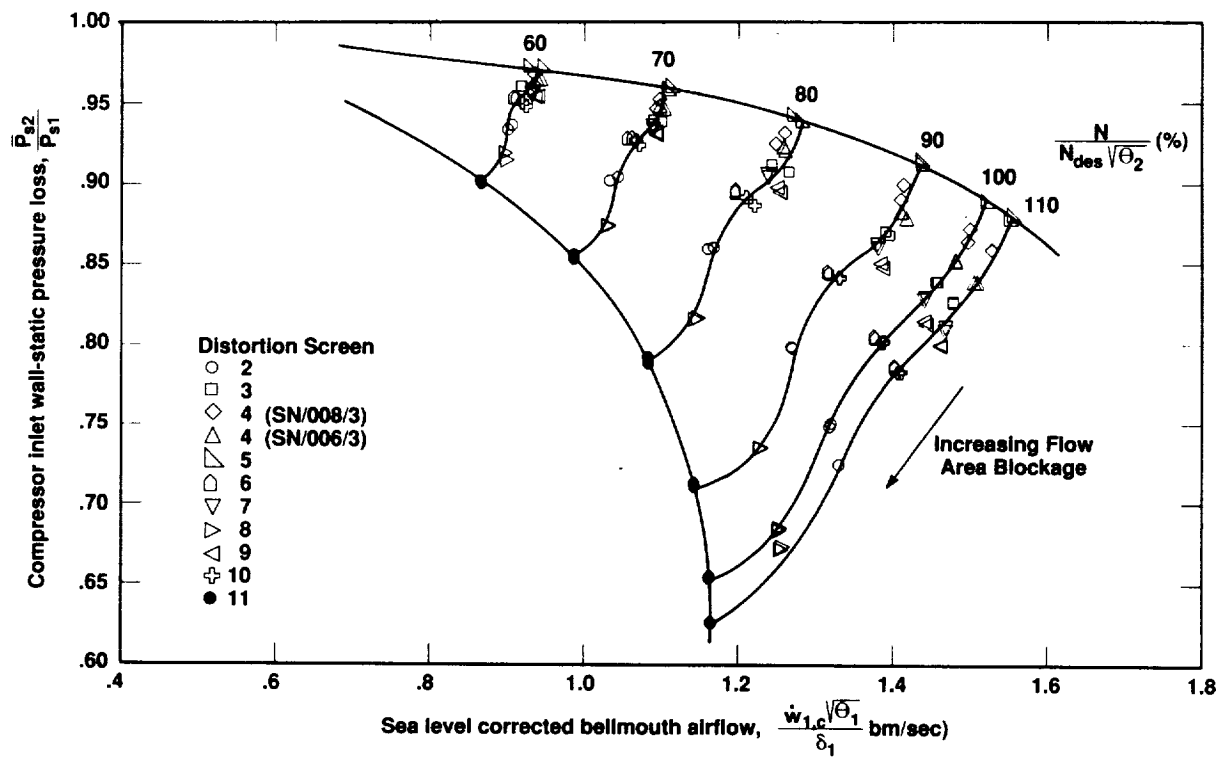


Figure 37. Compressor inlet wall static pressure loss along the min-op line with distortion screens.

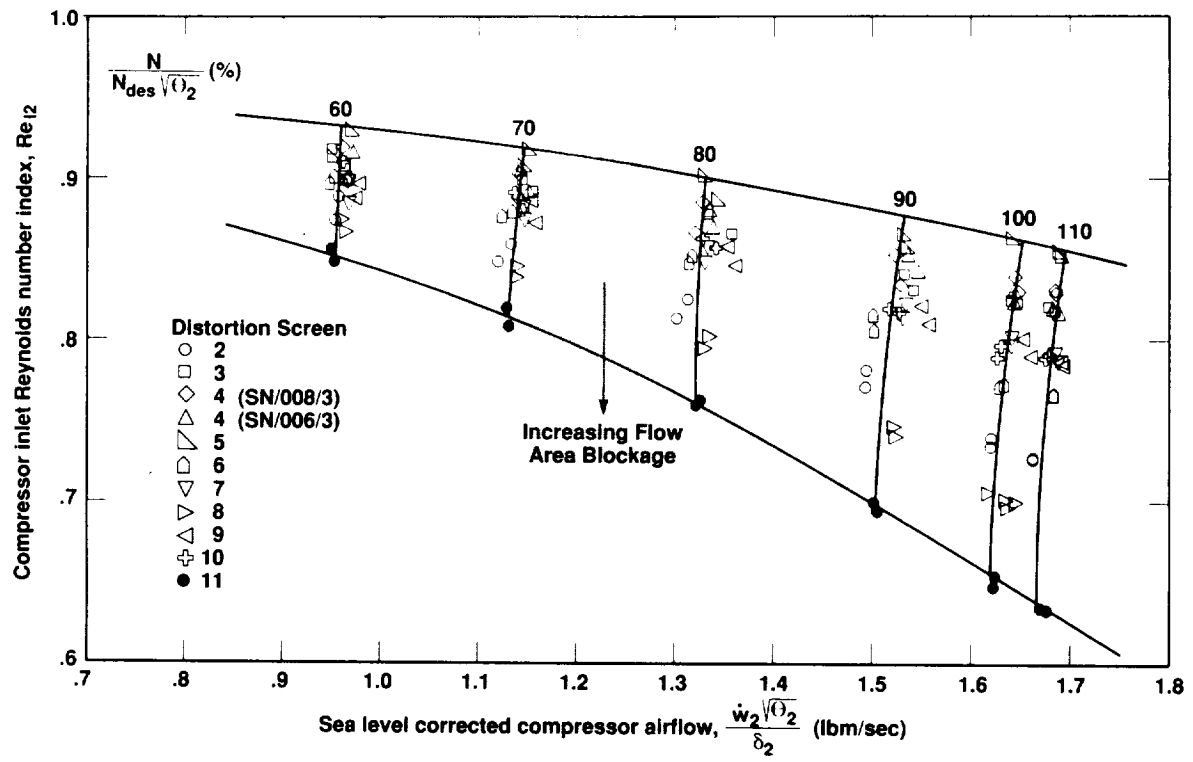


Figure 38. Reynolds number index variation along the min-op line for all configurations.

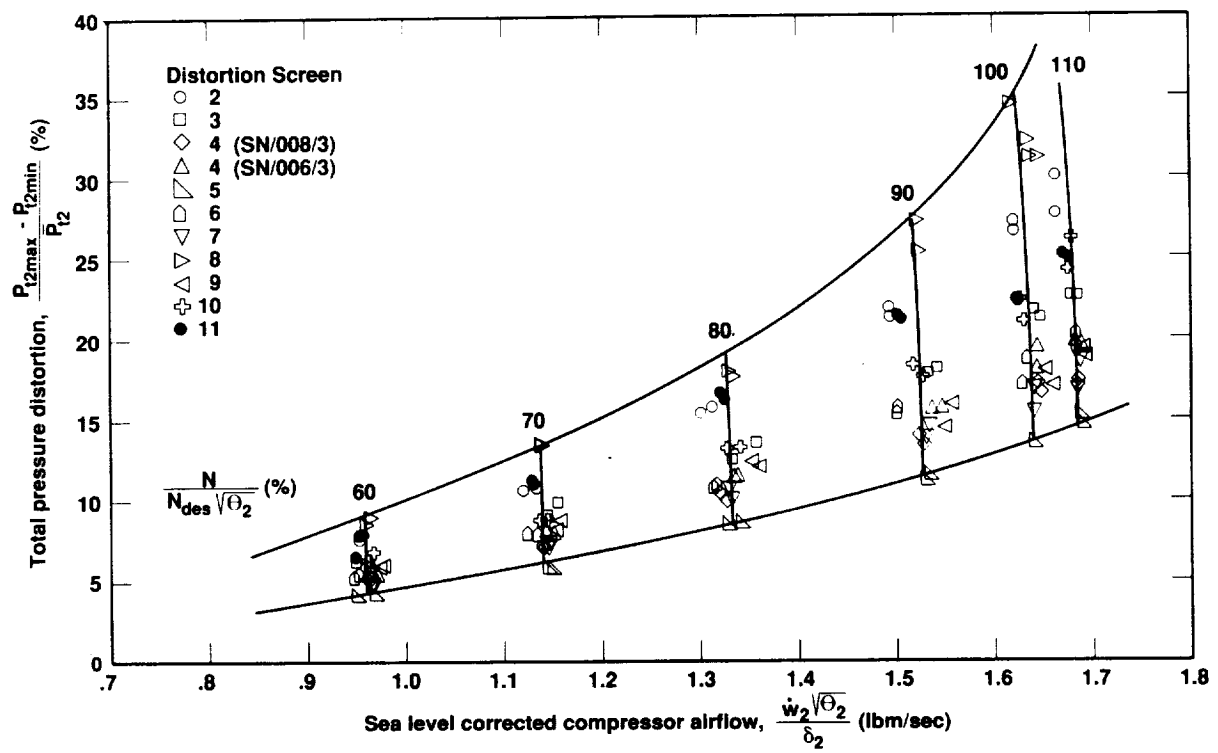


Figure 39. Compressor inlet total pressure distortion along the min-op line with distortion screens.

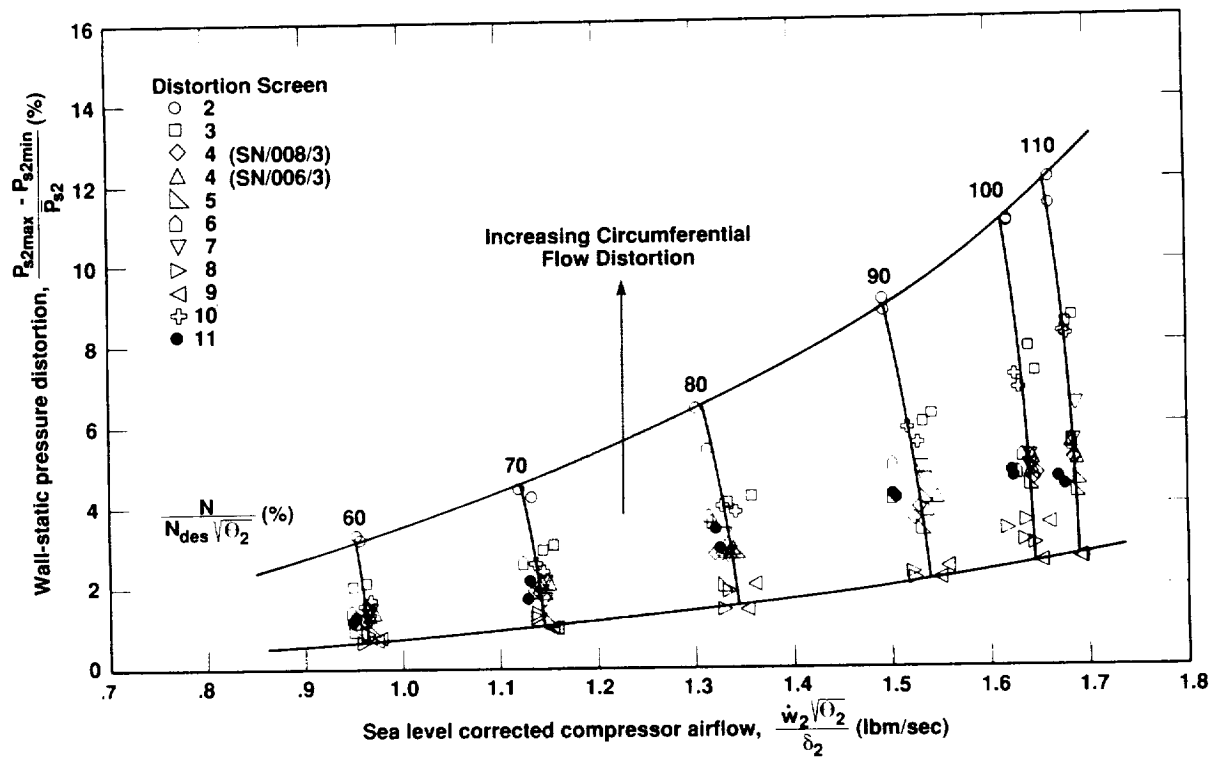


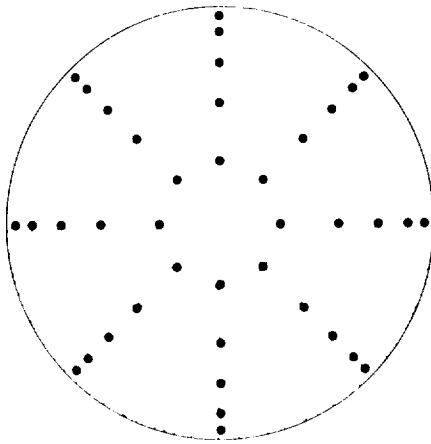
Figure 40. Compressor inlet wall static pressure distortion along the min-op line with distortion screens.

$$\frac{P_{12} - P_{12}}{P_{12}} \text{ Color range}$$

Red: 0.168

Blue: -0.132

Screen orientation



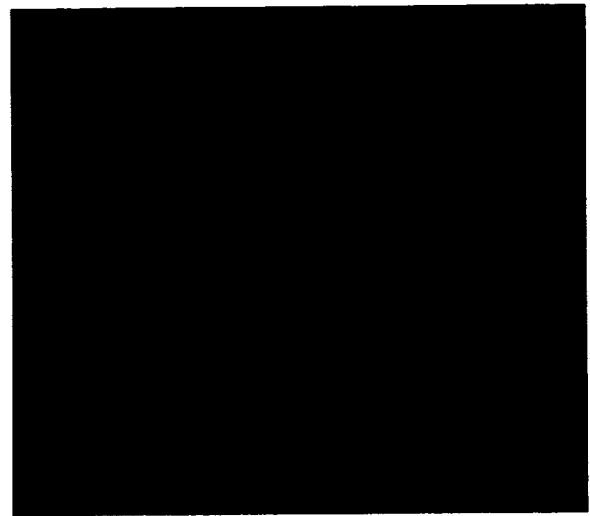
$$\text{Distortion, } \frac{P_{12\max} - P_{12\min}}{P_{12}} (\%)$$

(a) 7.94

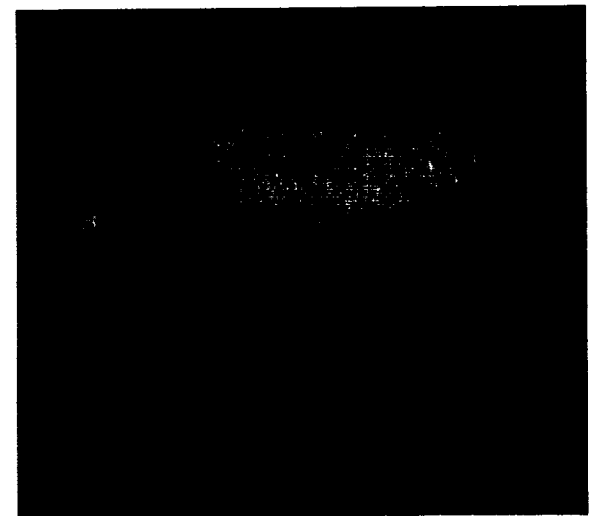
(b) 15.76

(c) 30.03

(a)



(b)



(c)



Figure 41. Compressor inlet total pressure distributions for screen No. 2 along the min-op line. (a) 60% corrected speed; (b) 80% corrected speed; (c) 110% corrected speed.

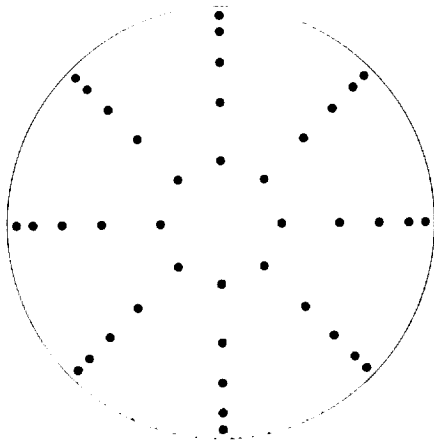
ORIGINAL PAGE IS
OF POOR QUALITY

$$\frac{P_{12} - P_{12}}{P_{12}} \text{ Color range}$$

Red: 0.078

Blue: -0.148

Screen orientation



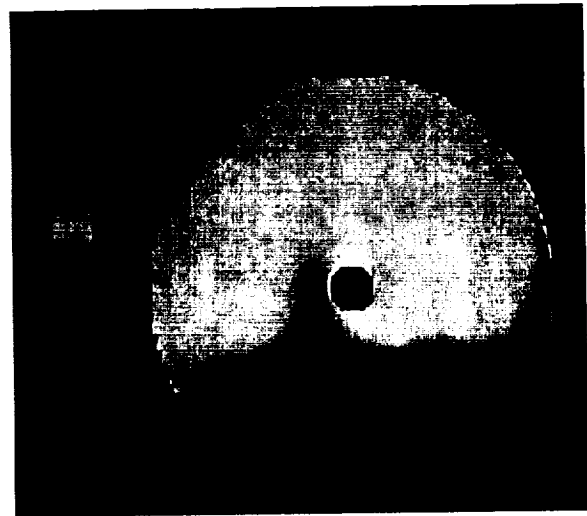
$$\text{Distortion, } \frac{P_{12\max} - P_{12\min}}{P_{12}} (\%)$$

(a) 6.27

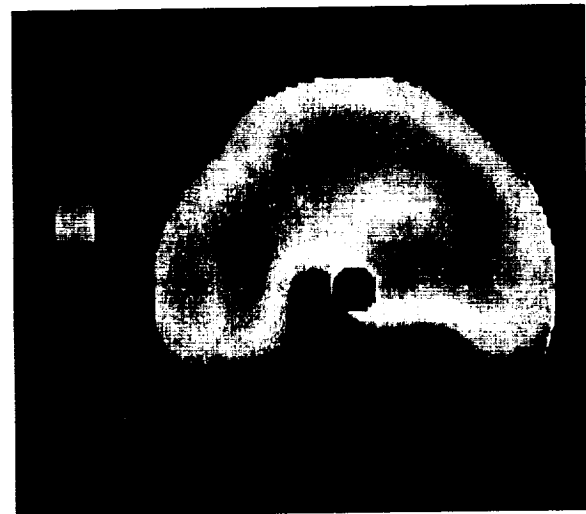
(b) 12.54

(c) 22.60

(a)



(b)



(c)

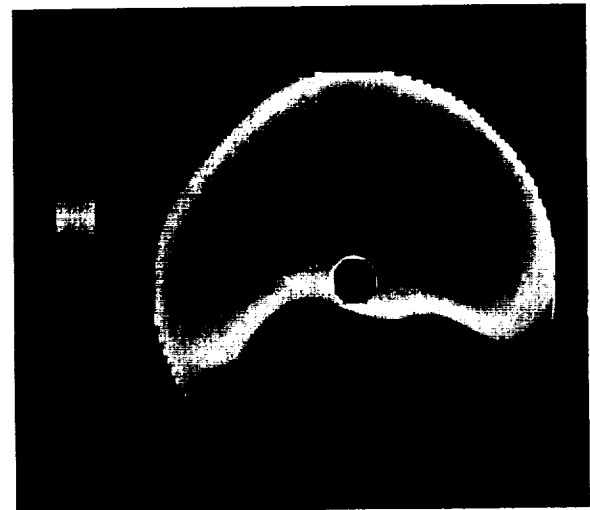


Figure 42. Compressor inlet total pressure distributions for screen No. 3 along the min-op line. (a) 60% corrected speed; (b) 80% corrected speed; (c) 110% corrected speed.

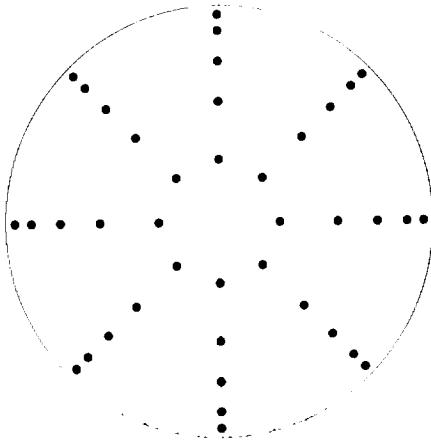
ORIGINAL PAGE IS
OF POOR QUALITY

$$\frac{P_{t2} - P_{t2}}{P_{t2}} \text{ Color range}$$

Red: 0.050

Blue: -0.147

Screen orientation



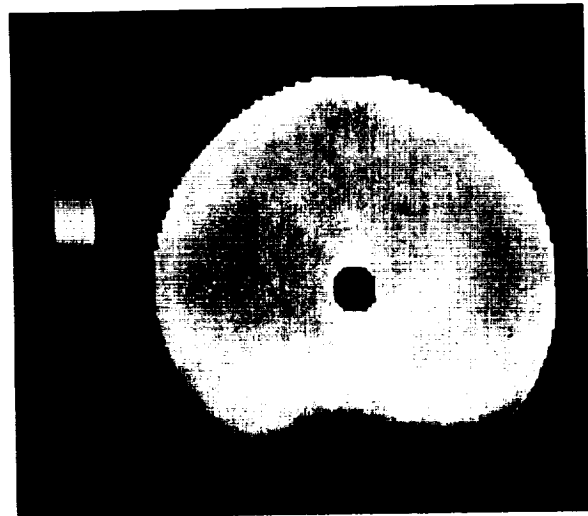
$$\text{Distortion, } \frac{P_{t2\max} - P_{t2\min}}{P_{t2}} (\%)$$

(a) 5.35

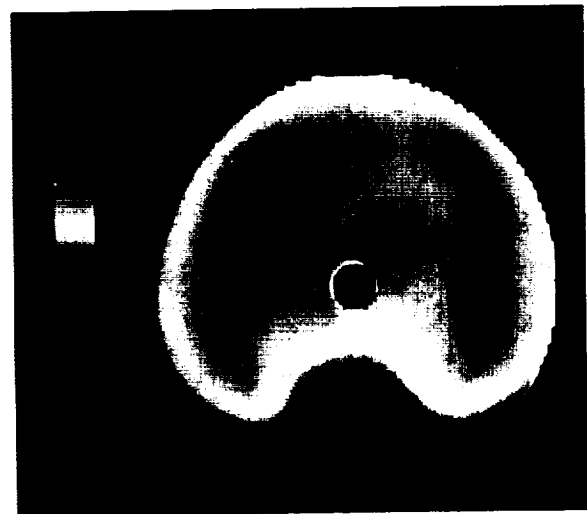
(b) 11.39

(c) 19.70

(a)



(b)



(c)

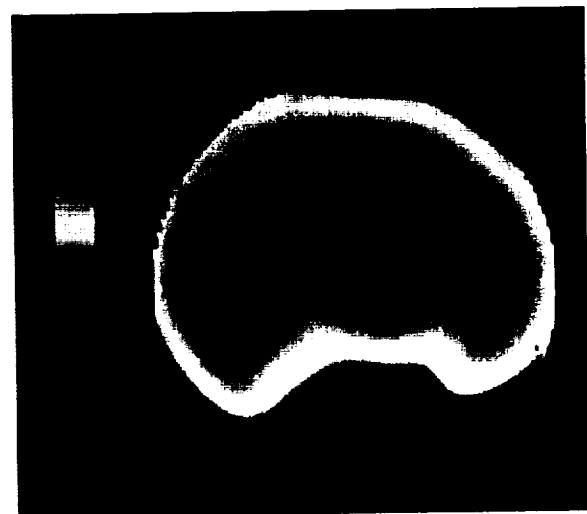


Figure 43. CMAPS SN/006/3 compressor inlet total pressure distributions for screen No. 4 along the min-op line. (a) 60% corrected speed; (b) 80% corrected speed; (c) 110% corrected speed.

ORIGINAL PAGE 1
OF POOR QUALITY

89

88 INTENTIONALLY BLANK

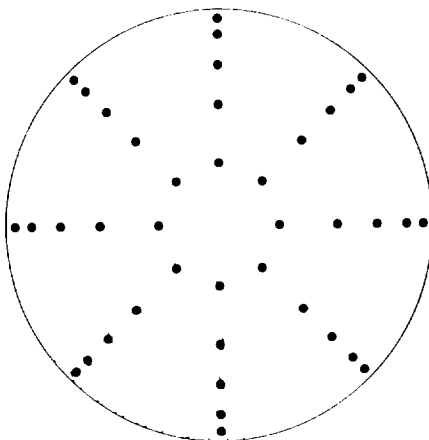
PRECEDING PAGE BLANK NOT FILMED

$$\frac{P_{t2} - \bar{P}_{t2}}{\bar{P}_{t2}} \text{ Color range}$$

Red: 0.050

Blue: -0.147

Screen orientation



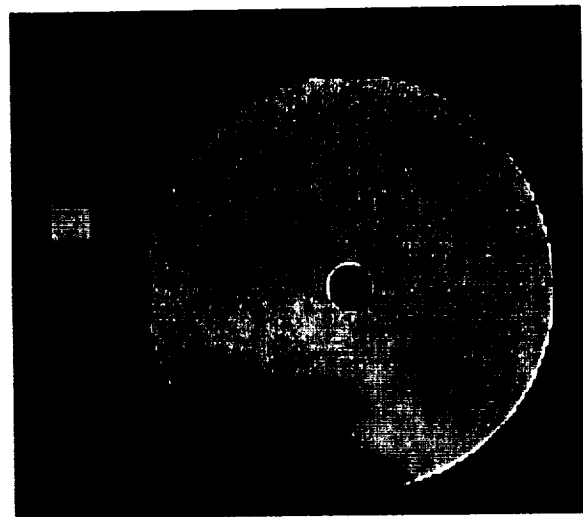
$$\text{Distortion, } \frac{P_{t2\max} - P_{t2\min}}{\bar{P}_{t2}} (\%)$$

(a) 5.35

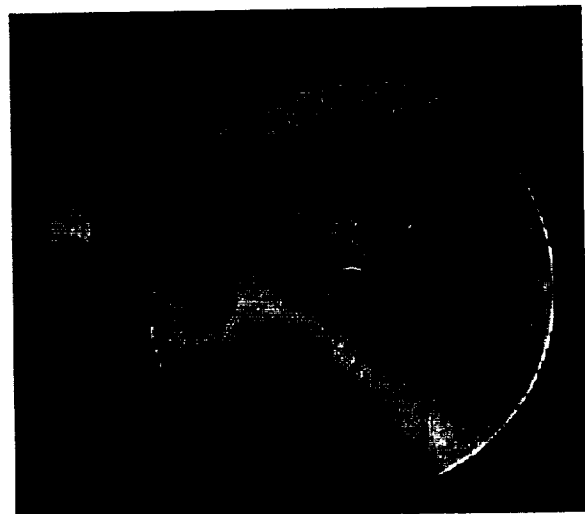
(b) 9.94

(c) 17.03

(a)



(b)



(c)

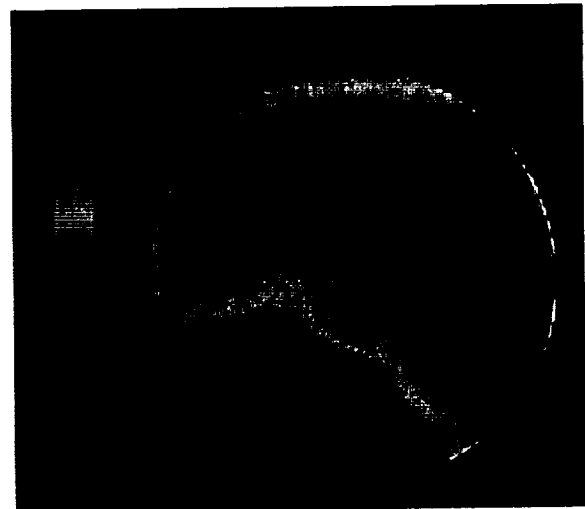


Figure 44. CMAPS SN/008/3 compressor inlet total pressure distributions for screen No. 4 along the min-op line. (a) 60% corrected speed; (b) 80% corrected speed; (c) 110% corrected speed.

ORIGINAL PAGE IS
OF POOR QUALITY

91

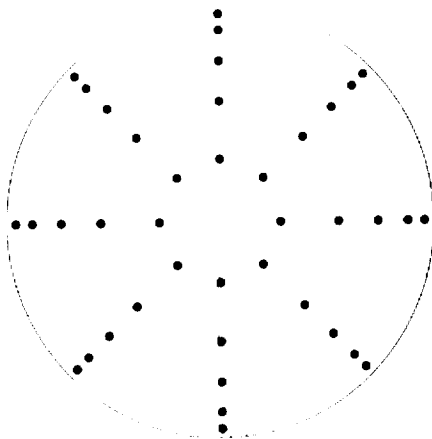
PRECEDING PAGE BLANK NOT FILMED

$$\frac{P_{12} - P_{12}}{P_{12}} \text{ Color range}$$

Red: 0.040

Blue: -0.133

Screen orientation



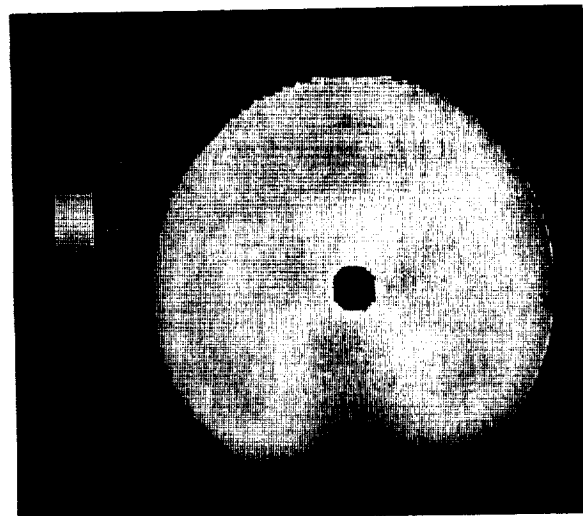
$$\text{Distortion, } \frac{P_{12\max} - P_{12\min}}{P_{12}} (\%)$$

(a) 4.19

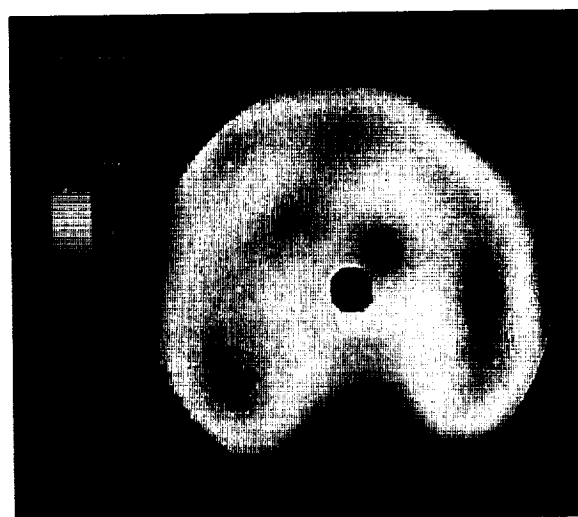
(b) 8.44

(c) 15.21

(a)



(b)



(c)

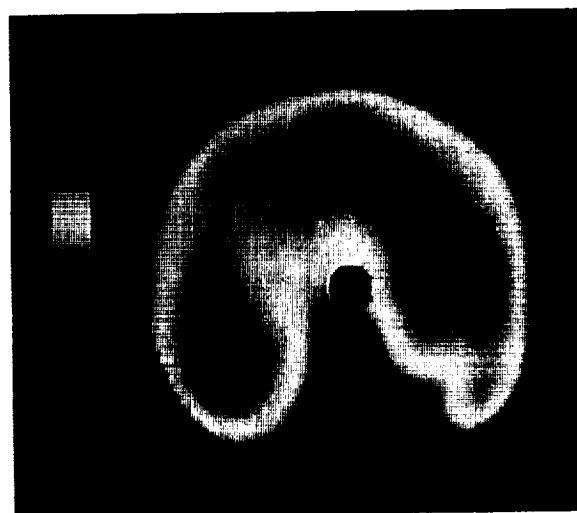


Figure 45. Compressor inlet total pressure distributions for screen No. 5 along the min-op line. (a) 60% corrected speed; (b) 80% corrected speed; (c) 110% corrected speed.

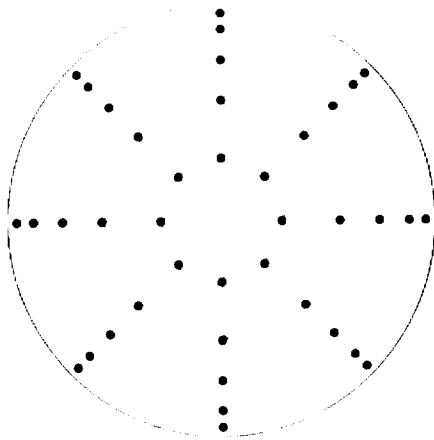
ORIGINAL PAGE IS
OF POOR QUALITY

$$\frac{P_{t2} - P_{t2}}{P_{t2}} \text{ Color range}$$

Red: 0.084

Blue: -0.111

Screen orientation



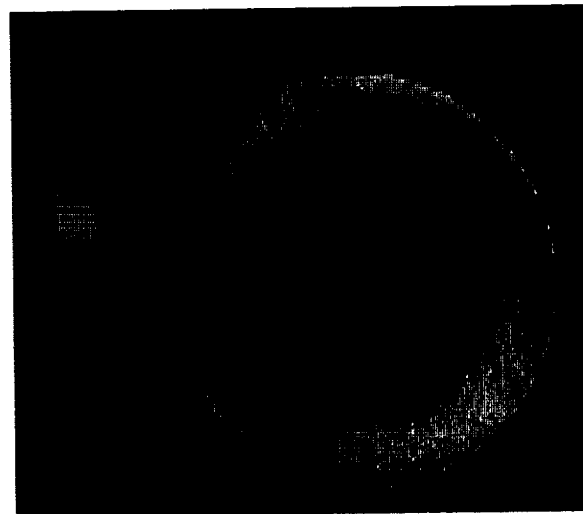
$$\text{Distortion, } \frac{P_{t2\max} - P_{t2\min}}{P_{t2}} (\%)$$

(a) 5.47

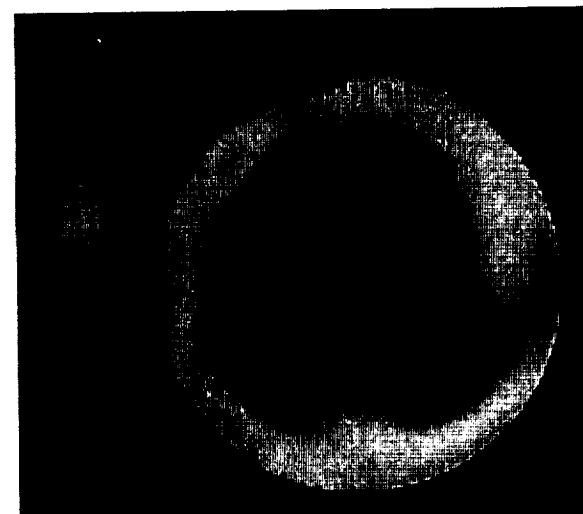
(b) 10.94

(c) 19.47

(a)



(b)



(c)

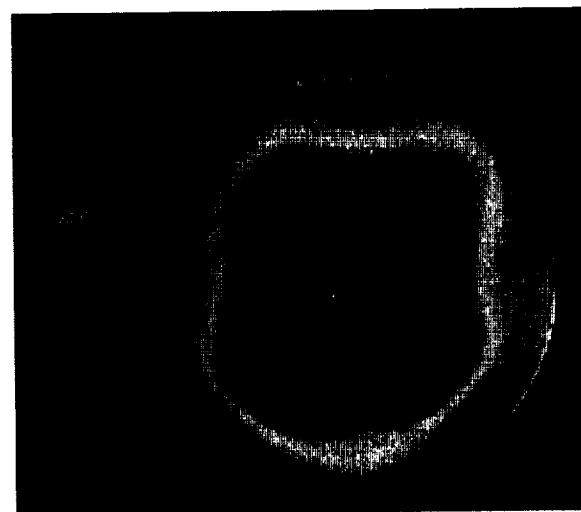


Figure 46. Compressor inlet total pressure distributions for screen No. 6 along the min-op line. (a) 60% corrected speed; (b) 80% corrected speed; (c) 110% corrected speed.

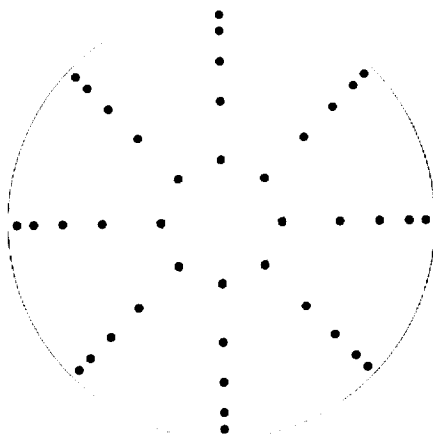
ORIGINAL PAGE IS
OF POOR QUALITY

$$\frac{P_{t2} - P_{t2}}{P_{t2}} \text{ Color range}$$

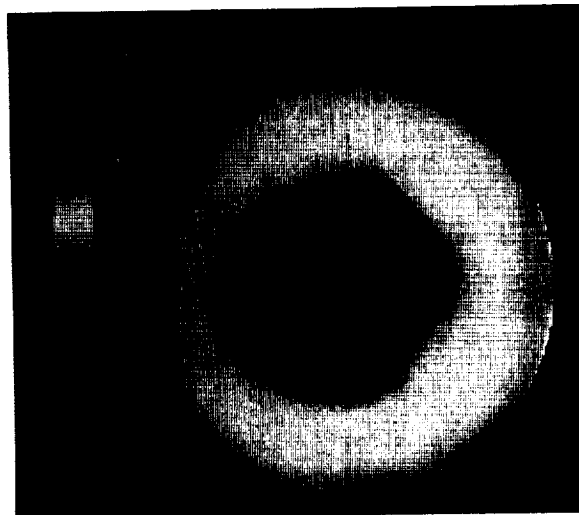
Red: 0.065

Blue: -0.116

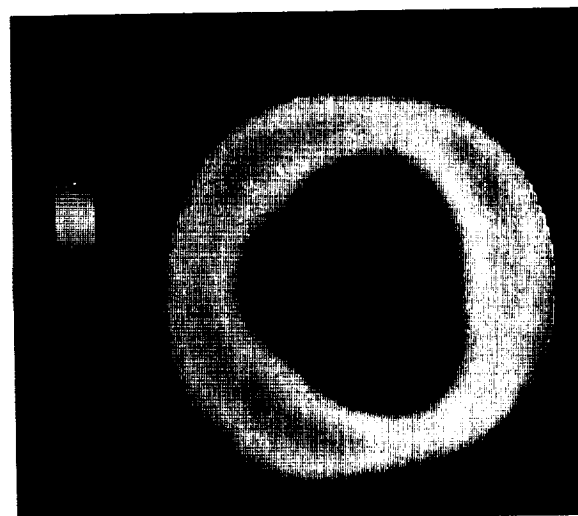
Screen orientation



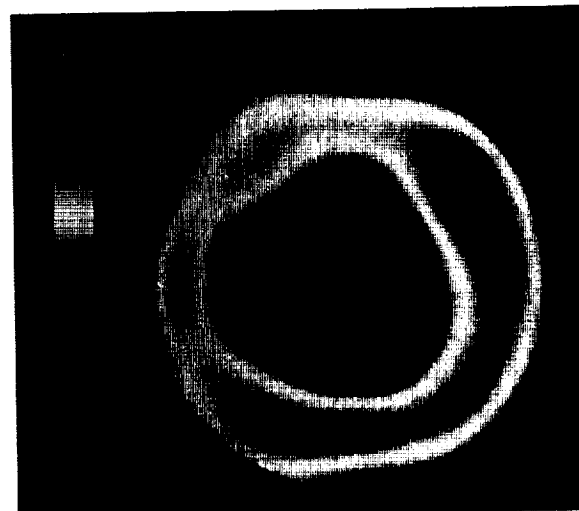
(a)



(b)



(c)



$$\text{Distortion, } \frac{P_{t2\max} - P_{t2\min}}{P_{t2}} (\%)$$

(a) 5.03

(b) 10.20

(c) 18.14

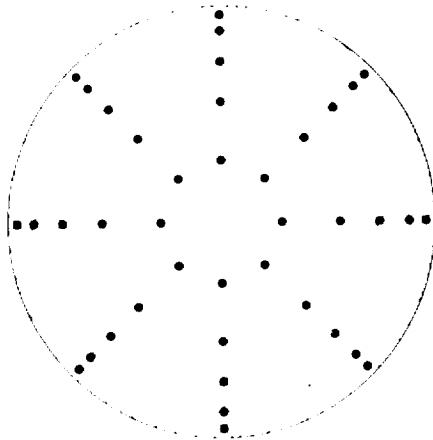
Figure 47. Compressor inlet total pressure distributions for screen No. 7 along the min-op line. (a) 60% corrected speed; (b) 80% corrected speed; (c) 110% corrected speed.

ORIGINAL PAGE IS
OF POOR QUALITY

$$\frac{P_{t2} - P_{t2}}{P_{t2}} \text{ Color range}$$

Red: 0.188
Blue: -0.133

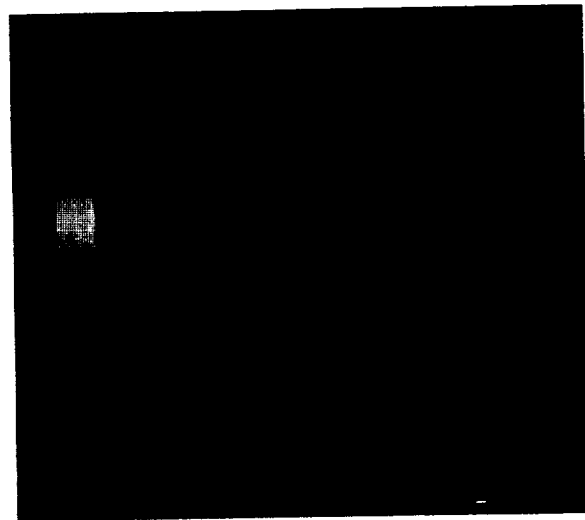
Screen orientation



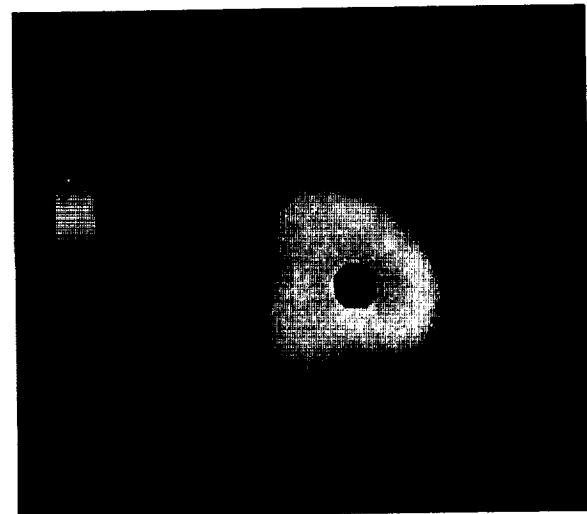
$$\text{Distortion, } \frac{P_{t2\max} - P_{t2\min}}{P_{t2}} (\%)$$

- (a) 8.55
- (b) 17.63
- (c) 32.22

(a)



(b)



(c)

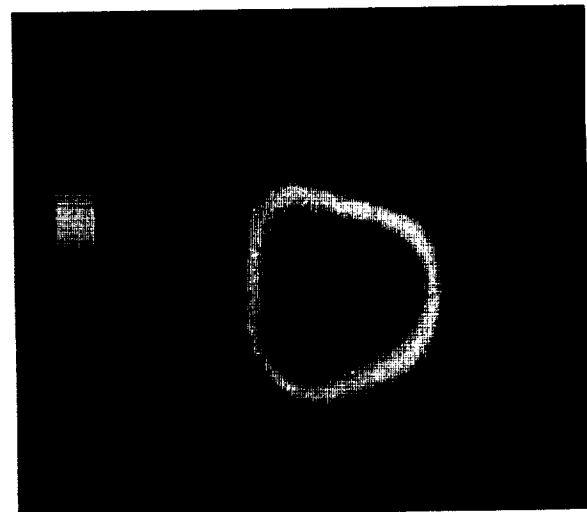


Figure 48. Compressor inlet total pressure distributions for screen No. 8 along the min-op line. (a) 60% corrected speed; (b) 80% corrected speed; (c) 105% corrected speed.

ORIGINAL PAGE IS
OF POOR QUALITY

99

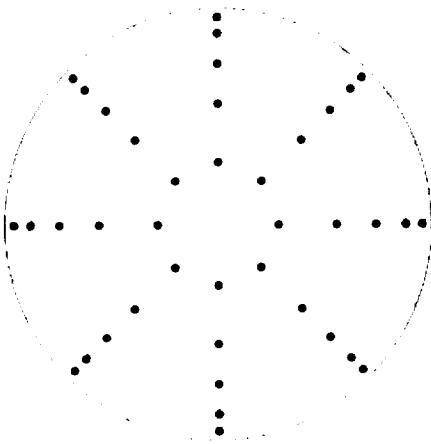
PRECEDING PAGE BLANK NOT FILMED

$$\frac{P_{t2} - P_{t2}}{P_{t2}} \text{ Color range}$$

Red: 0.083

Blue: -0.111

Screen orientation



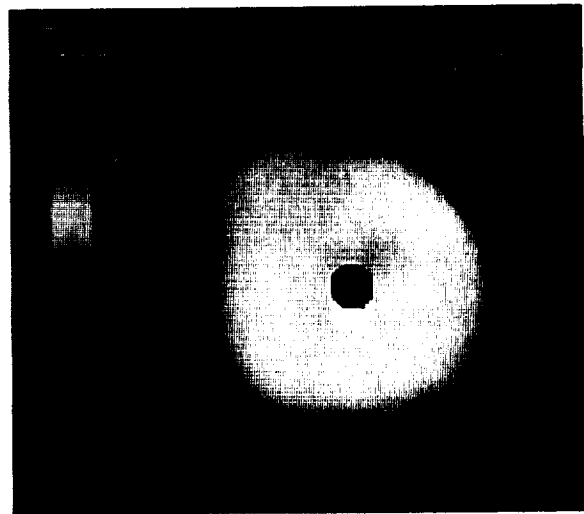
$$\text{Distortion, } \frac{P_{t2\max} - P_{t2\min}}{P_{t2}} (\%)$$

(a) 6.05

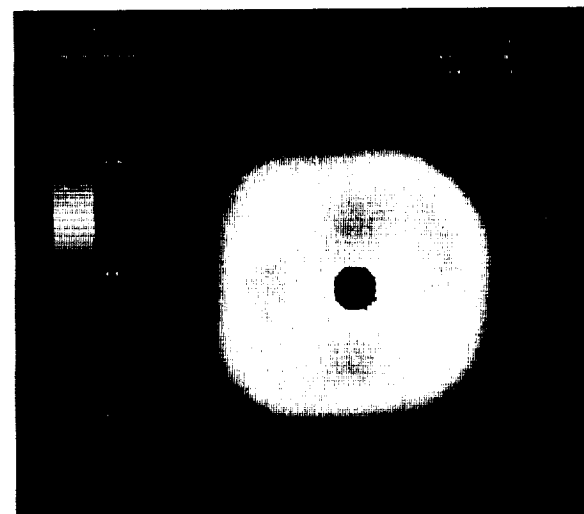
(b) 12.43

(c) 19.38

(a)



(b)



(c)

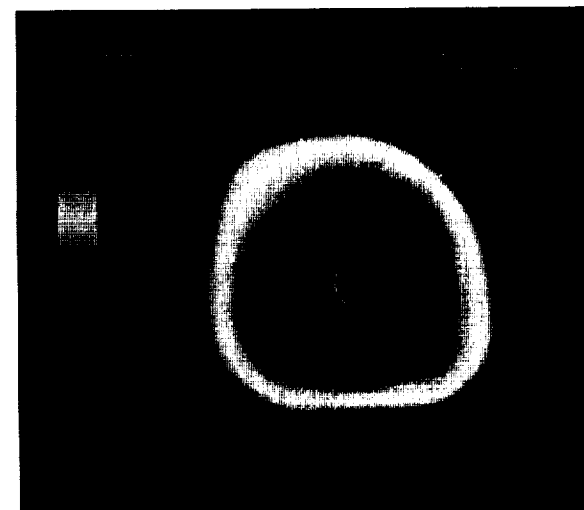


Figure 49. Compressor inlet total pressure distributions for screen No. 9 along the min-op line. (a) 60% corrected speed; (b) 80% corrected speed; (c) 110% corrected speed.

ORIGINAL PAGE IS
OF POOR QUALITY 101

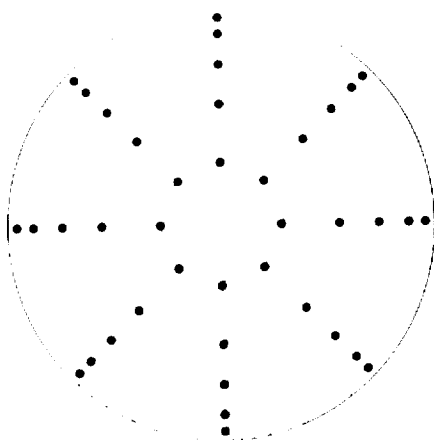
PRECEDING PAGE BLANK NOT FILMED

$$\frac{P_{12} - P_{12}}{P_{12}} \text{ Color range}$$

Red: 0.138

Blue: -0.123

Screen orientation



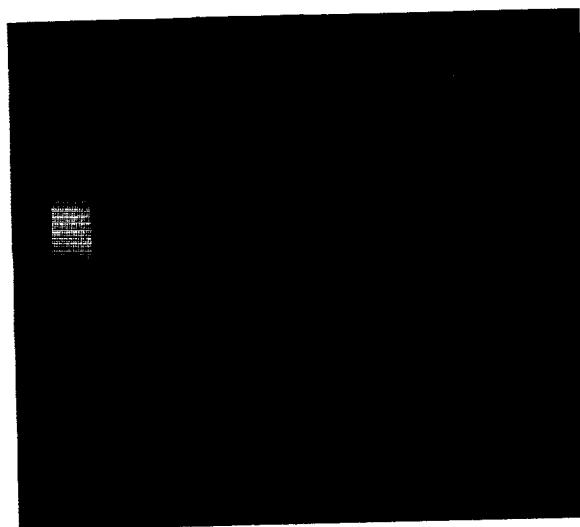
$$\text{Distortion, } \frac{P_{12\max} - P_{12\min}}{P_{12}} (\%)$$

(a) 6.34

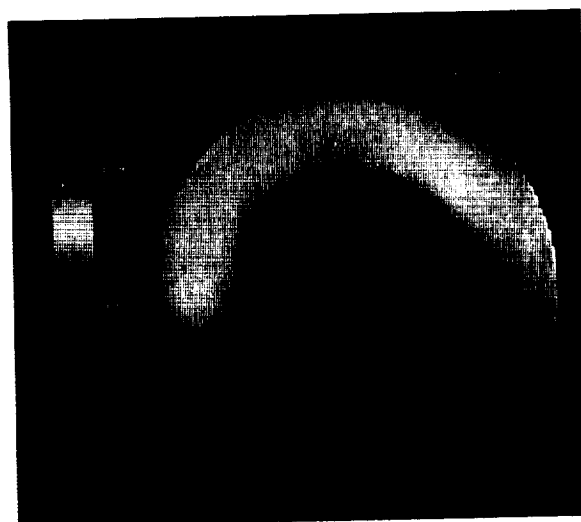
(b) 13.20

(c) 26.15

(a)



(b)



(c)

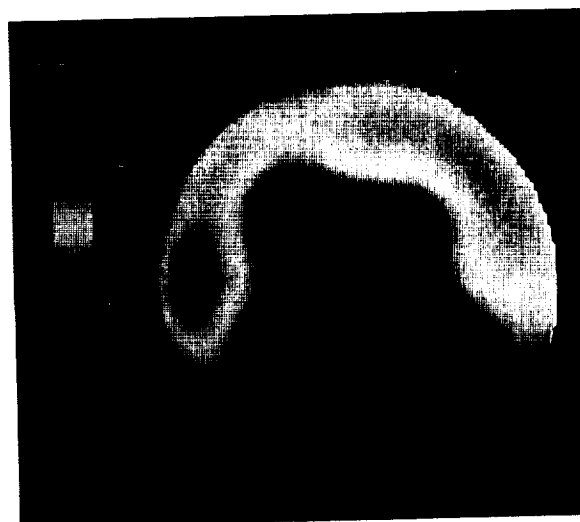


Figure 50. Compressor inlet total pressure distributions for screen No. 10 along the min-op line. (a) 60% corrected speed; (b) 80% corrected speed; (c) 110% corrected speed.

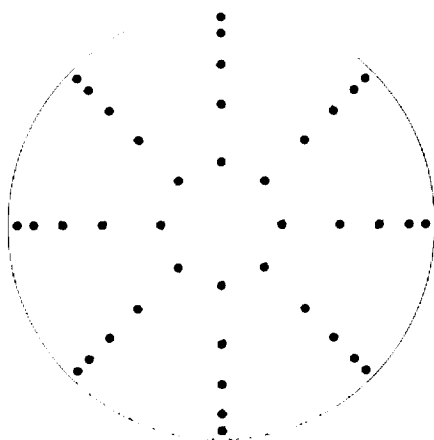
ORIGINAL PAGE IS
OF POOR QUALITY

$$\frac{P_{t2} - P_{t2}}{P_{t2}} \text{ Color range}$$

Red: 0.156

Blue: -0.096

Screen orientation



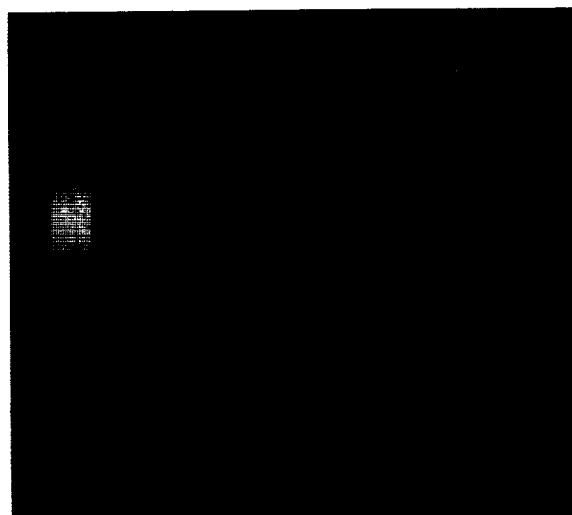
$$\text{Distortion, } \frac{P_{t2\max} - P_{t2\min}}{P_{t2}} (\%)$$

(a) 6.56

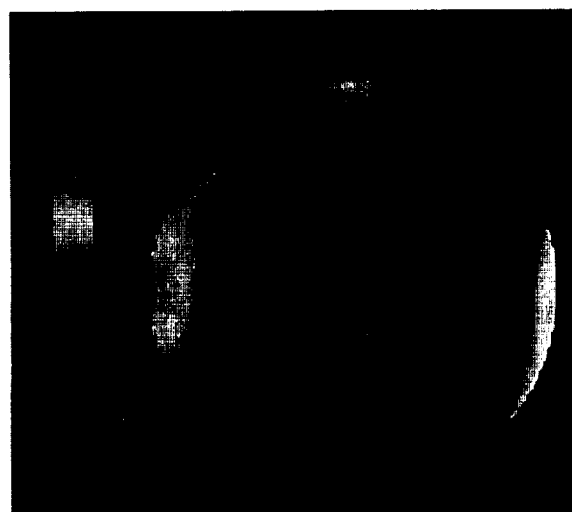
(b) 16.21

(c) 25.16

(a)



(b)



(c)

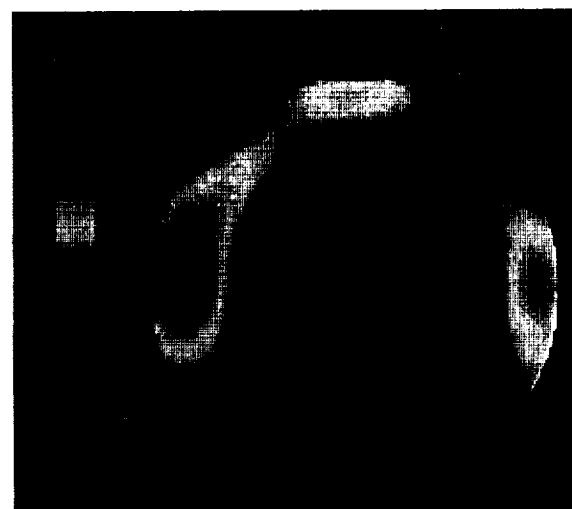


Figure 51. Compressor inlet total pressure distributions for screen No. 11 along the min-op line. (a) 60% corrected speed; (b) 80% corrected speed; (c) 110% corrected speed.

ORIGINAL PAGE IS
OF POOR QUALITY

C2

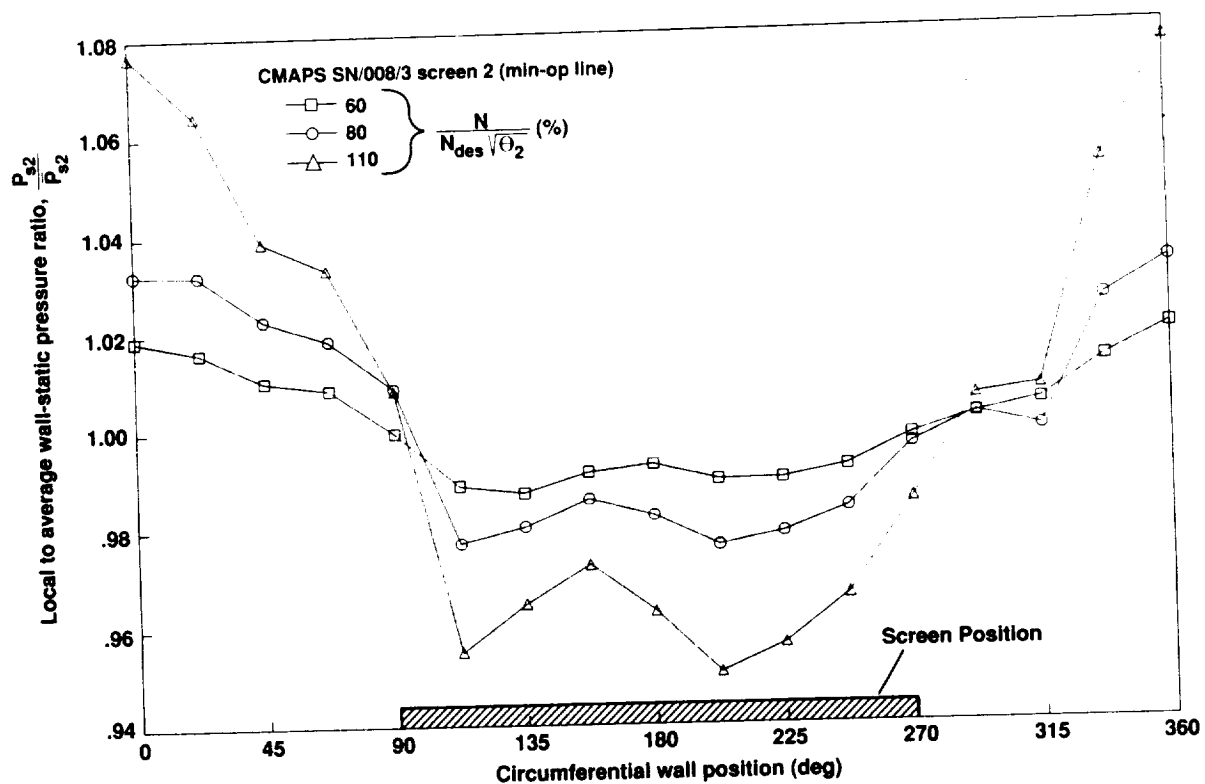


Figure 52. Compressor inlet wall static pressure profiles for screen No. 2 along the min-op line.

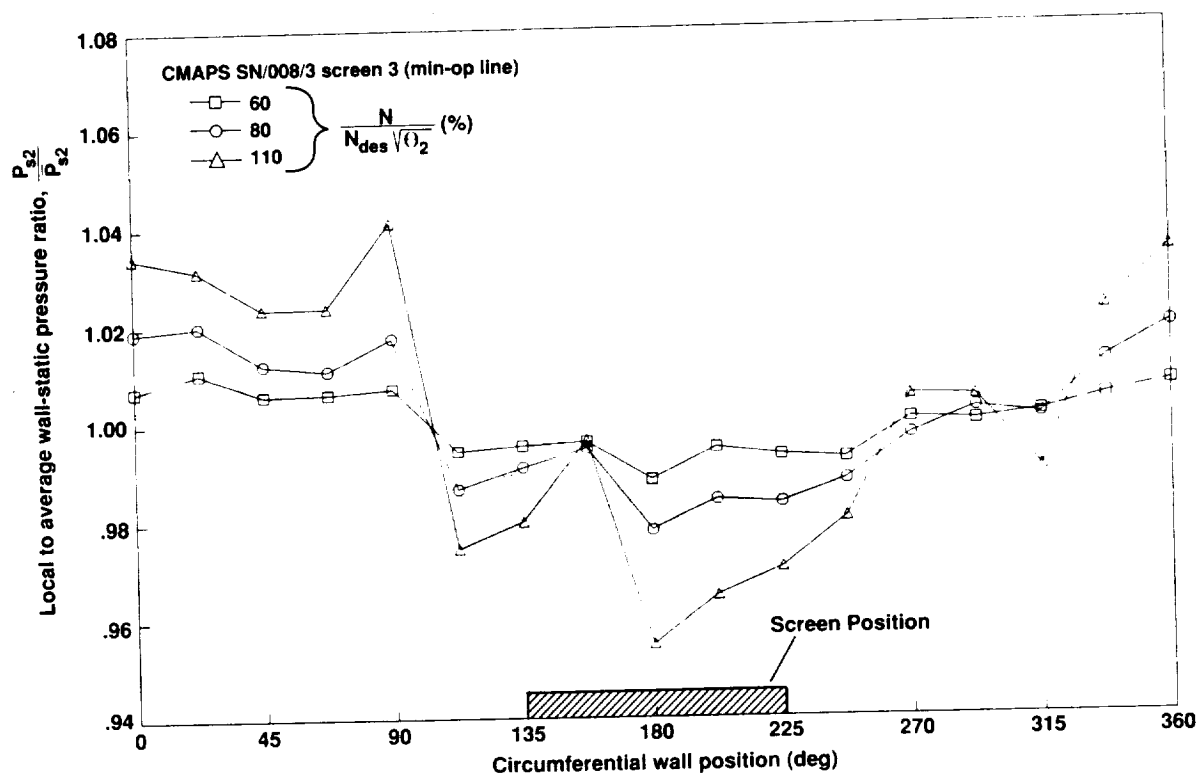


Figure 53. Compressor inlet wall static pressure profiles for screen No. 3 along the min-op line.

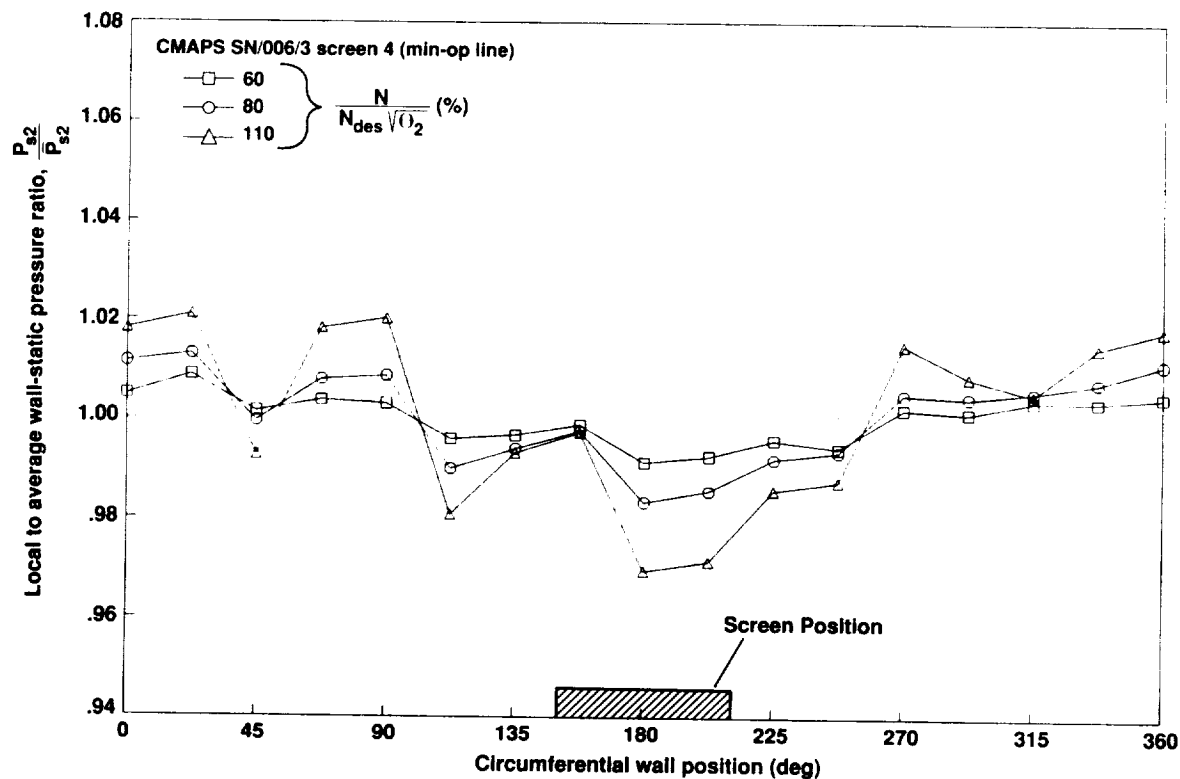


Figure 54. CMAPS SN/006/3 compressor inlet wall static pressure profiles for screen No. 4 along the min-op line.

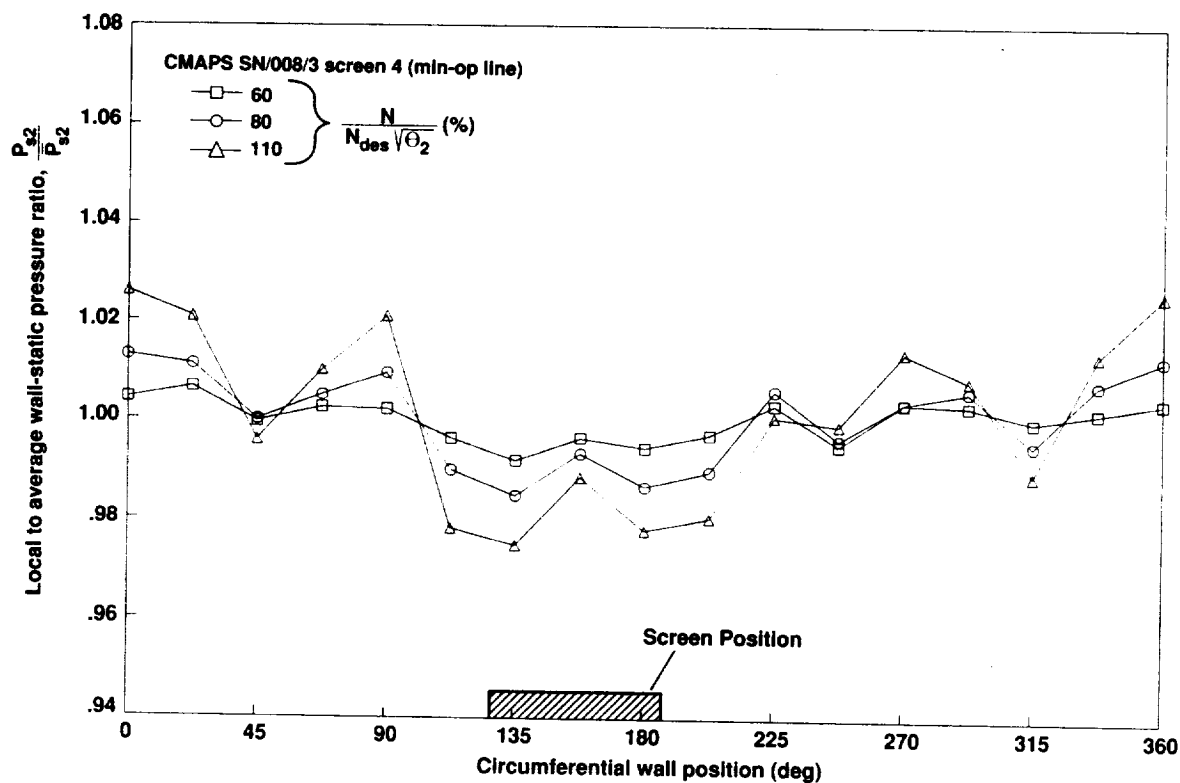


Figure 55. CMAPS SN/008/3 compressor inlet wall static pressure profiles for screen No. 4 along the min-op line.

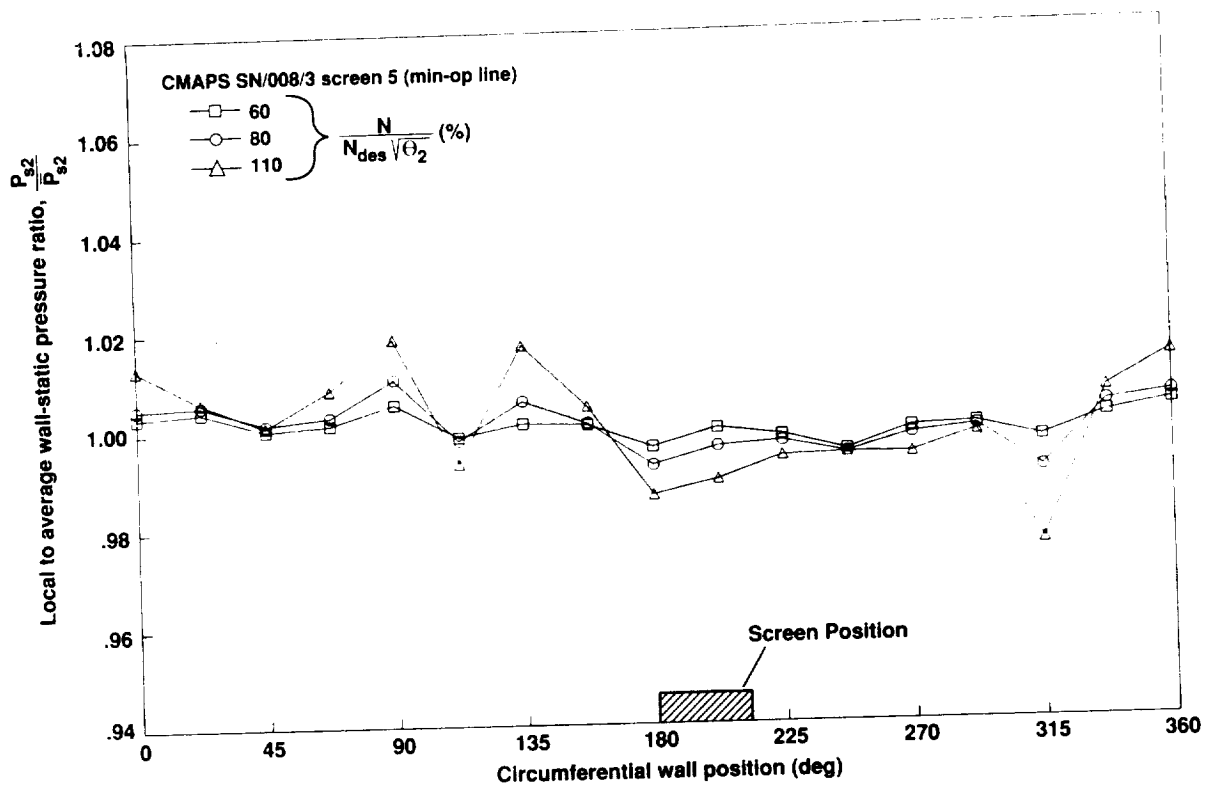


Figure 56. Compressor inlet wall static pressure profiles for screen No. 5 along the min-op line.

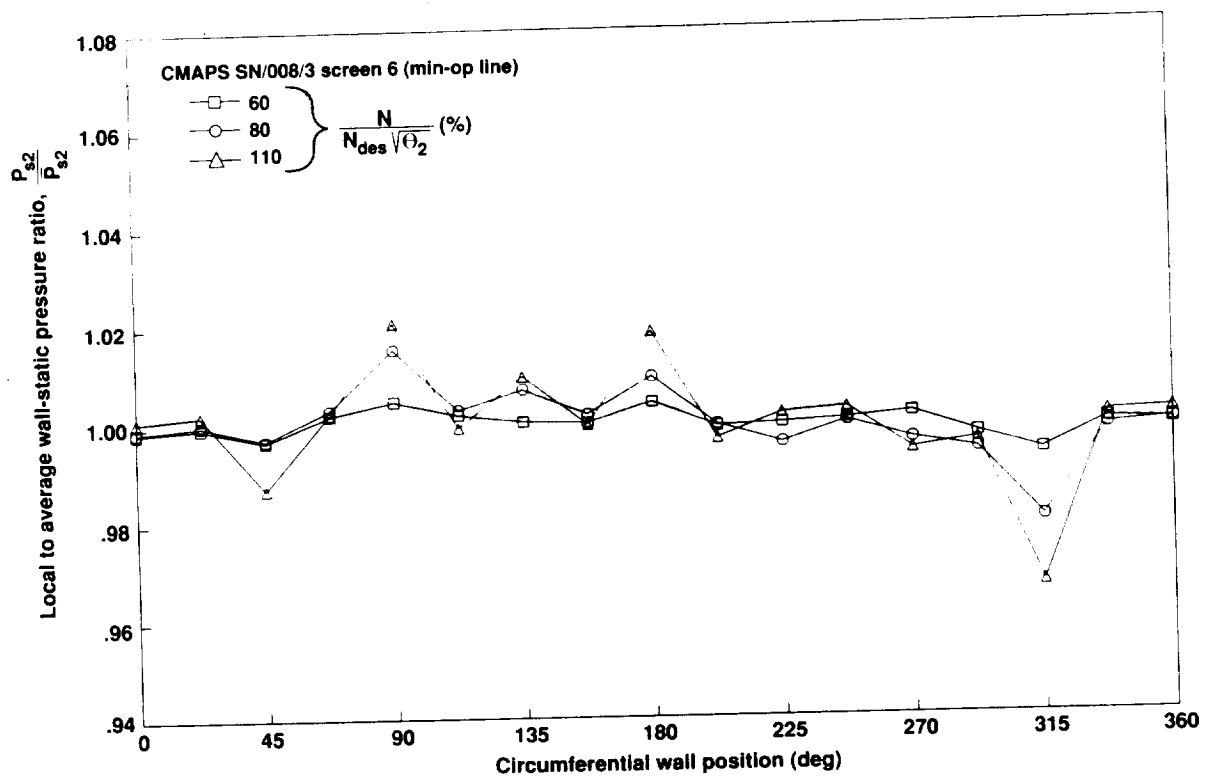


Figure 57. Compressor inlet wall static pressure profiles for screen No. 6 along the min-op line.

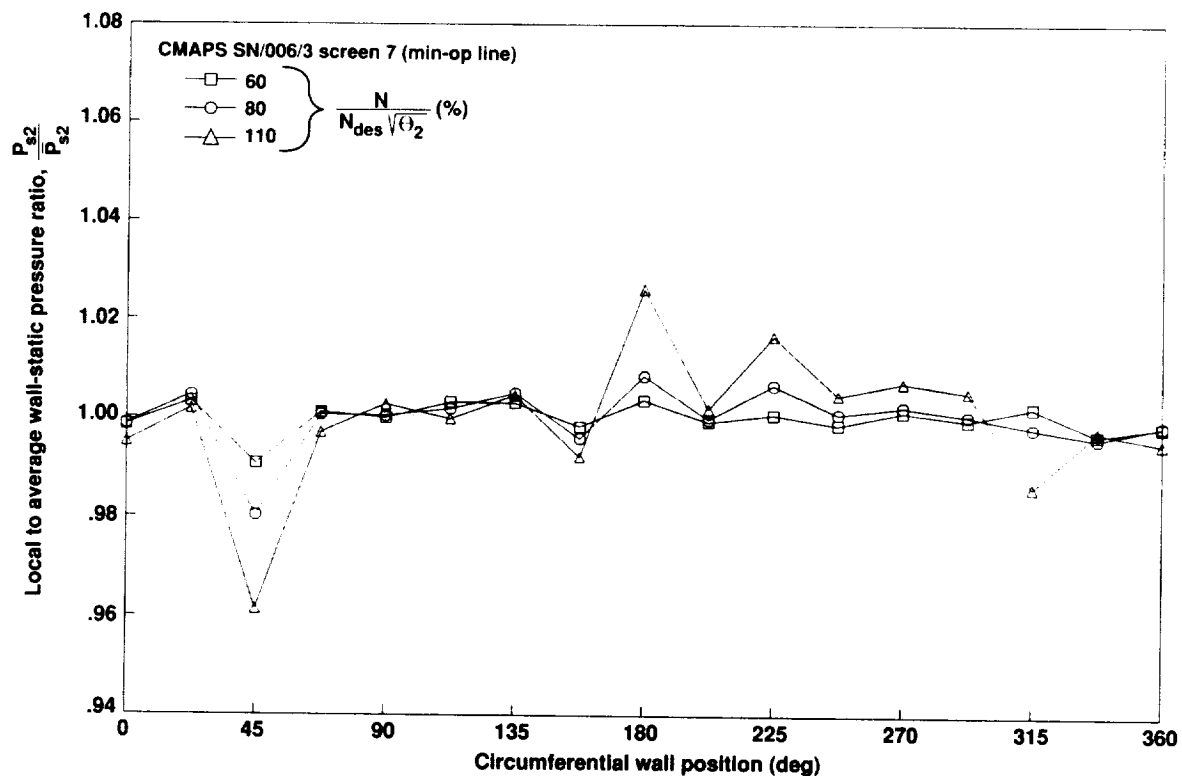


Figure 58. Compressor inlet wall static pressure profiles for screen No. 7 along the min-op line.

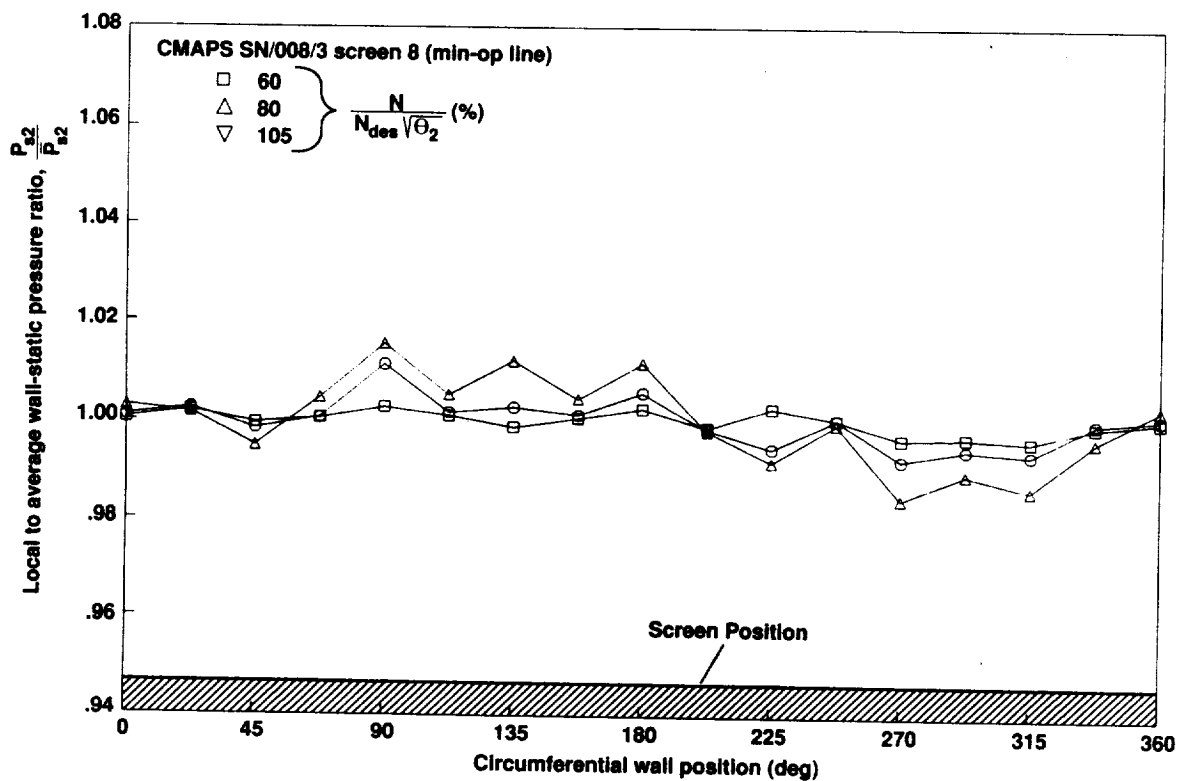


Figure 59. Compressor inlet wall static pressure profiles for screen No. 8 along the min-op line.

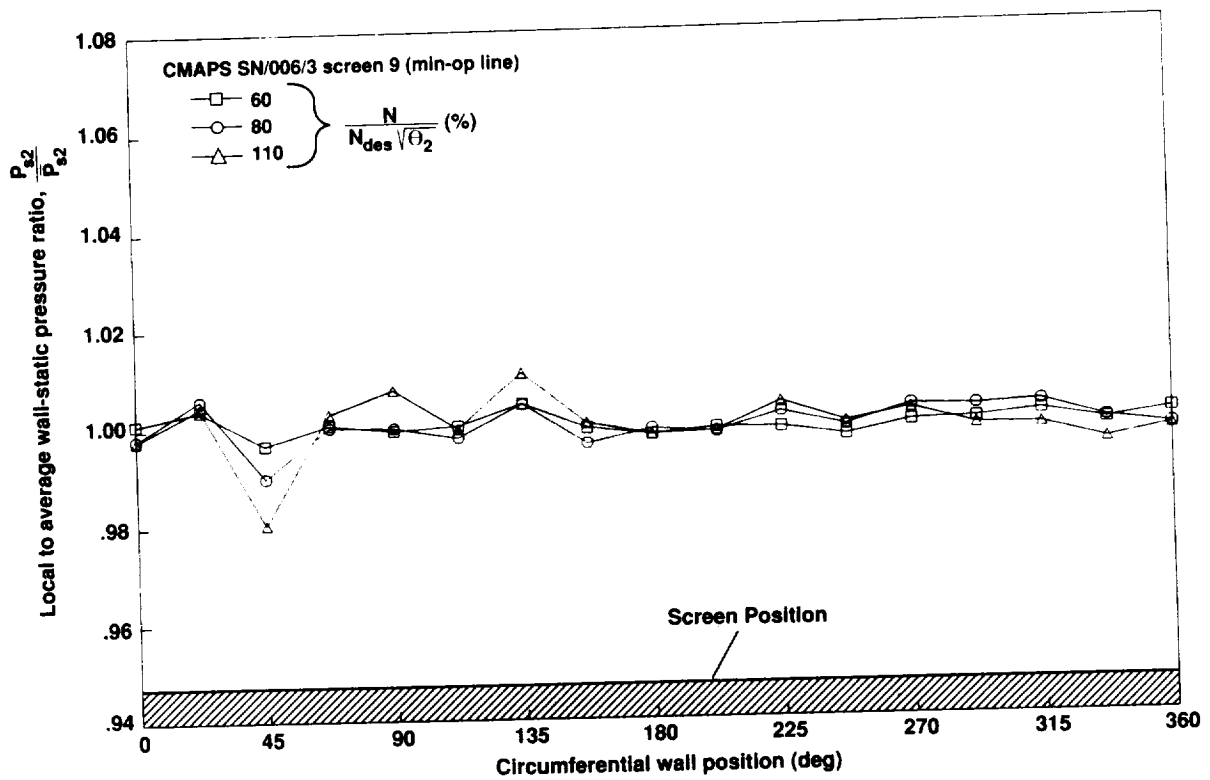


Figure 60. Compressor inlet wall static pressure profiles for screen No. 9 along the min-op line.

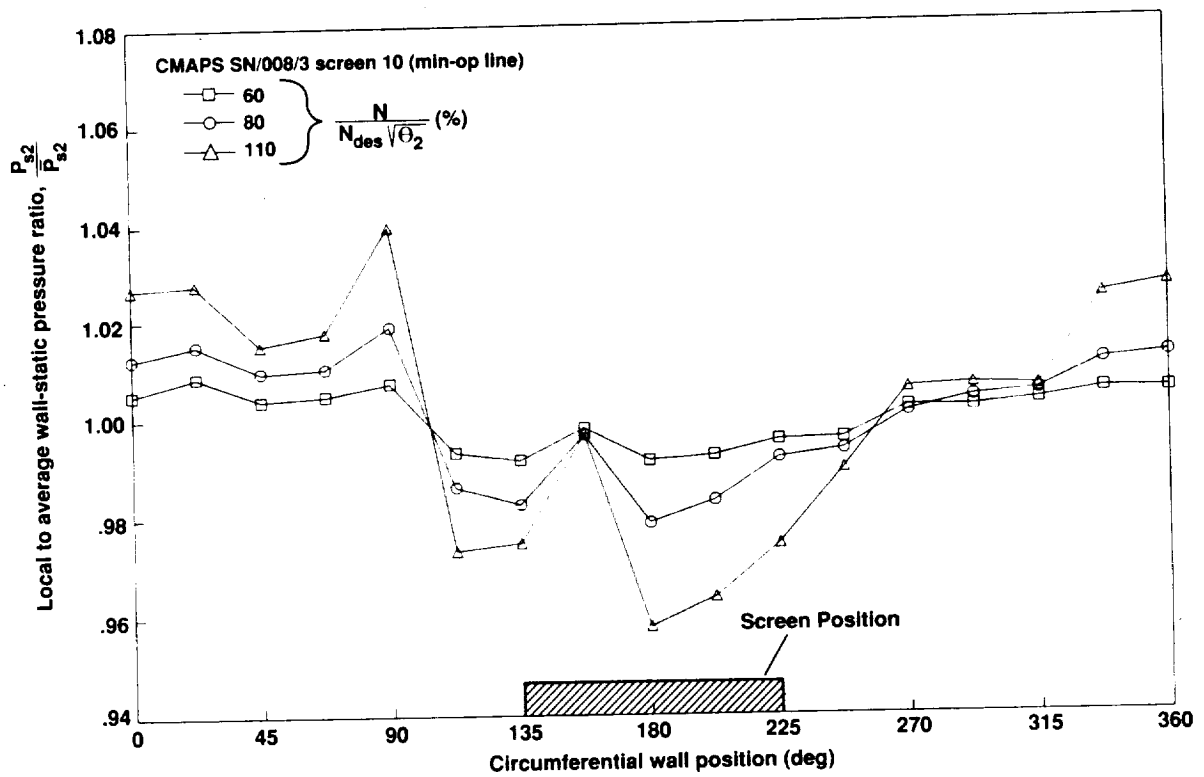


Figure 61. Compressor inlet wall static pressure profiles for screen No. 10 along the min-op line.

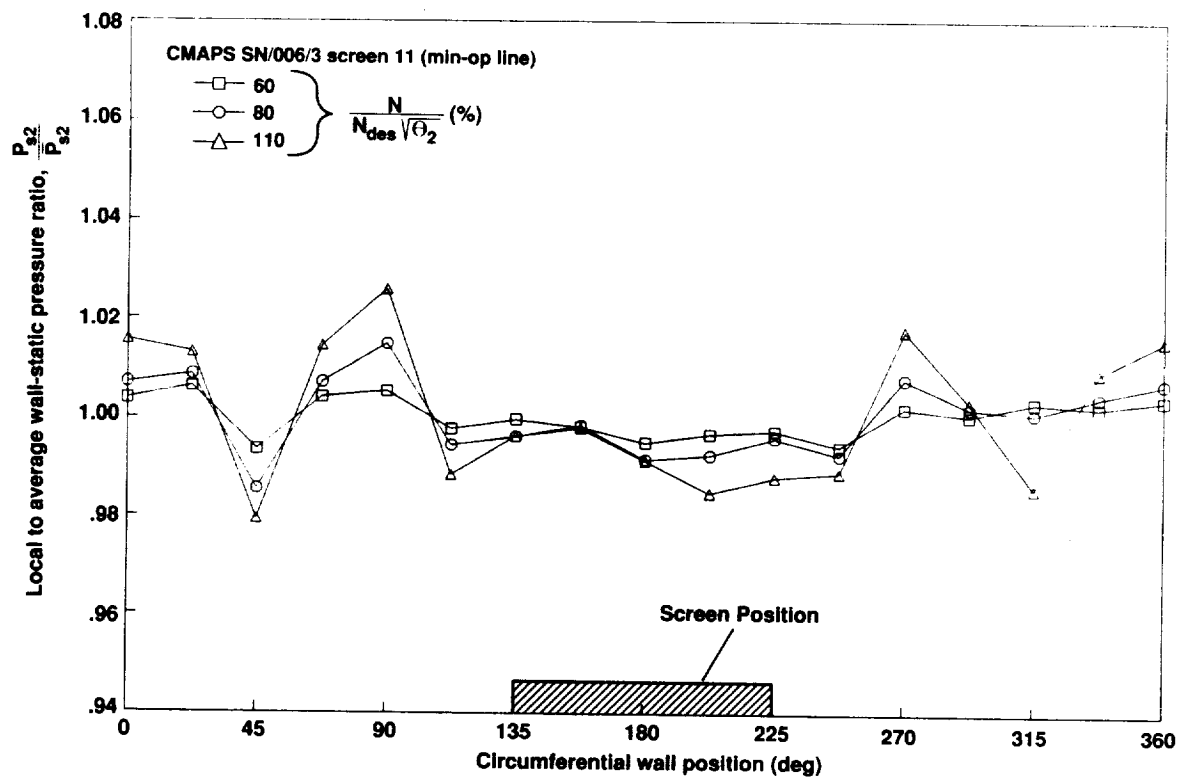


Figure 62. Compressor inlet wall static pressure profiles for screen No. 11 along the min-op line.

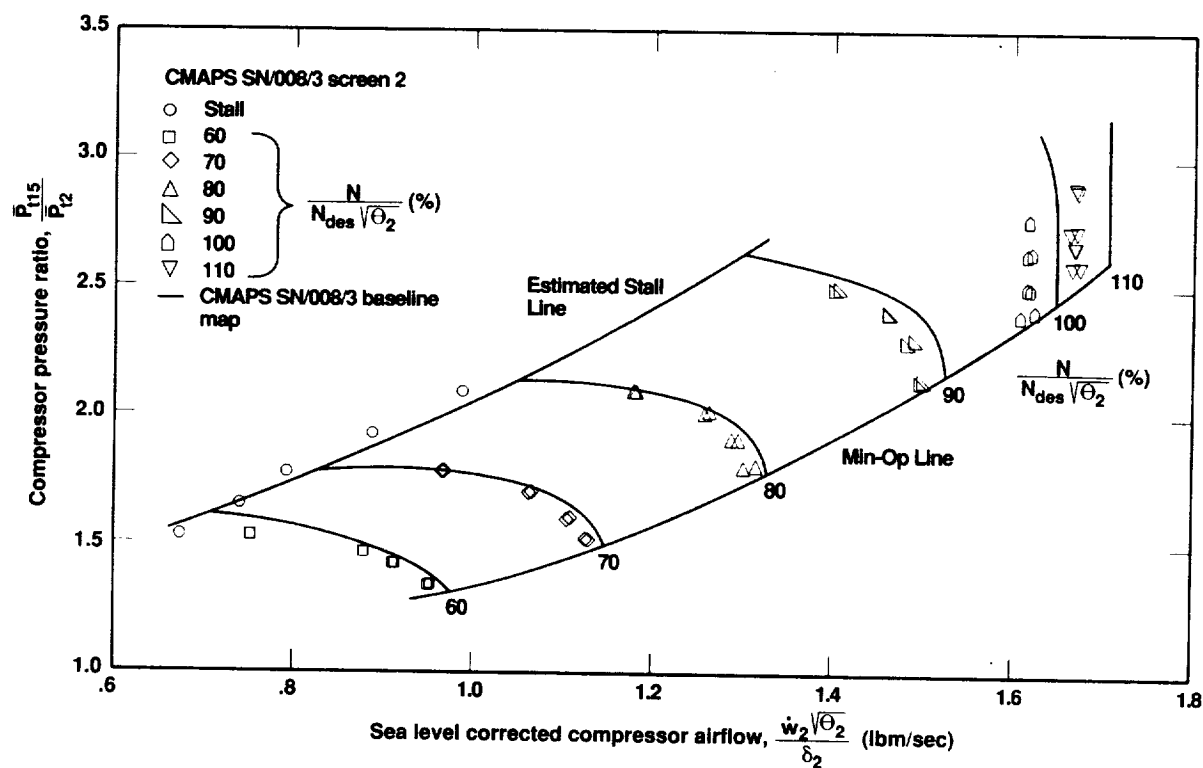


Figure 63. CMAPS SN/008/3 compressor operating map for screen No. 2.

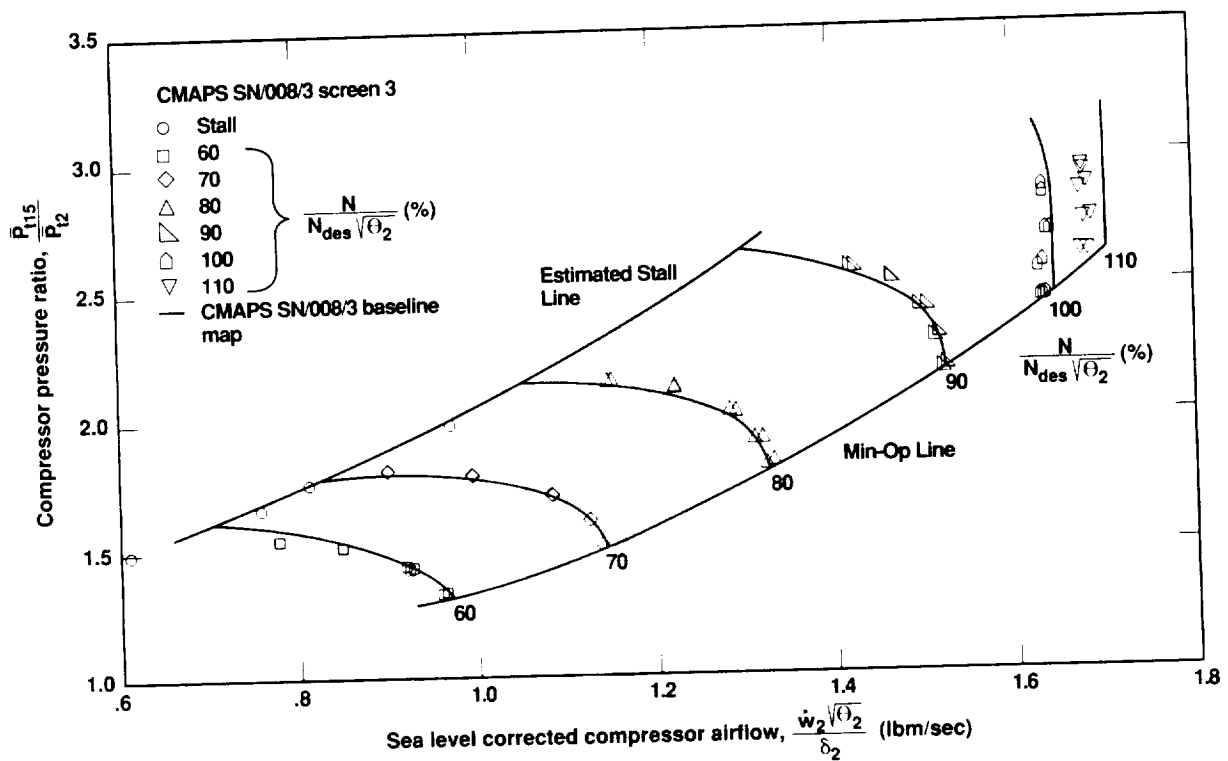


Figure 64. CMAPS SN/008/3 compressor operating map for screen No. 3.

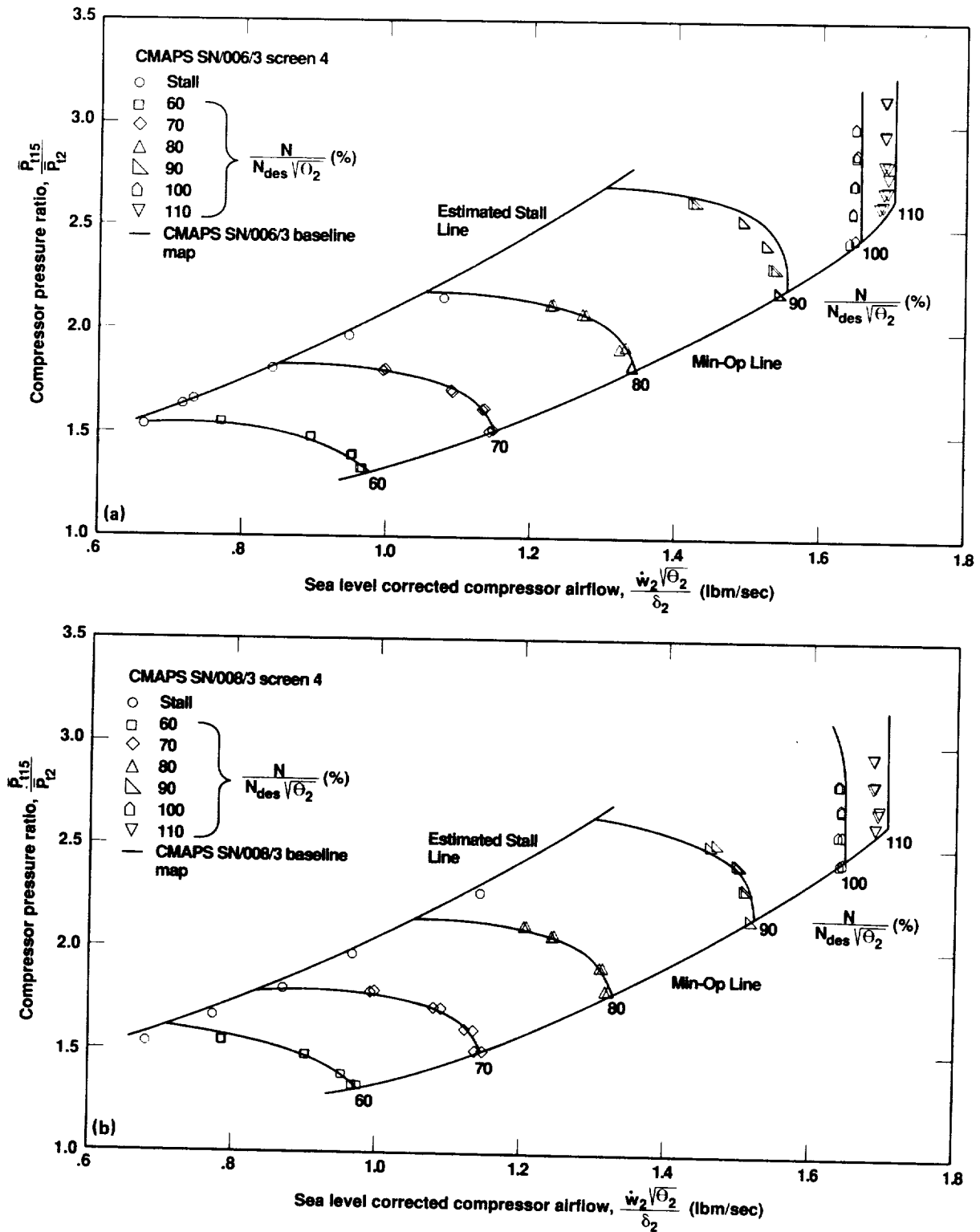


Figure 65. Compressor operating maps for screen No. 4. (a) CMAPS SN/006/3; (b) CMAPS SN/008/3.

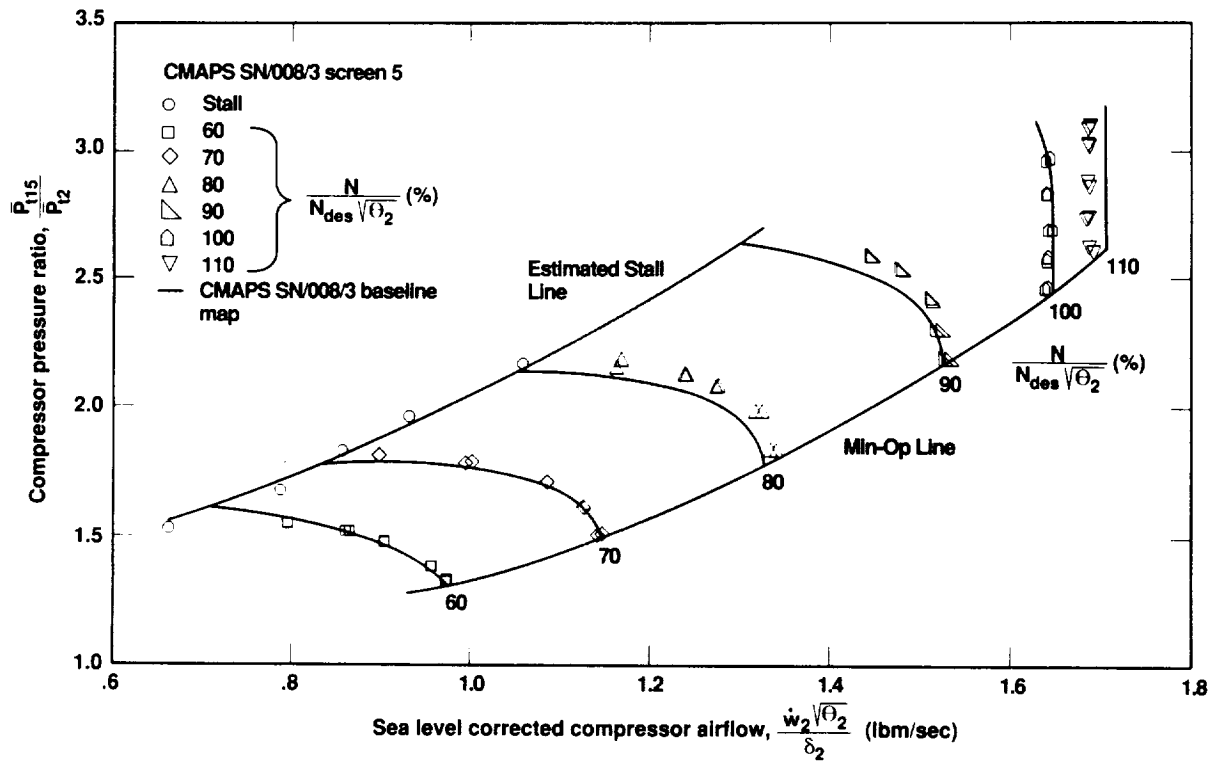


Figure 66. CMAPS SN/008/3 compressor operating map for screen No. 5.

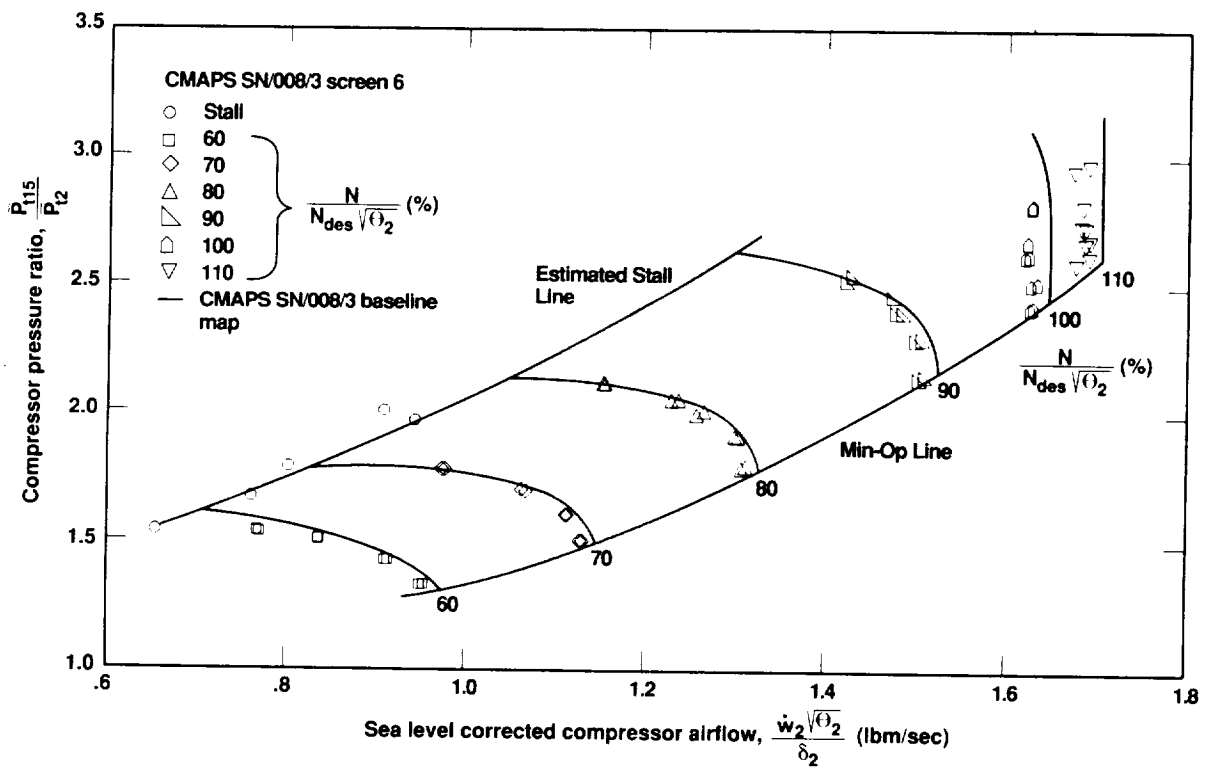


Figure 67. CMAPS SN/008/3 compressor operating map for screen No. 6.

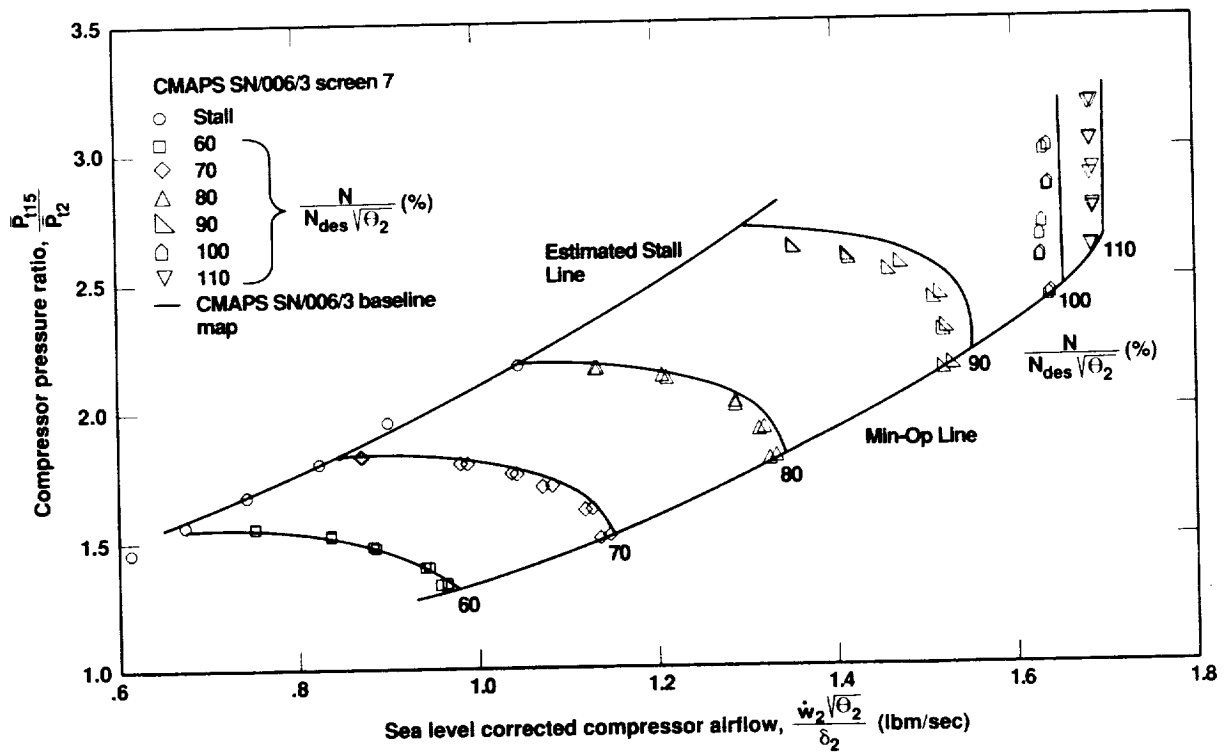


Figure 68. CMAPS SN/006/3 compressor operating map for screen No. 7.

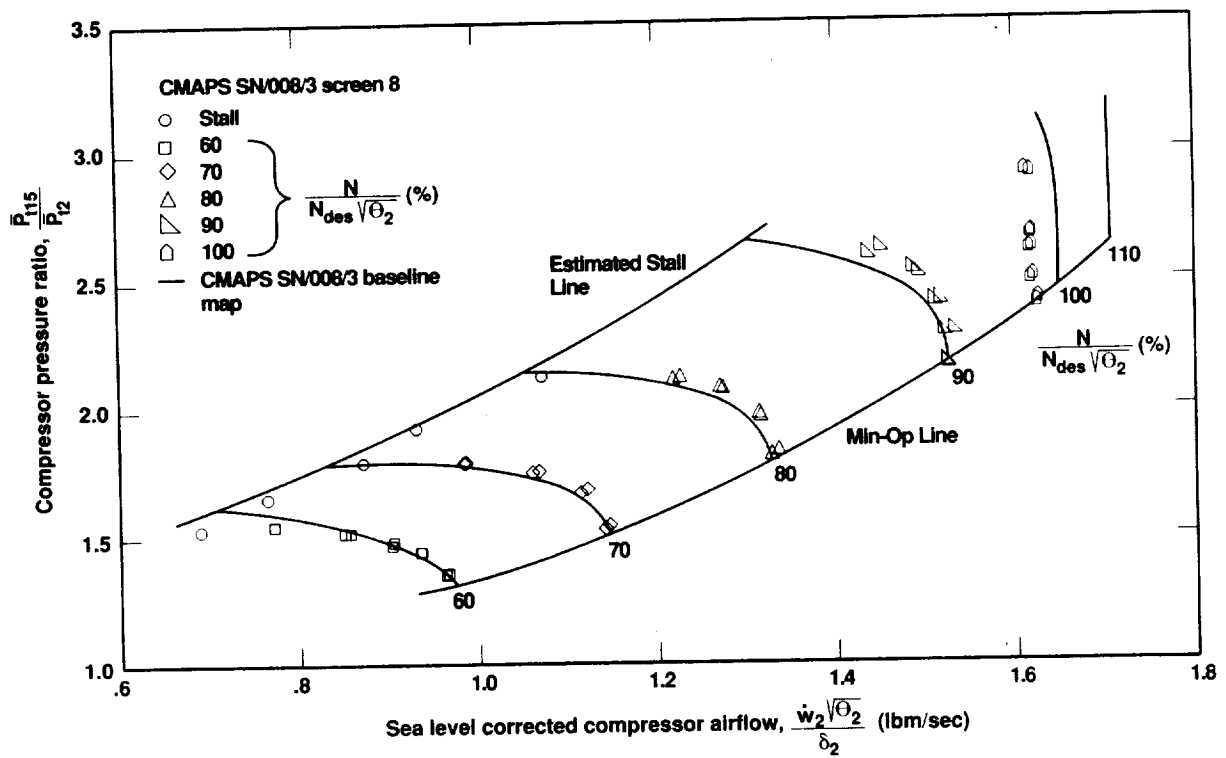


Figure 69. CMAPS SN/008/3 compressor operating map for screen No. 8.

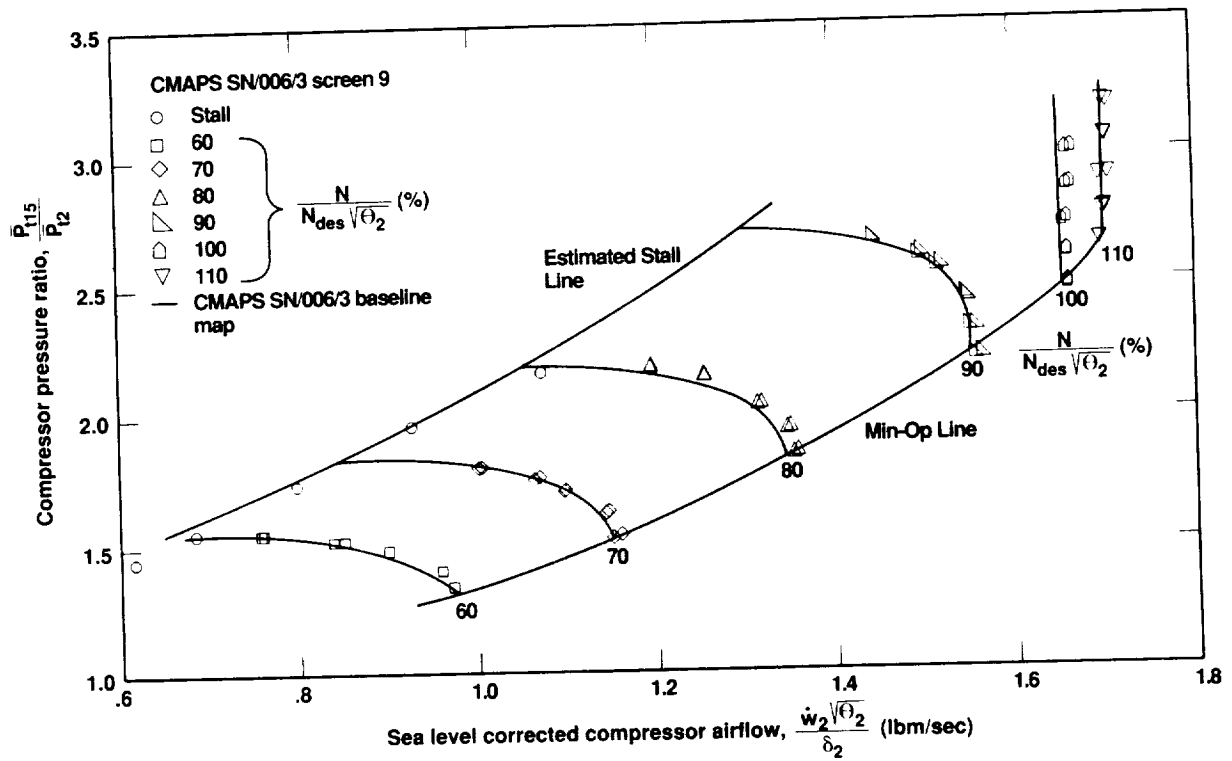


Figure 70. CMAPS SN/006/3 compressor operating map for screen No. 9.

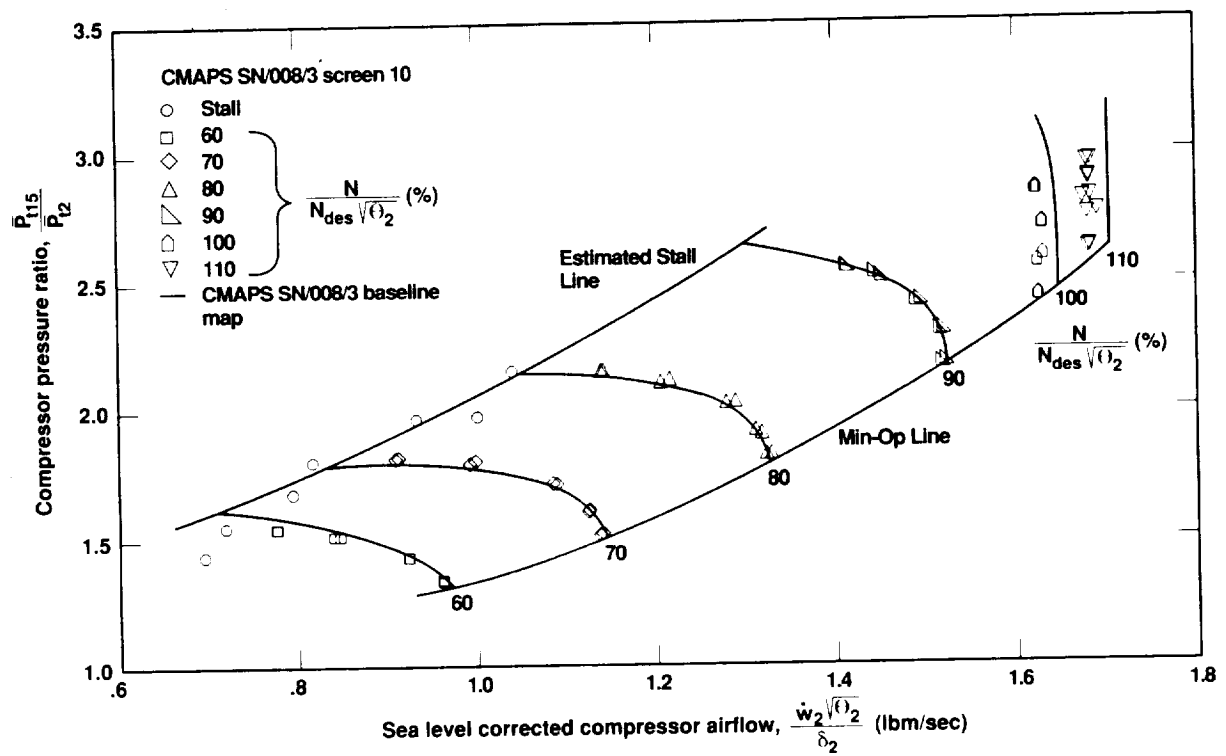


Figure 71. CMAPS SN/008/3 compressor operating map for screen No. 10.

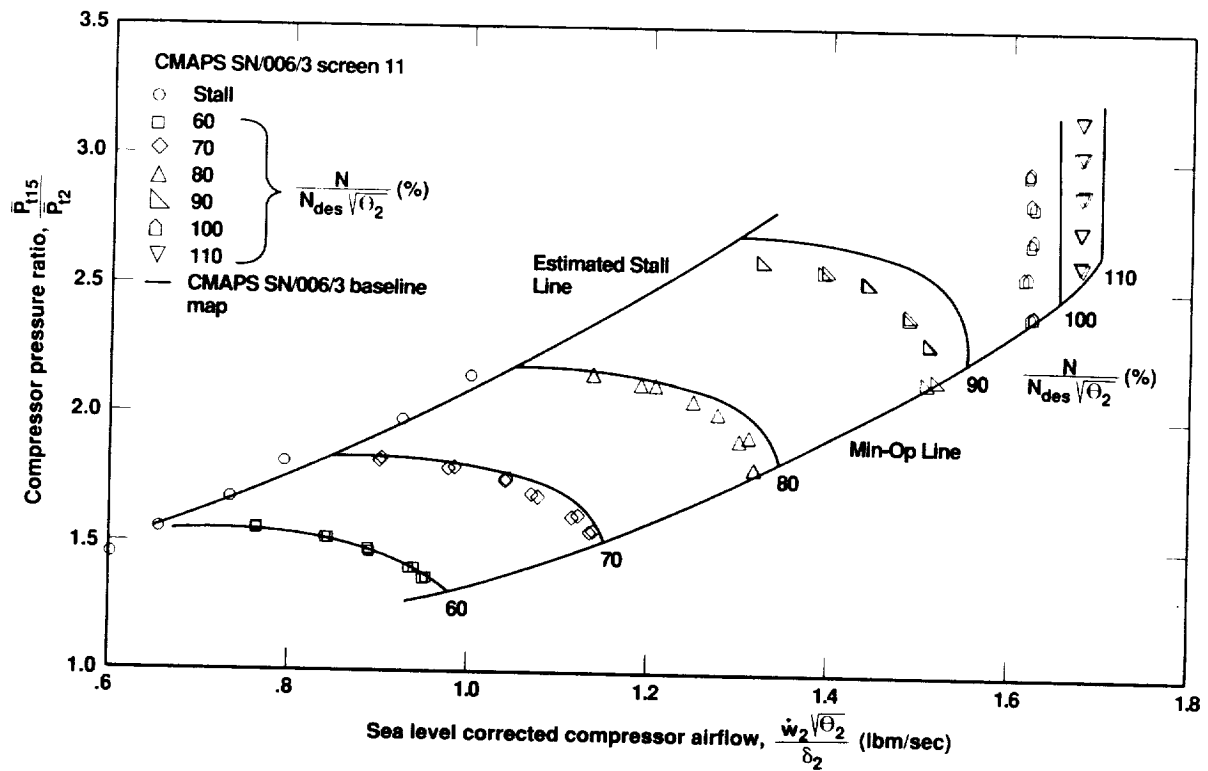


Figure 72. CMAPS SN/006/3 compressor operating map for screen No. 11.

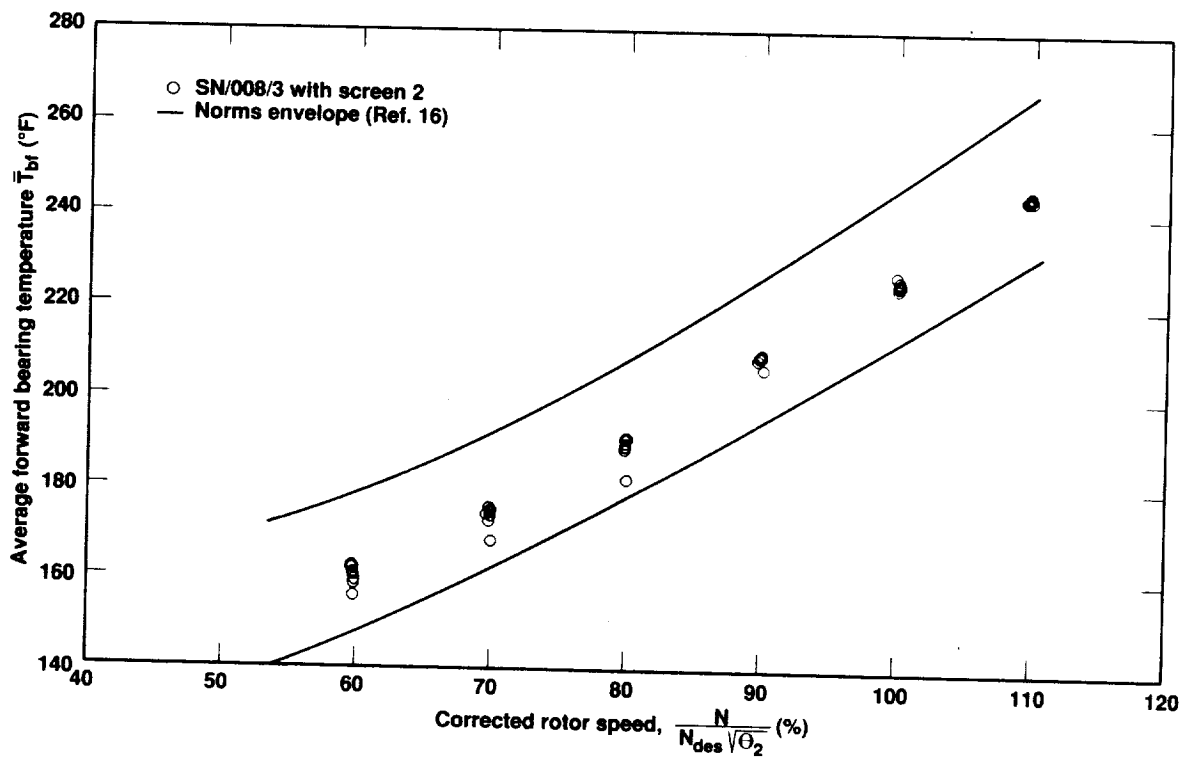


Figure 73. CMAPS SN/008/3 forward bearing temperature for screen No. 2.

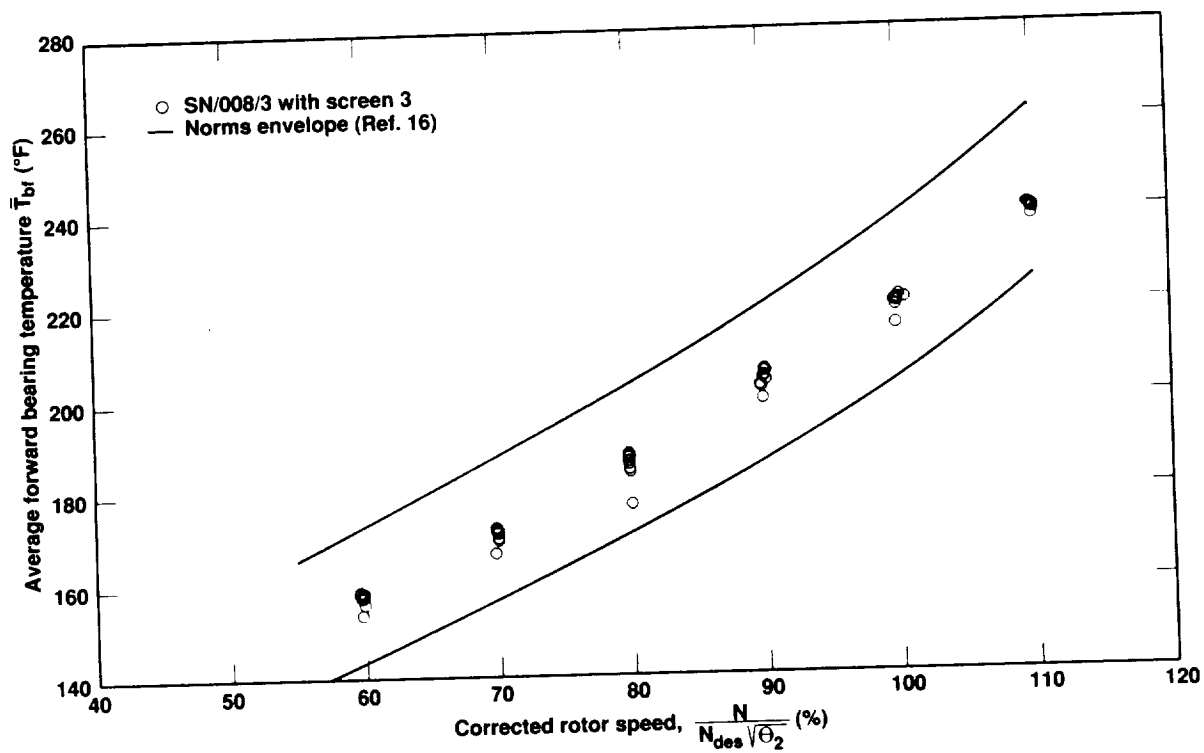


Figure 74. CMAPS SN/008/3 forward bearing temperature for screen No. 3.

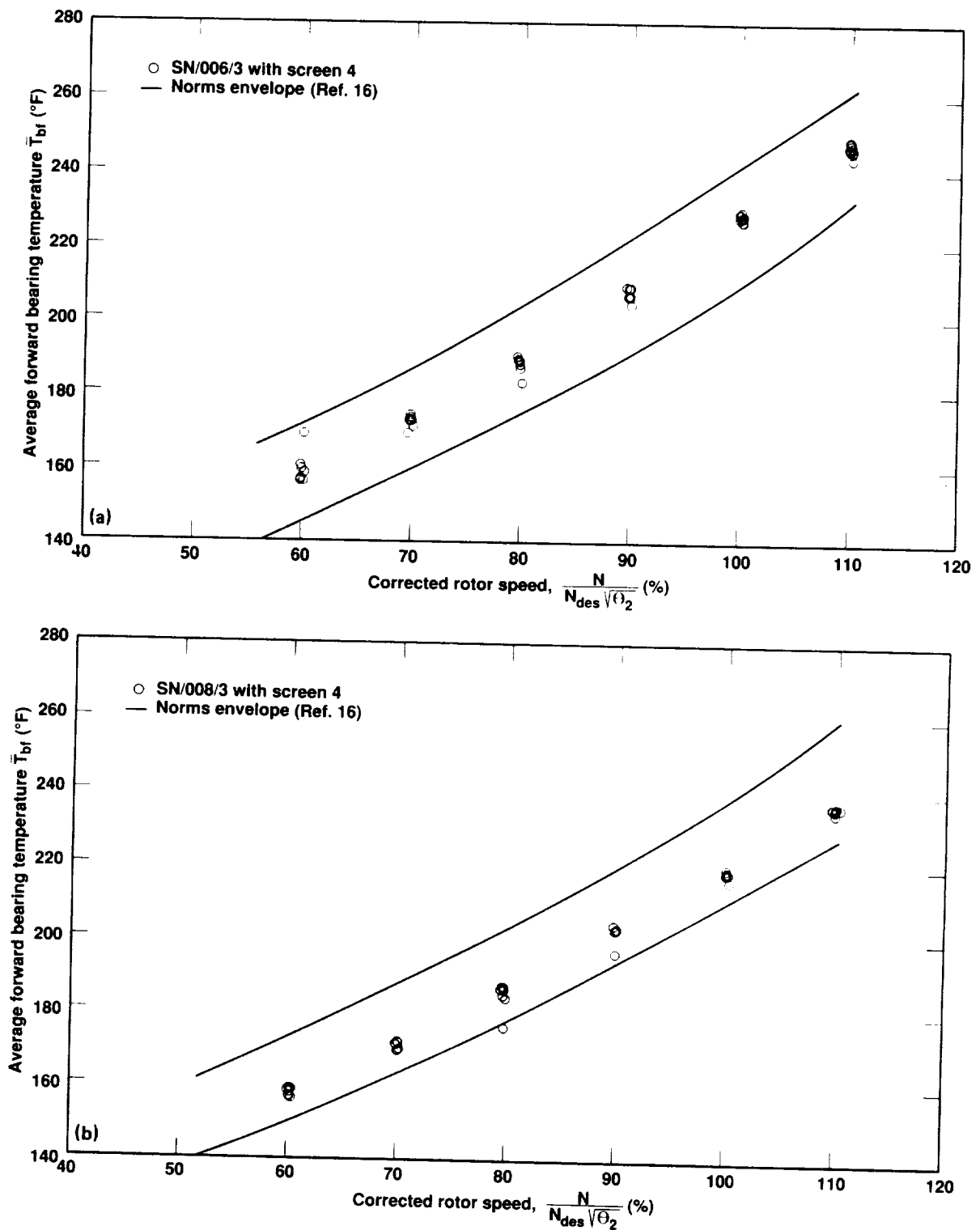


Figure 75. Forward bearing temperatures for screen No. 4. (a) CMAPS SN/006/3; (b) CMAPS SN/008/3.

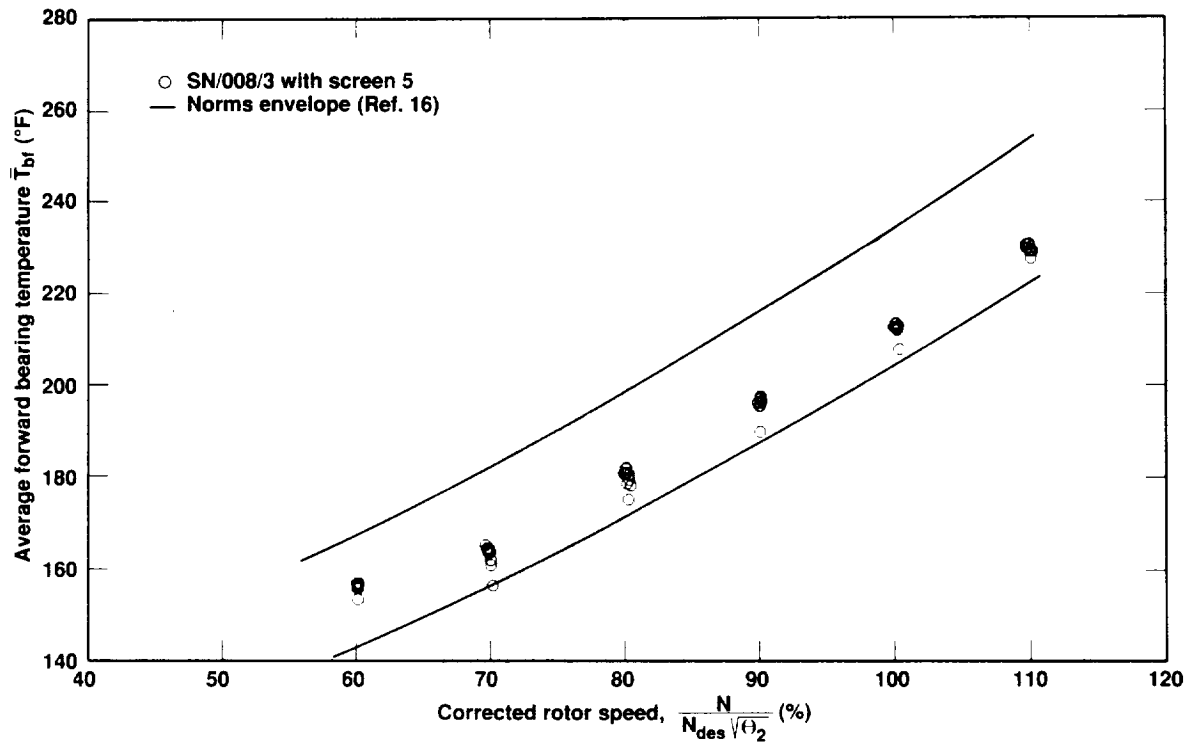


Figure 76. CMAPS SN/008/3 forward bearing temperature for screen No. 5.

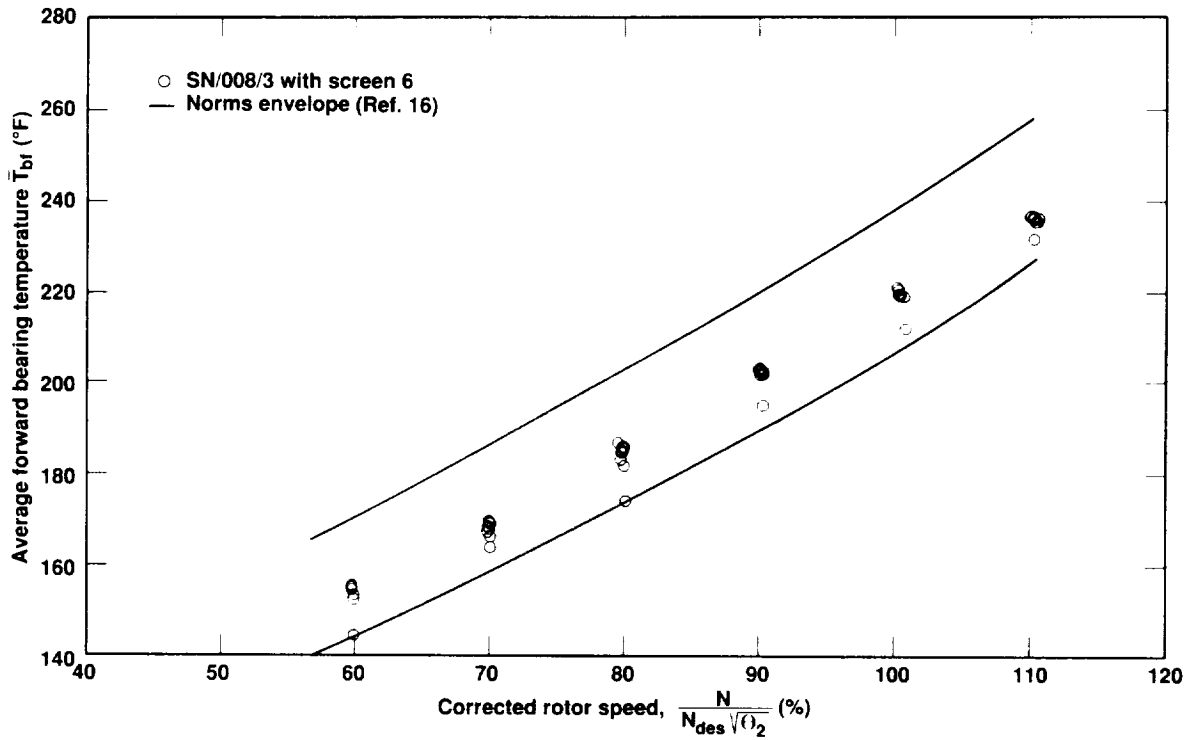


Figure 77. CMAPS SN/008/3 forward bearing temperature for screen No. 6.

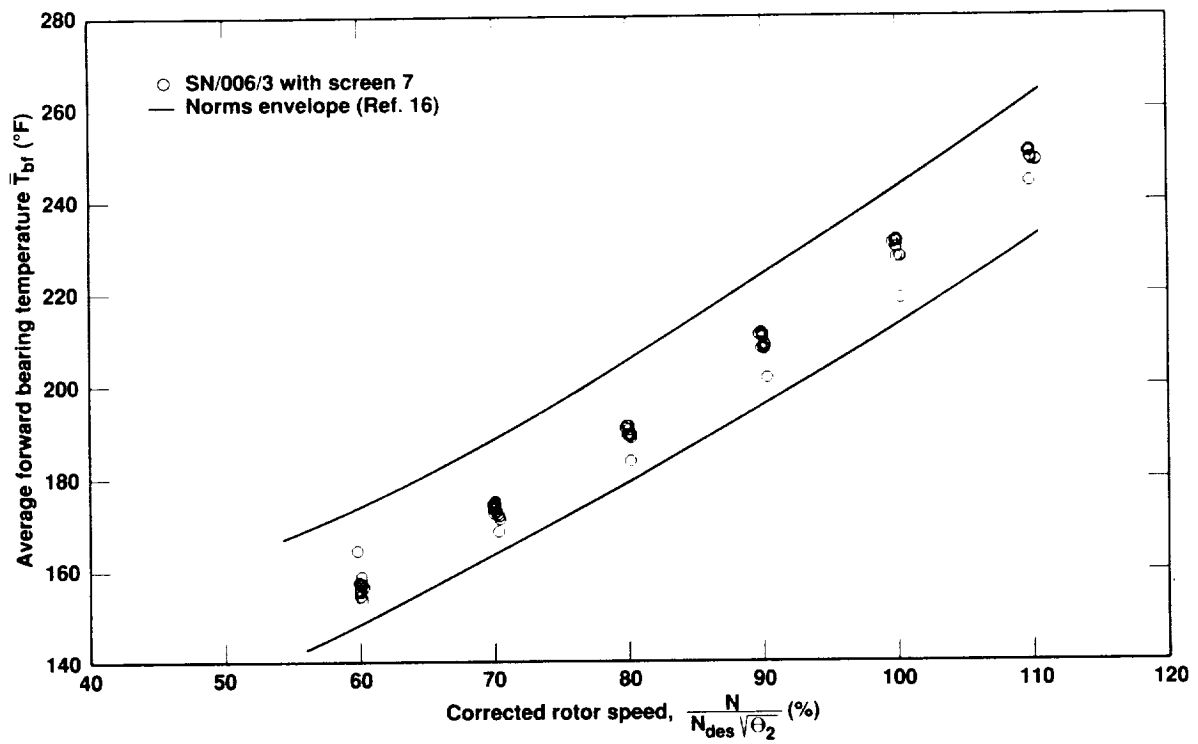


Figure 78. CMAPS SN/006/3 forward bearing temperature for screen No. 7.

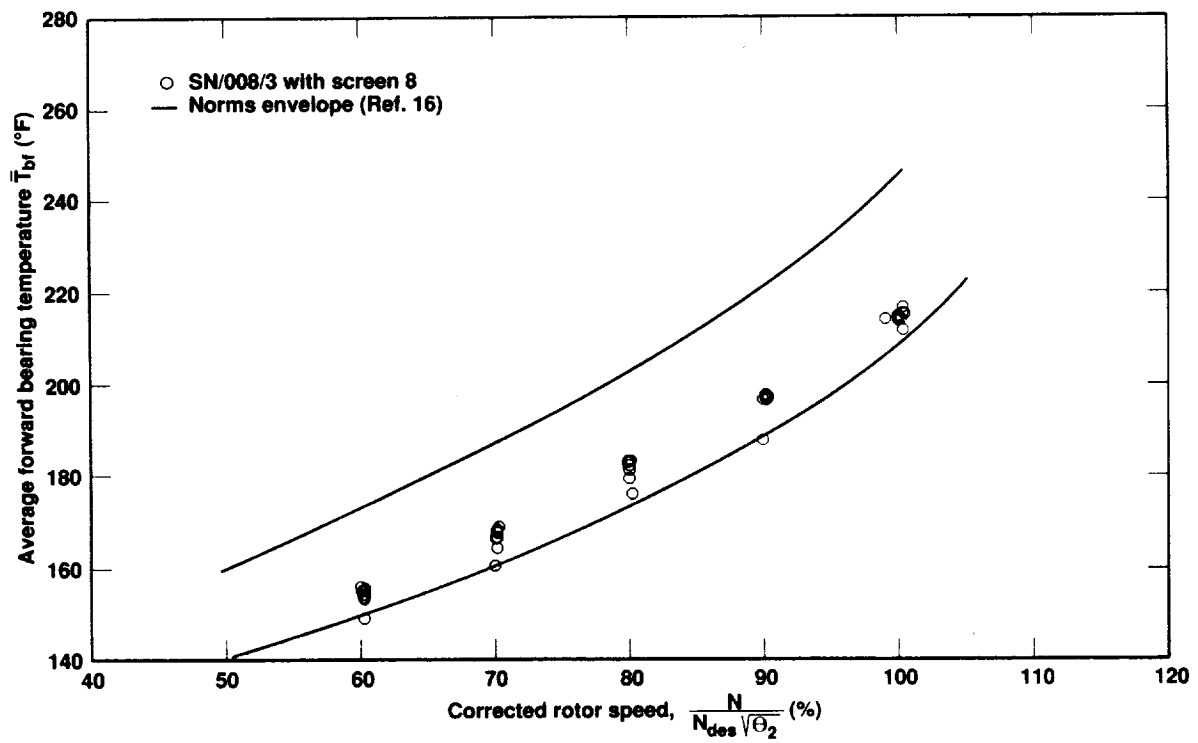


Figure 79. CMAPS SN/008/3 forward bearing temperature for screen No. 8.

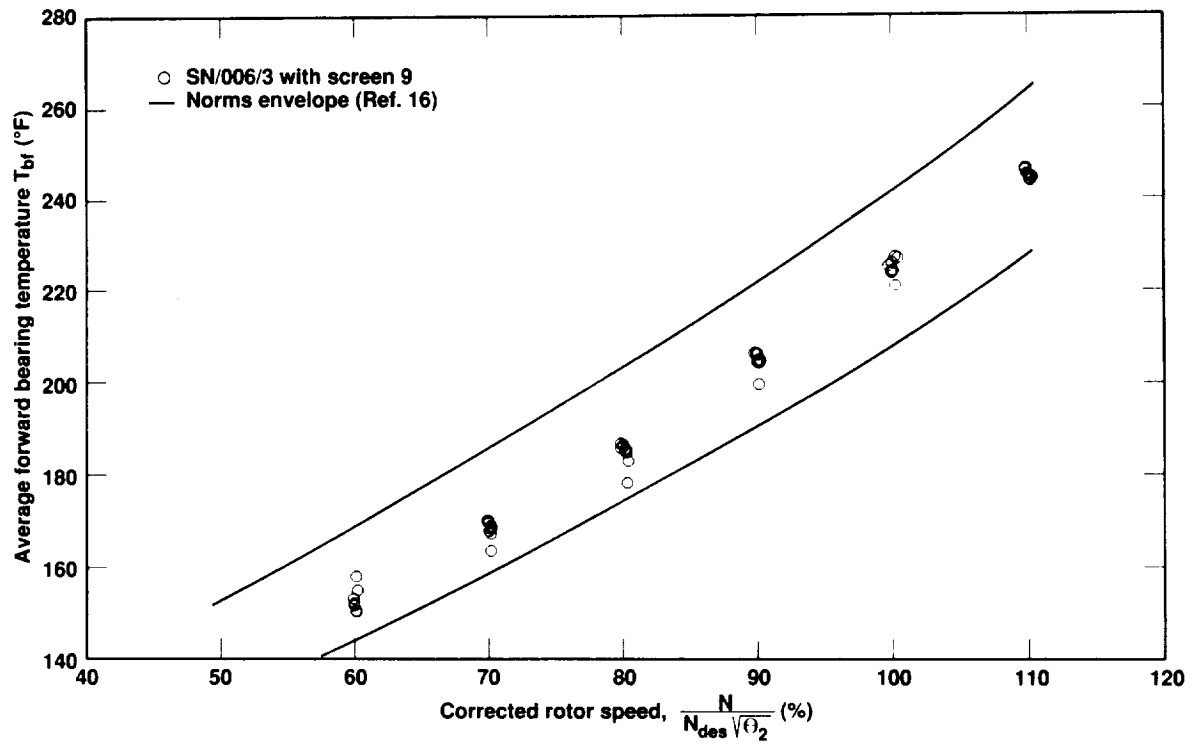


Figure 80. CMAPS SN/006/3 forward bearing temperature for screen No. 9.

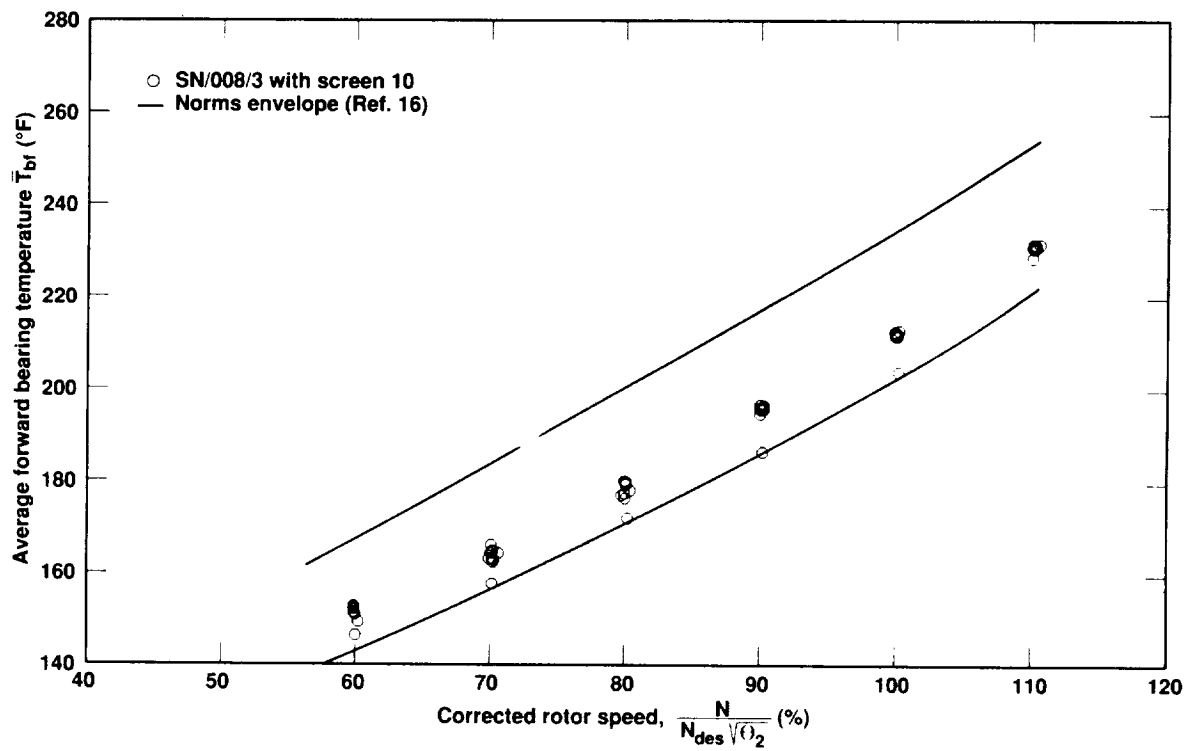


Figure 81. CMAPS SN/008/3 forward bearing temperature for screen No. 10.

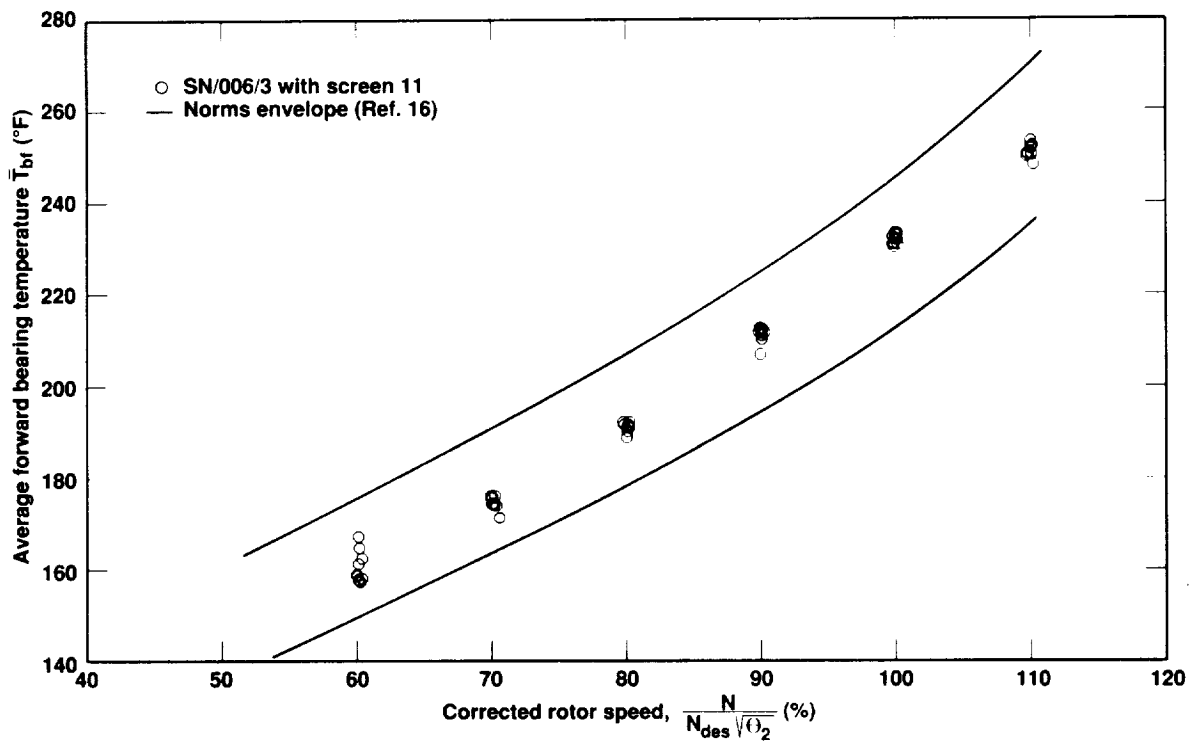


Figure 82. CMAPS SN/006/3 forward bearing temperature for screen No. 11.

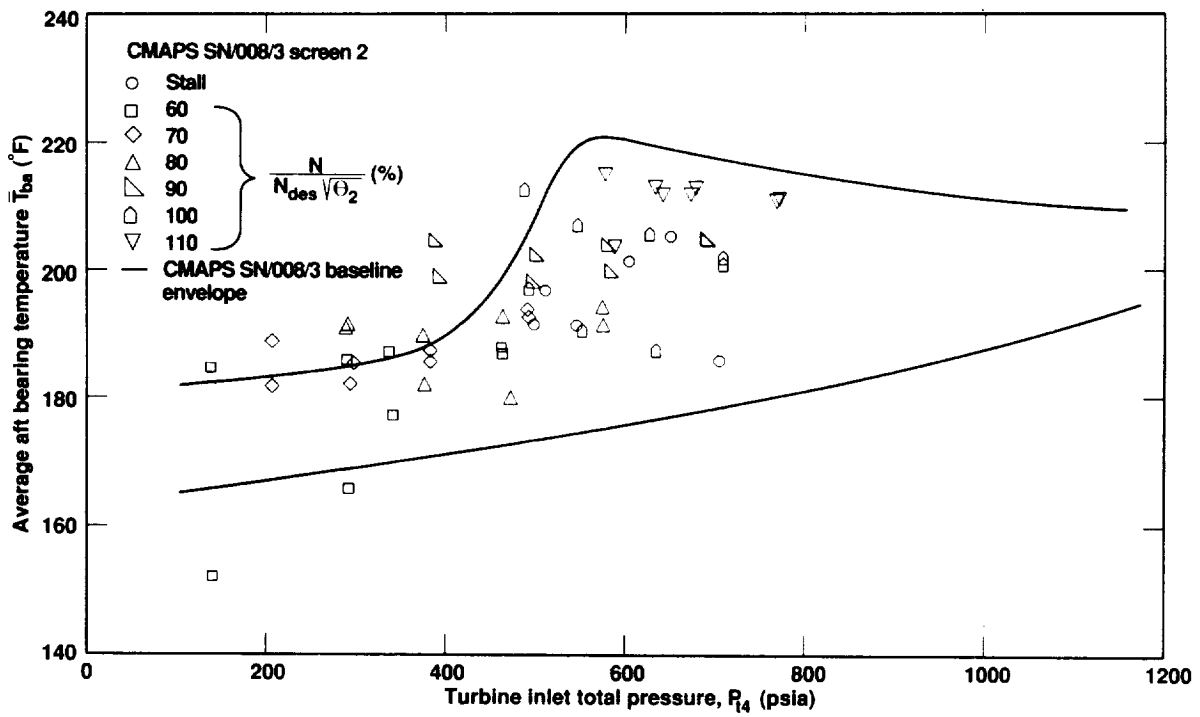


Figure 83. CMAPS SN/008/3 aft bearing temperature for screen No. 2.

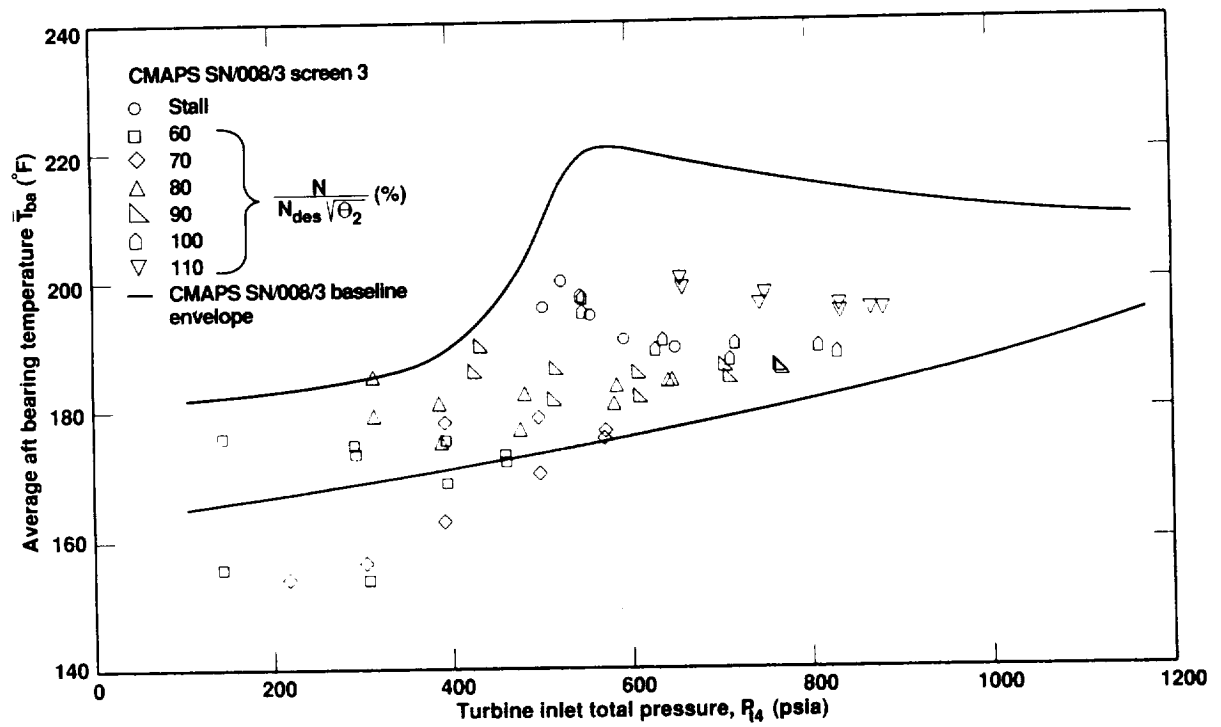


Figure 84. CMAPS SN/008/3 aft bearing temperature for screen No. 3.

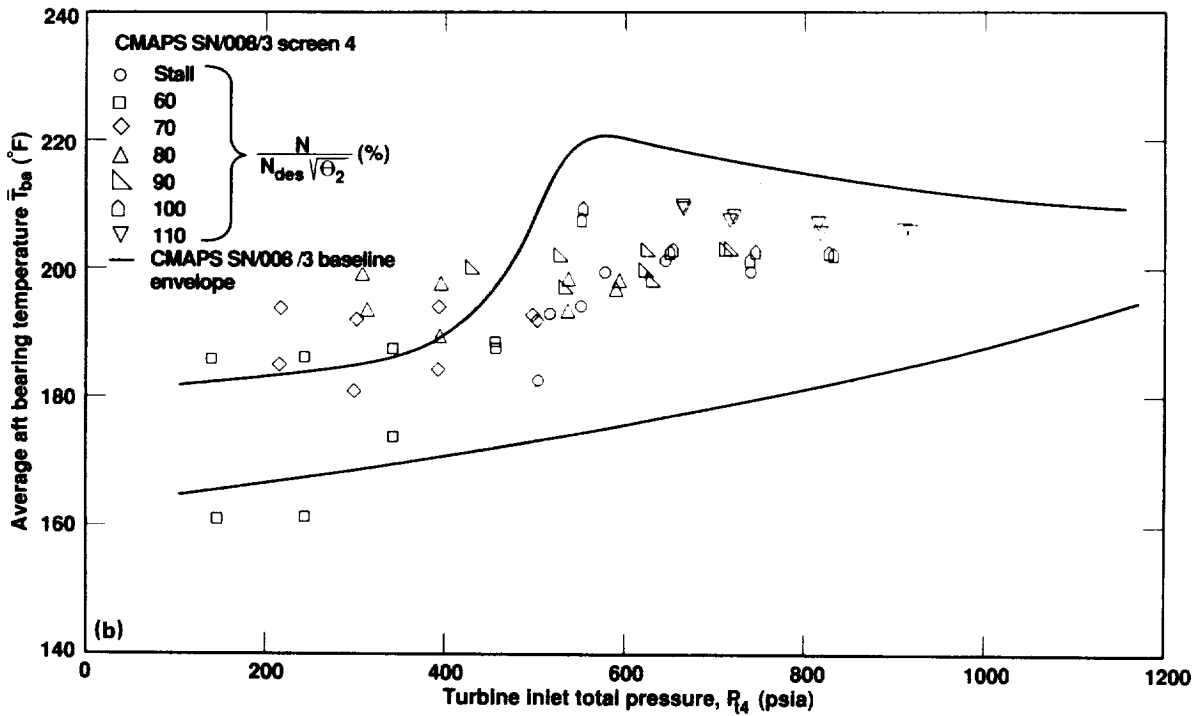
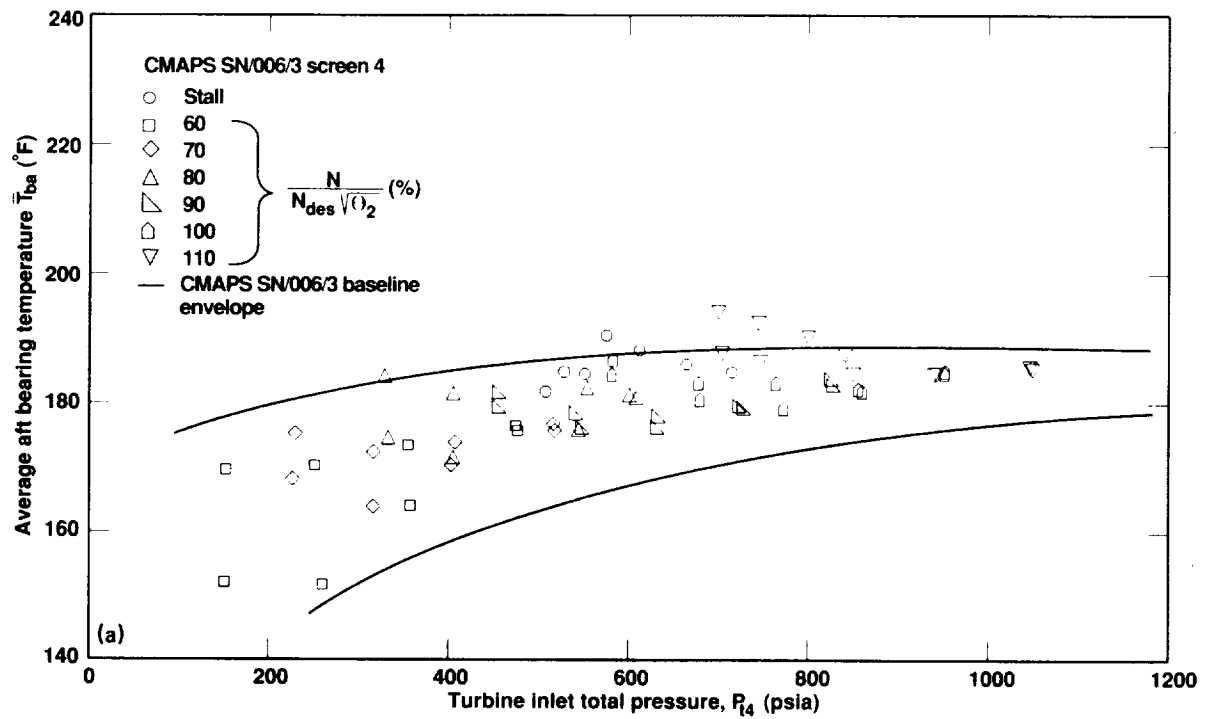


Figure 85. Aft bearing temperatures for screen No. 4. (a) CMAPS SN/006/3; (b) CMAPS SN/008/3.

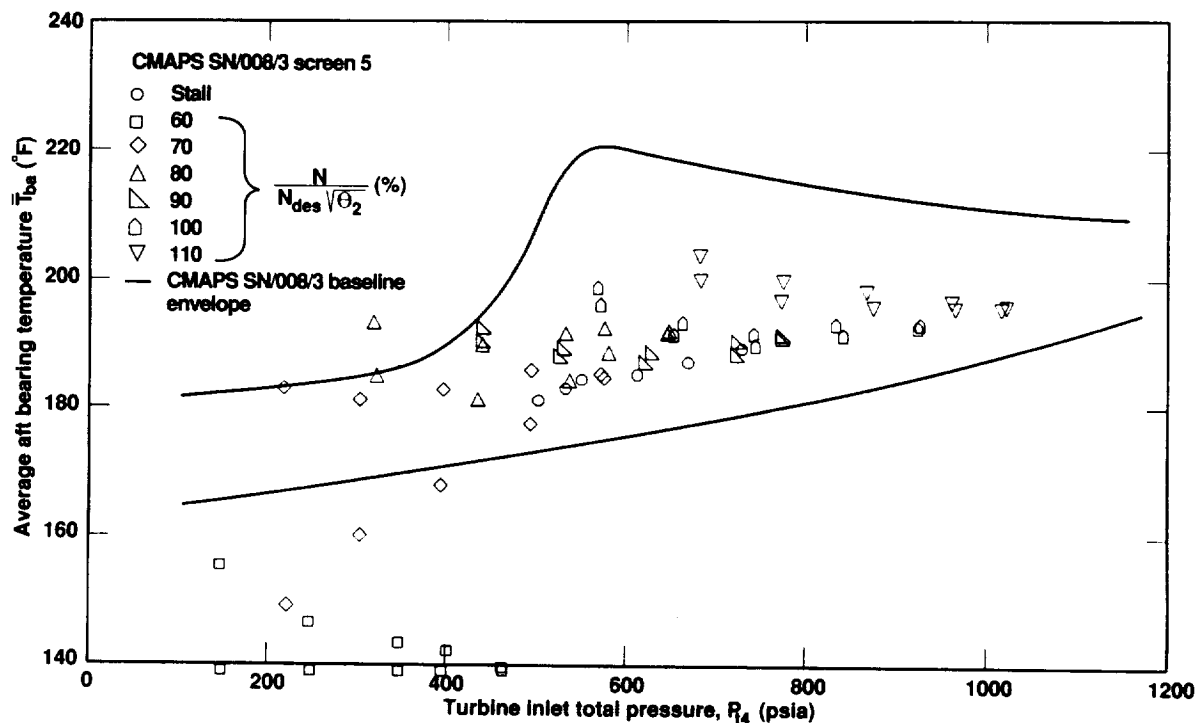


Figure 86. CMAPS SN/008/3 aft bearing temperature for screen No. 5.

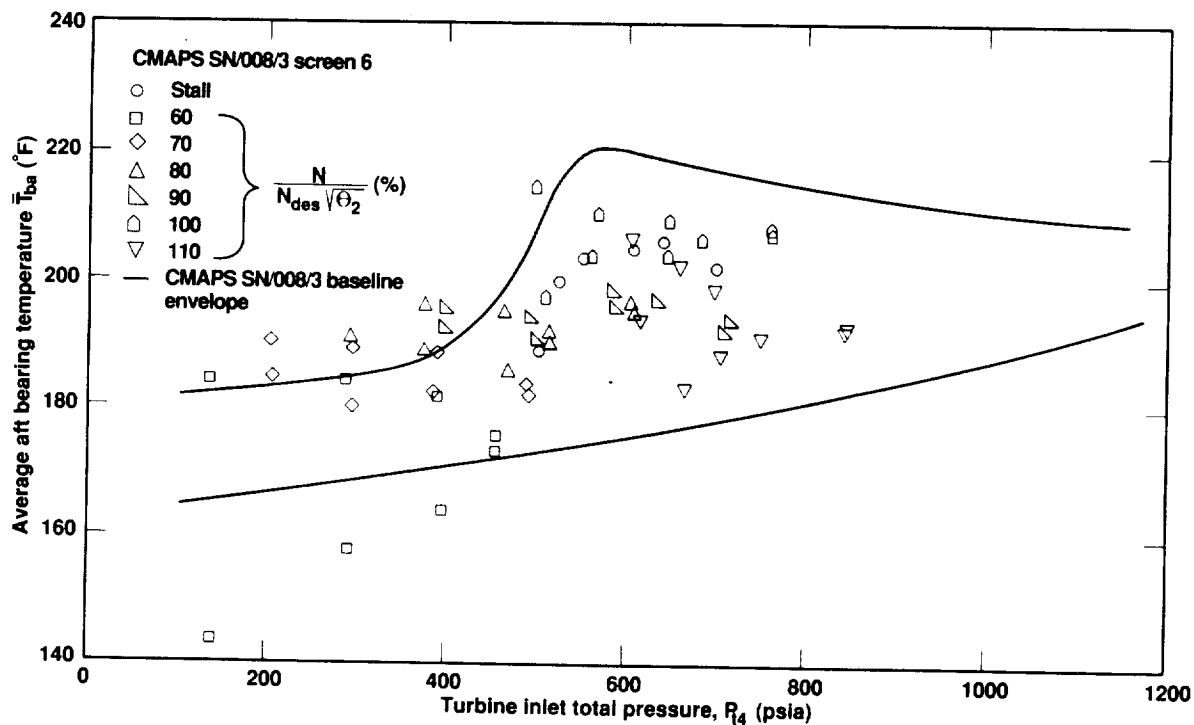


Figure 87. CMAPS SN/008/3 aft bearing temperature for screen No. 6.

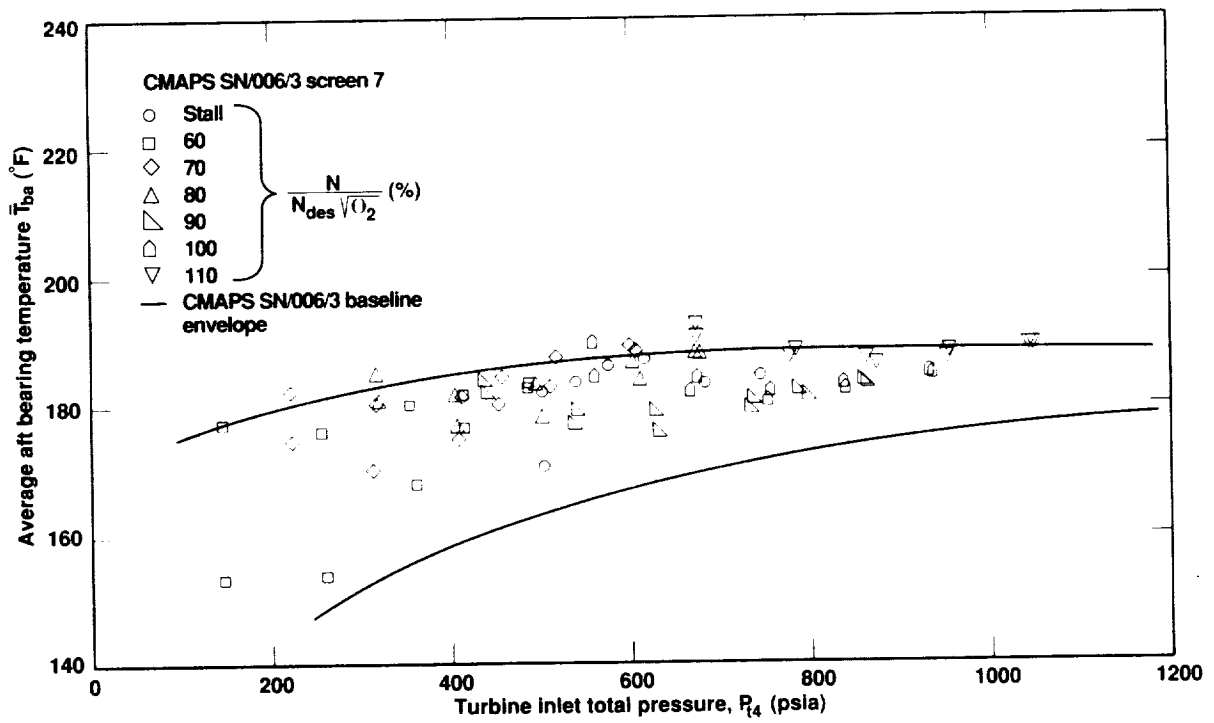


Figure 88. CMAPS SN/006/3 aft bearing temperature for screen No. 7.

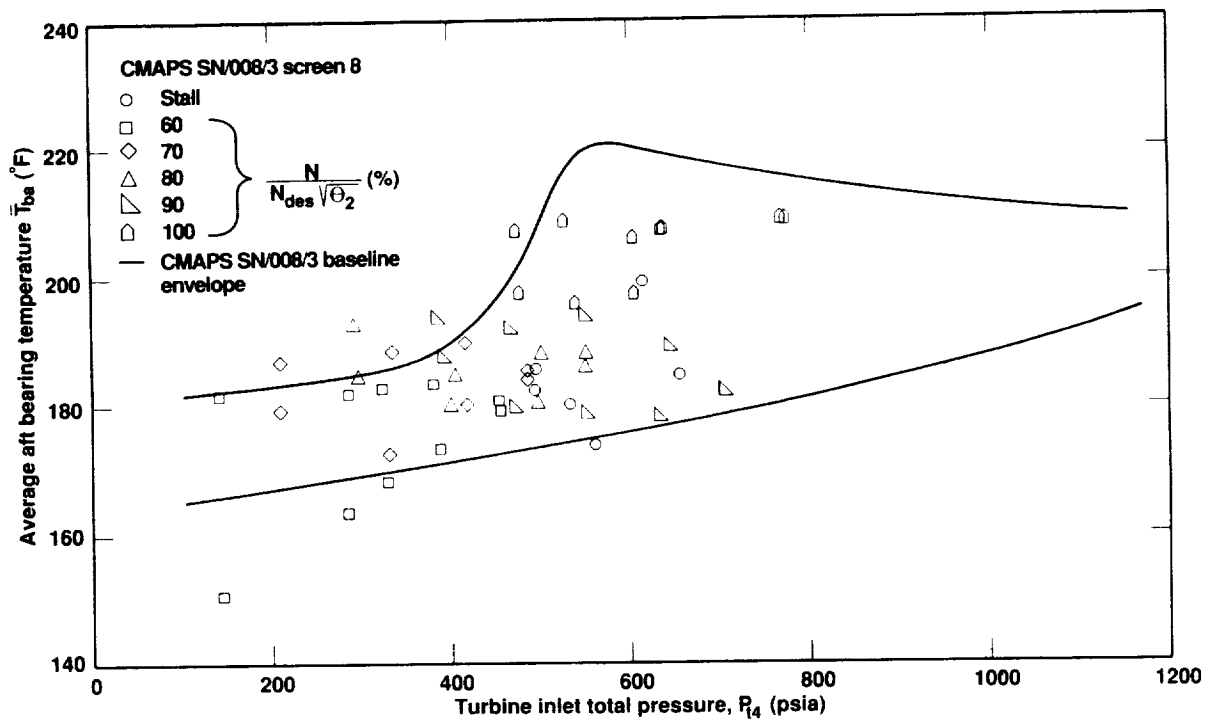


Figure 89. CMAPS SN/008/3 aft bearing temperature for screen No. 8.

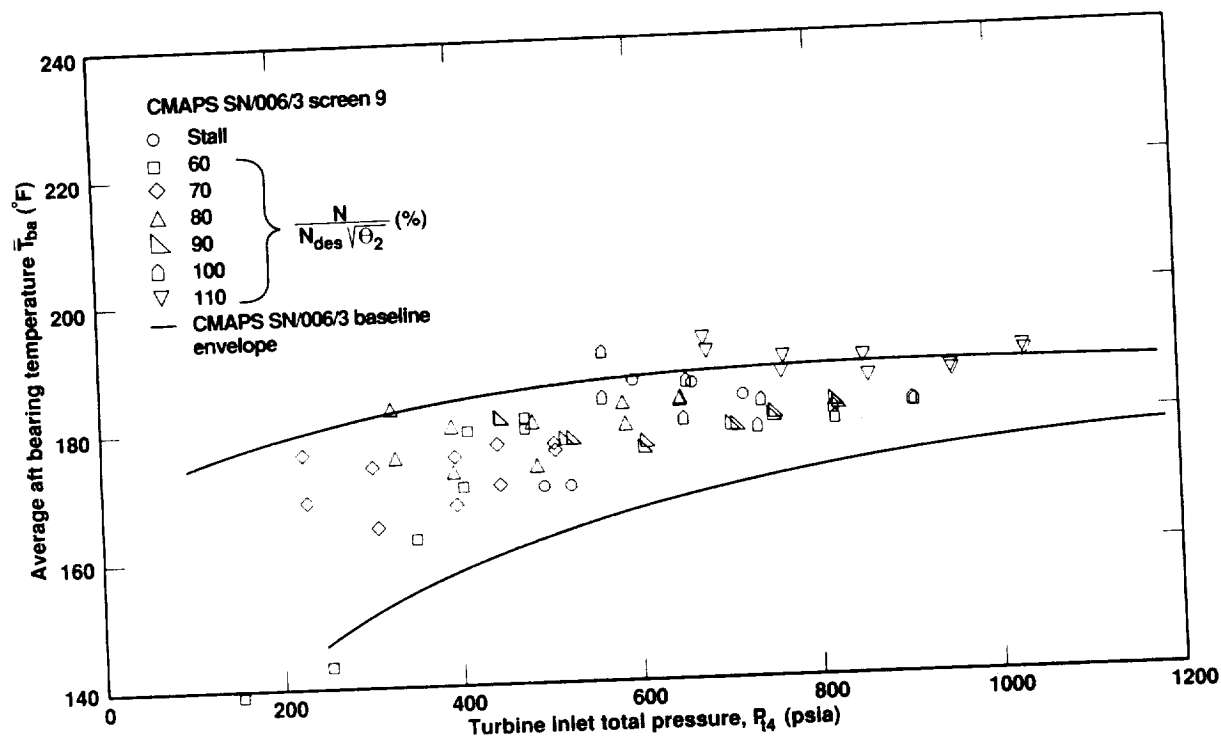


Figure 90. CMAPS SN/006/3 aft bearing temperature for screen No. 9.

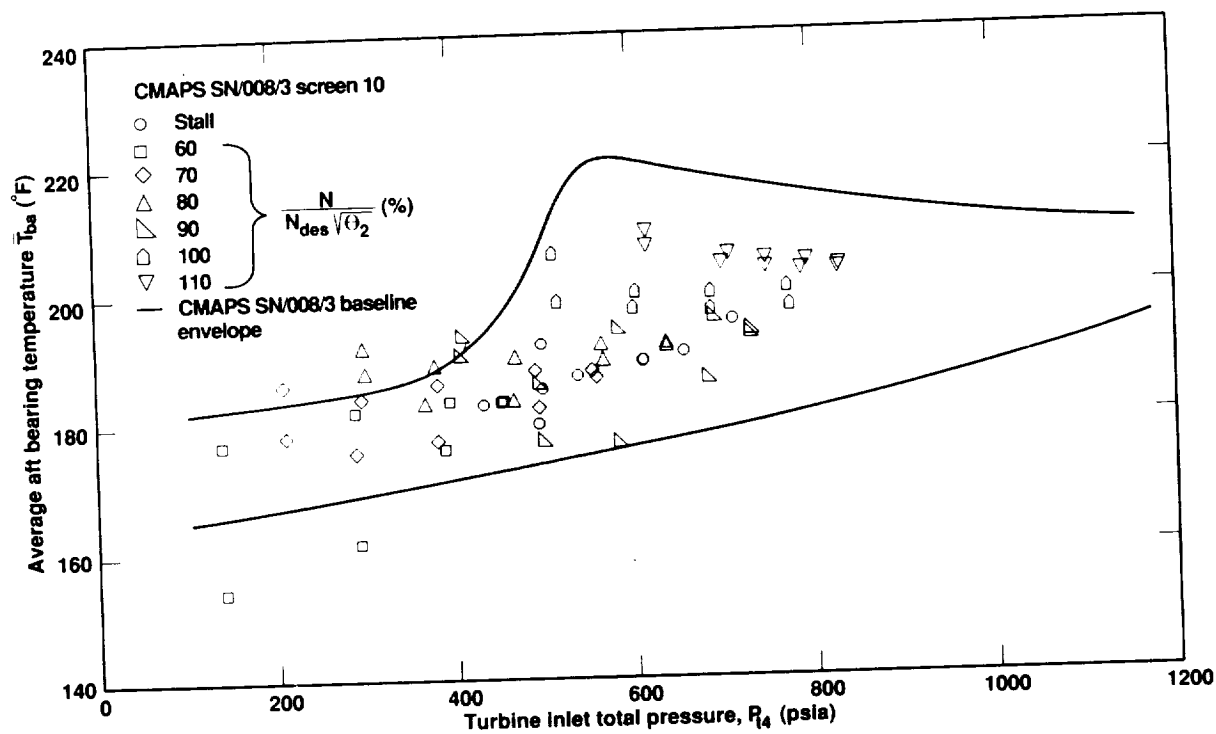


Figure 91. CMAPS SN/008/3 aft bearing temperature for screen No. 10.

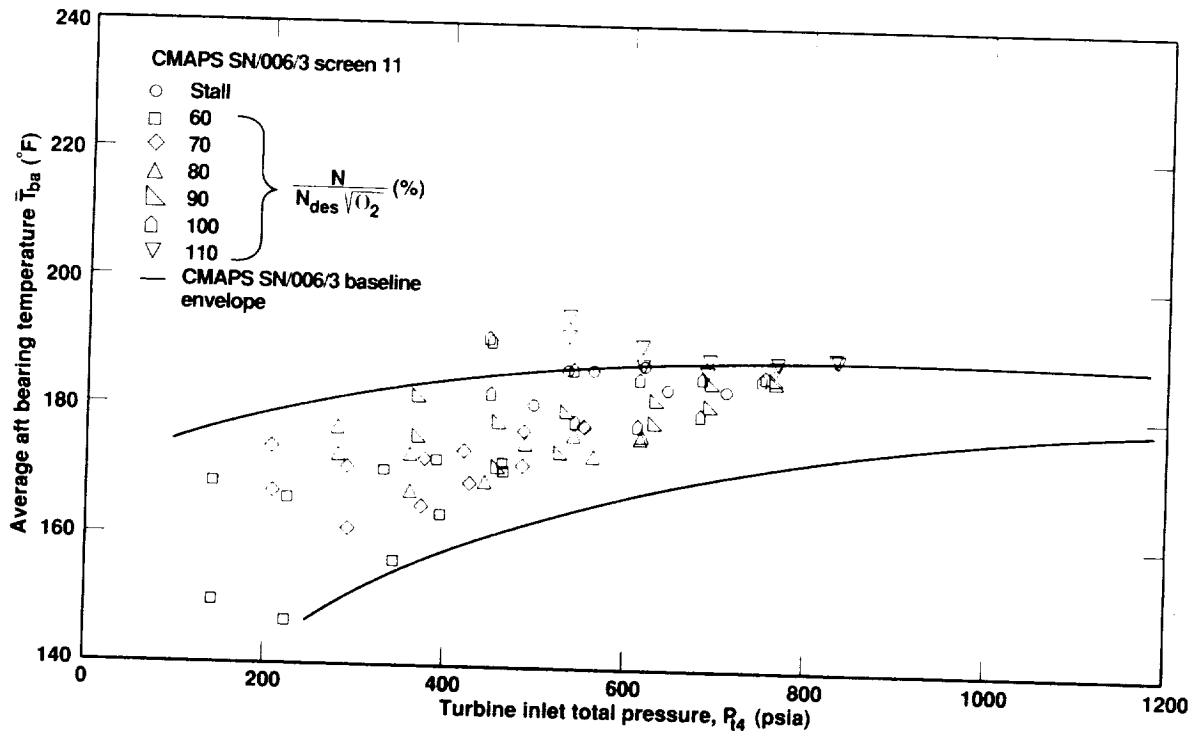


Figure 92. CMAPS SN/006/3 aft bearing temperature for screen No. 11.

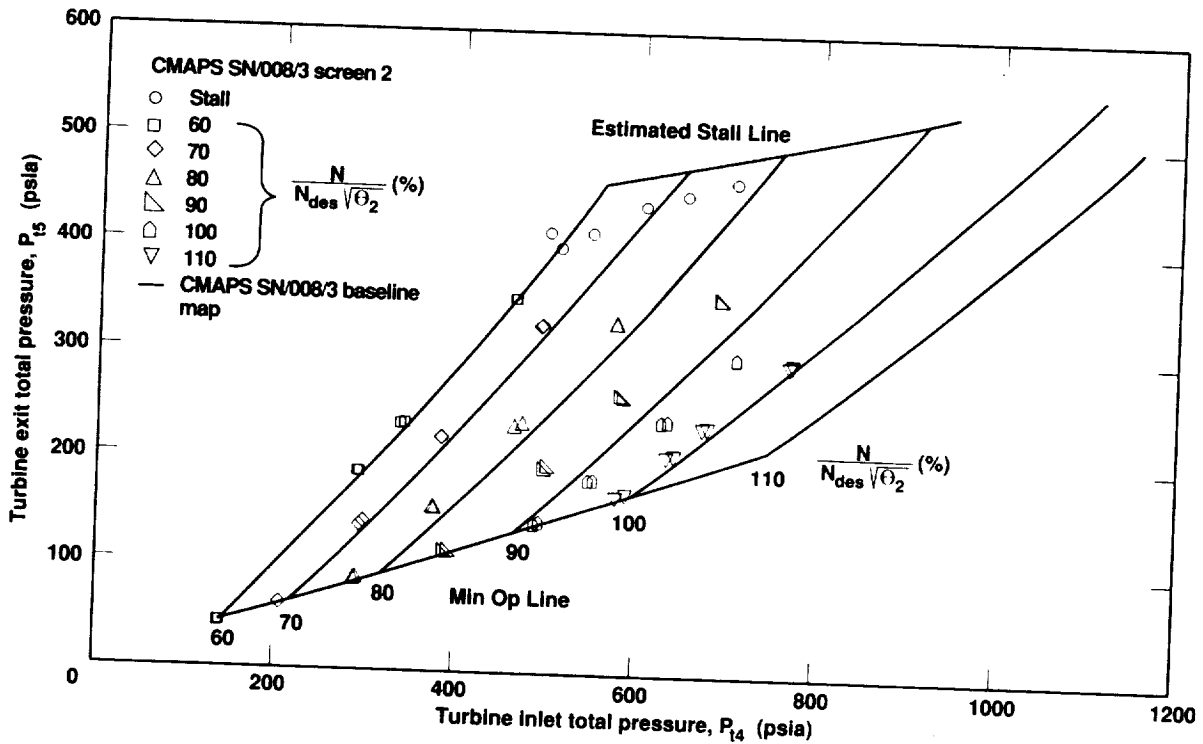


Figure 93. CMAPS SN/008/3 turbine pressure loss map for screen No. 2.

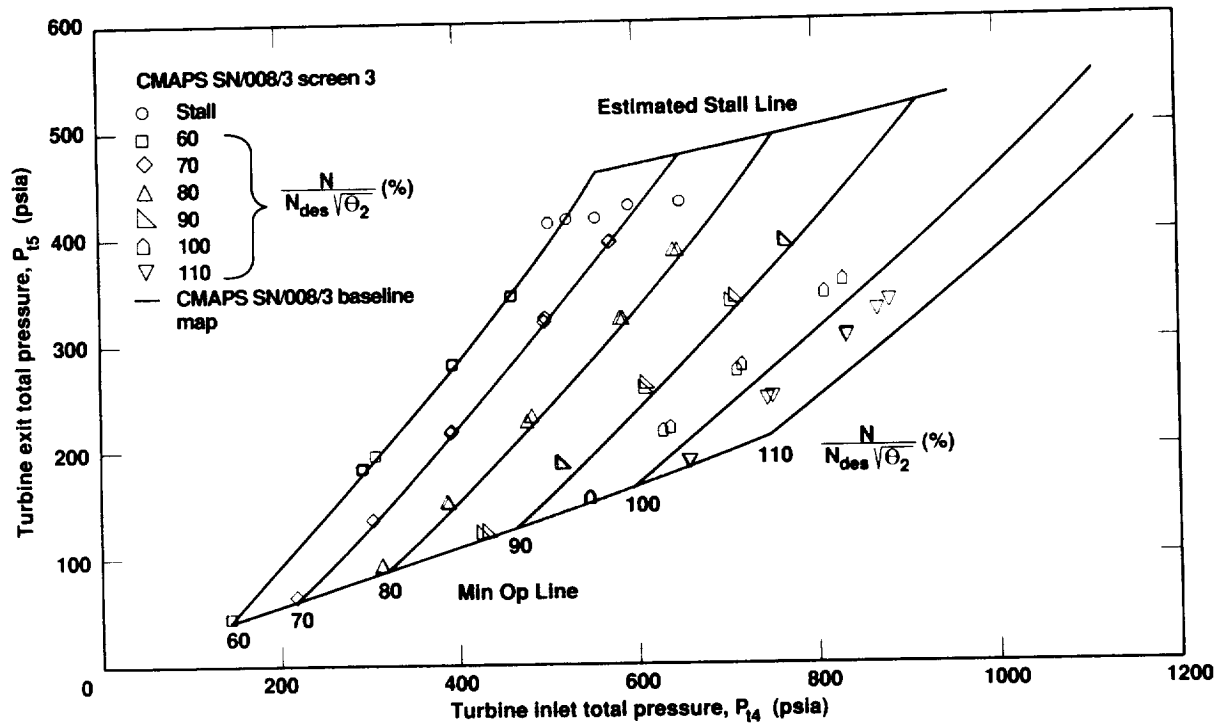


Figure 94. CMAPS SN/008/3 turbine pressure loss map for screen No. 3.

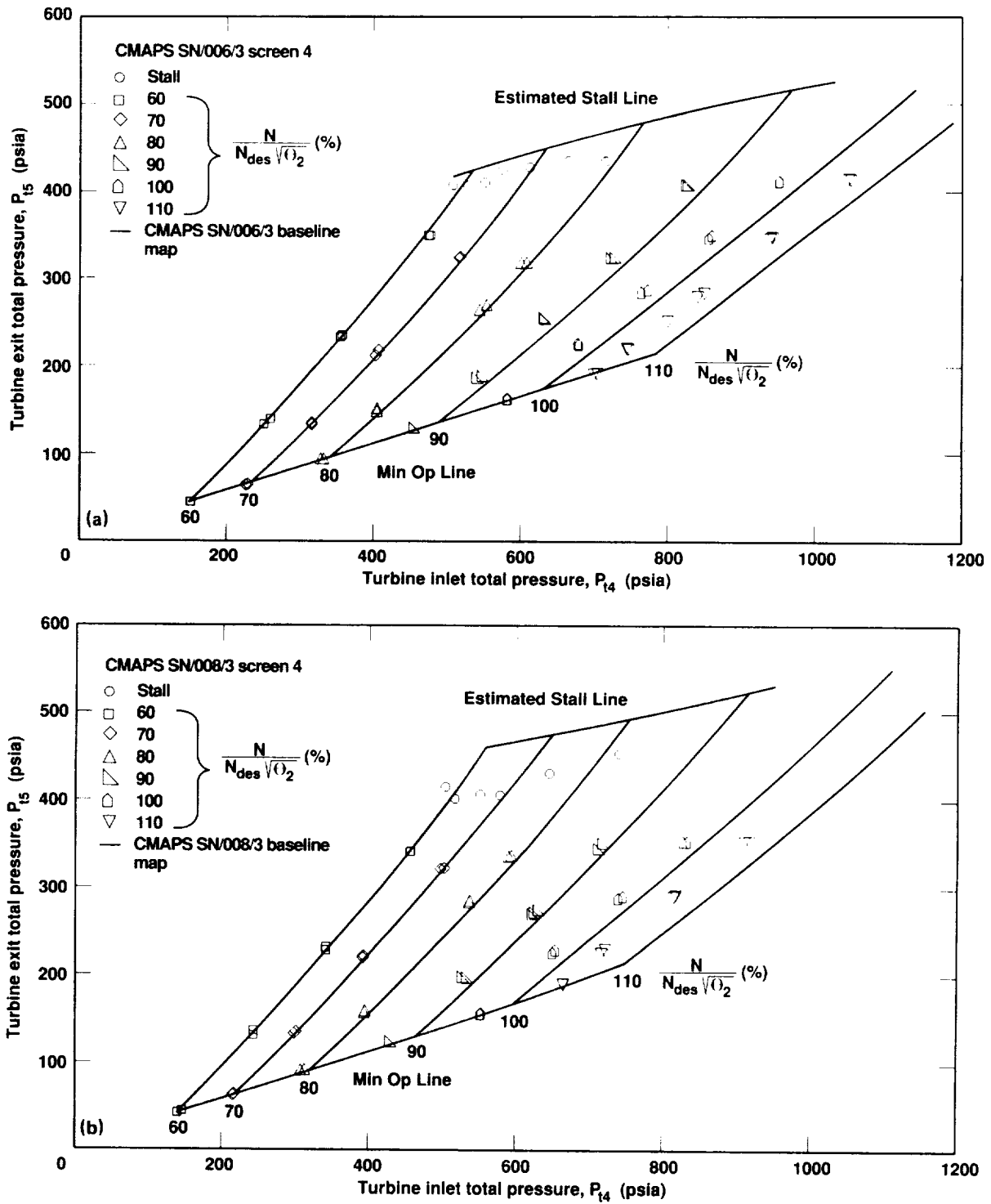


Figure 95. Turbine pressure loss maps for screen No. 4. (a) CMAPS SN/006/3; (b) CMAPS SN/008/3.

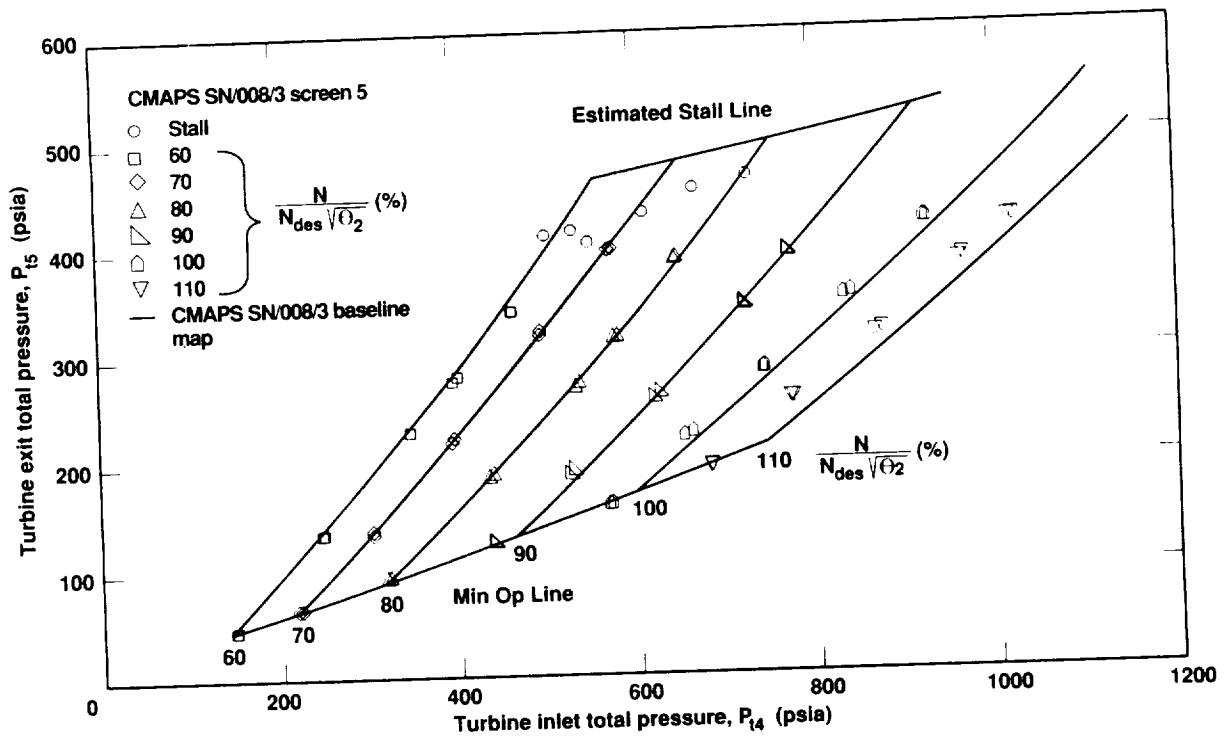


Figure 96. CMAPS SN/008/3 turbine pressure loss map for screen No. 5.

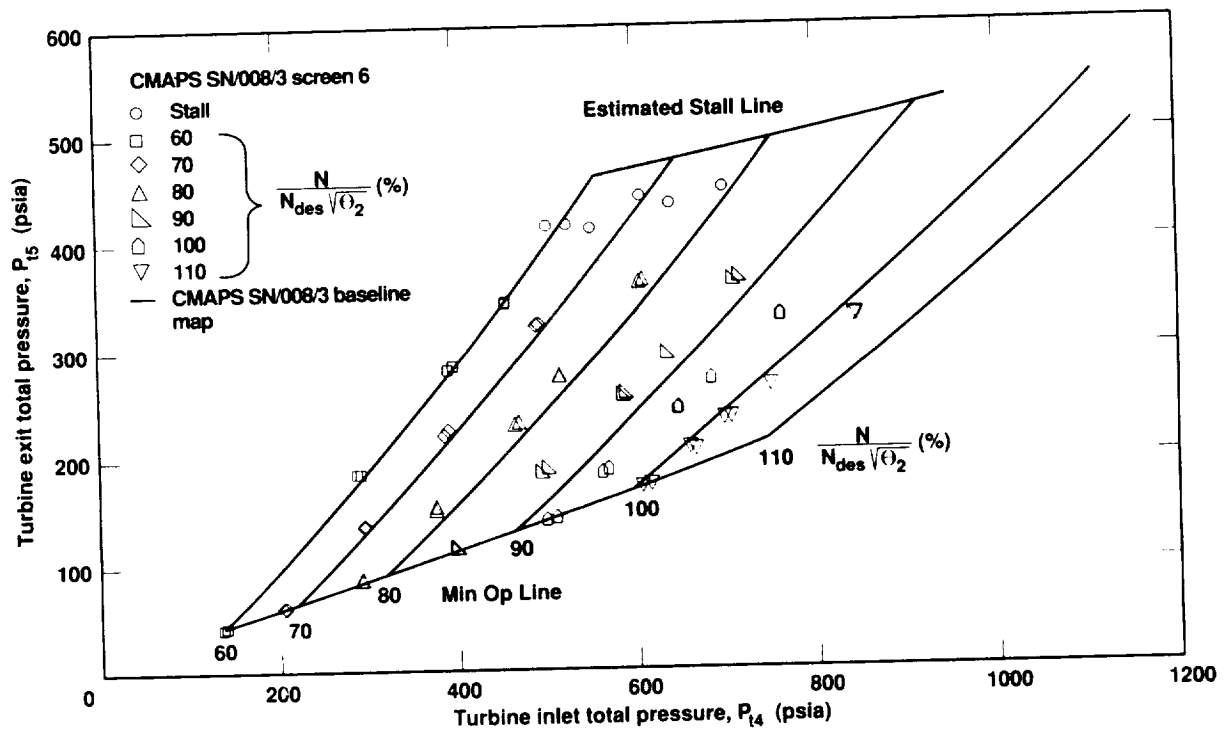


Figure 97. CMAPS SN/008/3 turbine pressure loss map for screen No. 6.

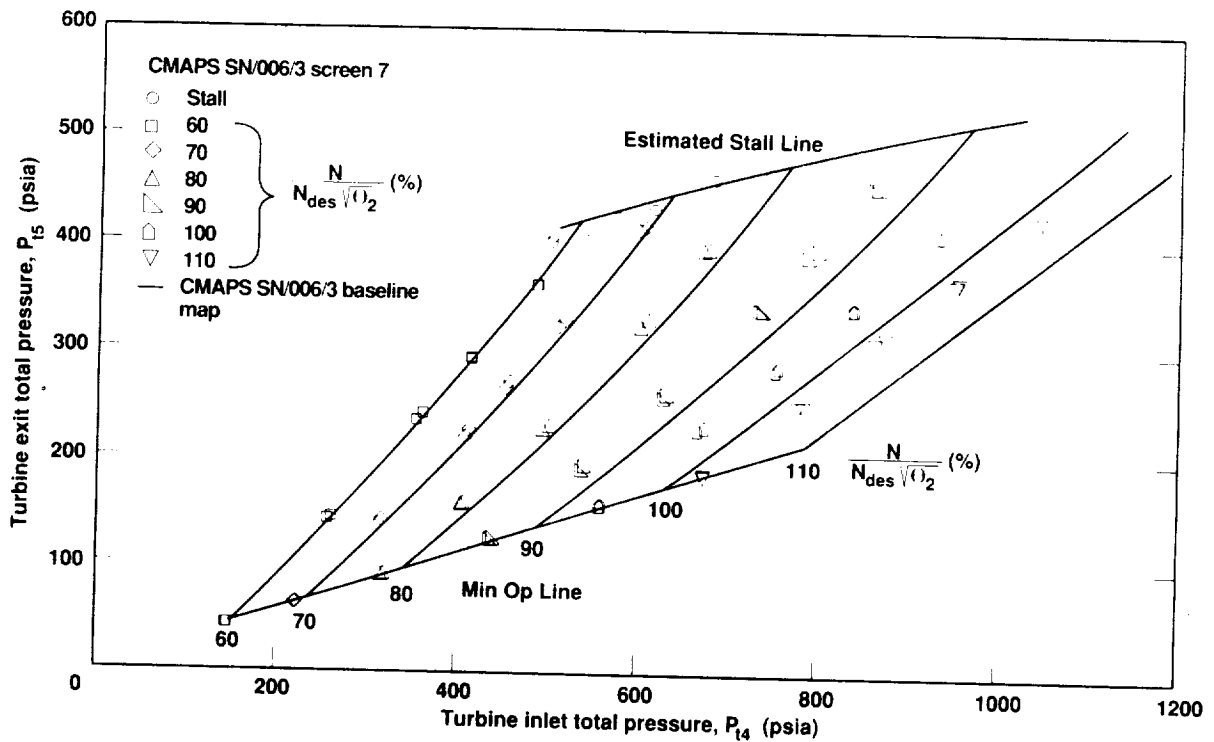


Figure 98. CMAPS SN/006/3 turbine pressure loss map for screen No. 7.

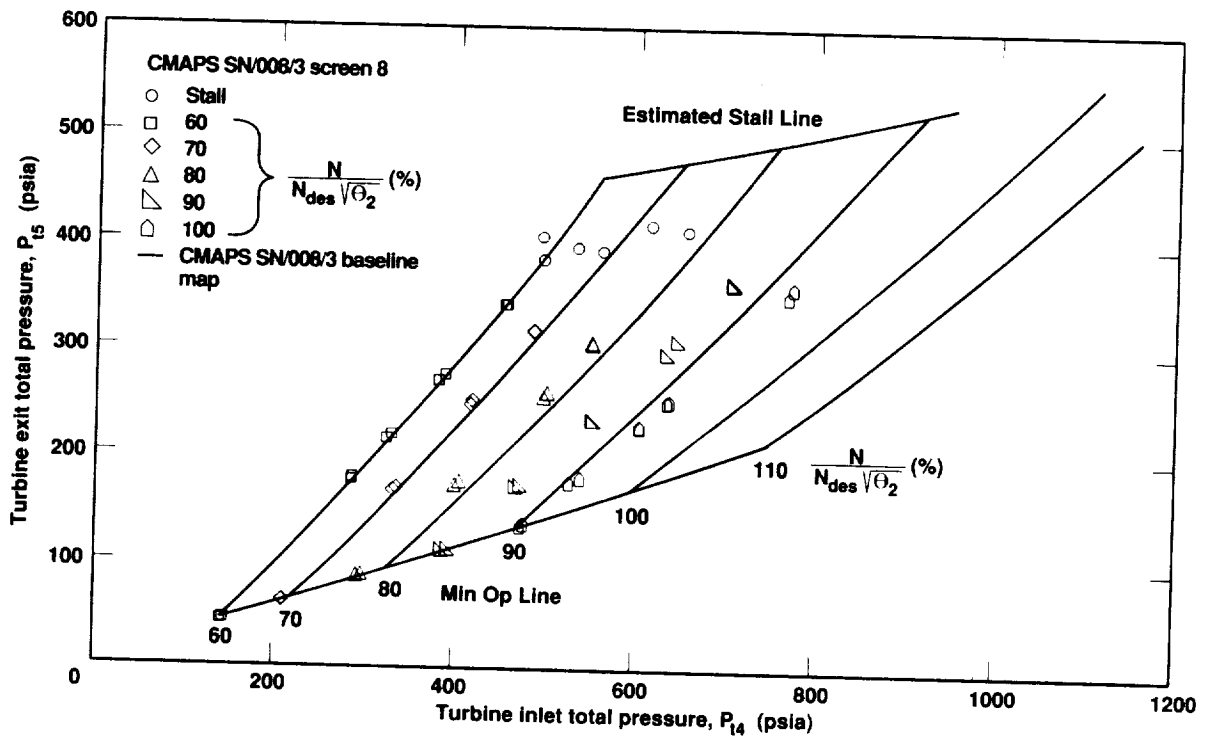


Figure 99. CMAPS SN/008/3 turbine pressure loss map for screen No. 8.

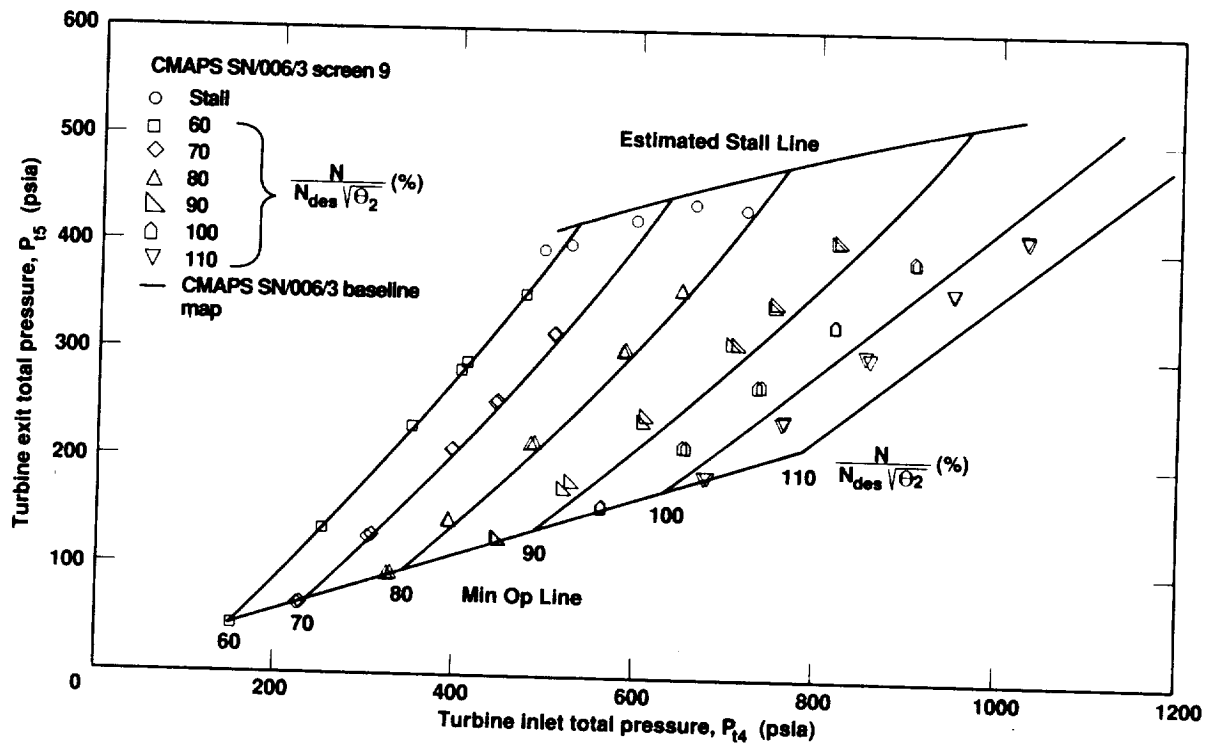


Figure 100. CMAPS SN/006/3 turbine pressure loss map for screen No. 9.

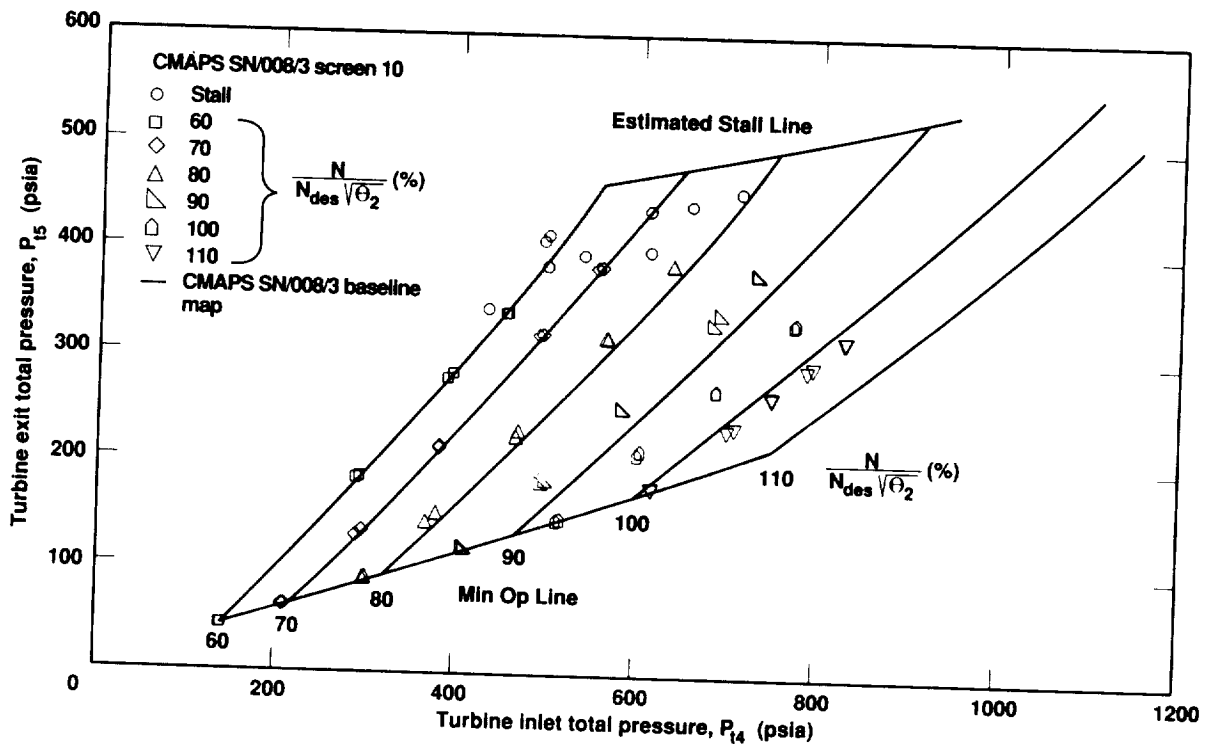


Figure 101. CMAPS SN/008/3 turbine pressure loss map for screen No. 10.

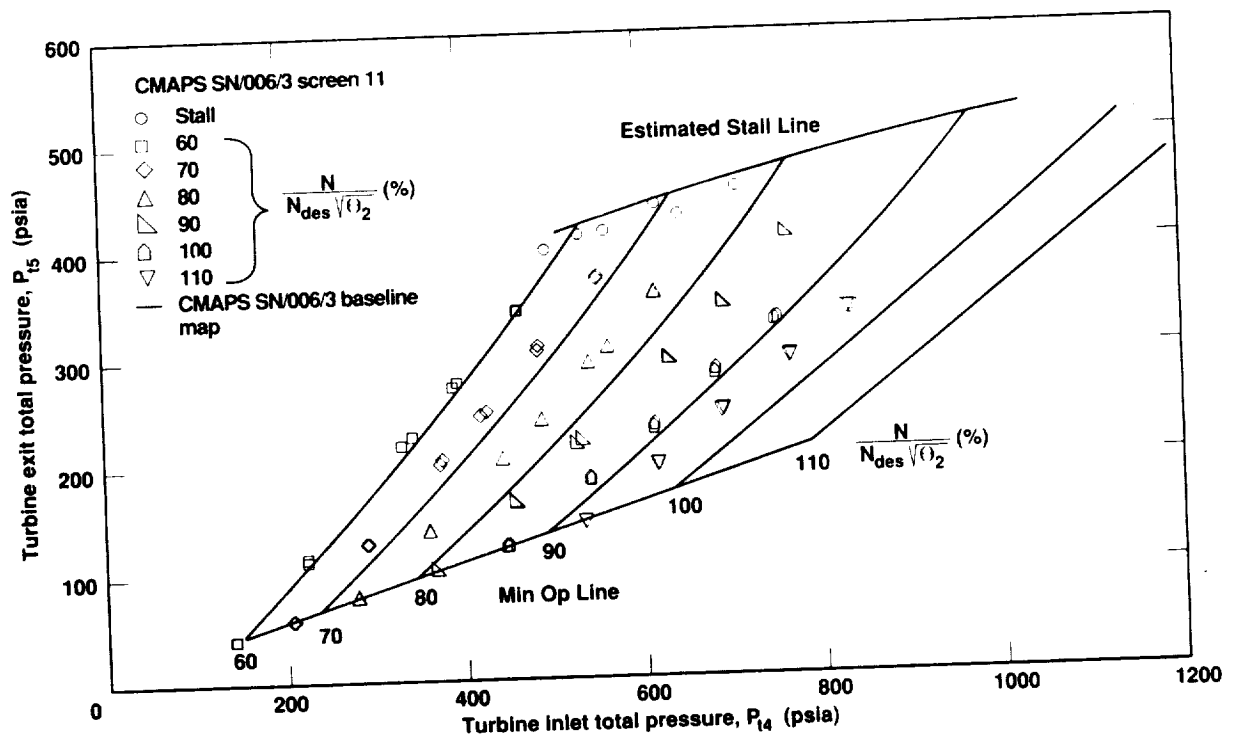


Figure 102. CMAPS SN/006/3 turbine pressure loss map for screen No. 11.

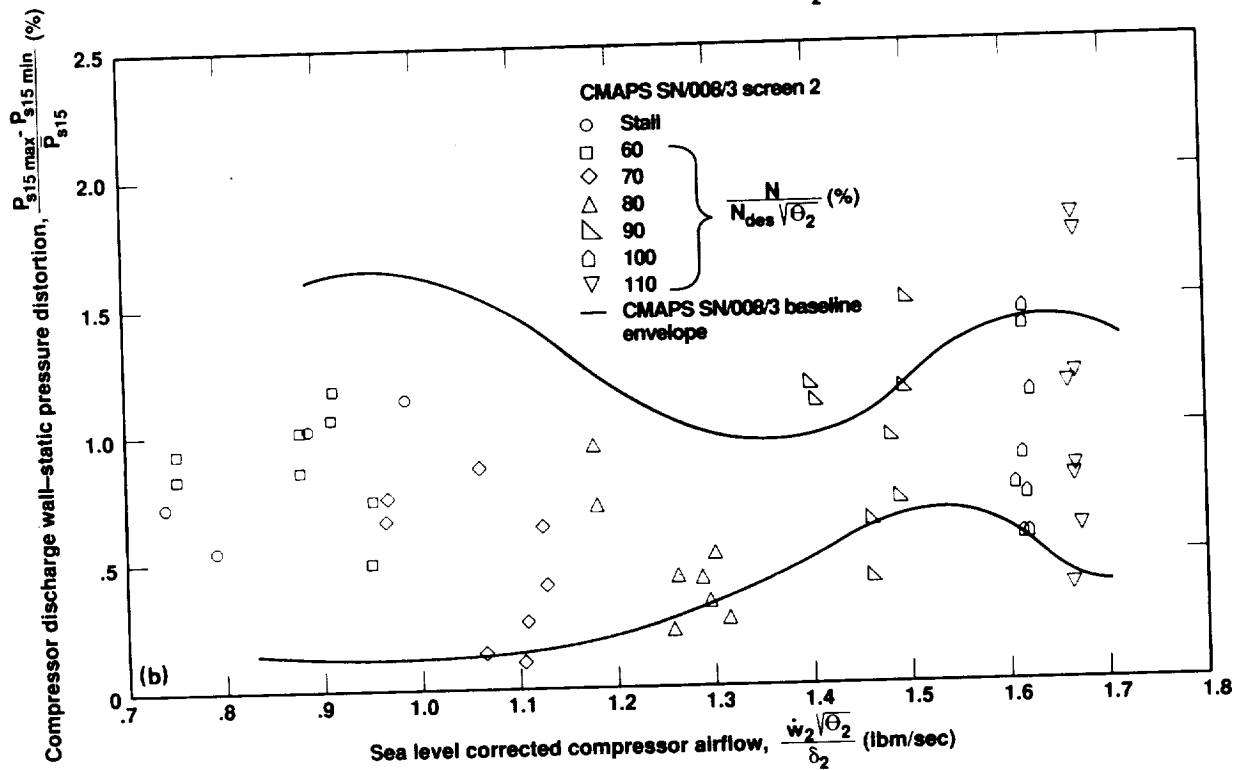
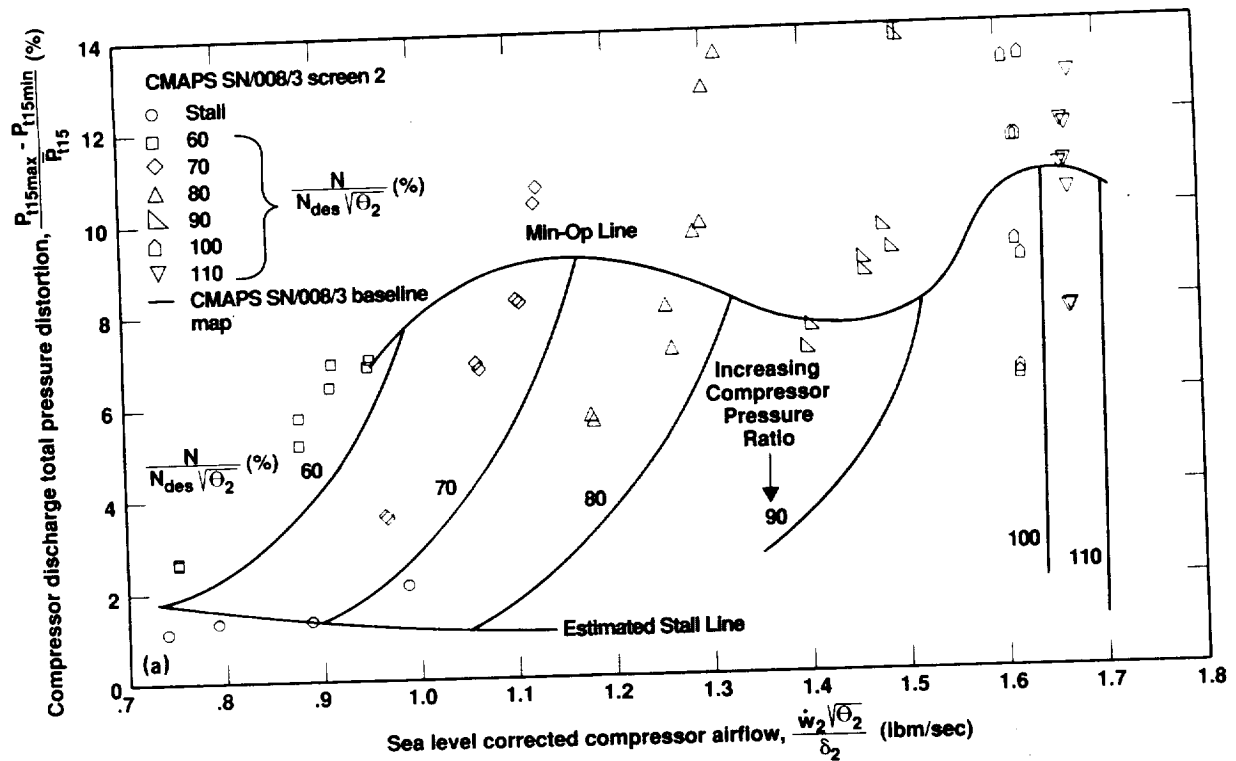


Figure 103. CMAPS SN/008/3 compressor discharge pressure distortions for screen No. 2. (a) Total pressure; (b) wall static pressure.

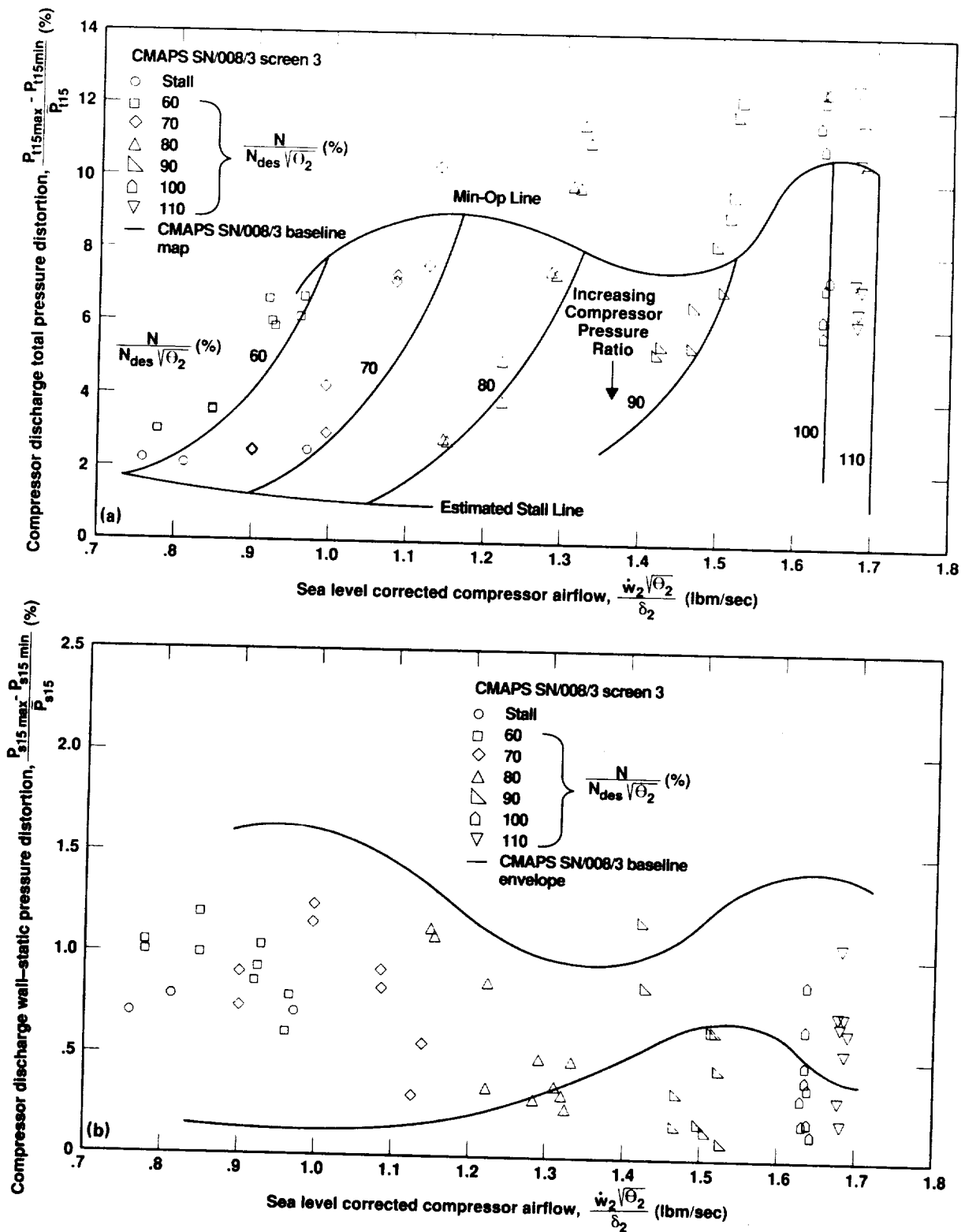


Figure 104. CMAPS SN/008/3 compressor discharge pressure distortions for screen No. 3. (a) Total pressure; (b) wall static pressure.

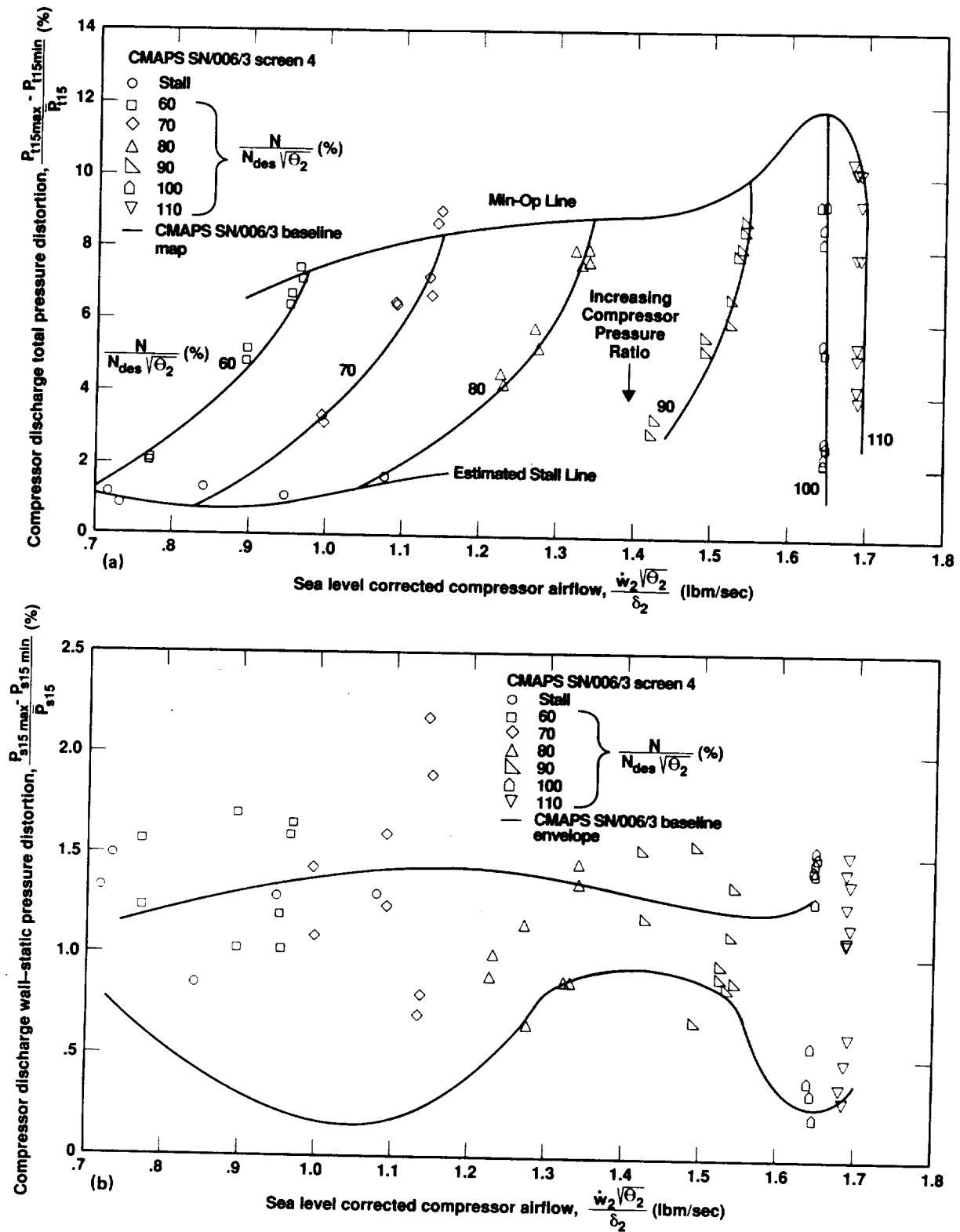


Figure 105. CMAPS SN/006/3 compressor discharge pressure distortions for screen No. 4. (a) Total pressure; (b) wall static pressure.

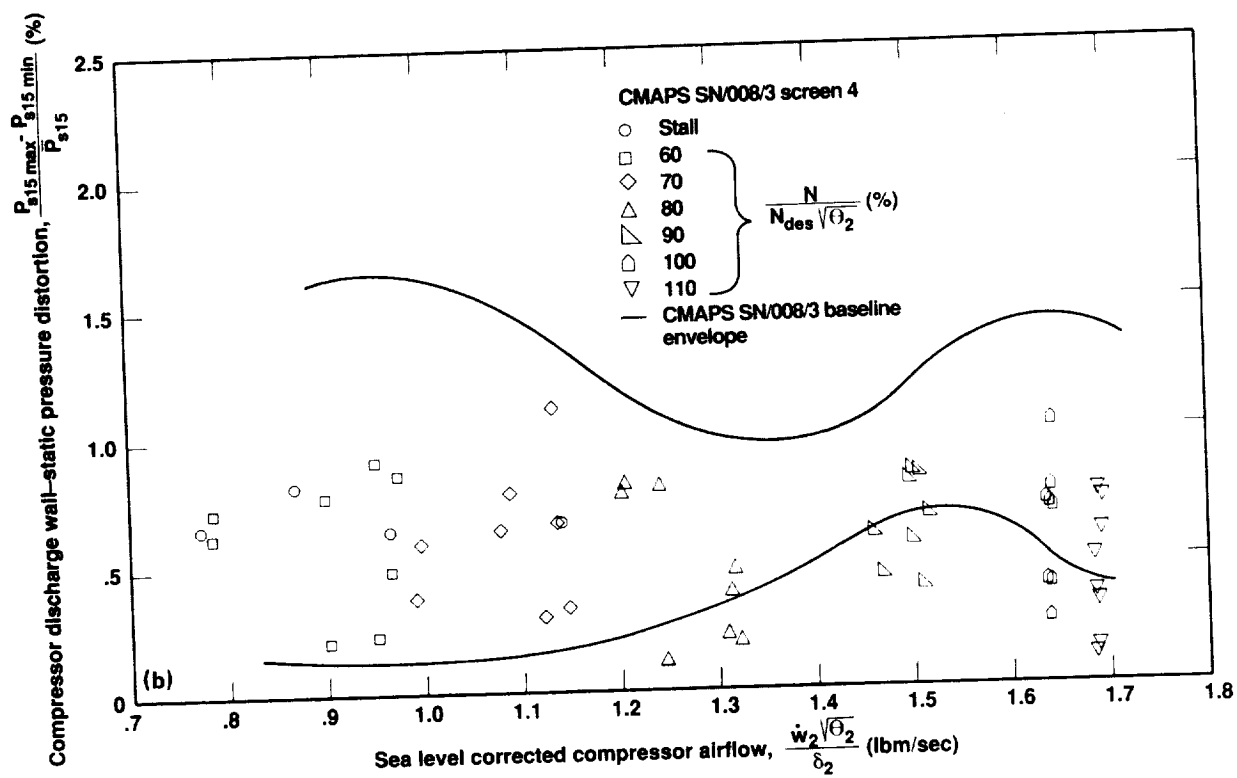
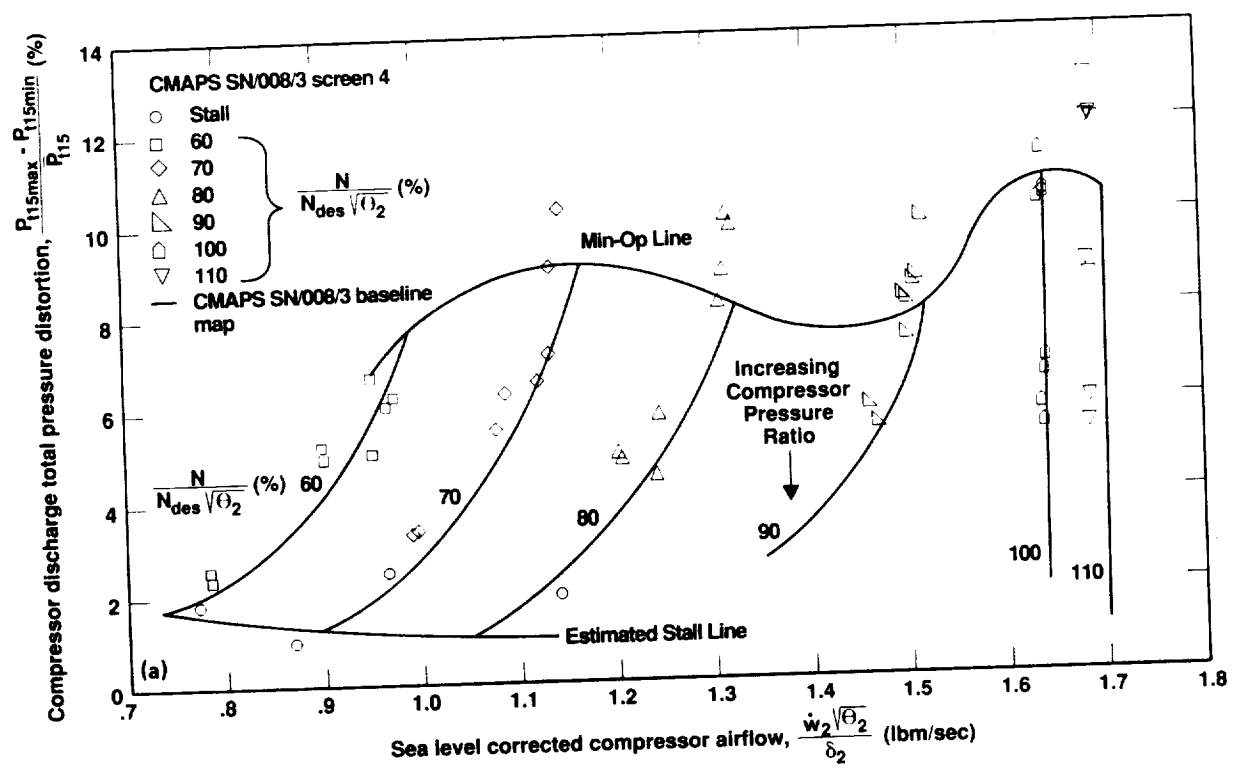


Figure 106. CMAPS SN/008/3 compressor discharge pressure distortions for screen No. 4. (a) Total pressure; (b) wall static pressure.

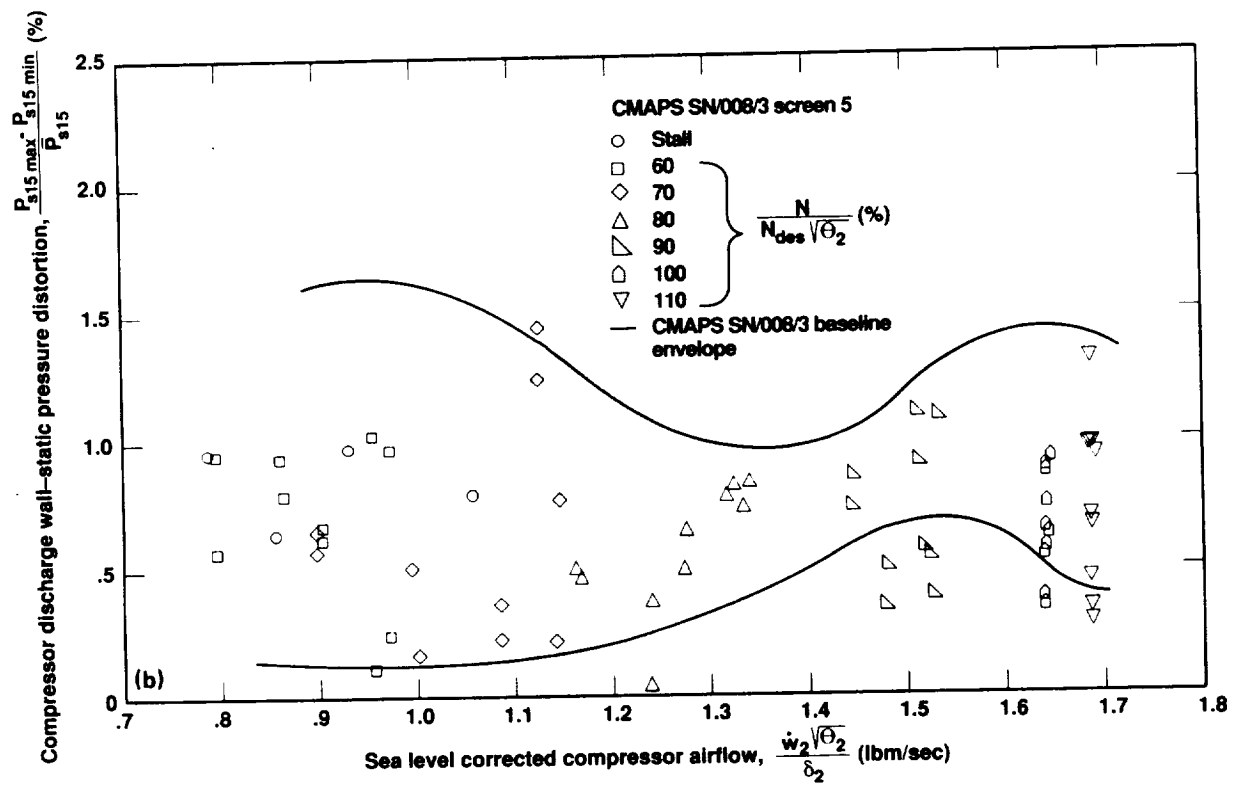
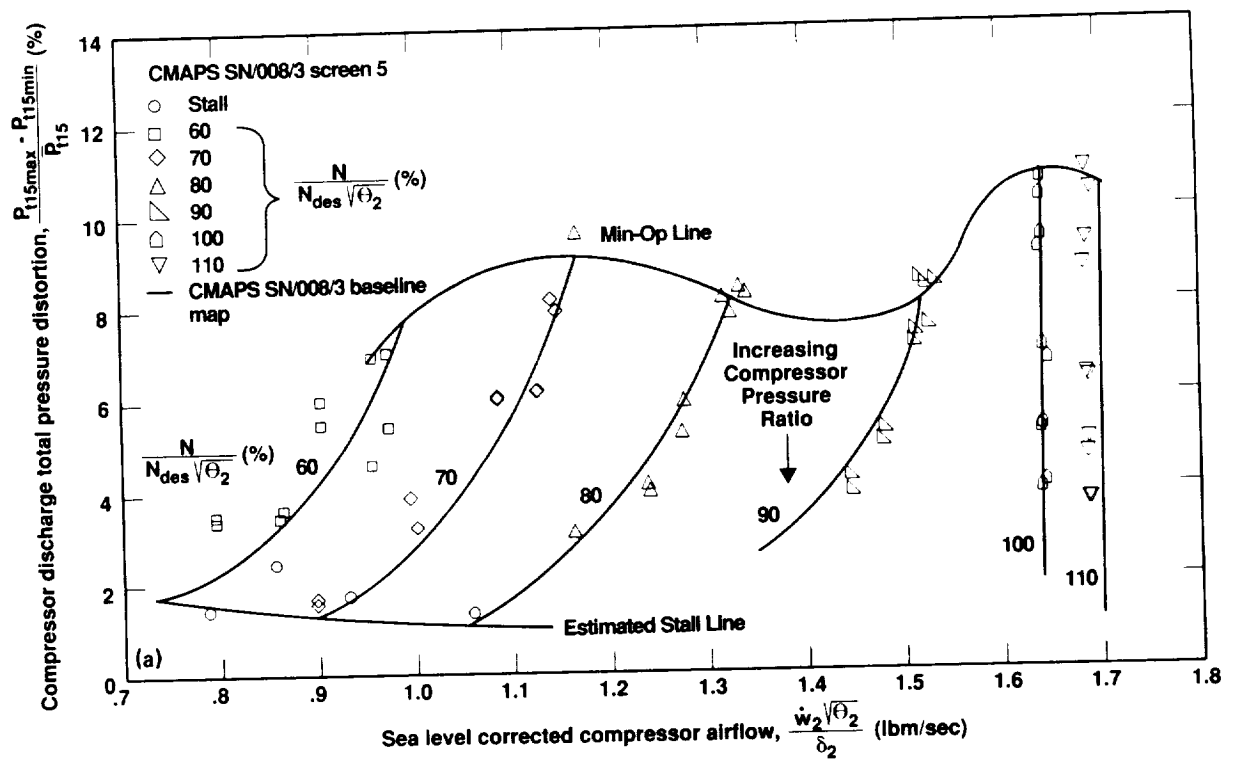


Figure 107. CMAPS SN/008/3 compressor discharge pressure distortions for screen No. 5. (a) Total pressure; (b) wall static pressure.

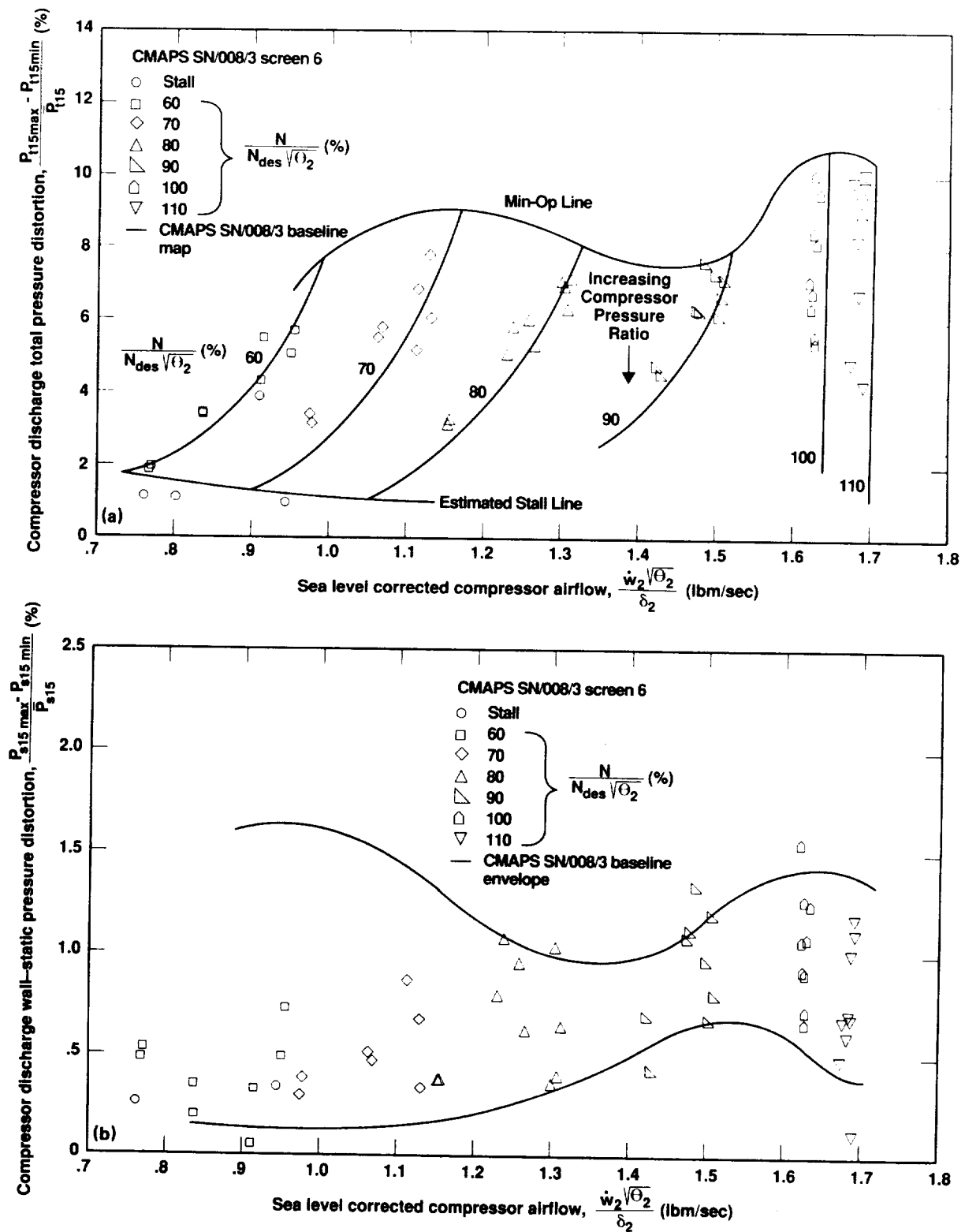


Figure 108. CMAPS SN/008/3 compressor discharge pressure distortions for screen No. 6. (a) Total pressure; (b) wall static pressure.

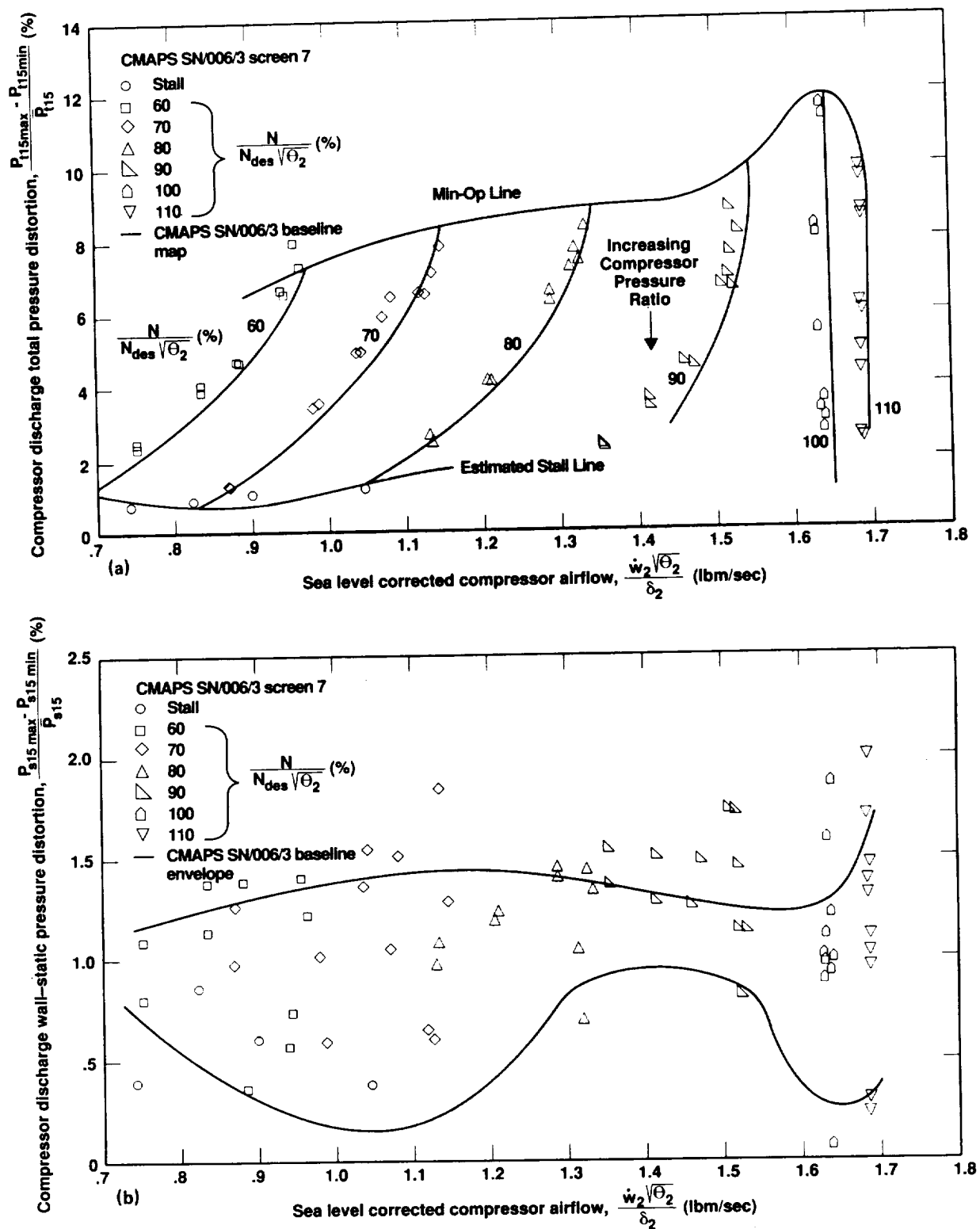


Figure 109. CMAPS SN/006/3 compressor discharge pressure distortions for screen No. 7. (a) Total pressure; (b) wall static pressure.

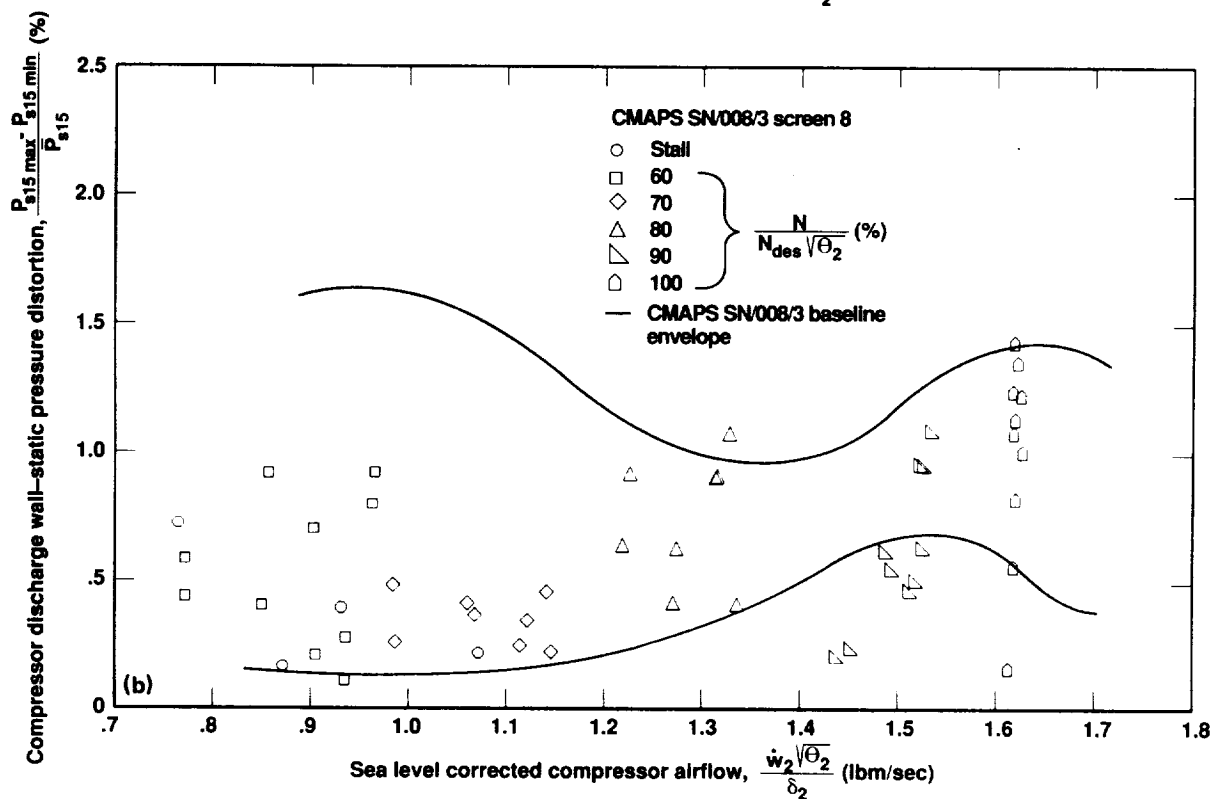
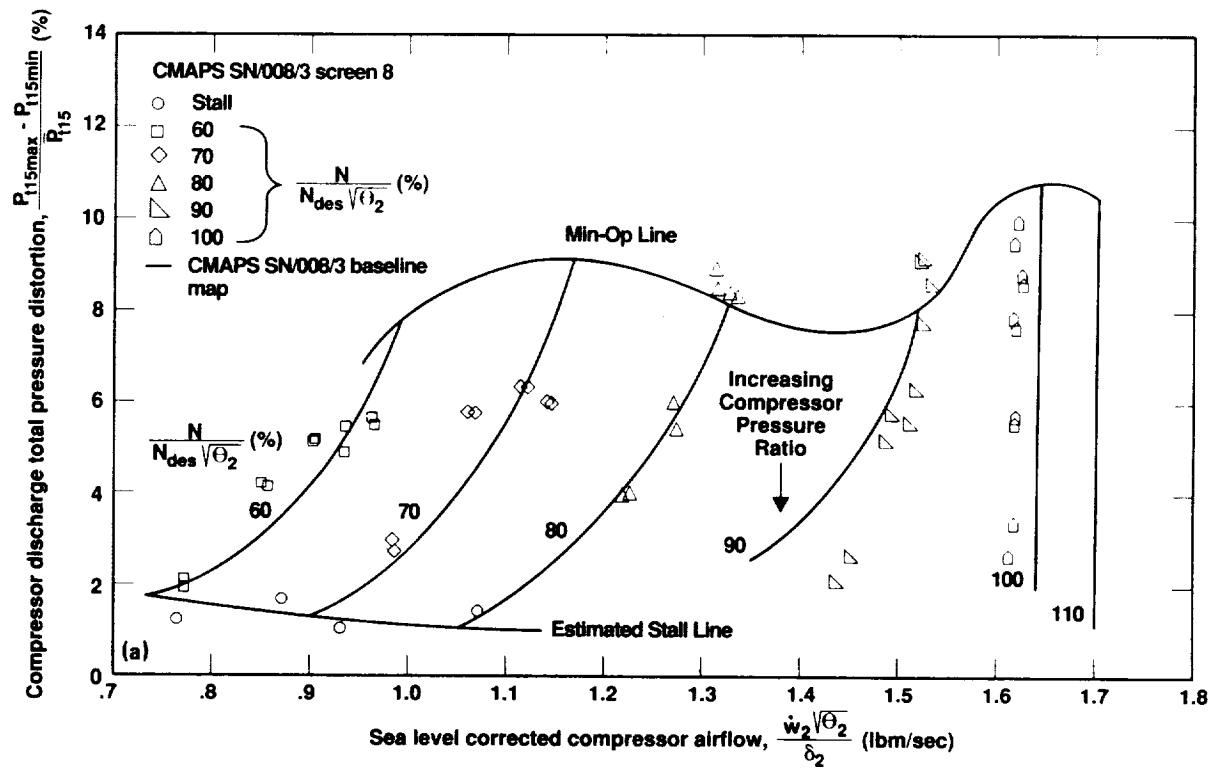


Figure 110. CMAPS SN/008/3 compressor discharge pressure distortions for screen No. 8. (a) Total pressure; (b) wall static pressure.

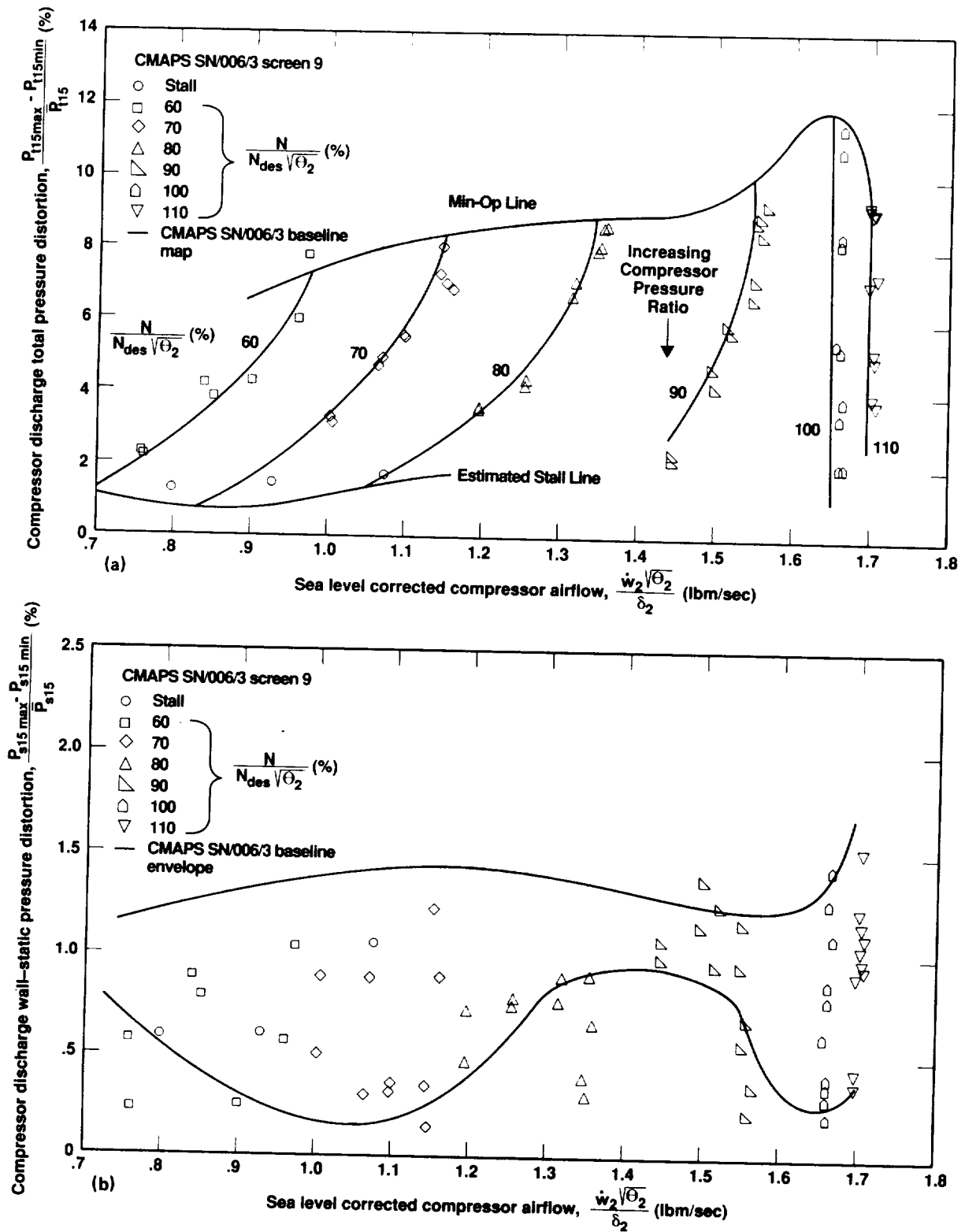


Figure 111. CMAPS SN/006/3 compressor discharge pressure distortions for screen No. 9. (a) Total pressure; (b) wall static pressure.

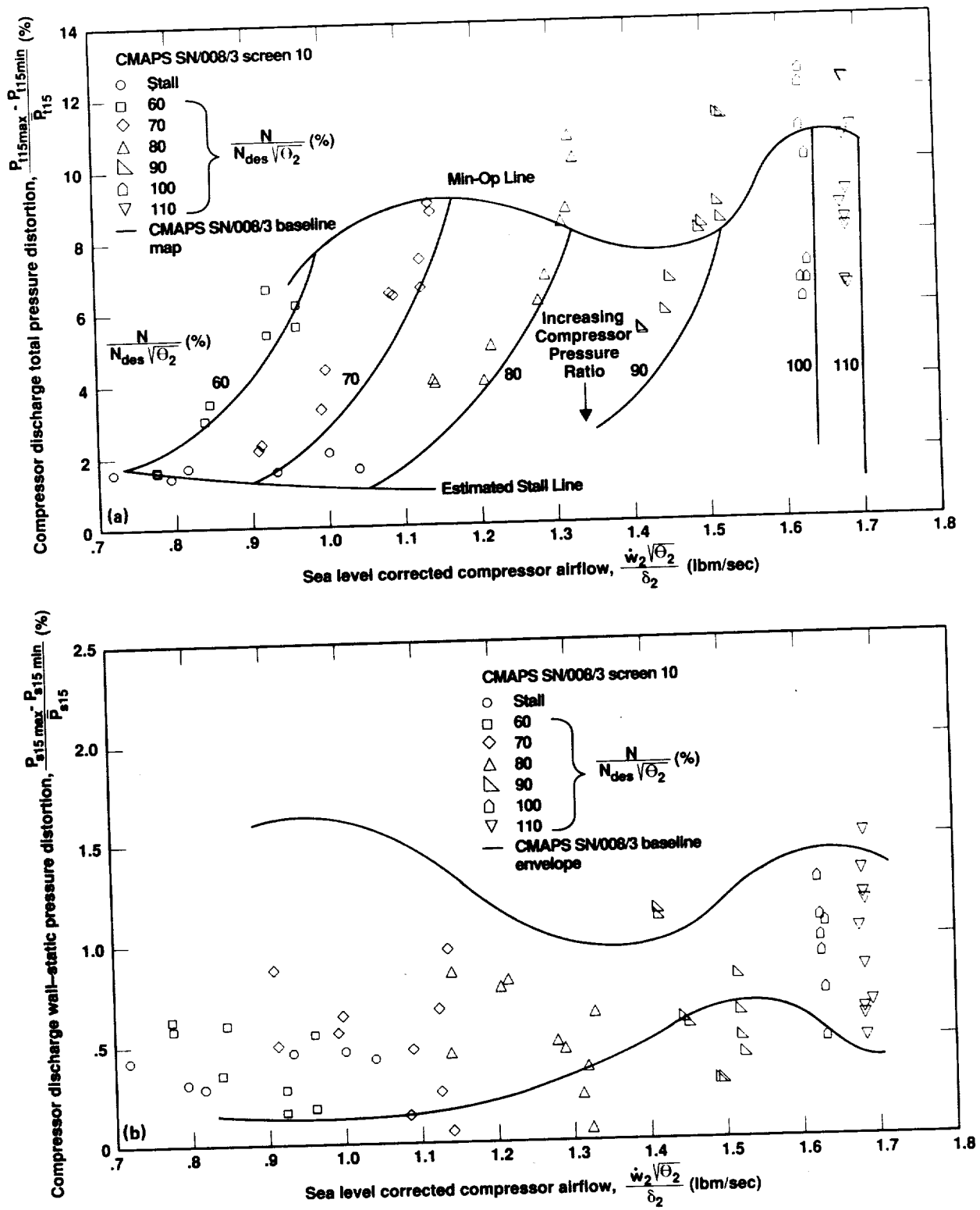


Figure 112. CMAPS SN/008/3 compressor discharge pressure distortions for screen No. 10. (a) Total pressure; (b) wall static pressure.

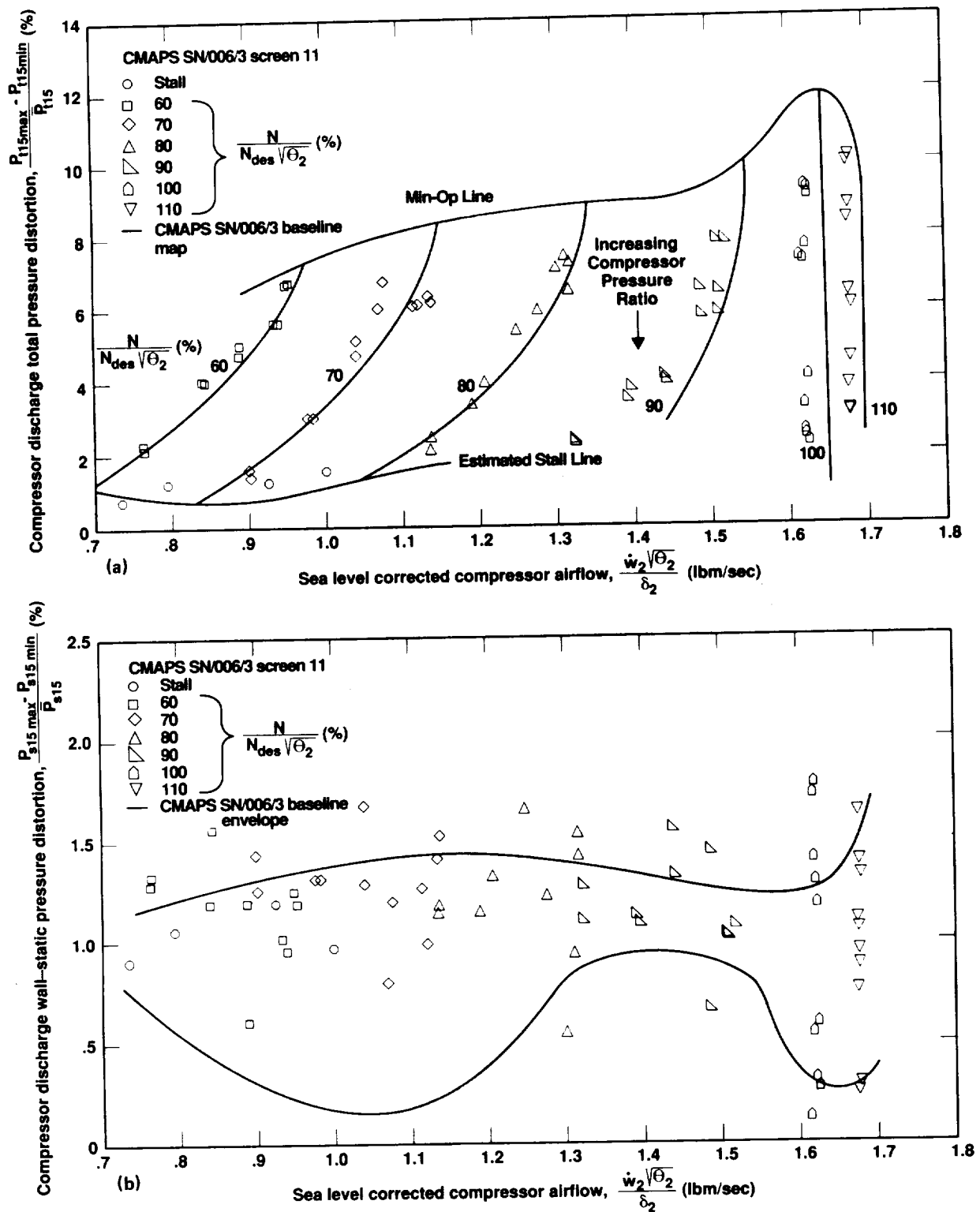


Figure 113. CMAPS SN/006/3 compressor discharge pressure distortions for screen No. 11. (a) Total pressure; (b) wall static pressure.

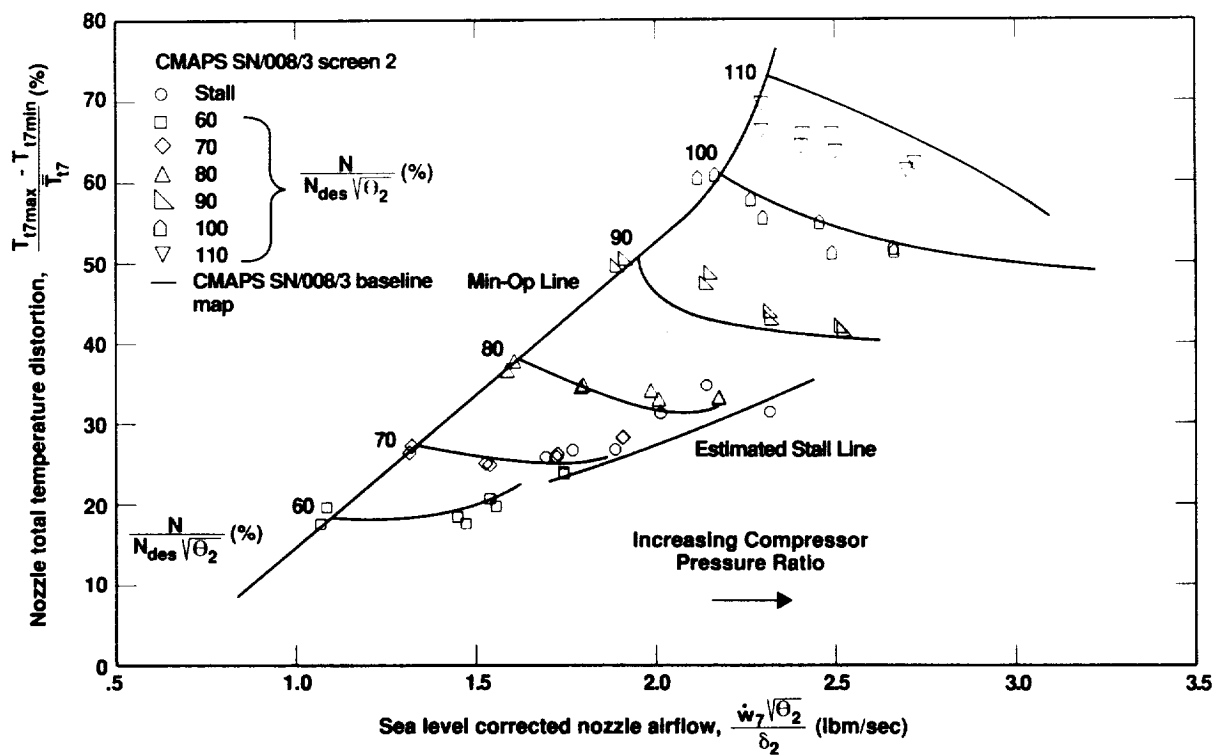


Figure 114. CMAPS SN/008/3 nozzle entrance total temperature distortion for screen No. 2.

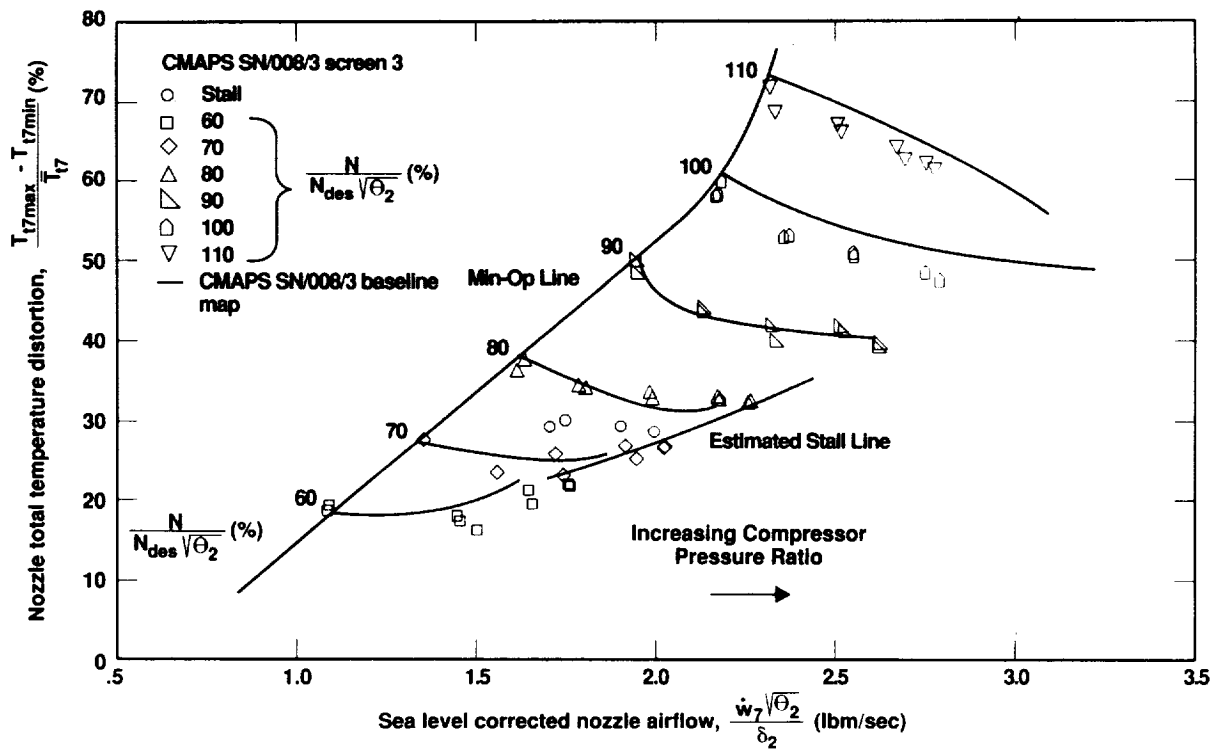


Figure 115. CMAPS SN/008/3 nozzle entrance total temperature distortion for screen No. 3.

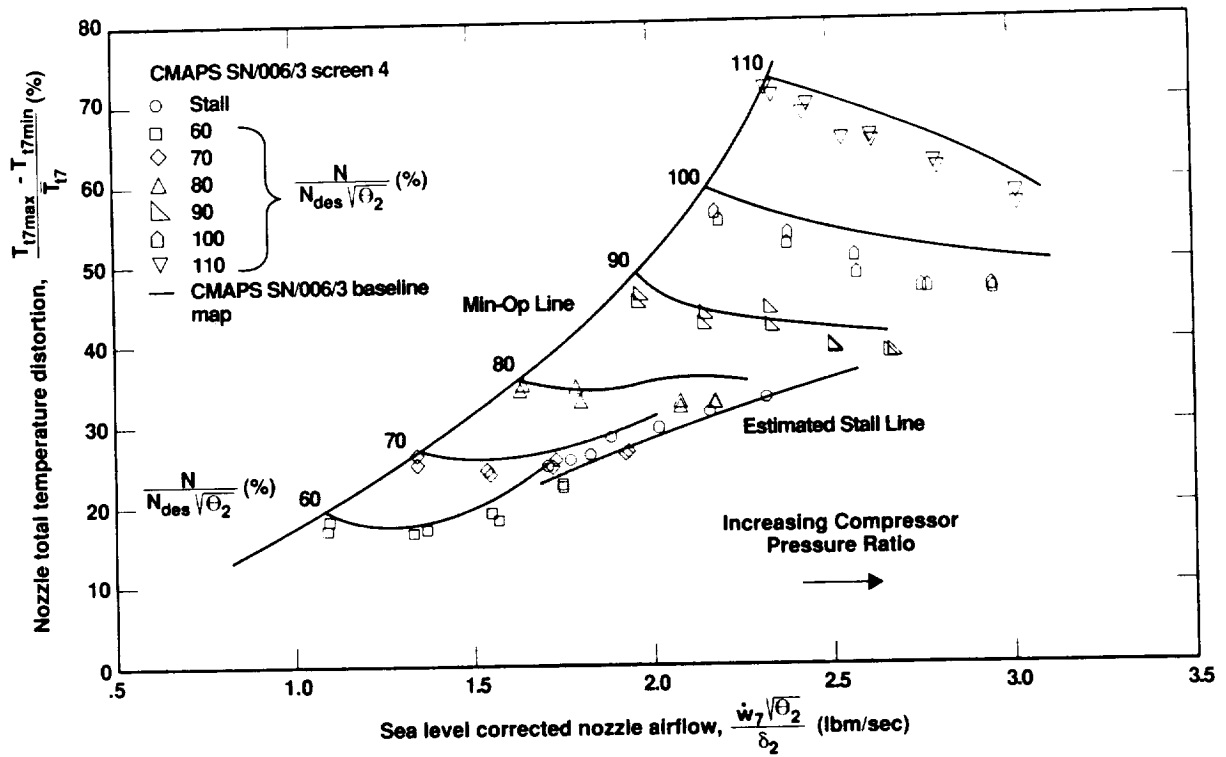


Figure 116. CMAPS SN/006/3 nozzle entrance total temperature distortion for screen No. 4.

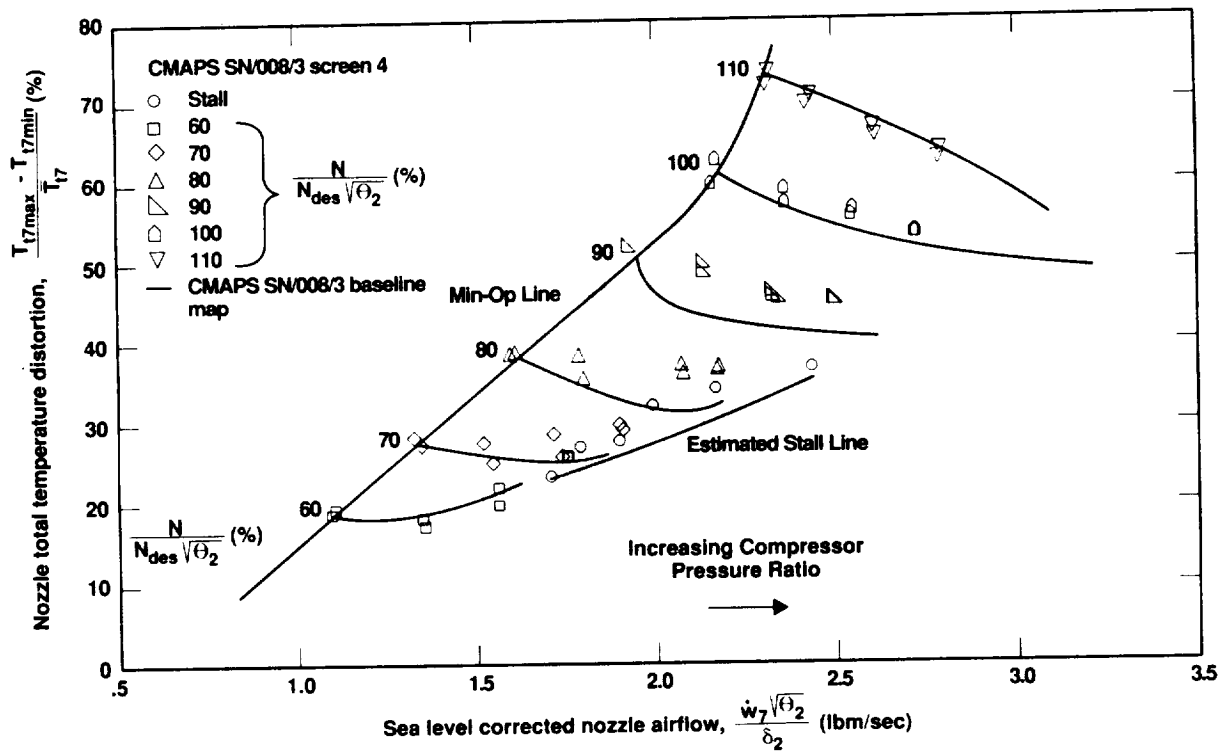


Figure 117. CMAPS SN/008/3 nozzle entrance total temperature distortion for screen No. 4.

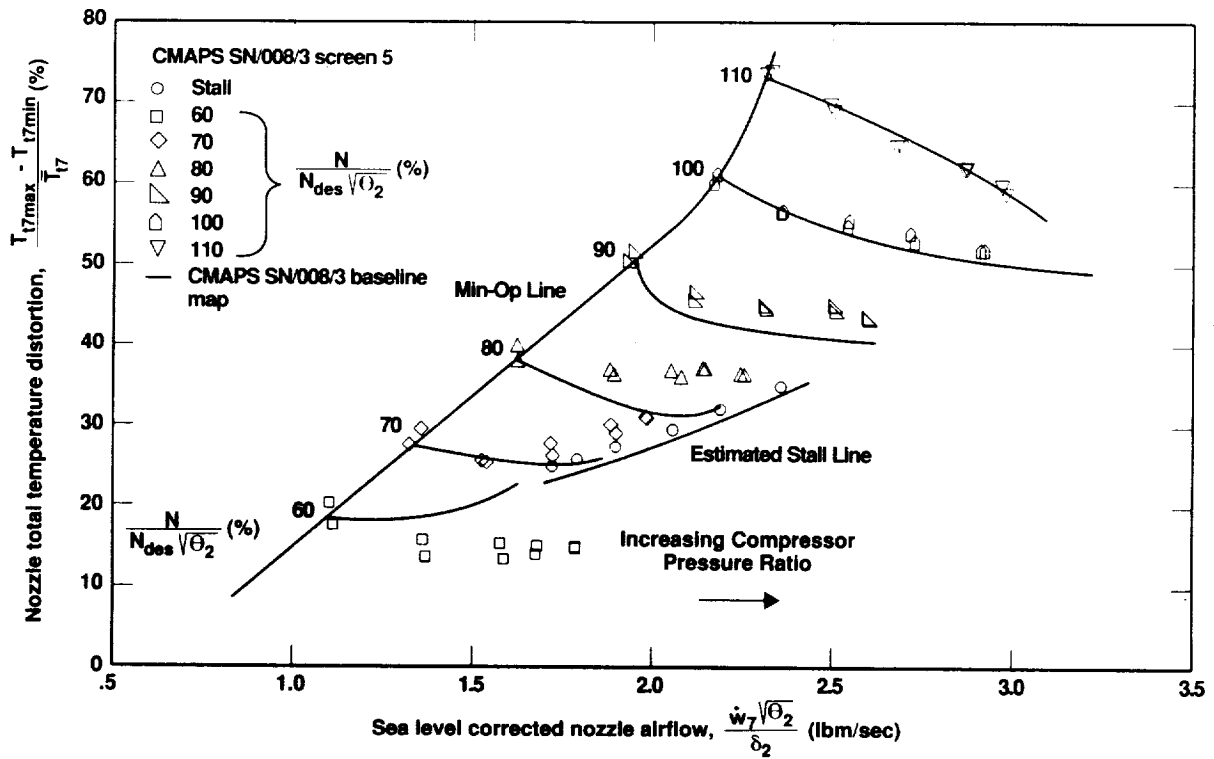


Figure 118. CMAPS SN/008/3 nozzle entrance total temperature distortion for screen No. 5.

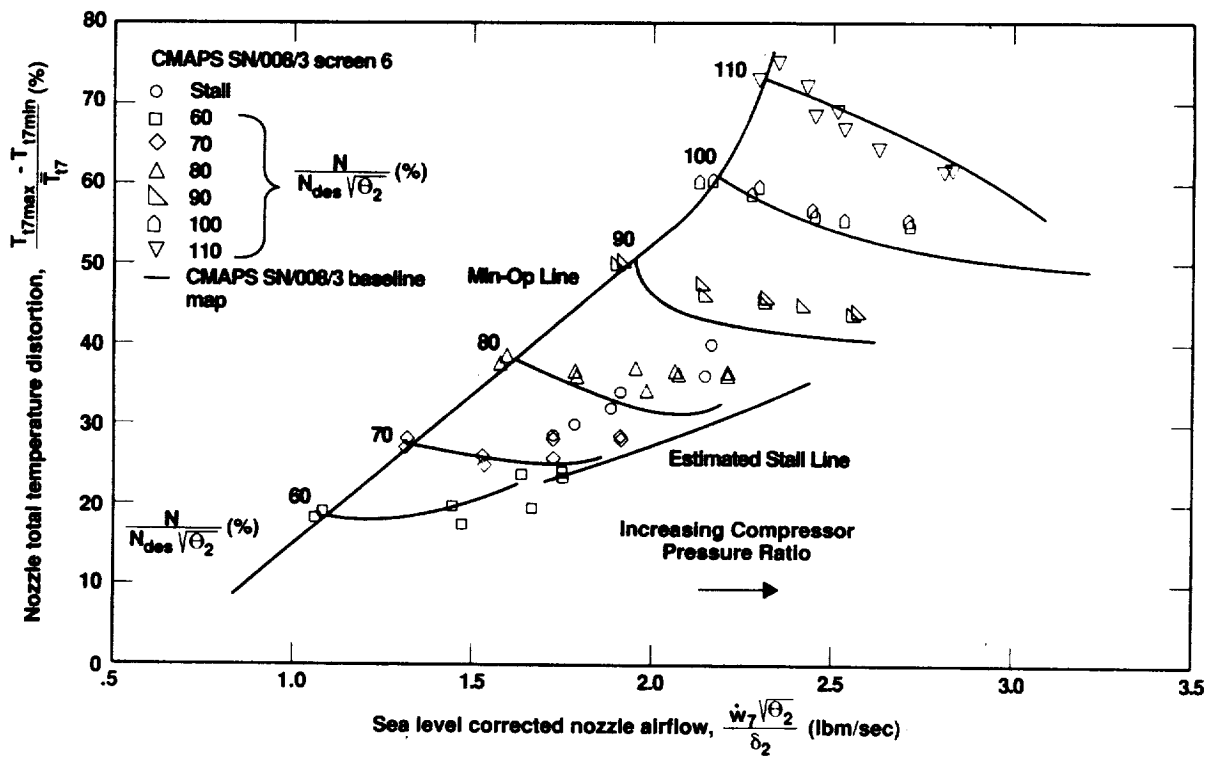


Figure 119. CMAPS SN/008/3 nozzle entrance total temperature distortion for screen No. 6.

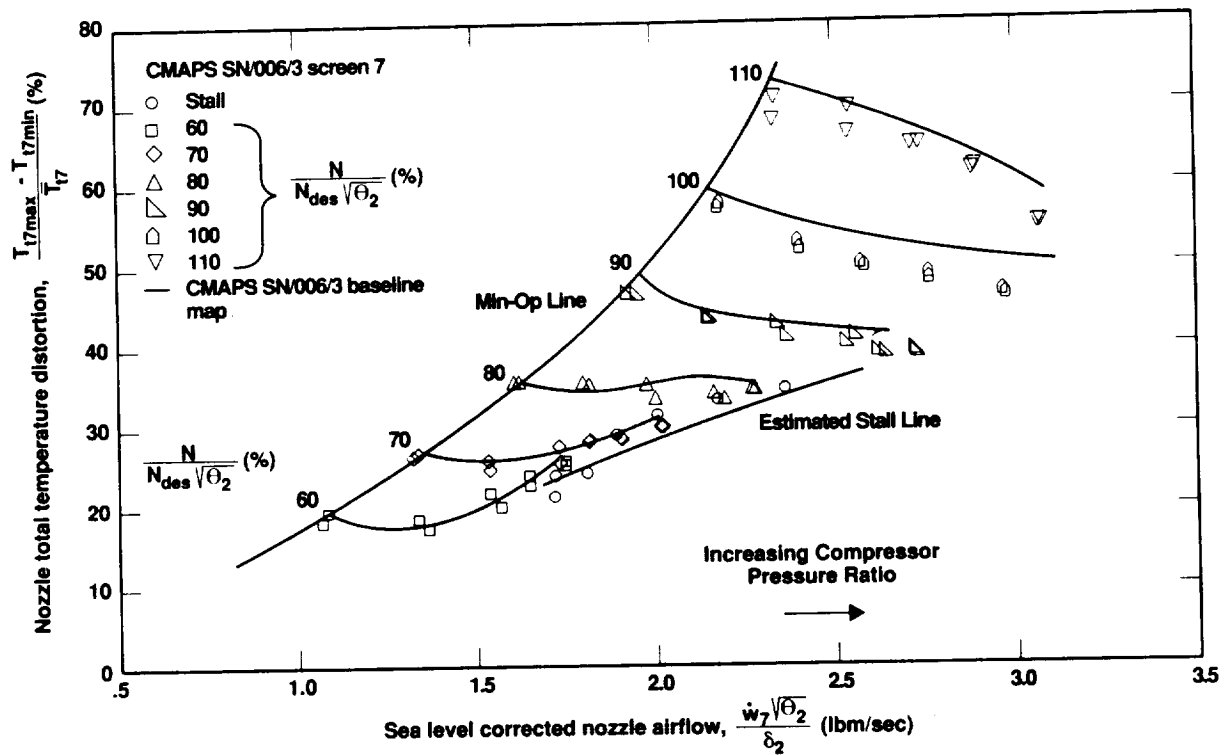


Figure 120. CMAPS SN/006/3 nozzle entrance total temperature distortion for screen No. 7.

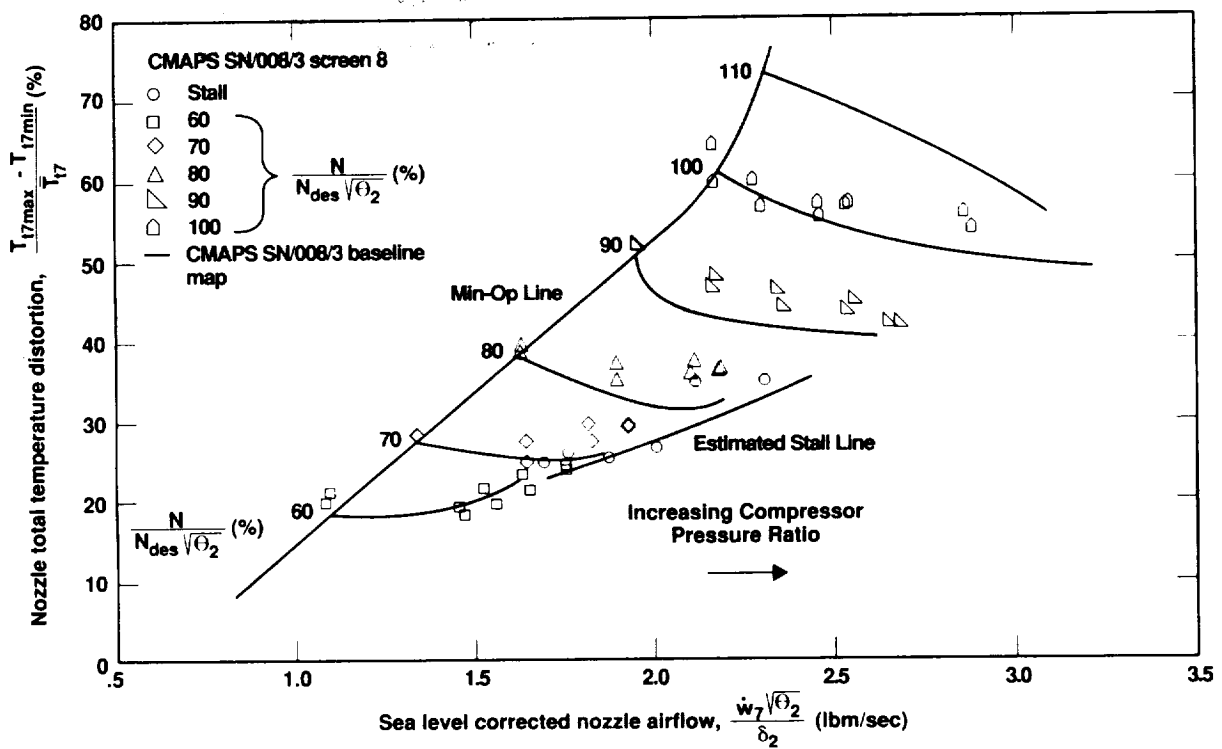


Figure 121. CMAPS SN/008/3 nozzle entrance total temperature distortion for screen No. 8.

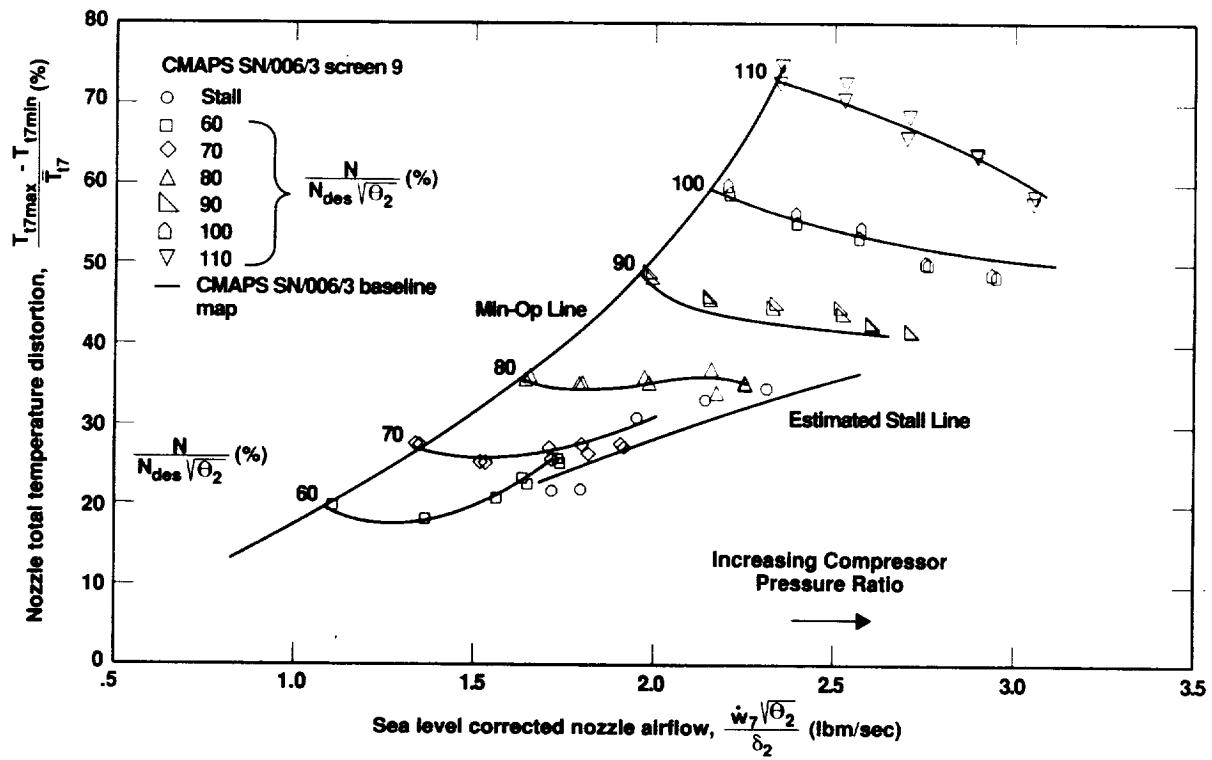


Figure 122. CMAPS SN/006/3 nozzle entrance total temperature distortion for screen No. 9.

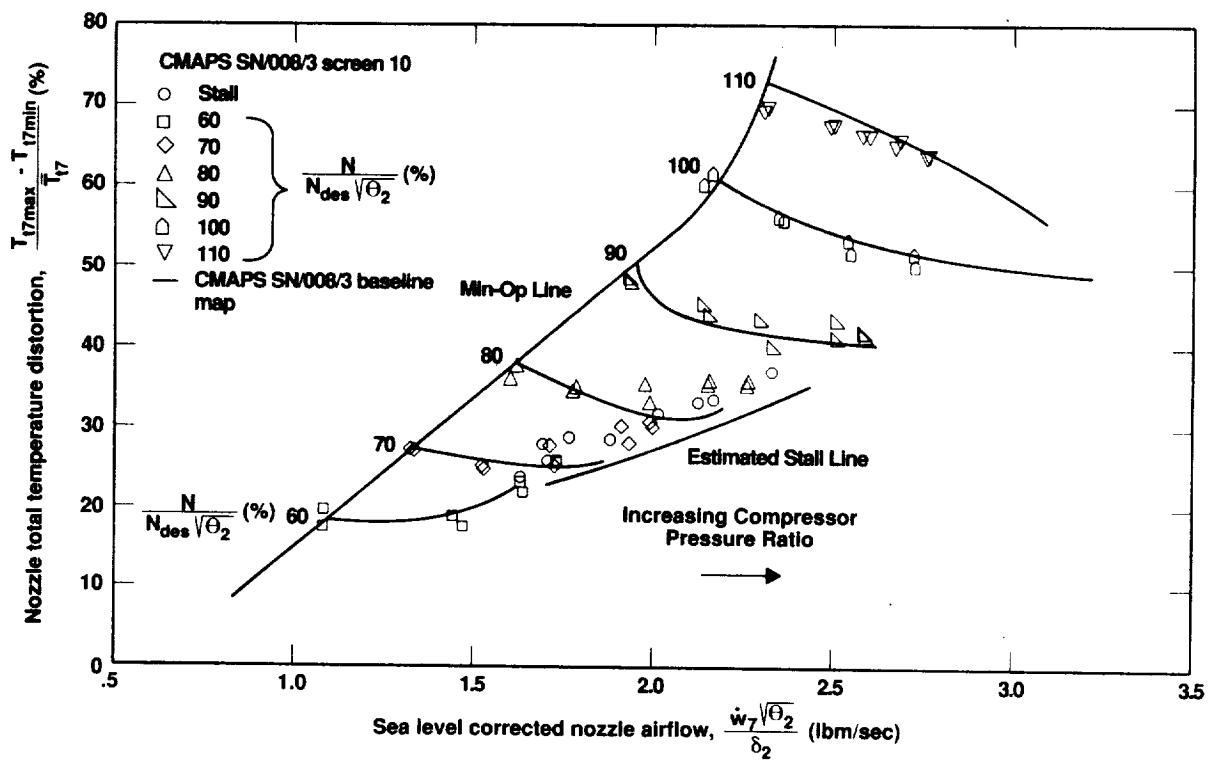


Figure 123. CMAPS SN/008/3 nozzle entrance total temperature distortion for screen No. 10.

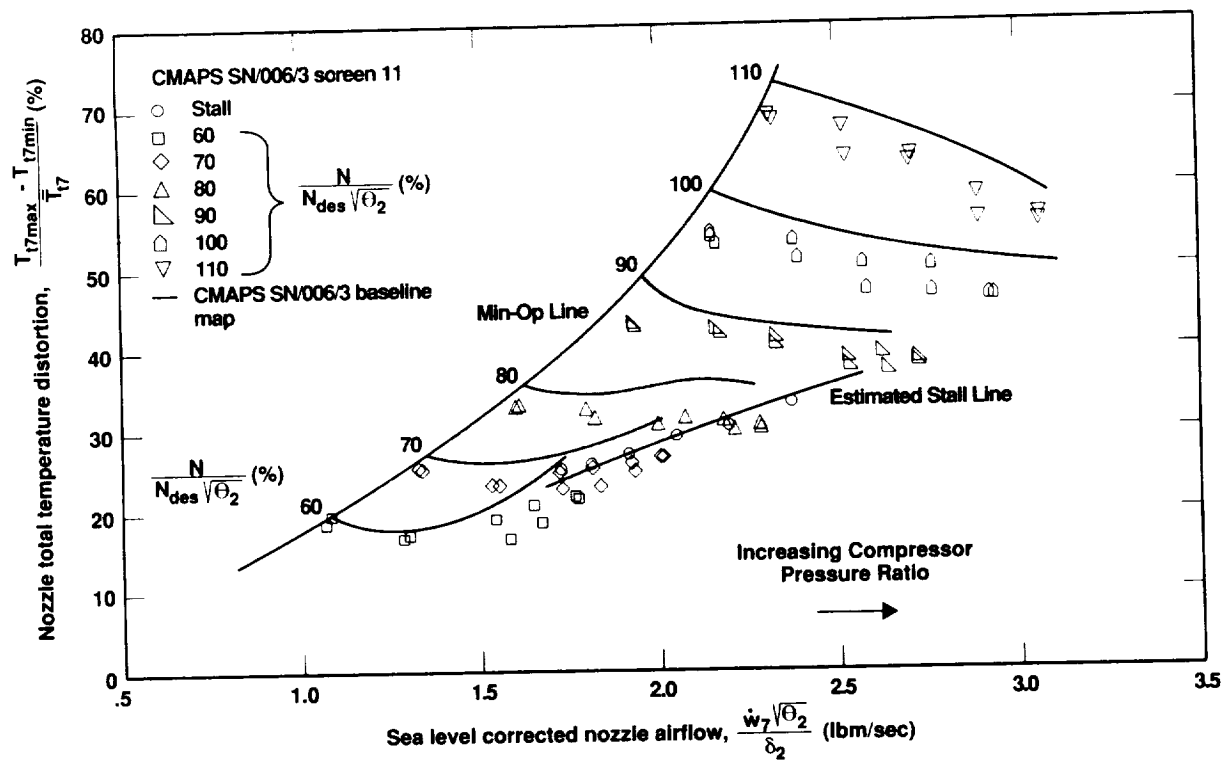


Figure 124. CMAPS SN/006/3 nozzle entrance total temperature distortion for screen No. 11.

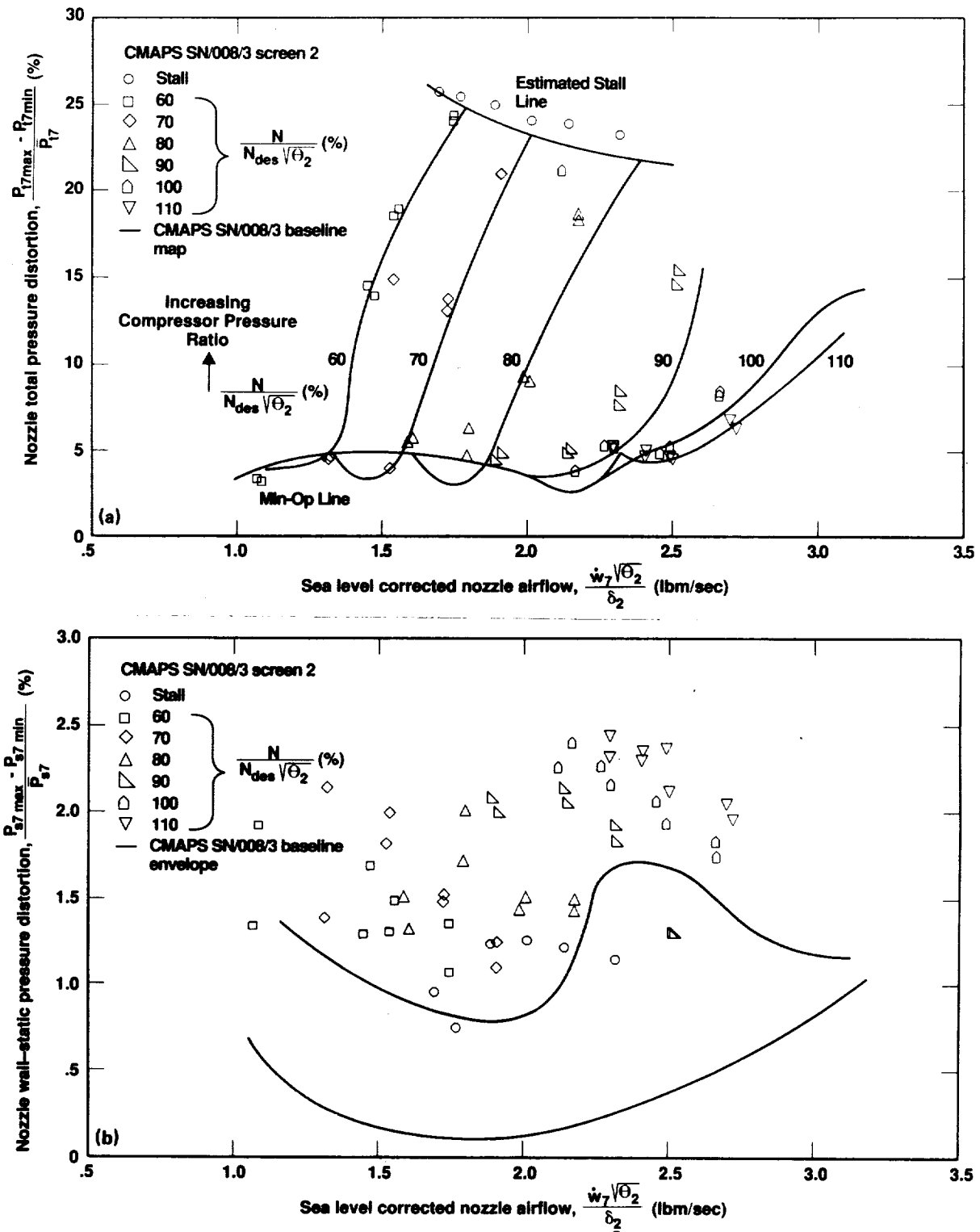


Figure 125. CMAPS SN/008/3 nozzle entrance pressure distortions for screen No. 2. (a) Total pressure; (b) wall static pressure.

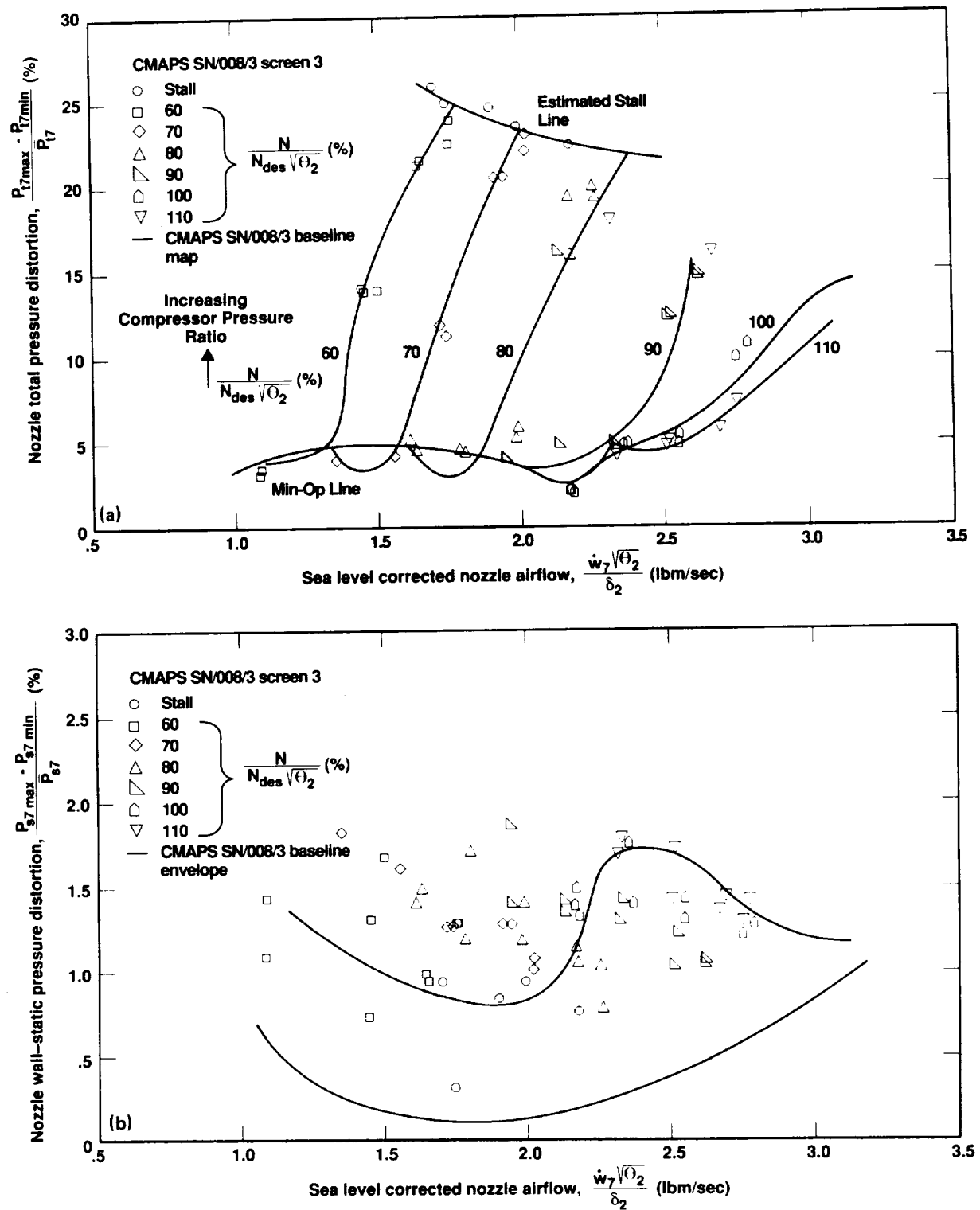


Figure 126. CMAPS SN/008/3 nozzle entrance pressure distortions for screen No. 3. (a) Total pressure; (b) wall static pressure.

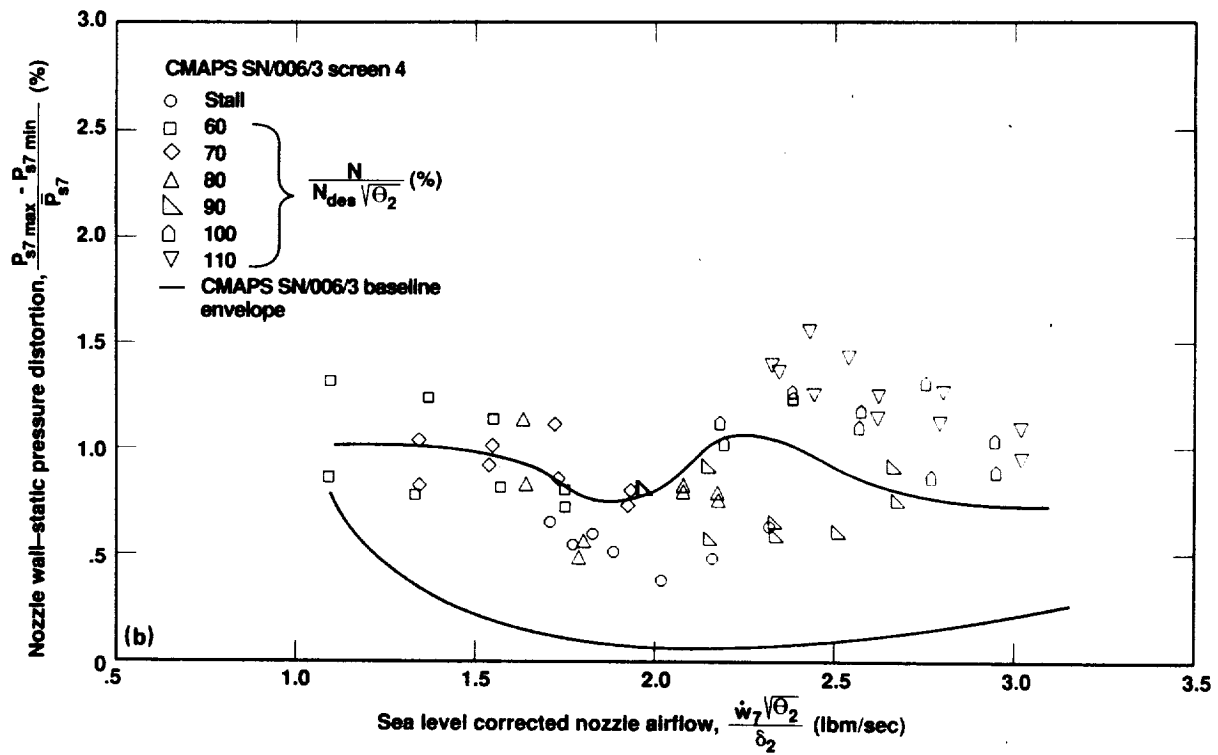
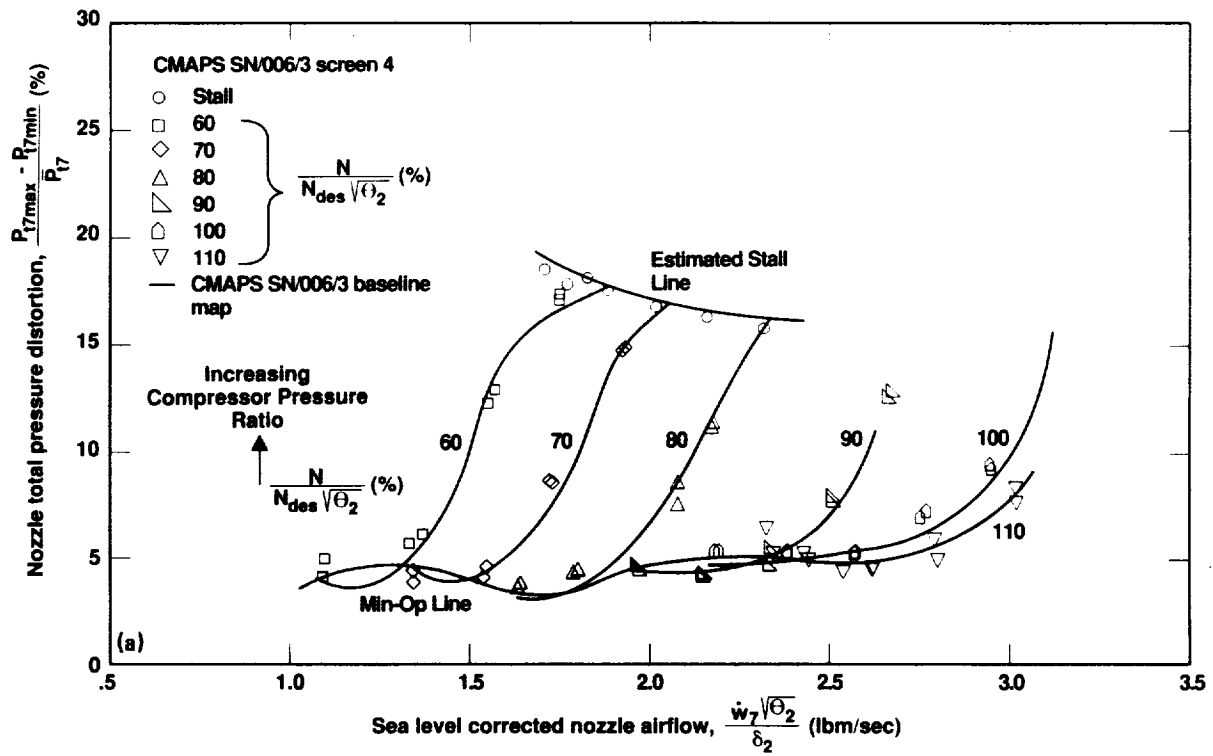


Figure 127. CMAPS SN/006/3 nozzle entrance pressure distortions for screen No. 4. (a) Total pressure; (b) wall static pressure.

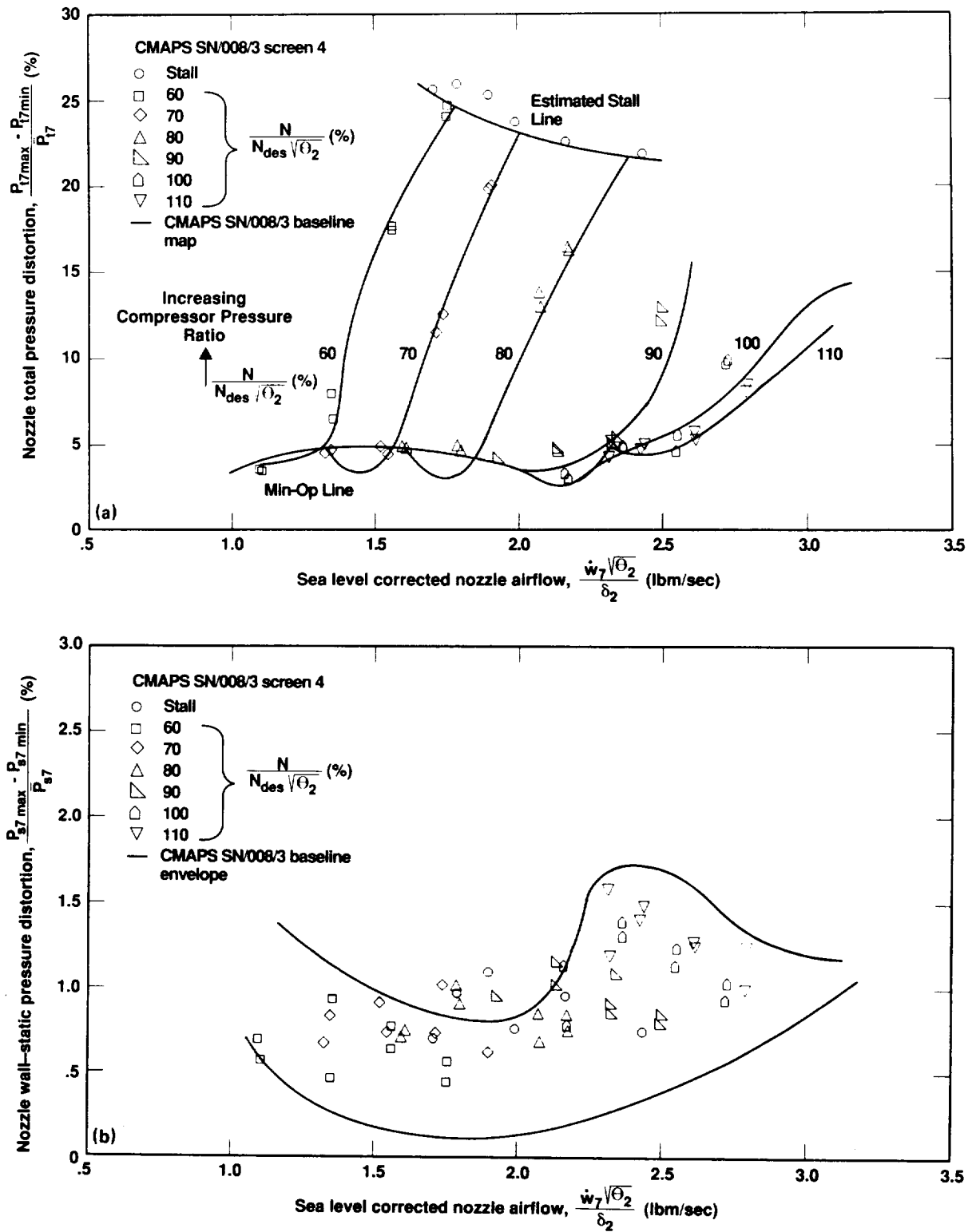


Figure 128. CMAPS SN/008/3 nozzle entrance pressure distortions for screen No. 4. (a) Total pressure; (b) wall static pressure.

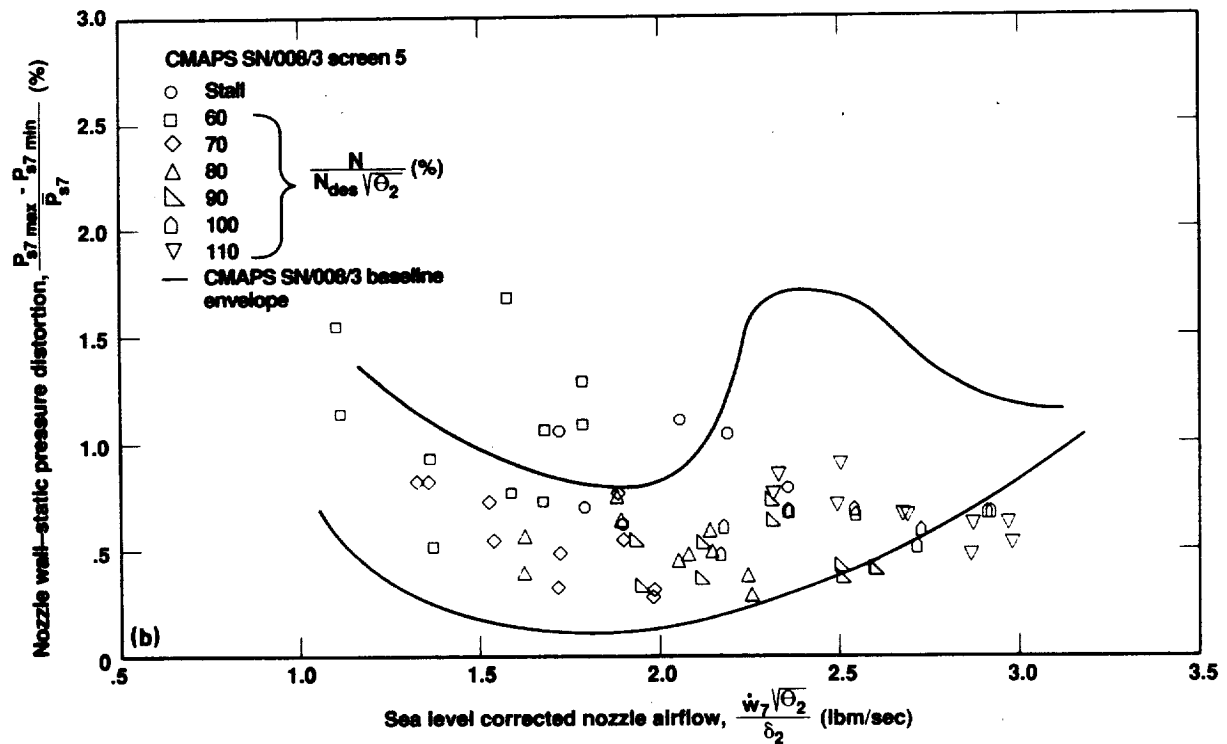
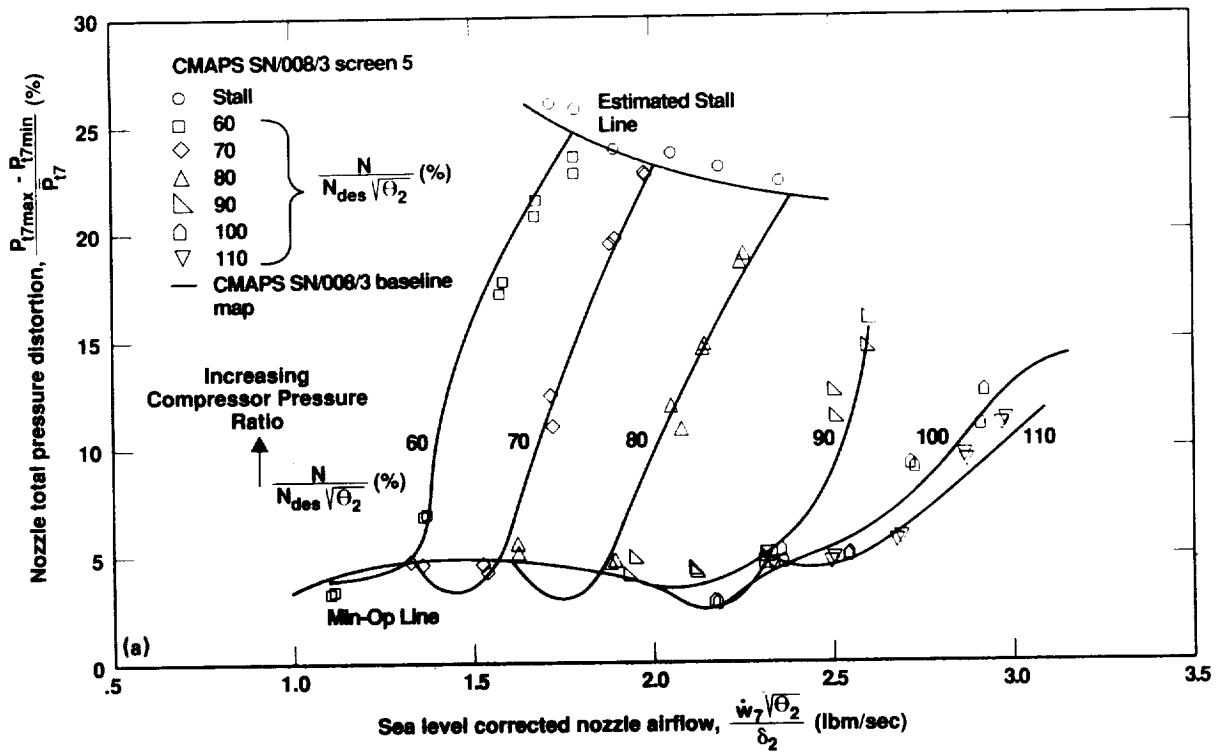


Figure 129. CMAPS SN/008/3 nozzle entrance pressure distortions for screen No. 5. (a) Total pressure; (b) wall static pressure.

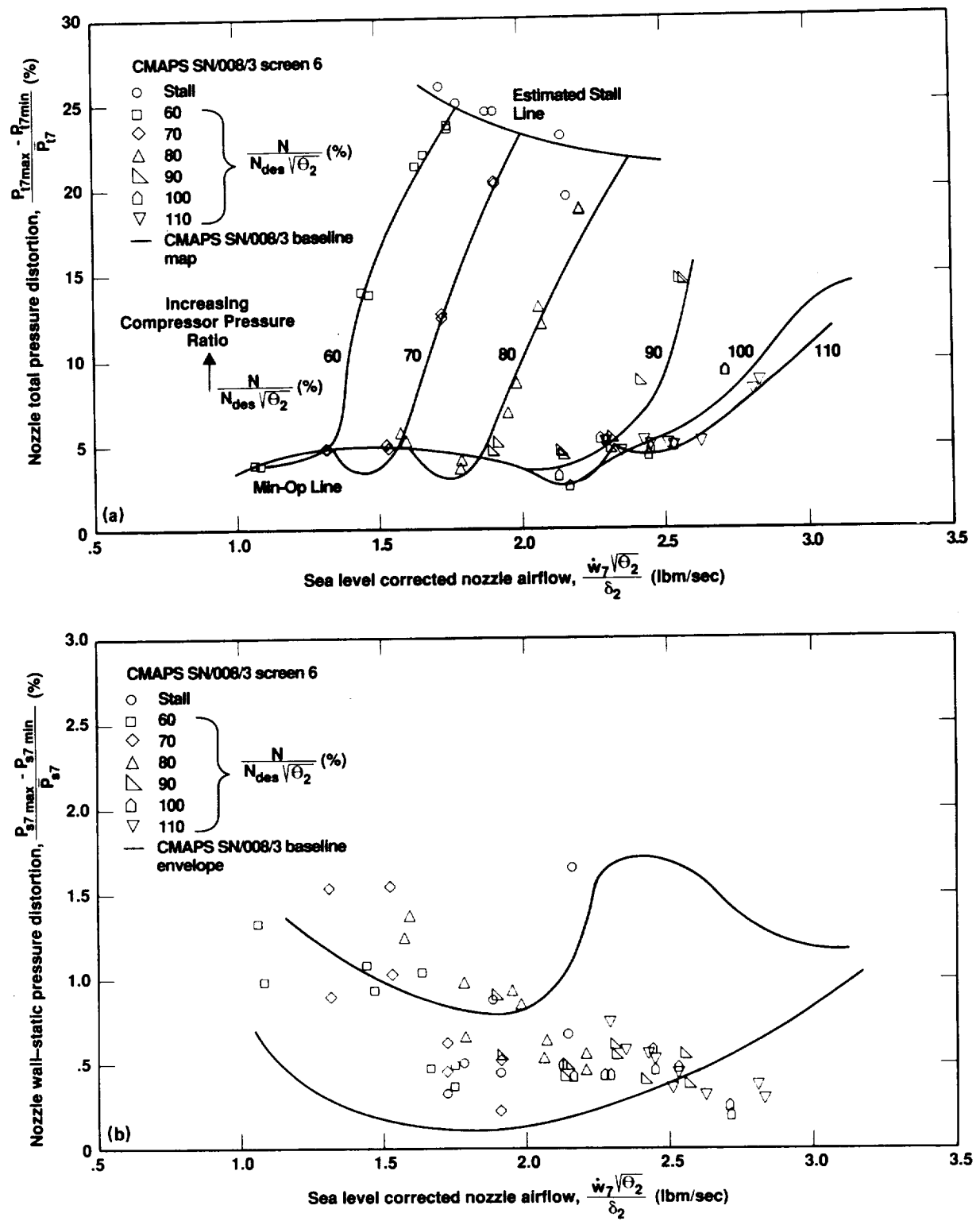


Figure 130. CMAPS SN/008/3 nozzle entrance pressure distortions for screen No. 6. (a) Total pressure; (b) wall static pressure.

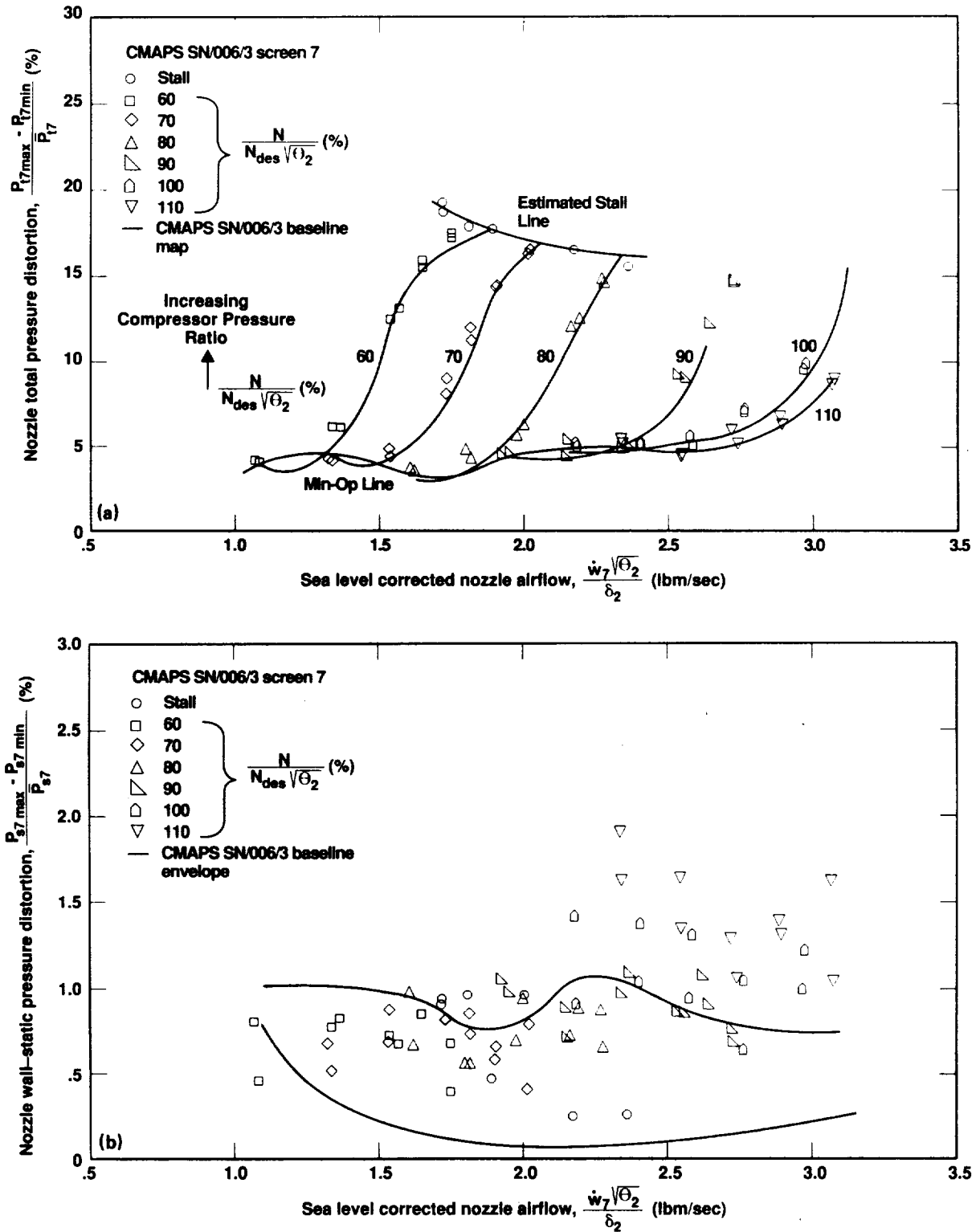


Figure 131. CMAPS SN/006/3 nozzle entrance pressure distortions for screen No. 7. (a) Total pressure; (b) wall static pressure.

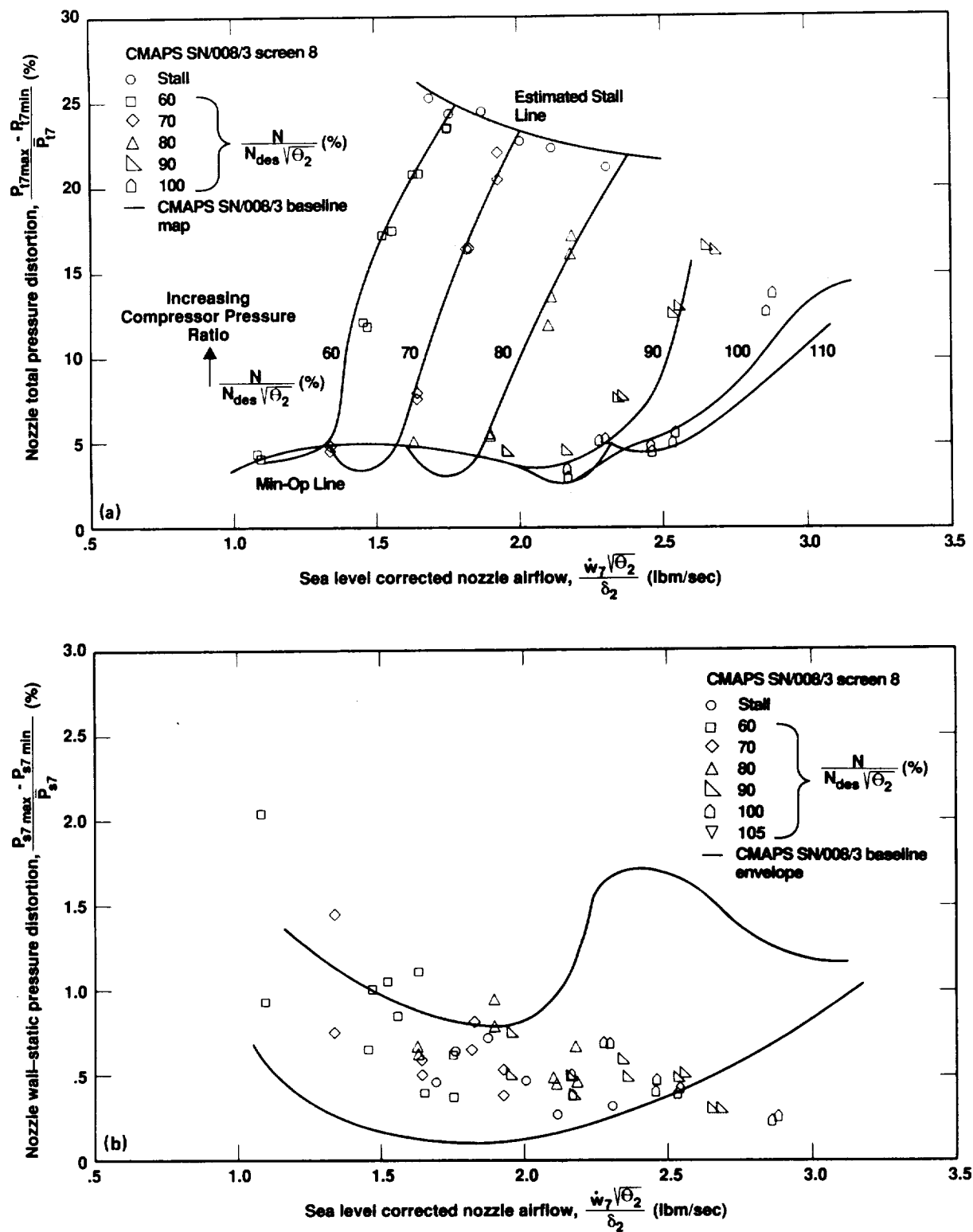


Figure 132. CMAPS SN/008/3 nozzle entrance pressure distortions for screen No. 8. (a) Total pressure; (b) wall static pressure.

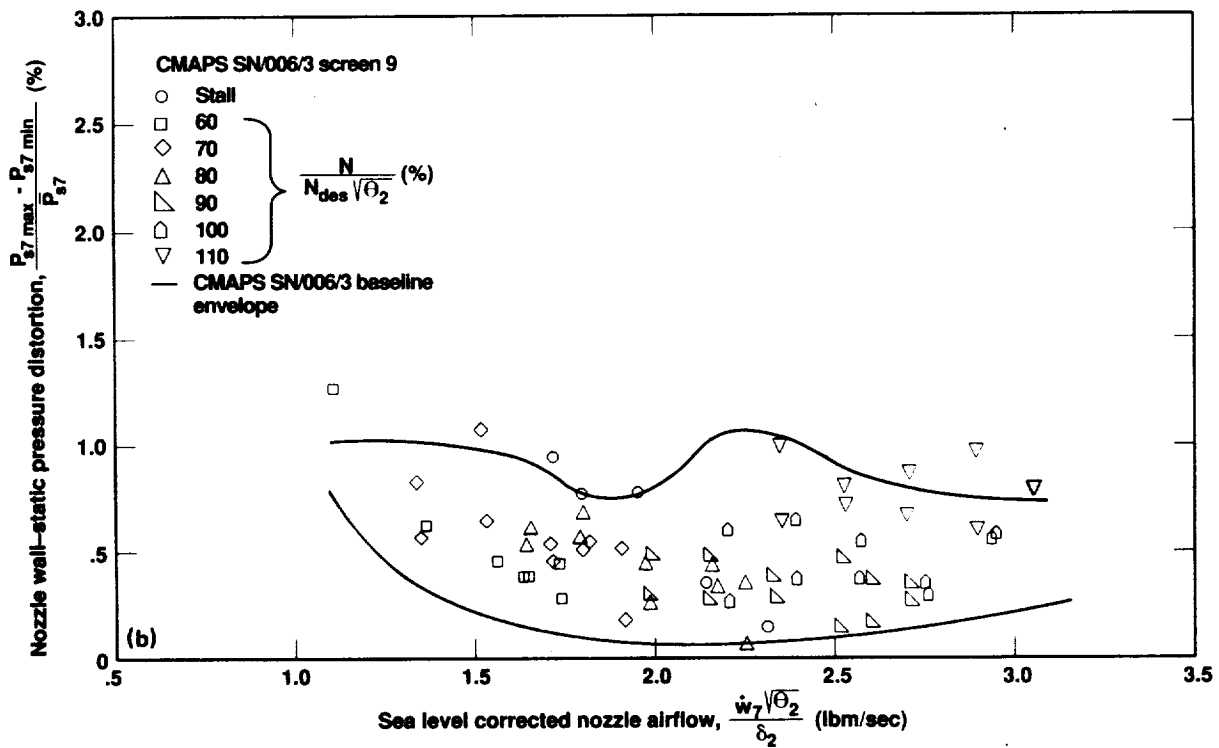
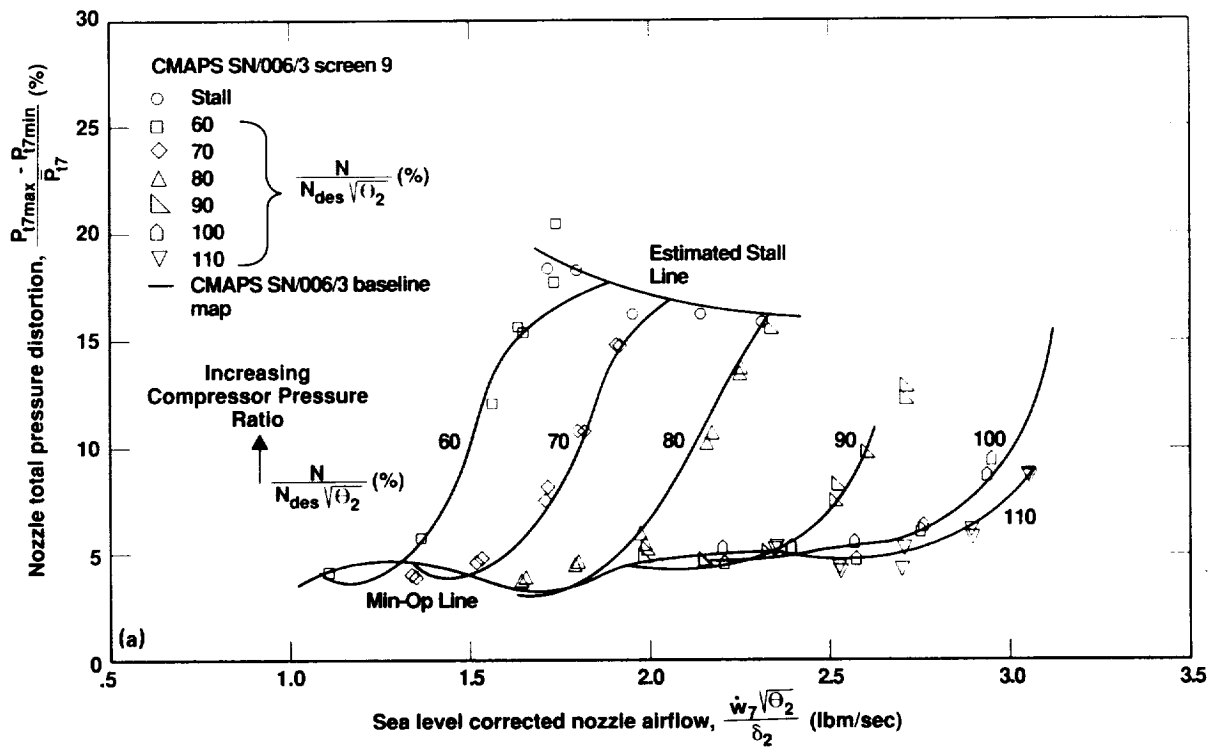


Figure 133. CMAPS SN/006/3 nozzle entrance pressure distortions for screen No. 9. (a) Total pressure; (b) wall static pressure.

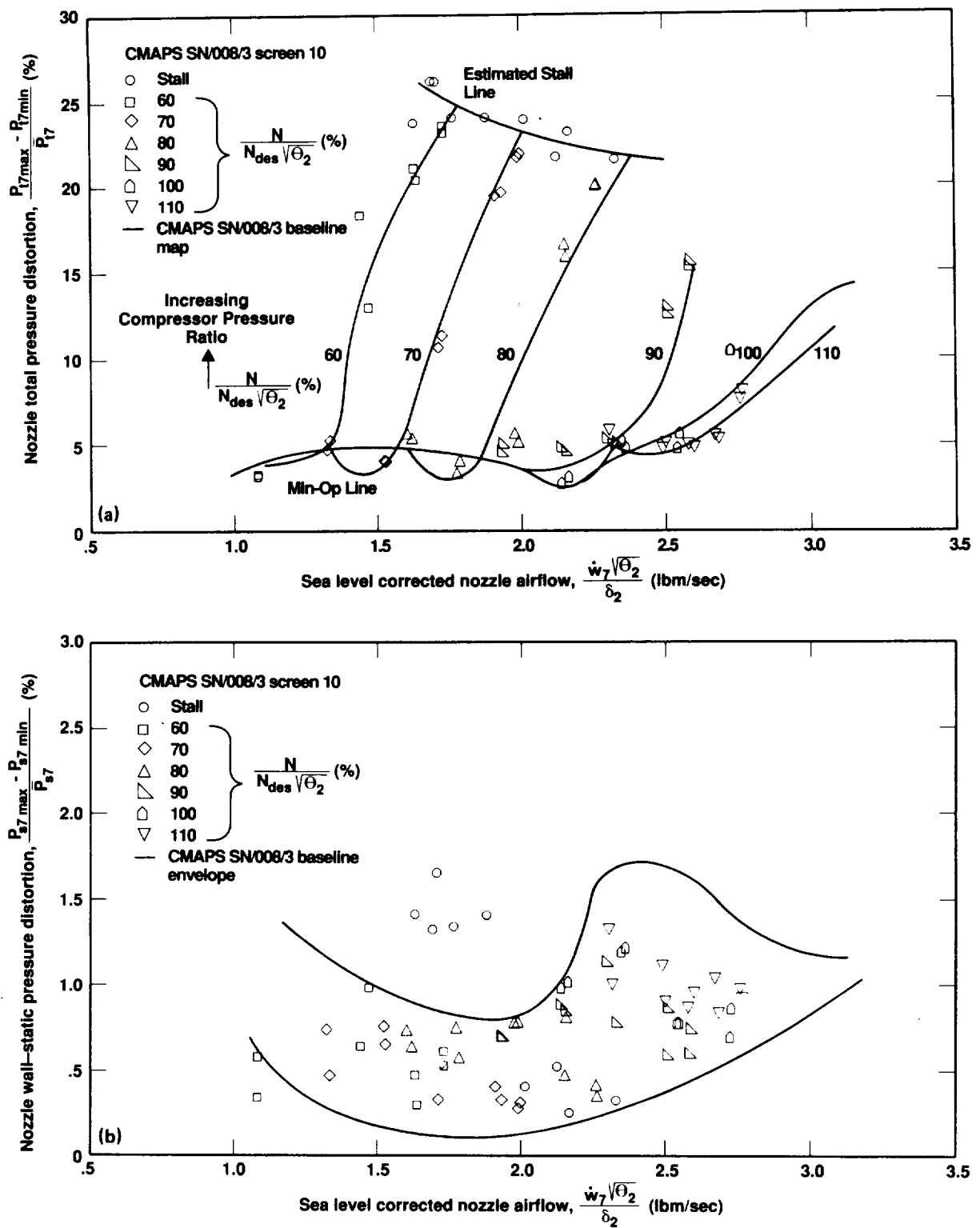


Figure 134. CMAPS SN/008/3 nozzle entrance pressure distortions for screen No. 10. (a) Total pressure; (b) wall static pressure.

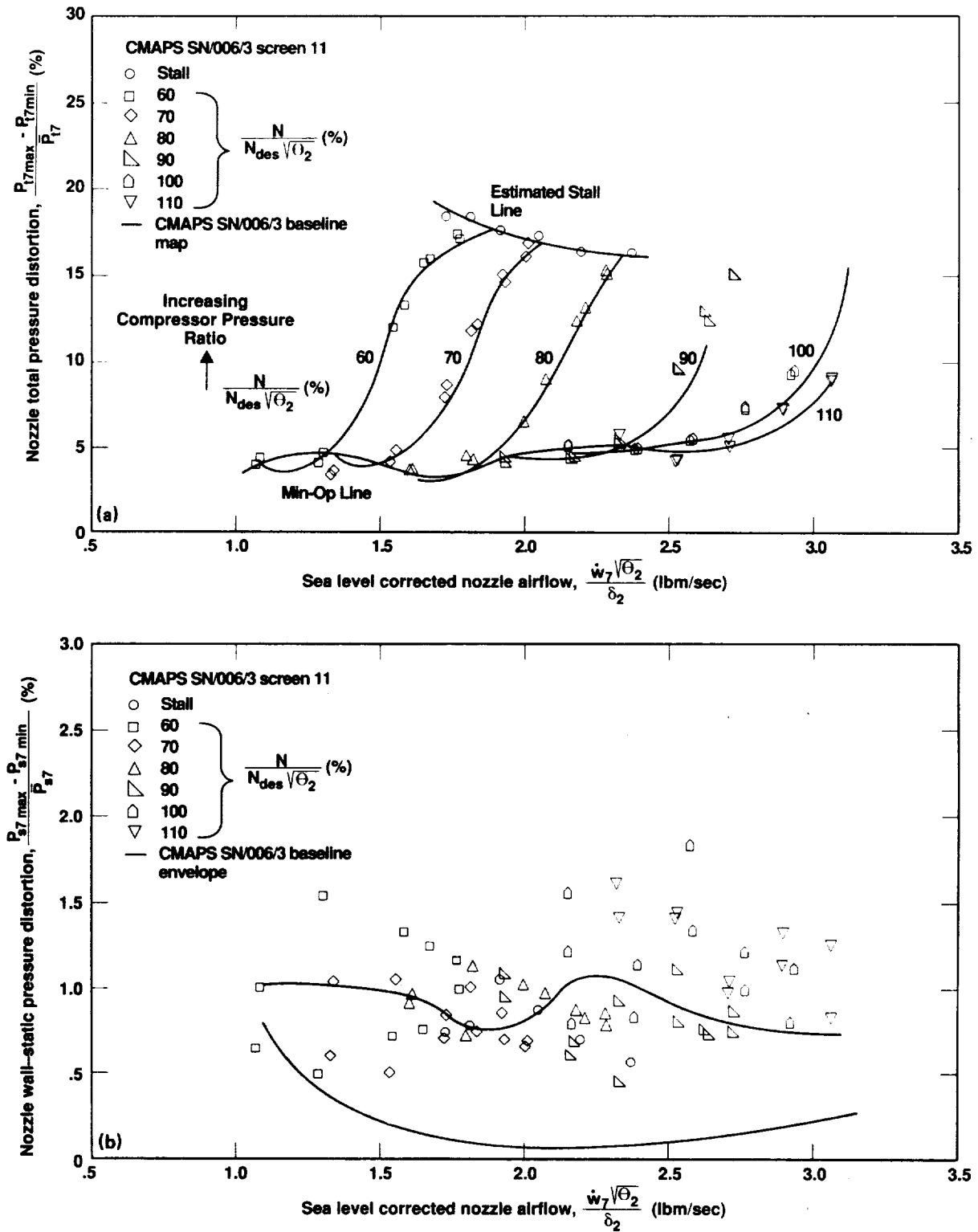


Figure 135. CMAPS SN/006/3 nozzle entrance pressure distortions for screen No. 11. (a) Total pressure; (b) wall static pressure.

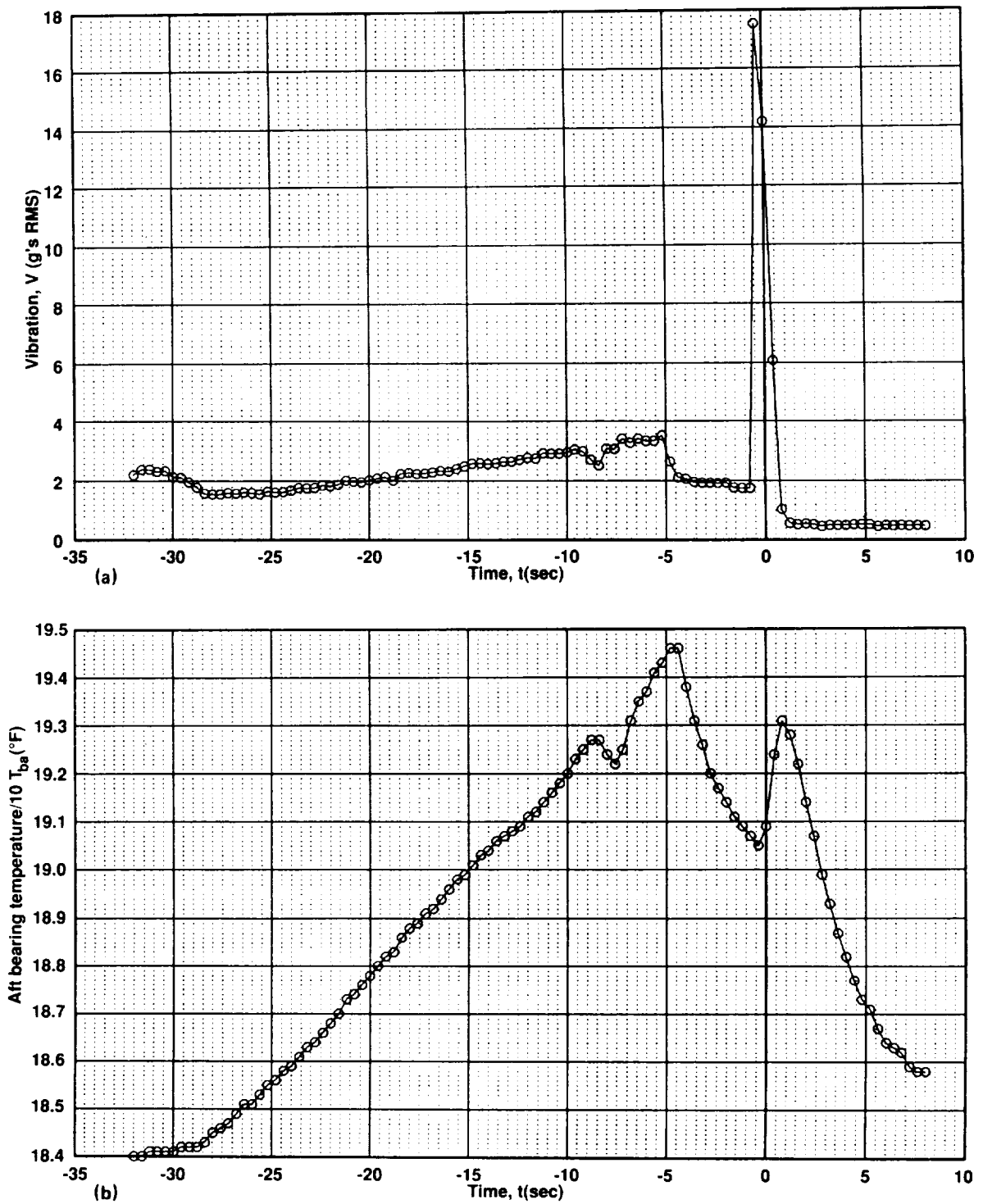


Figure 136. Time-histories during CMAPS SN/008/3 malfunction. (a) Vibration; (b) aft bearing temperature.

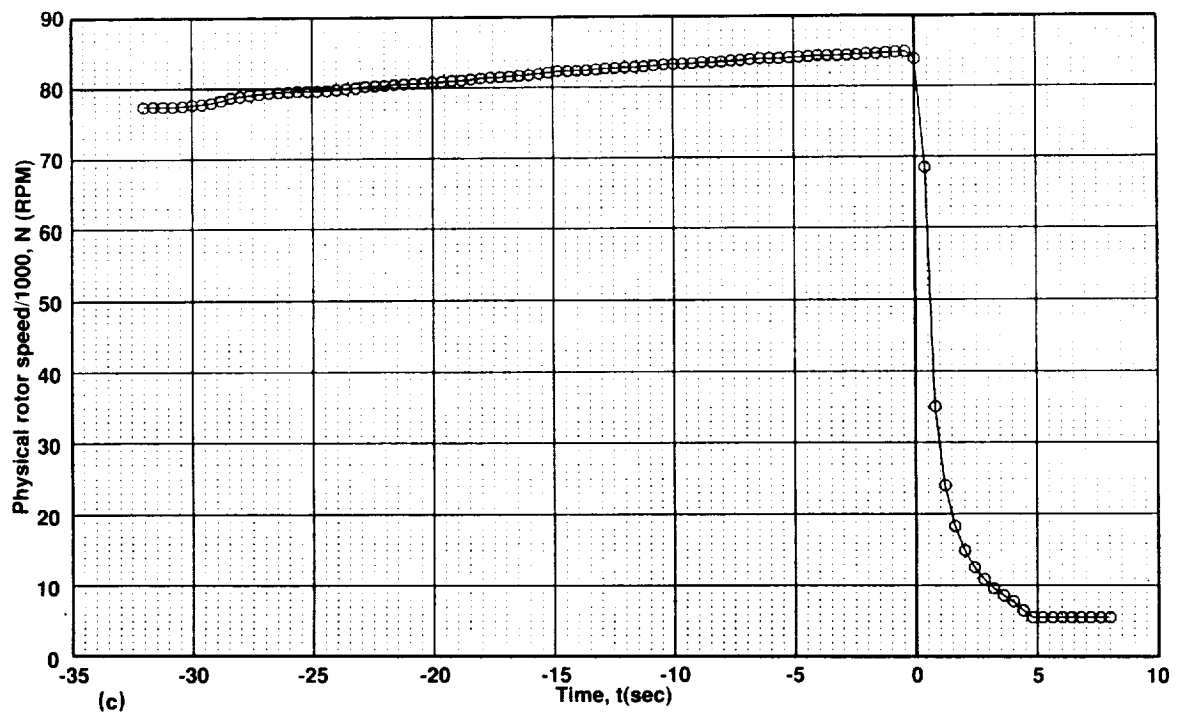
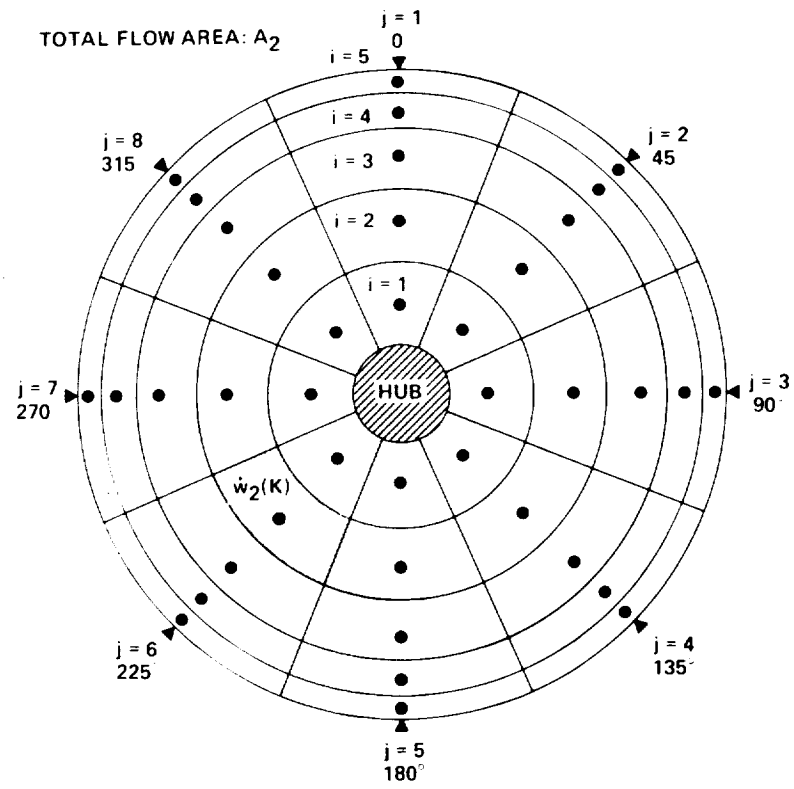


Figure 136. Concluded. (c) Rotor speed.



Kth FLOW ELEMENT, $\dot{w}_2(K)$,
WITH AREA, $A_2(K) = A_2/40$

$$\text{COMPRESSOR AIRFLOW, } \dot{w}_{2, \text{sum}} = \sum_{K=1}^{40} \dot{w}_2(K)$$

i = RADIAL INDEX
j = CIRCUMFERENTIAL INDEX
● TOTAL PRESSURE
▲ WALL-STATIC PRESSURE

Figure 137. Plane 2 area-weighted flow elements.

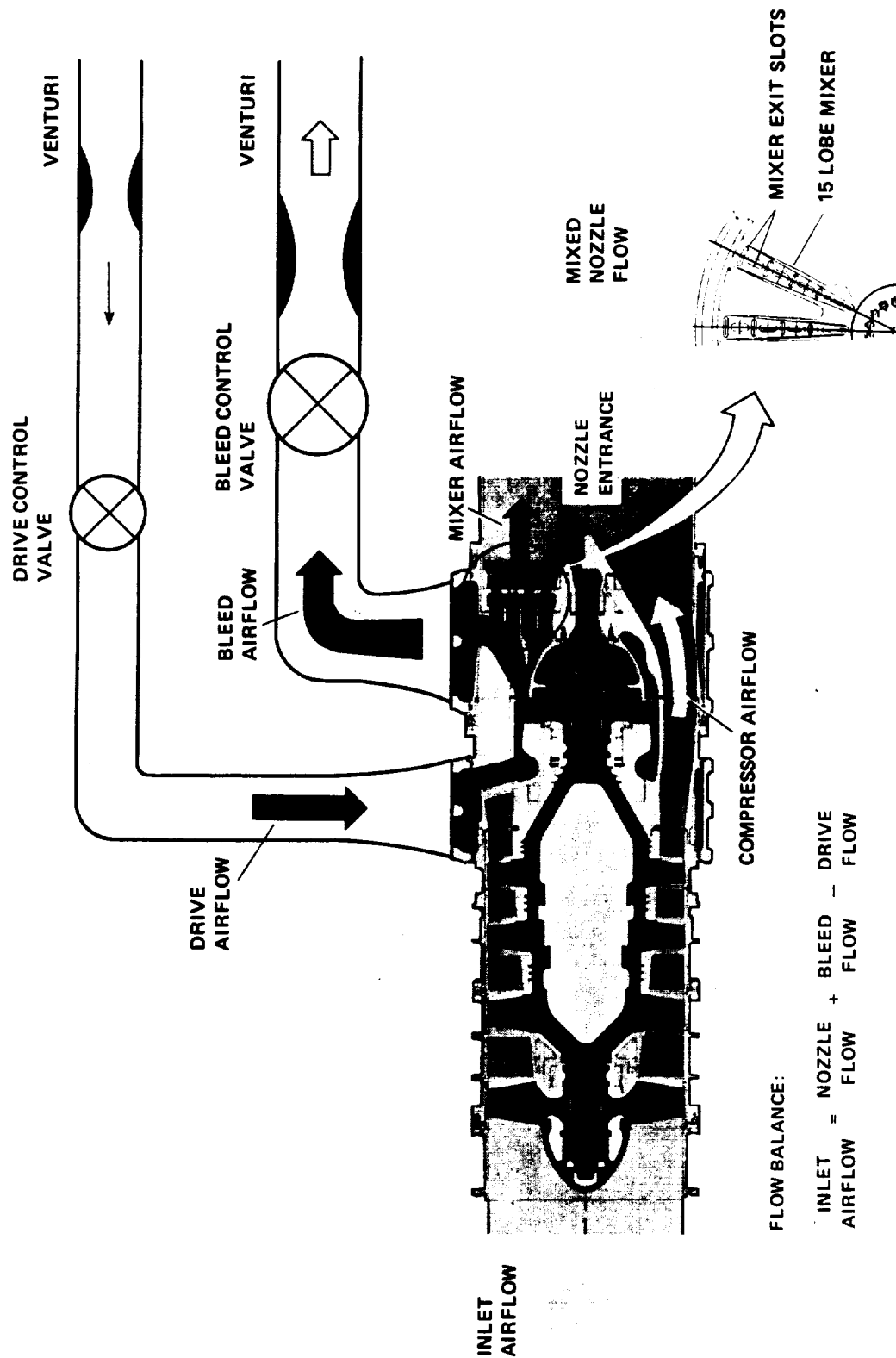


Figure 138. CMAPS entering/exiting flow balance relationship.

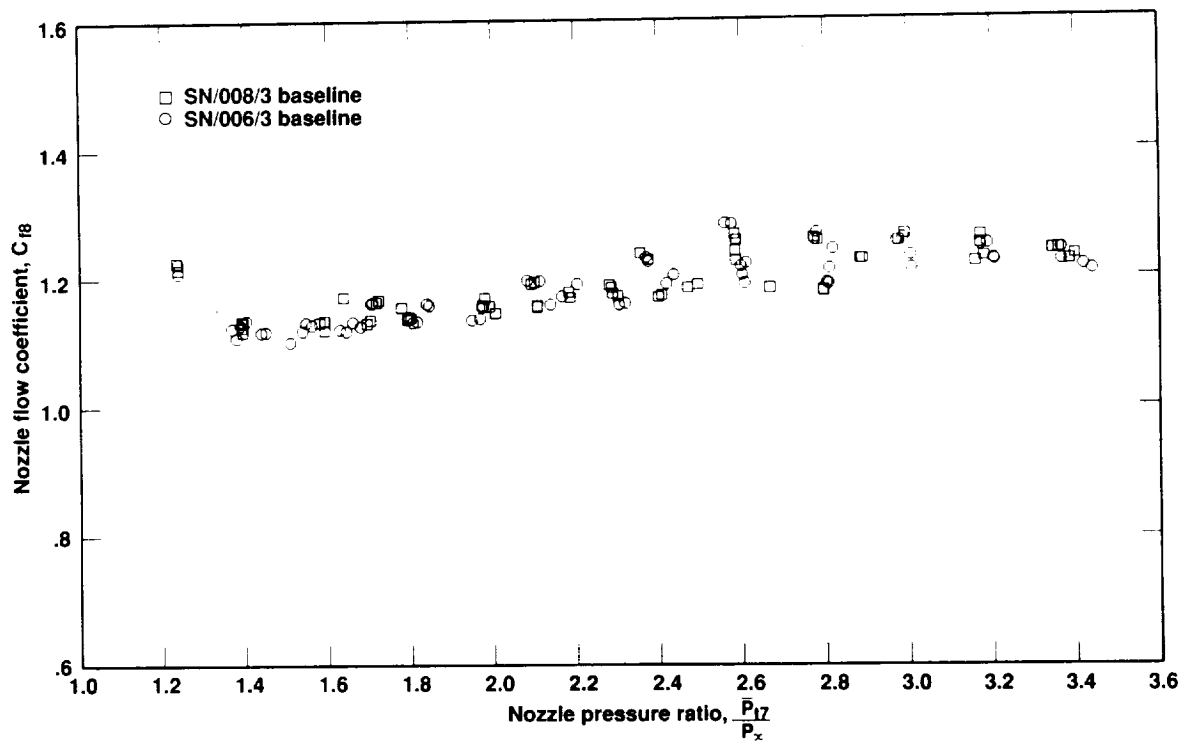


Figure 139. Nozzle flow coefficient distribution using the averaged Plane 7 temperature.

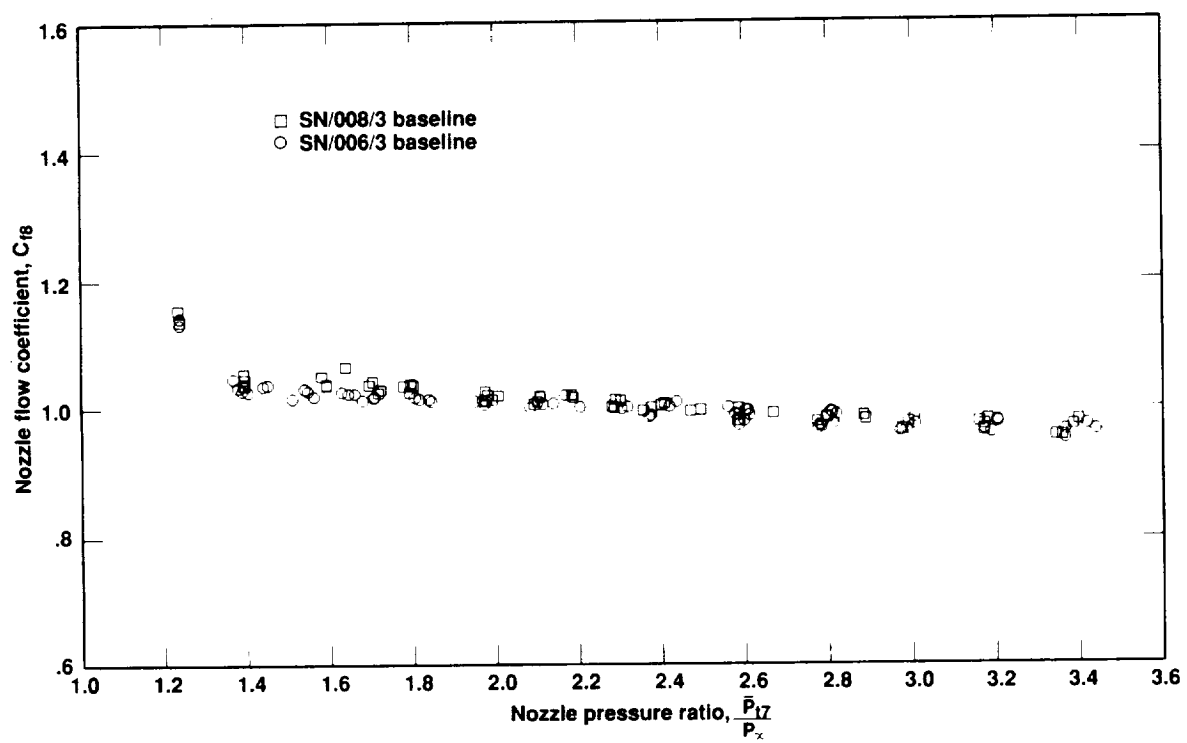


Figure 140. Nozzle flow coefficient distribution using the Plane 15 temperature.

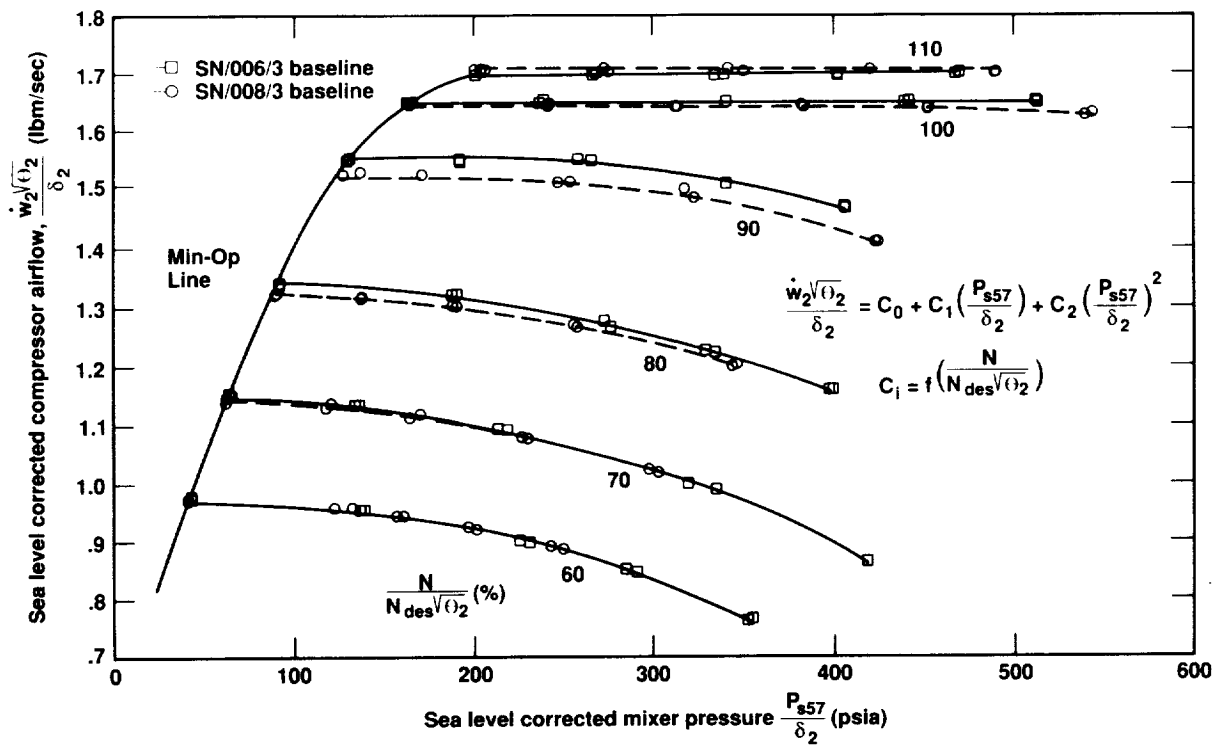


Figure 141. Baseline corrected mixer pressure and compressor airflow map for CMAPS SN/006/3 and SN/008/3.

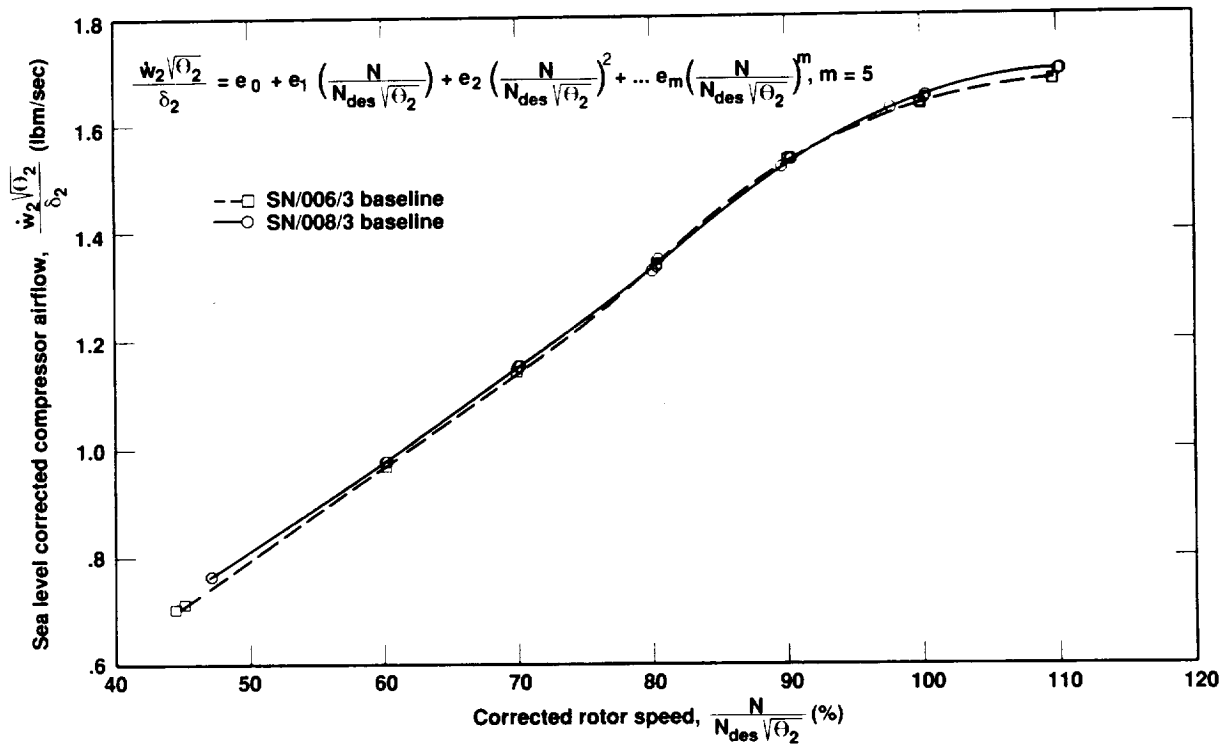


Figure 142. Min-op line corrected airflow-rotor speed relation for SN/006/3 and SN/008/3 baseline operation.

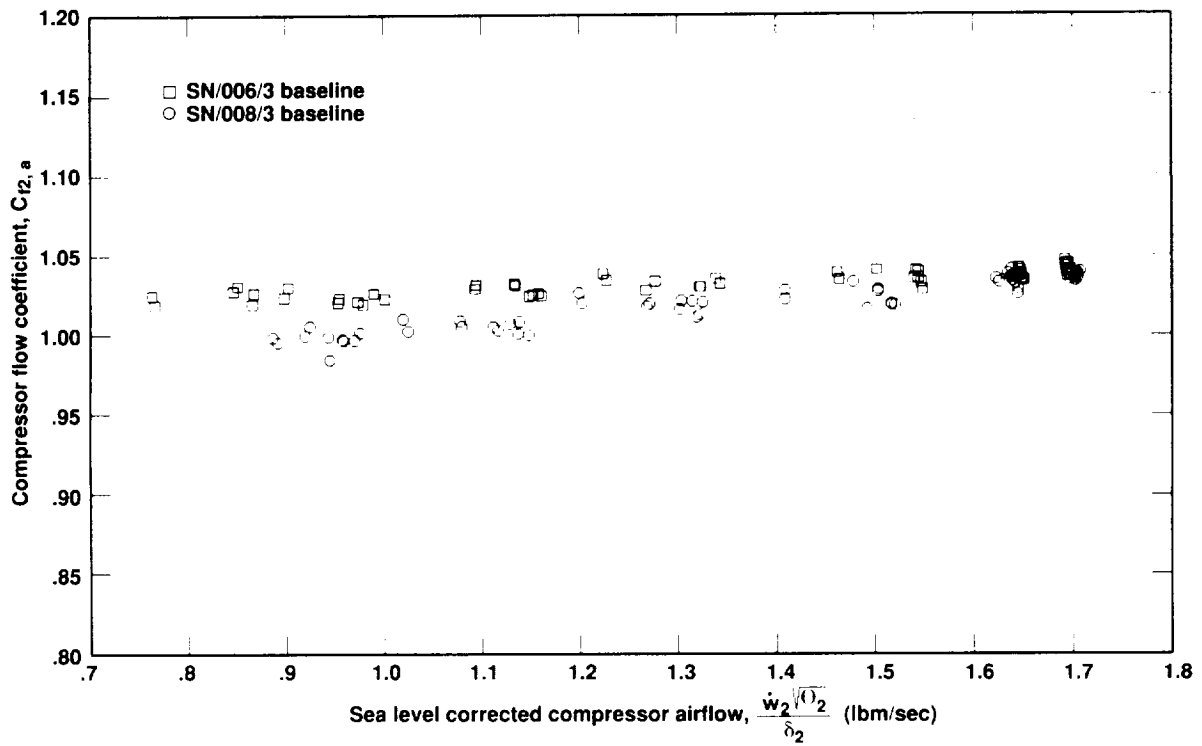


Figure 143. Baseline compressor flow coefficient distribution using averaged Plane 2 pressures.

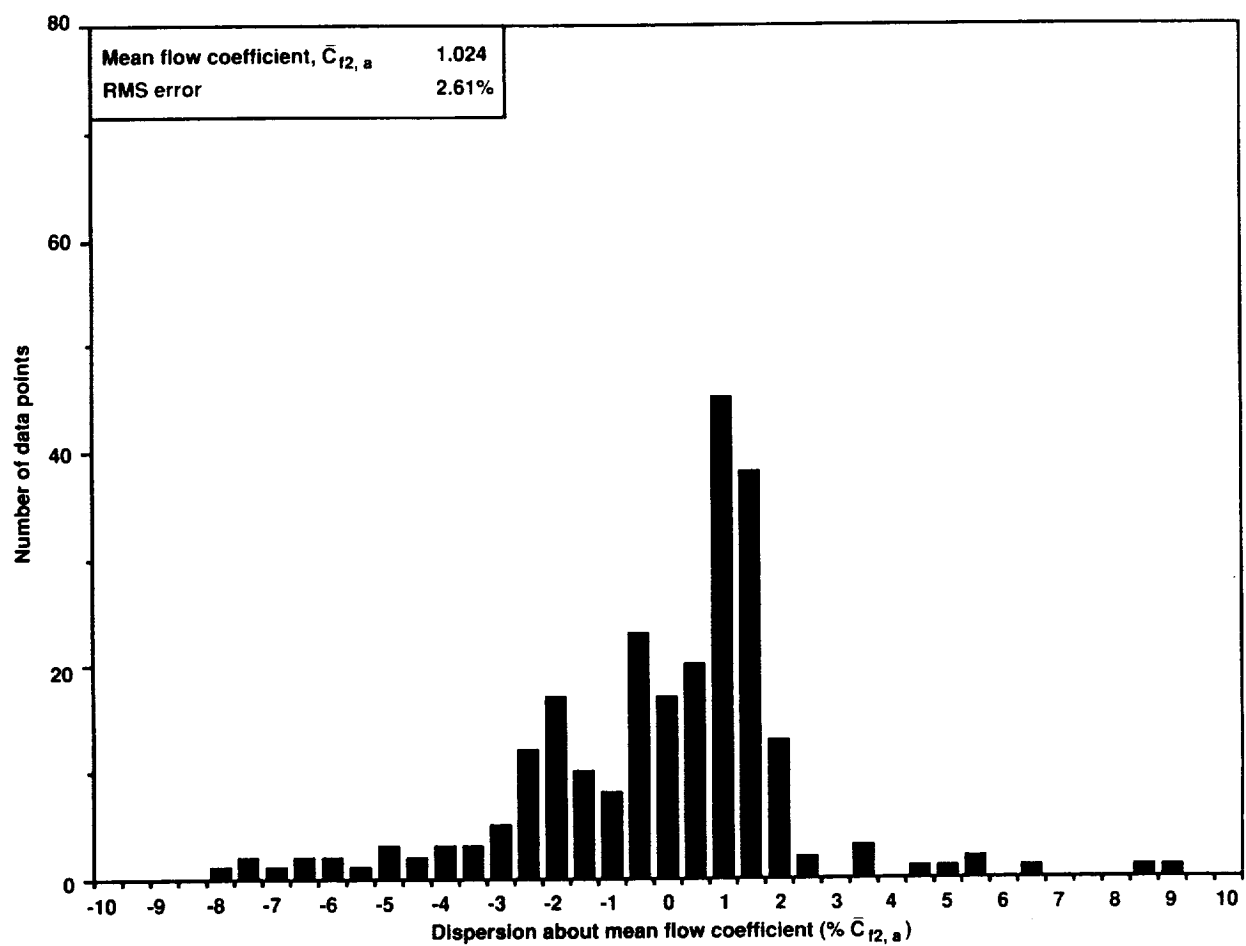


Figure 144. Compressor flow coefficient dispersion for averaged Plane 2 pressure method. (a) Baseline configuration.

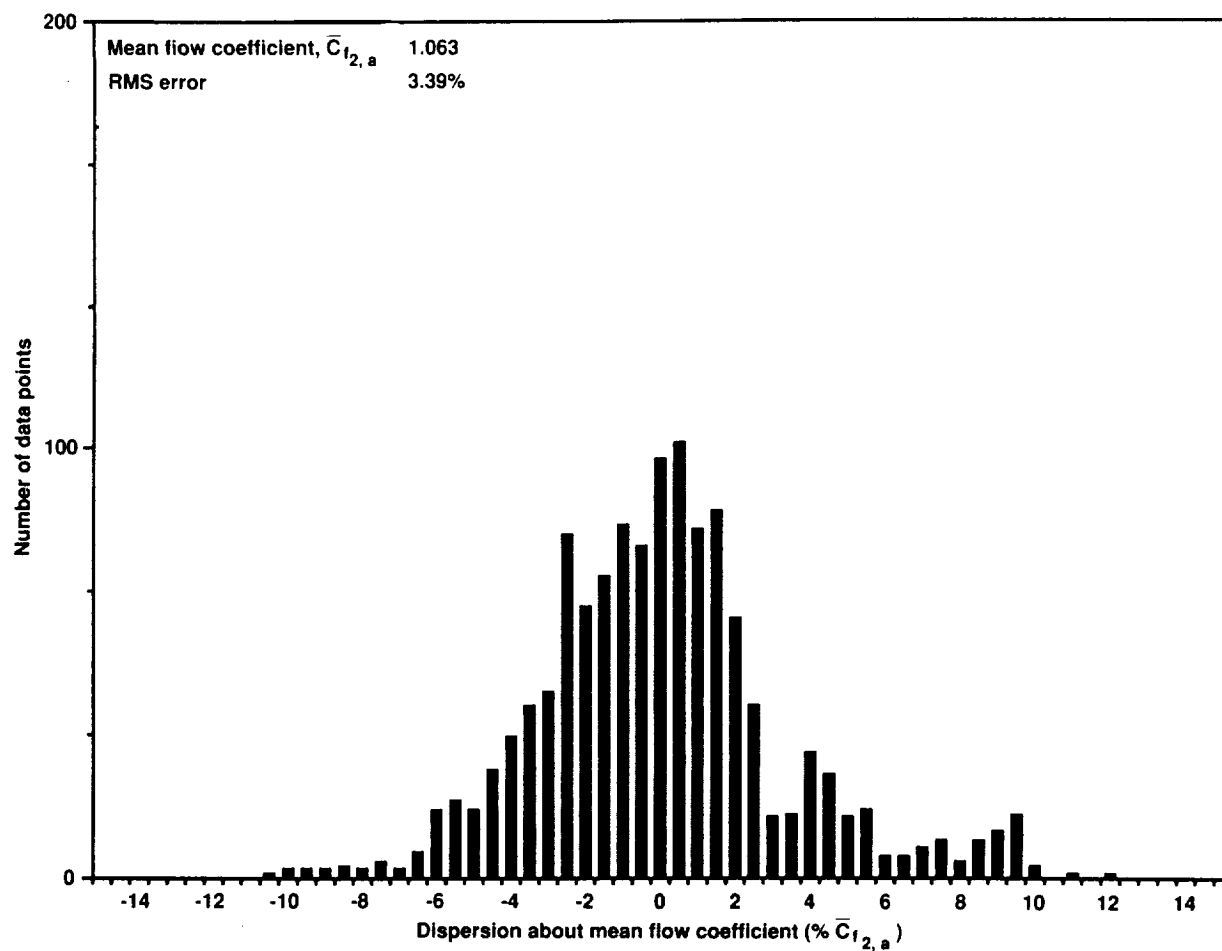


Figure 144. Concluded. (b) All configurations.

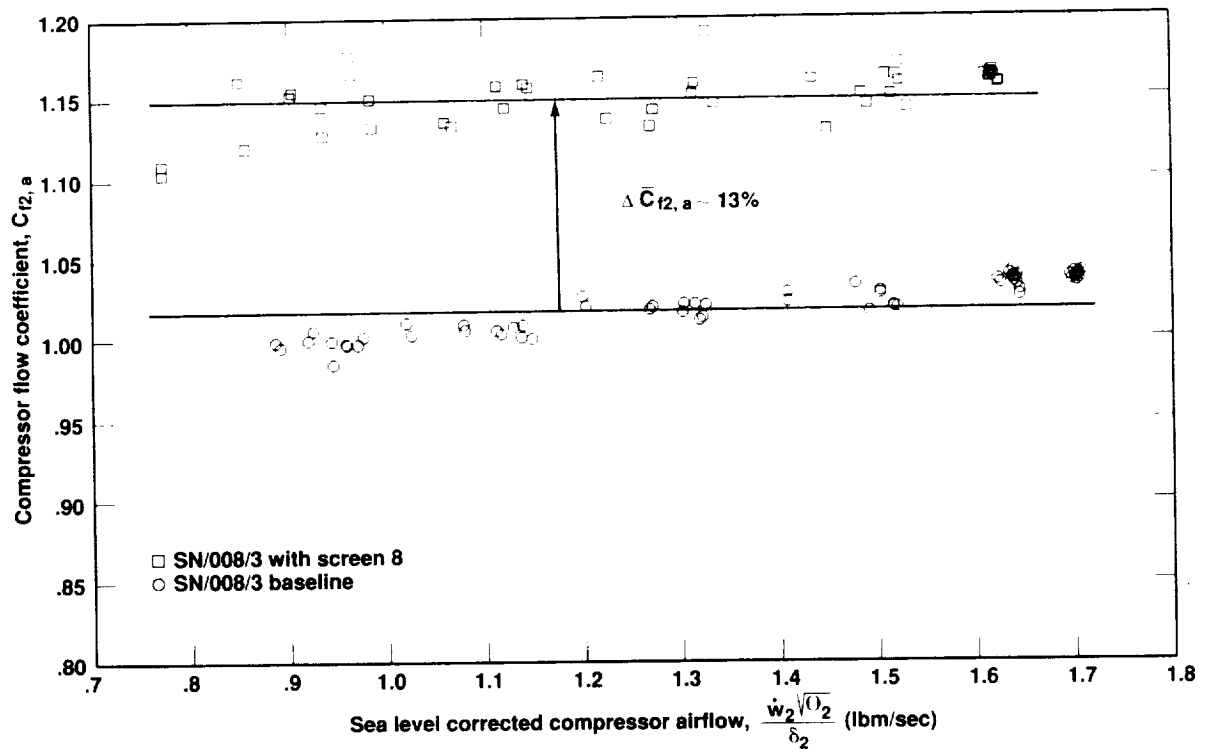


Figure 145. Compressor flow coefficient distribution comparison between baseline and screen No. 8 configurations for averaged Plane 2 pressure method.

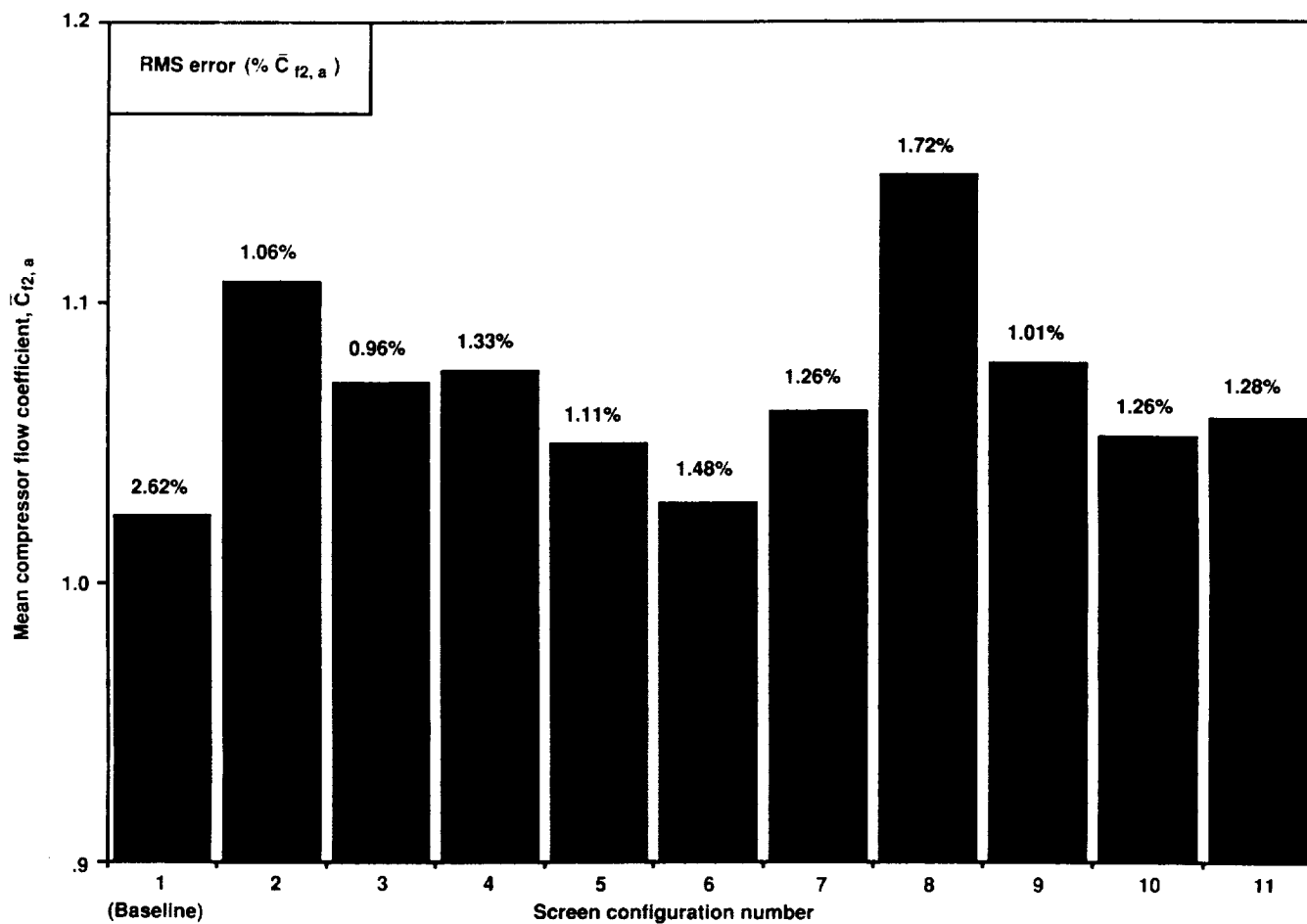


Figure 146. Mean compressor flow coefficients and RMS errors for all distortion screen configurations using averaged Plane 2 pressure method.

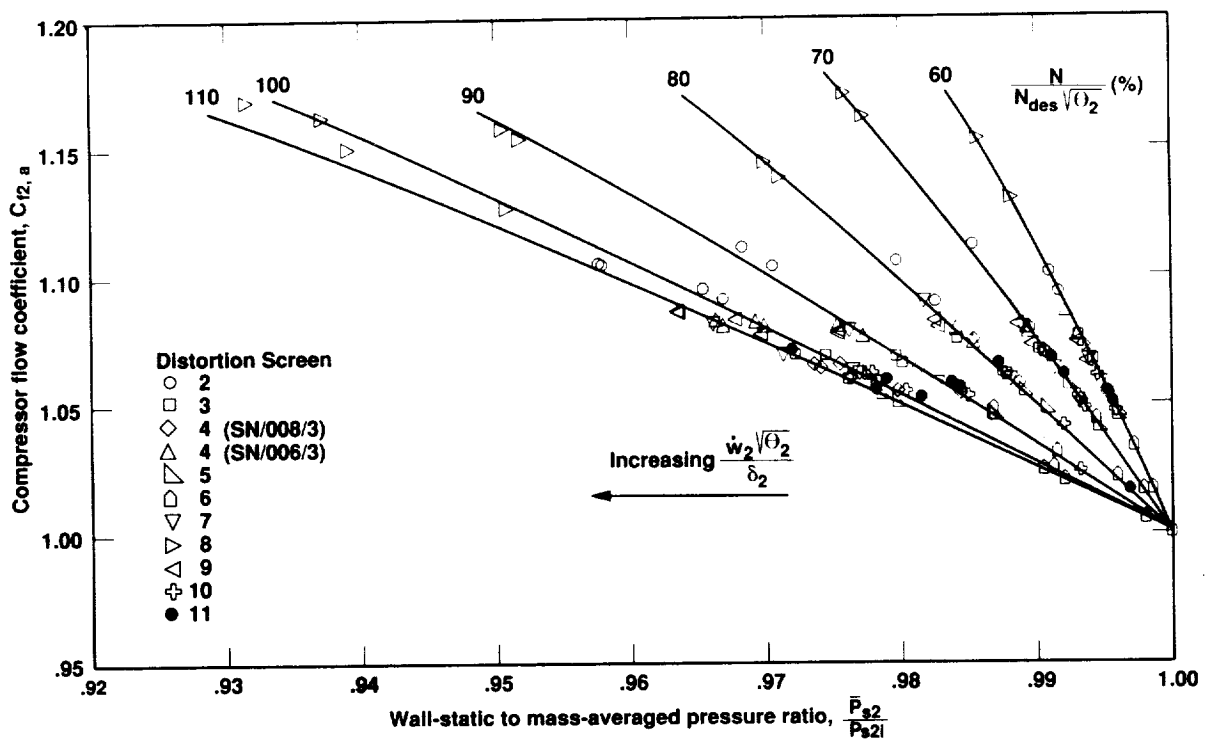


Figure 147. Compressor inlet wall-static pressure sensitivity to tip-radial distortion screens.

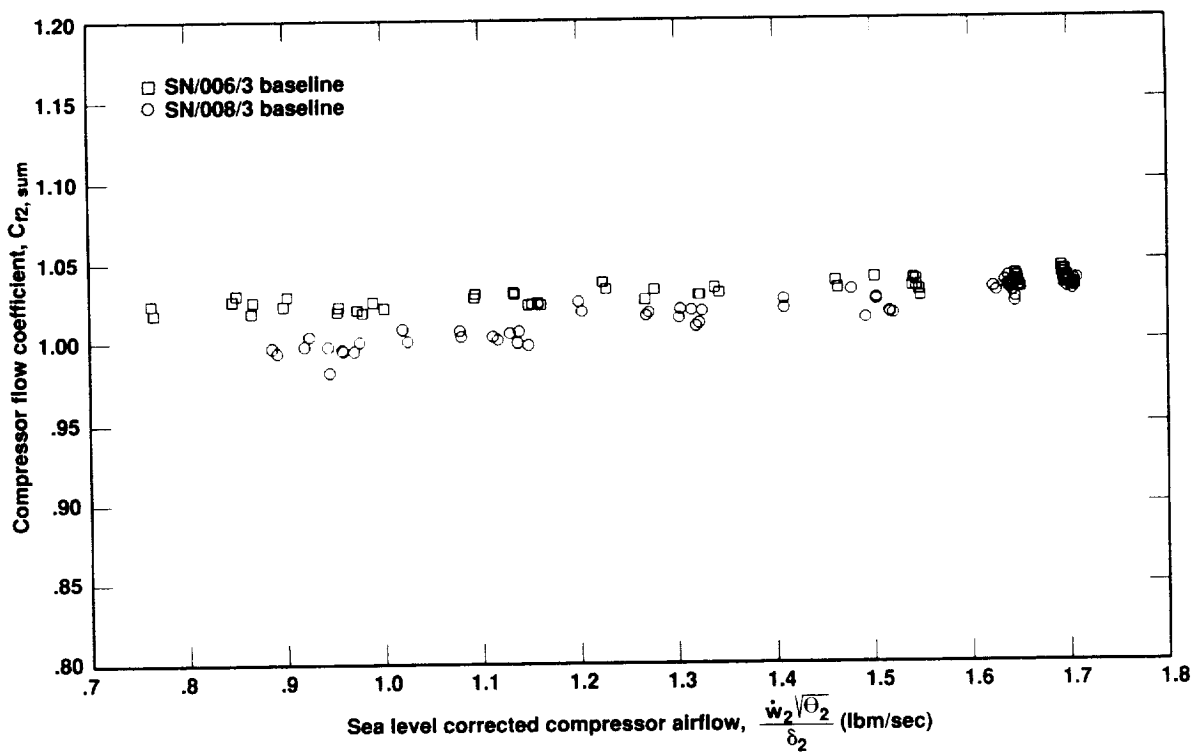


Figure 148. Baseline compressor flow coefficient distribution using summed Plane 2 flow elements method.

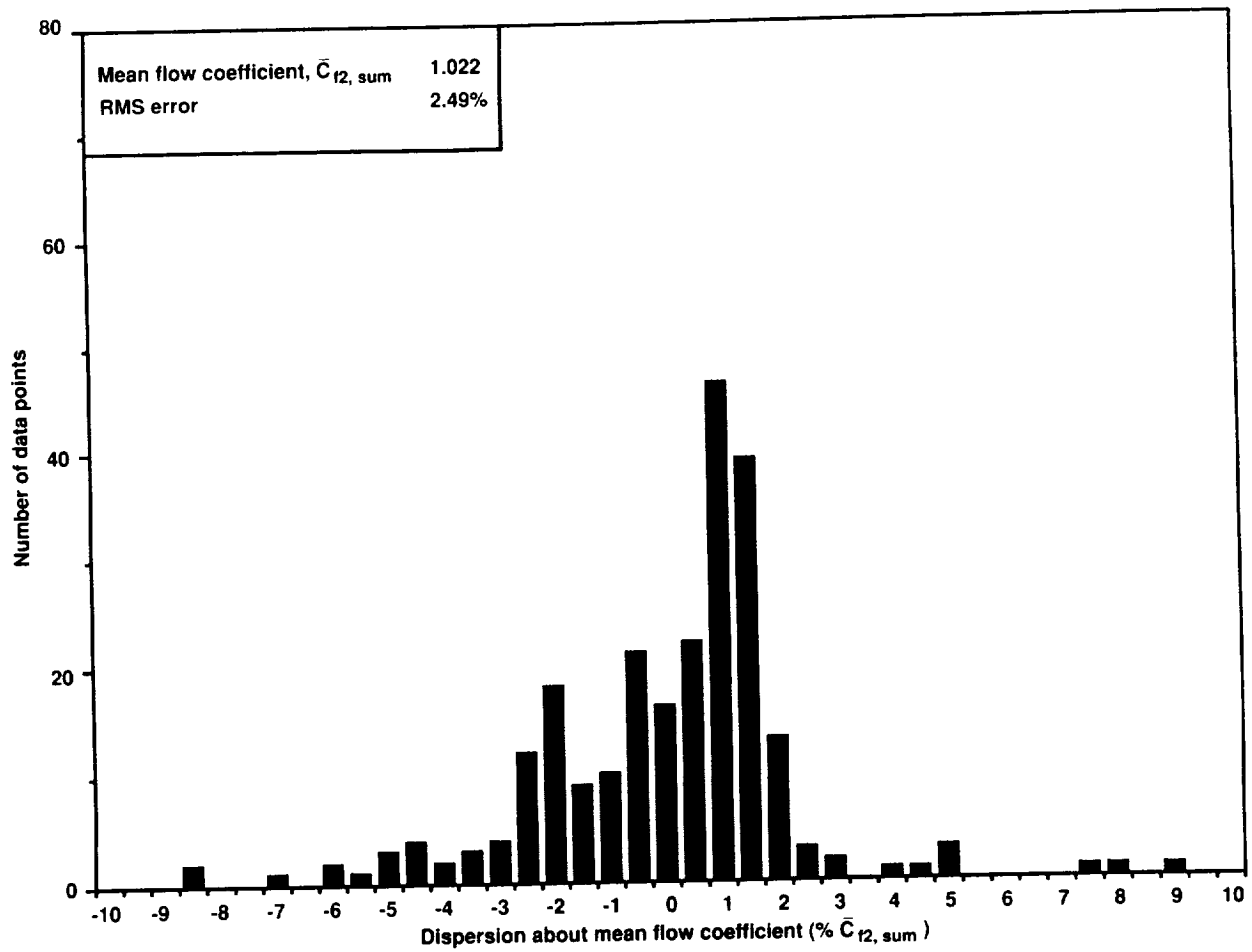


Figure 149. Compressor flow coefficient dispersion for summed Plane 2 flow elements method. (a) Base-line configuration.

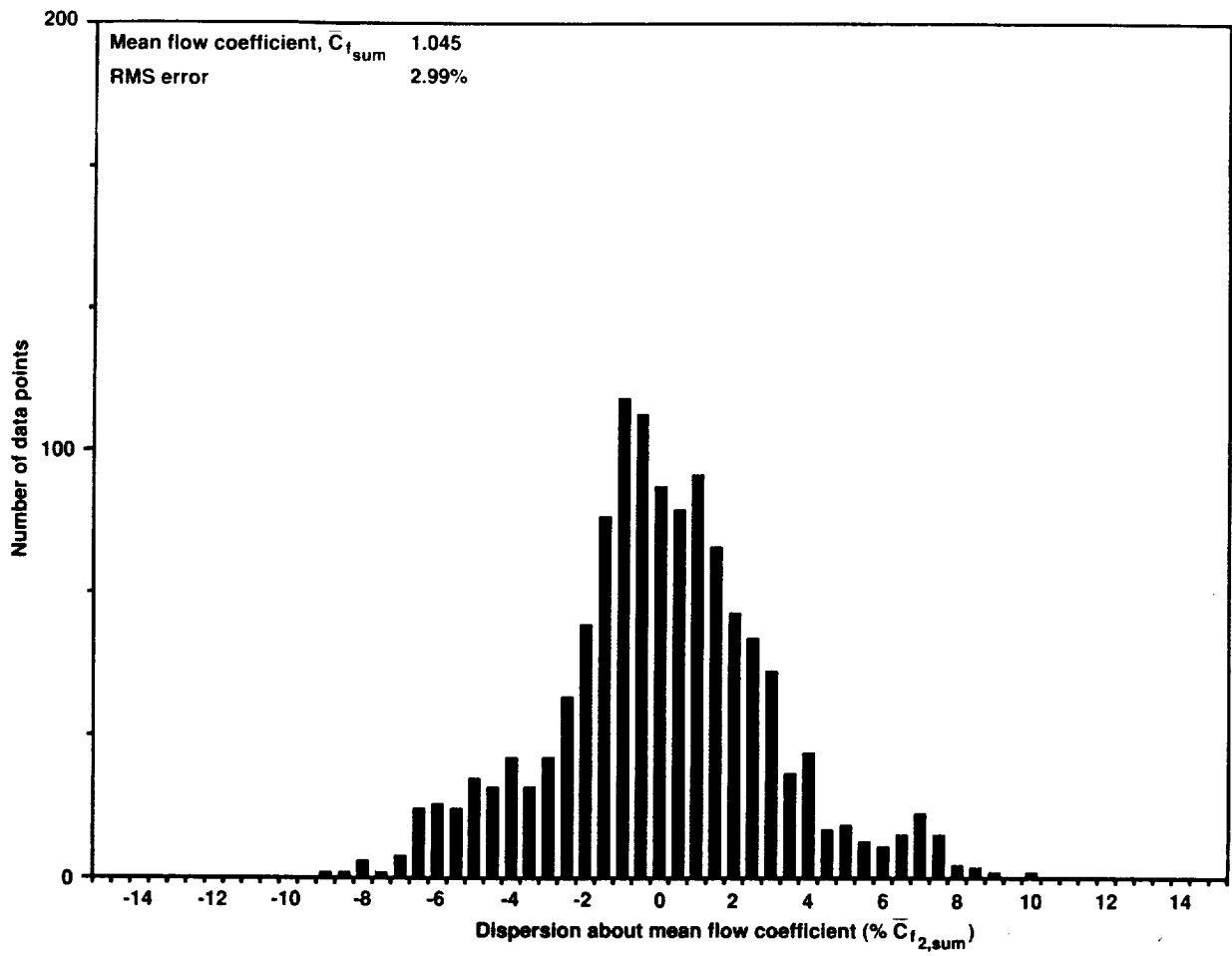


Figure 149. Concluded. (b) All configurations.

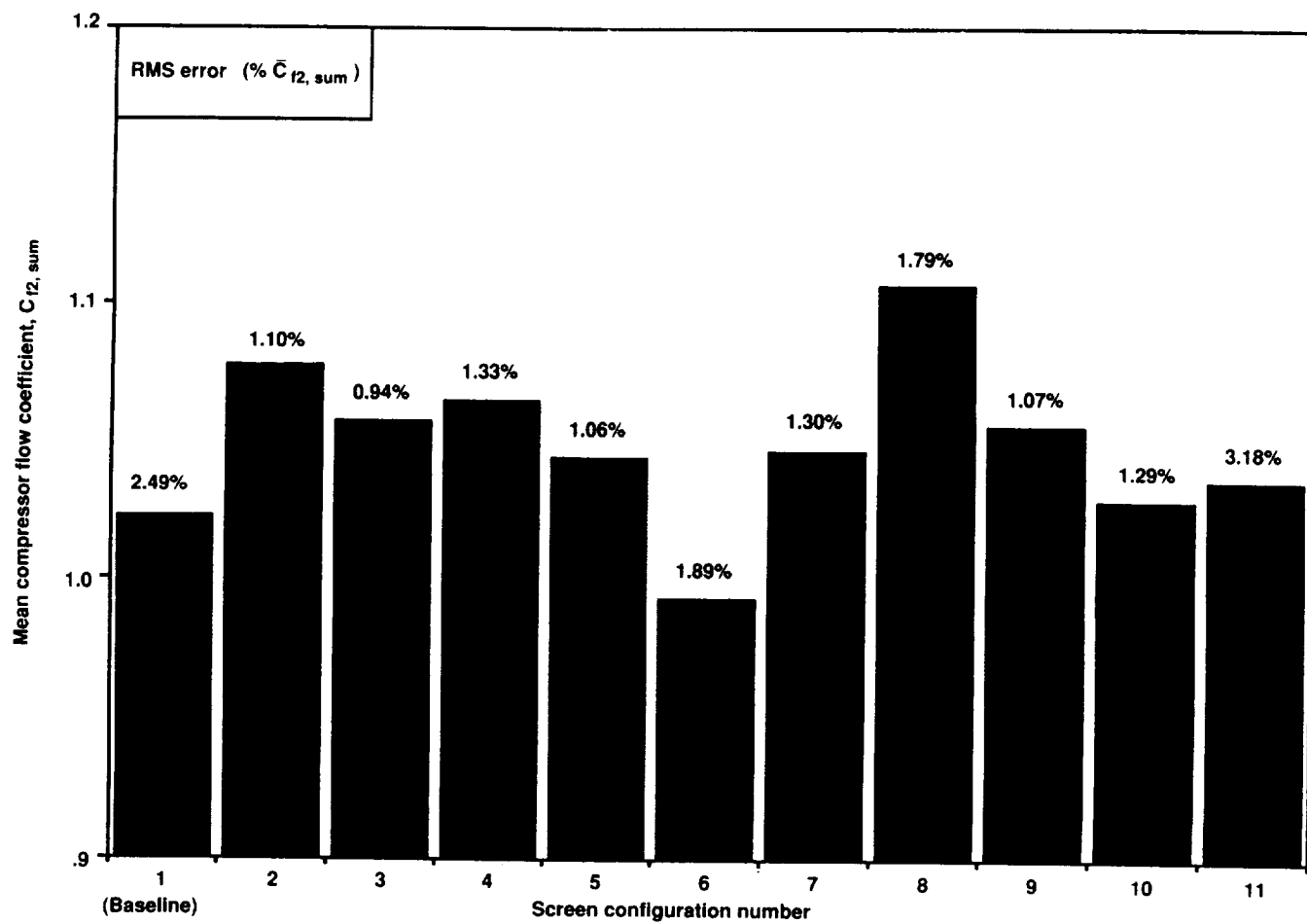


Figure 150. Mean compressor flow coefficients and rms errors for all distortion screen configurations using summed flow elements method.

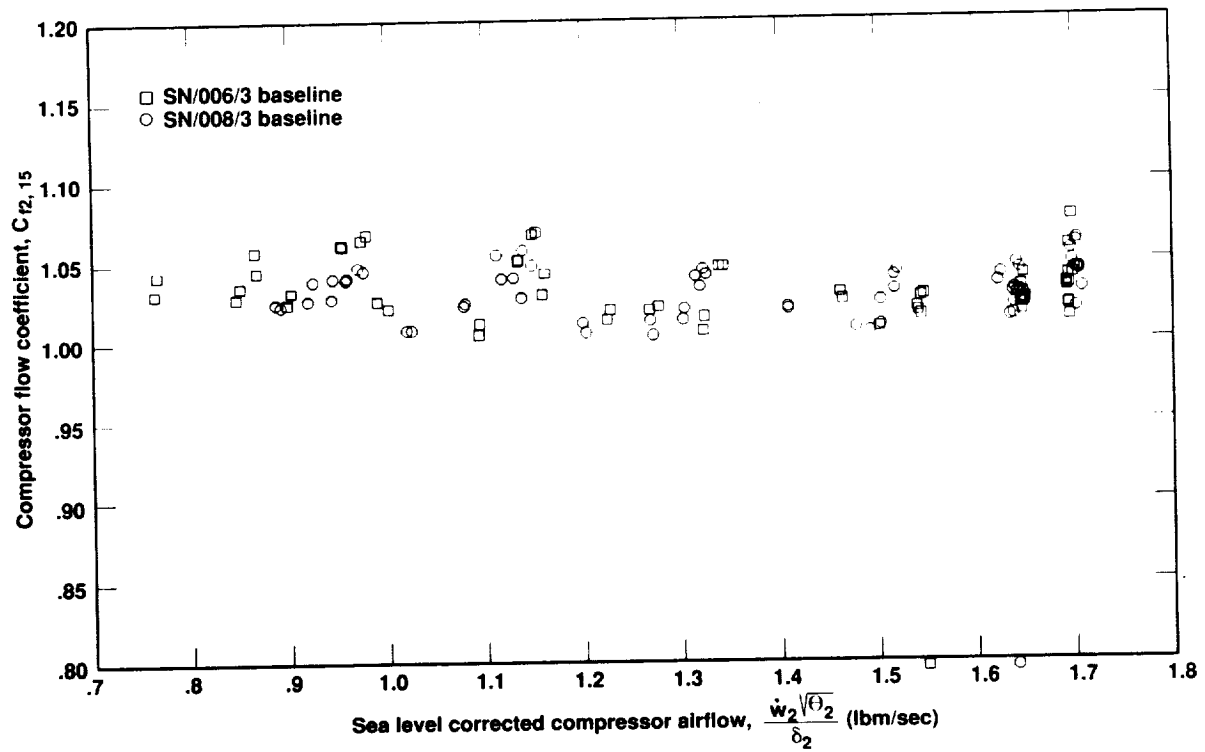


Figure 151. Baseline compressor flow coefficient distribution using compressor discharge flow method.

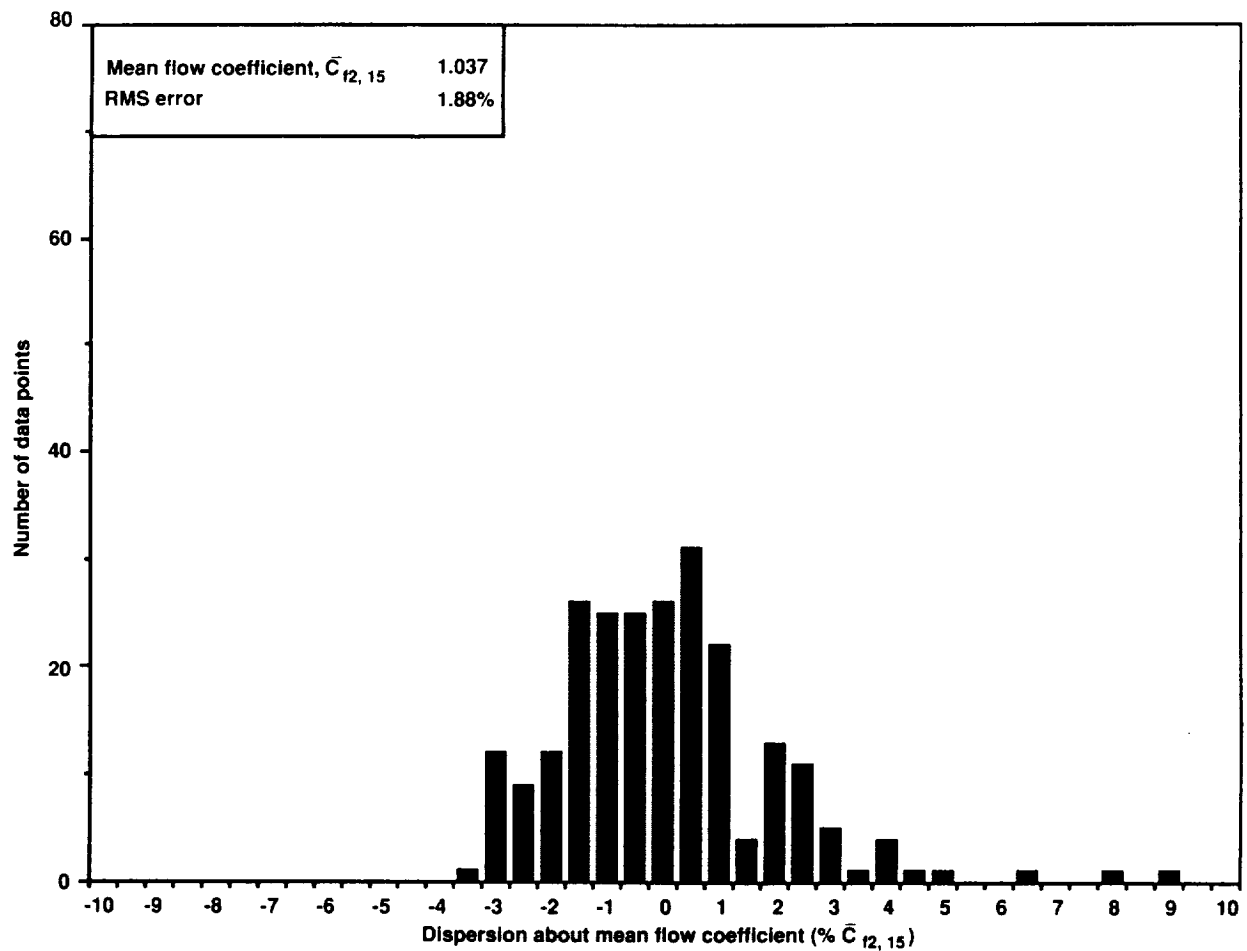


Figure 152. Compressor flow coefficient dispersion for compressor discharge flow method. (a) Baseline configuration.

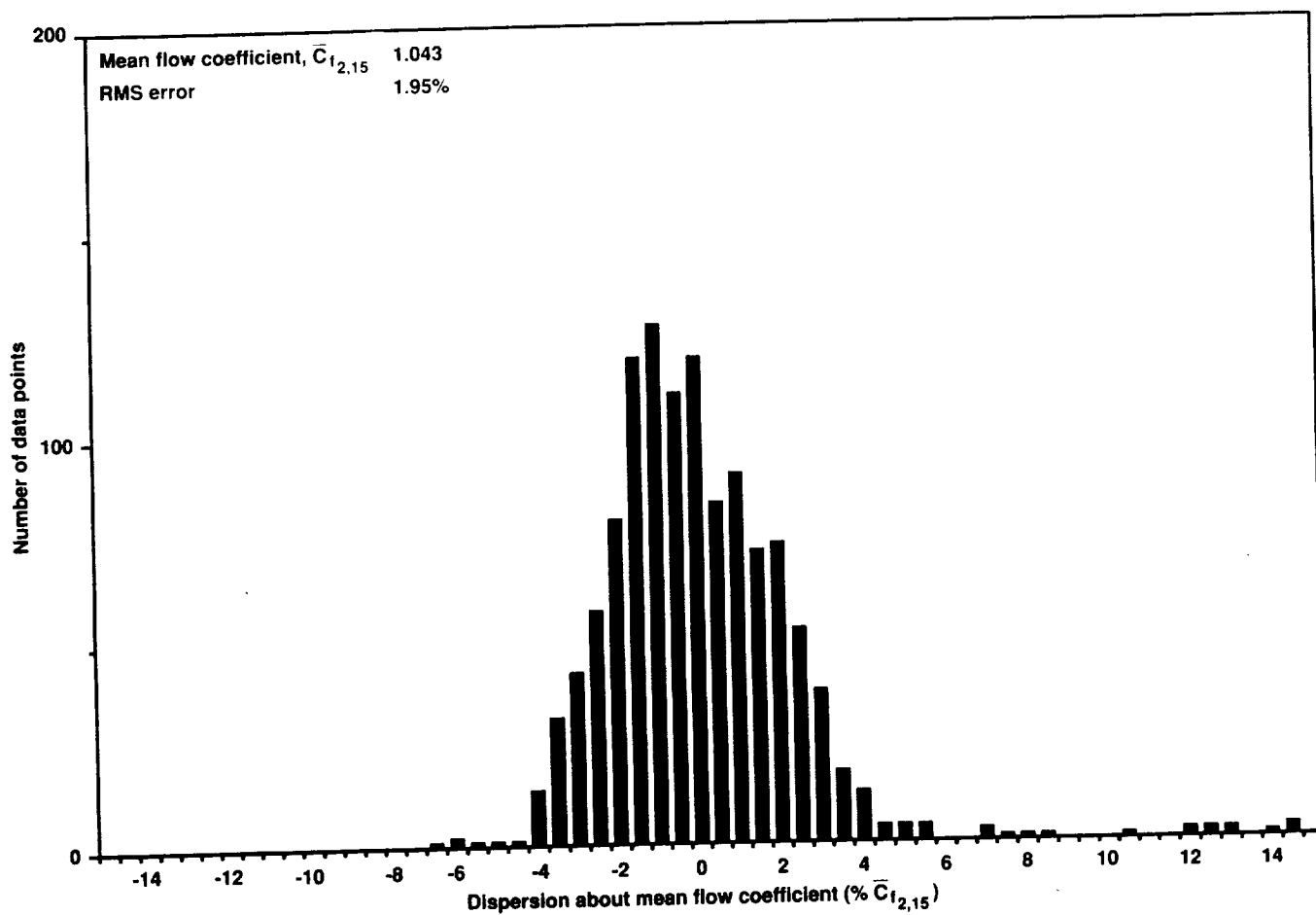


Figure 152. Concluded. (b) All configurations.

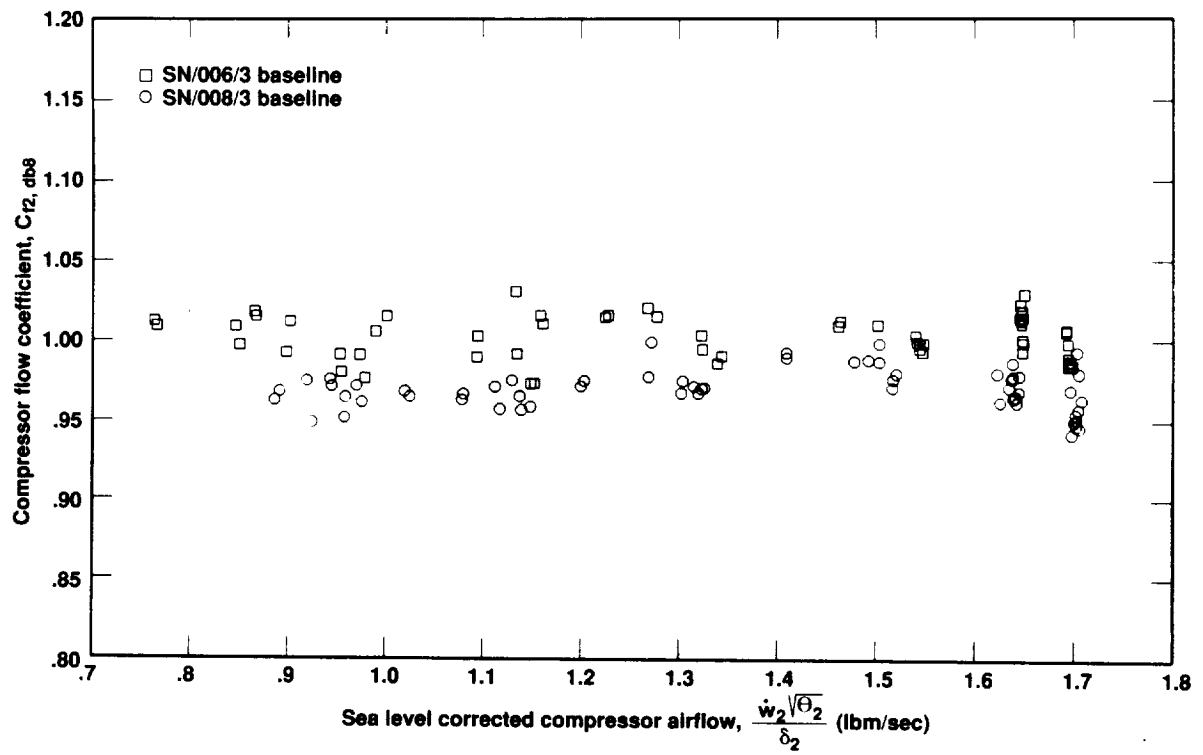


Figure 153. Baseline compressor flow coefficient distribution using the entering/exiting flow-balance method.

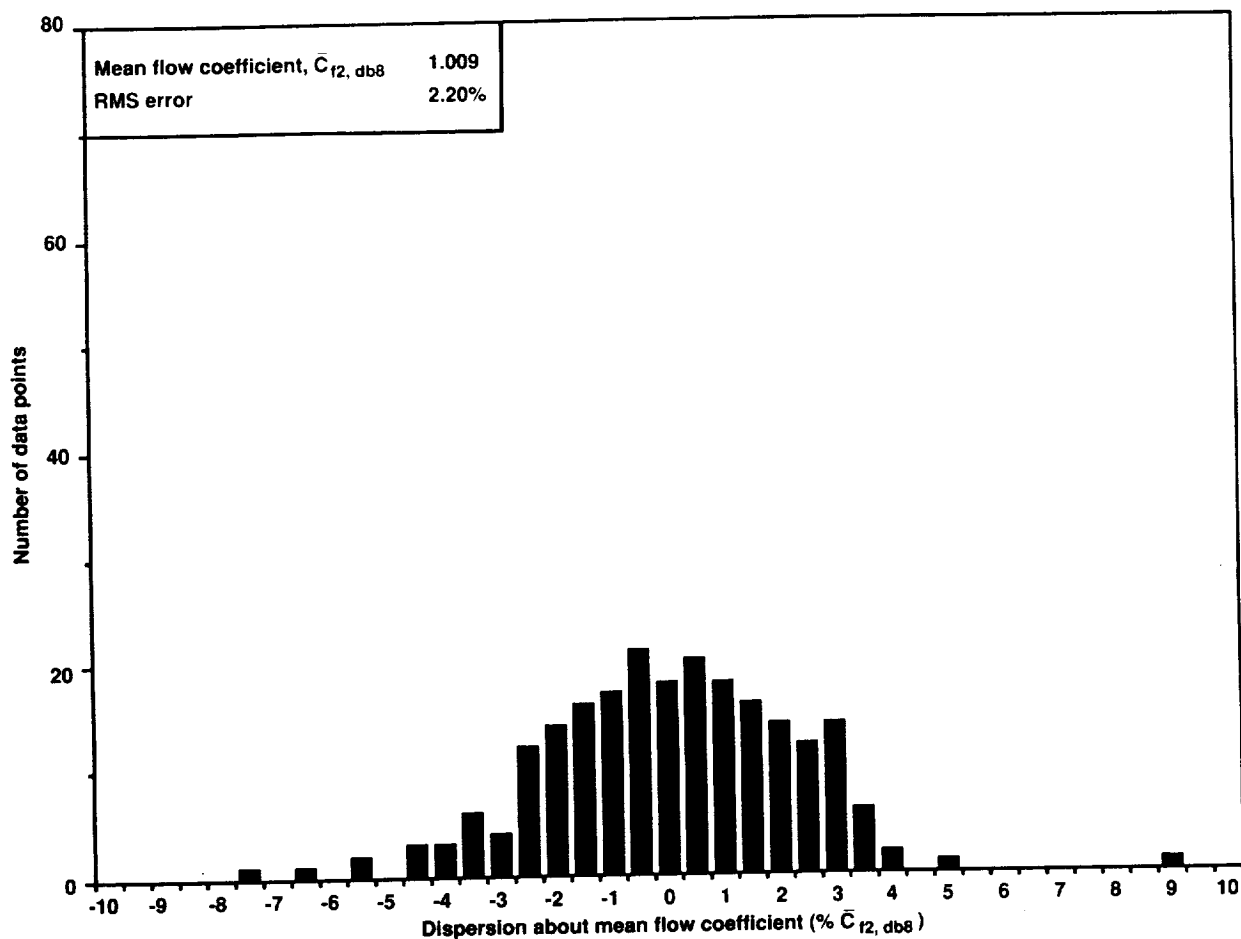


Figure 154. Compressor flow coefficient dispersion for the entering/exiting flow-balance method.
(a) Baseline configuration.

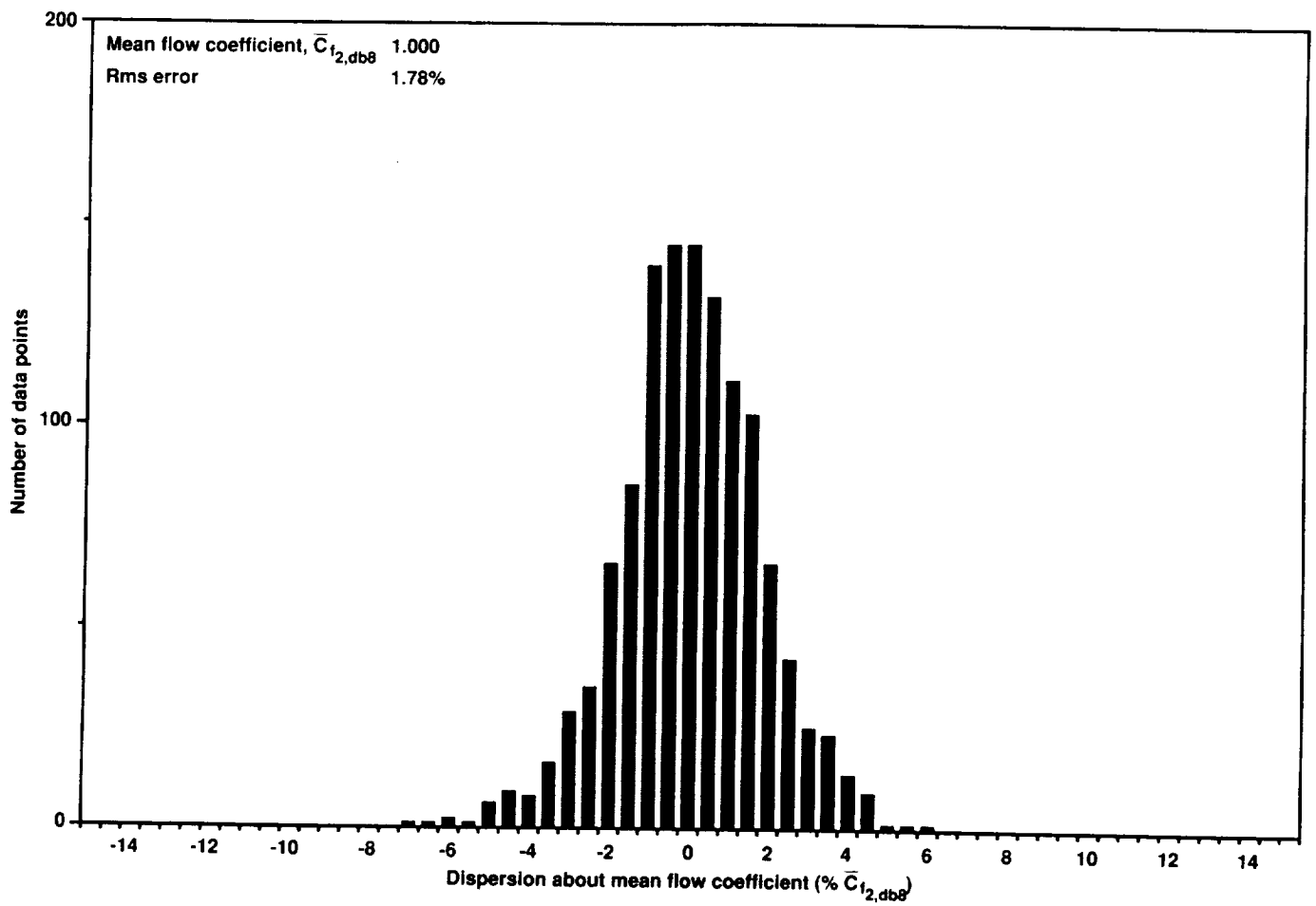


Figure 154. Concluded. (b) All configurations.

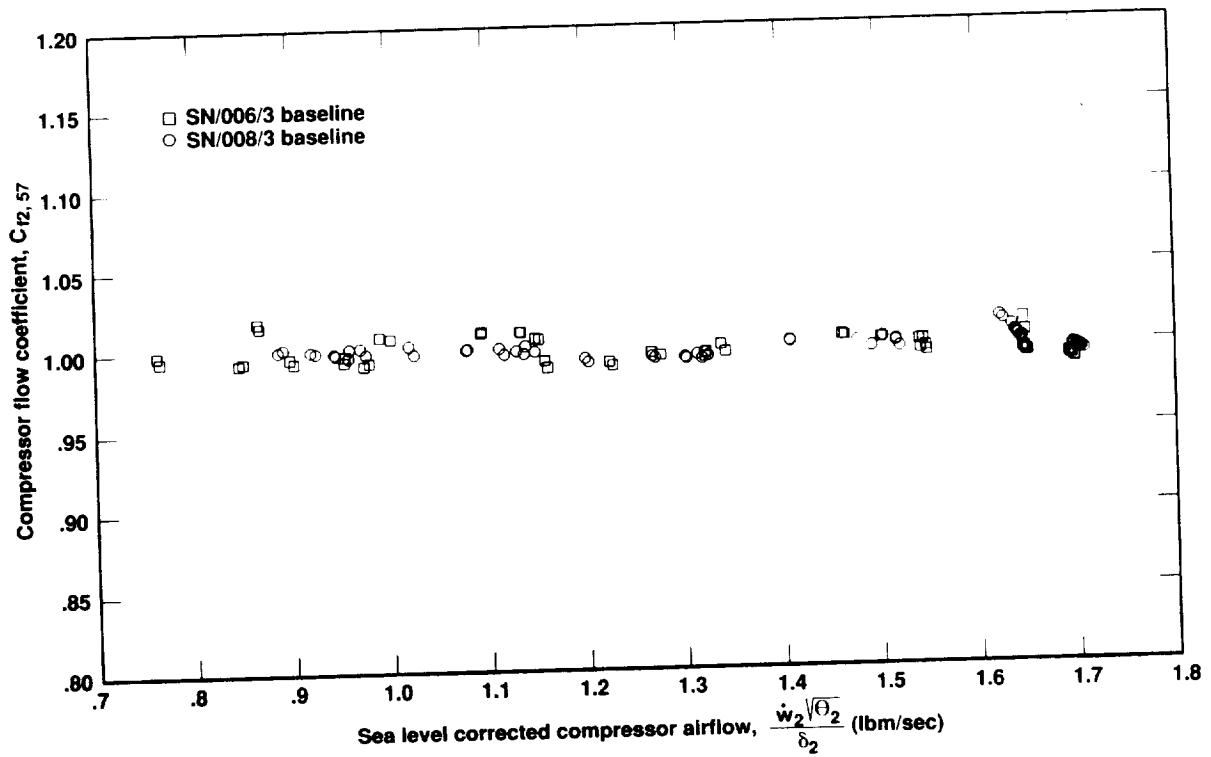


Figure 155. Baseline compressor flow coefficient distribution using the corrected mixer pressure-compressor airflow correlation method.

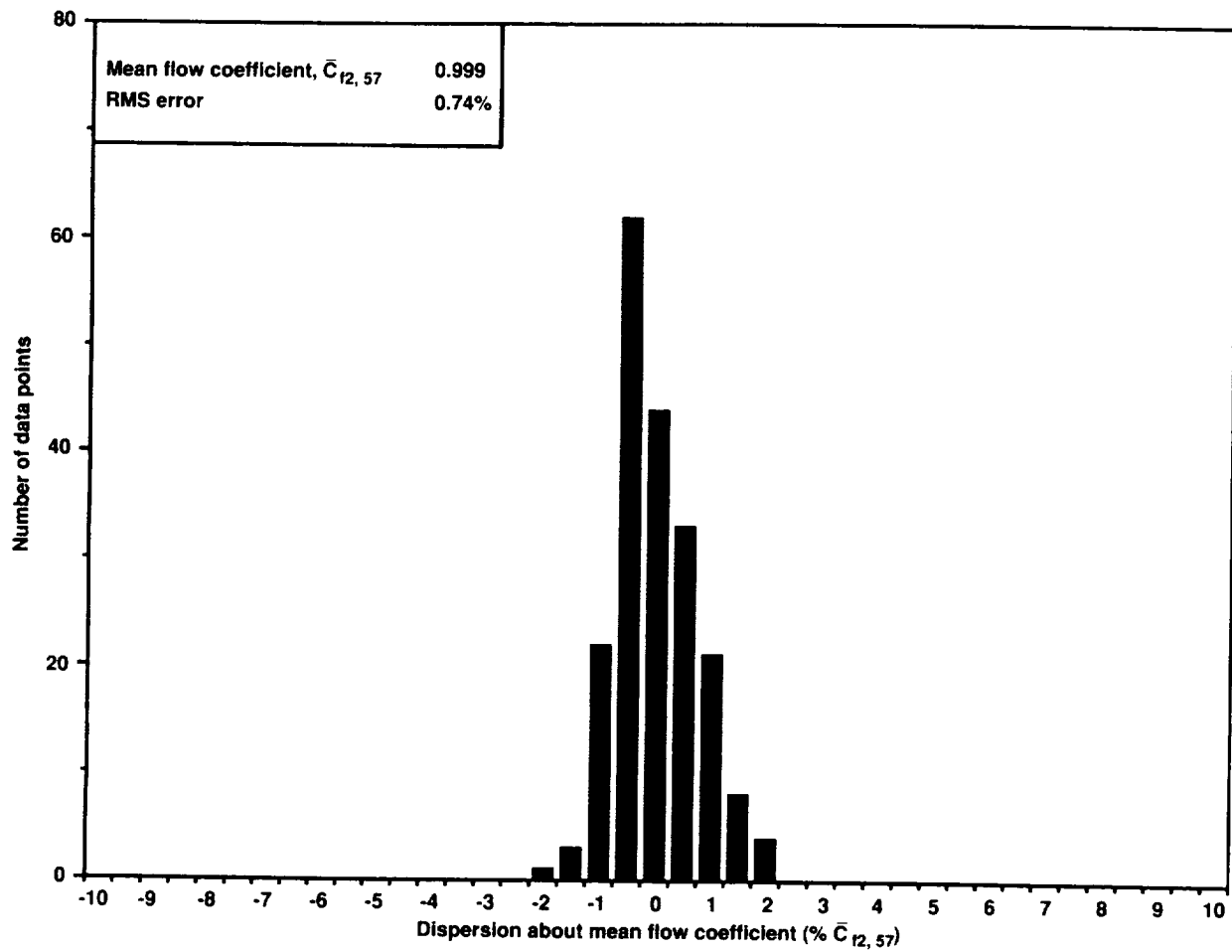


Figure 156. Compressor flow coefficient dispersion for the corrected mixer pressure correlation method.
(a) Baseline configuration.

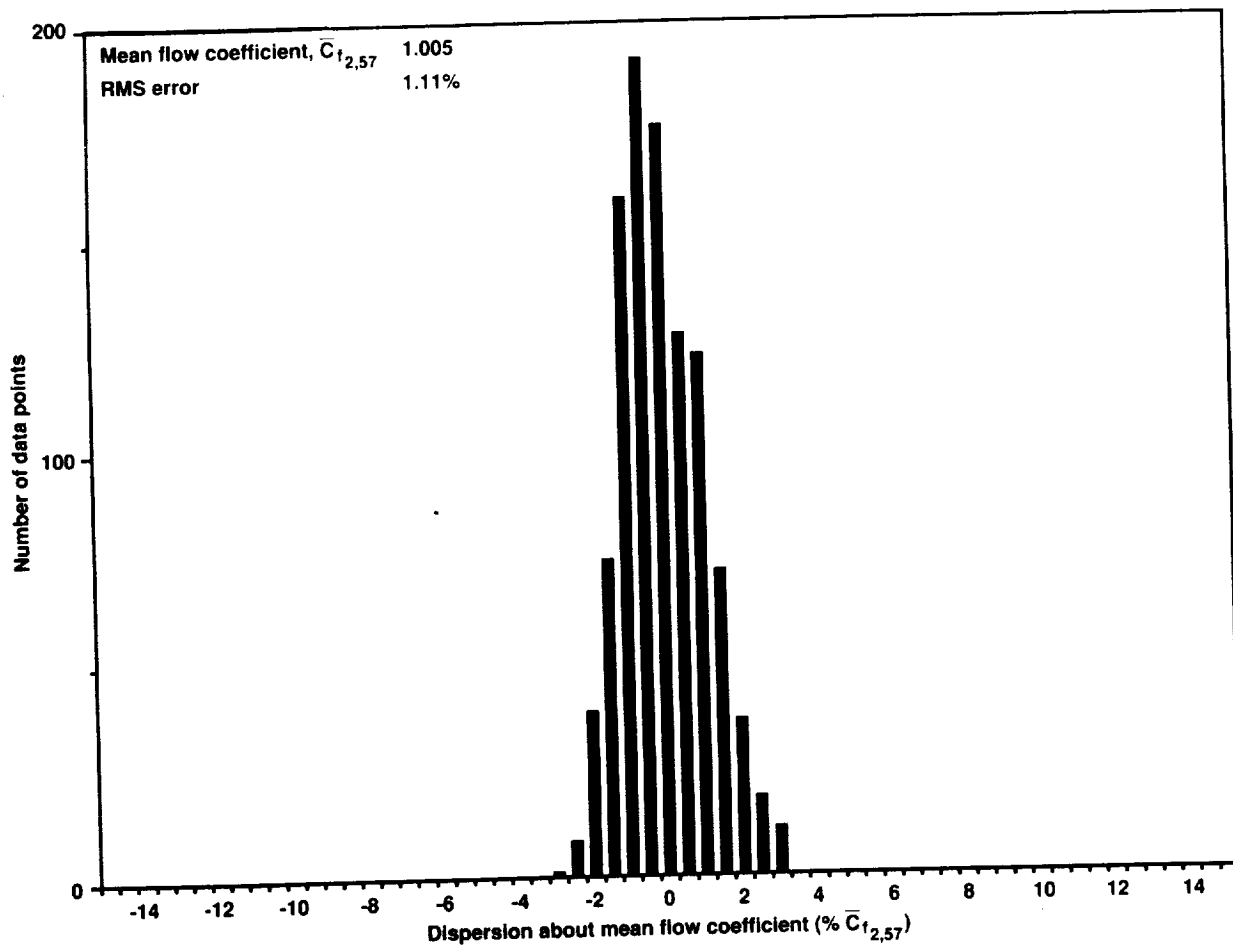


Figure 156. Concluded. (b) All configurations.

1. Report No. NASA TM-102838		2. Government Accession No.		3. Recipient's Catalog No.	
4. Title and Subtitle Sea Level Static Calibration of a Compact Multimission Aircraft Propulsion Simulator with Inlet Flow Distortion				5. Report Date November 1990	
				6. Performing Organization Code	
7. Author(s) Mark J. Won				8. Performing Organization Report No. A-90194	
				10. Work Unit No. 505-61-21	
9. Performing Organization Name and Address Ames Research Center Moffett Field, CA 94035-1000				11. Contract or Grant No.	
				13. Type of Report and Period Covered Technical Memorandum	
12. Sponsoring Agency Name and Address National Aeronautics and Space Administration Washington, DC 20546-0001				14. Sponsoring Agency Code	
15. Supplementary Notes Point of Contact: Mark J. Won, Ames Research Center, MS 227-6, Moffett Field, CA 94035-1000 (415) 604-5865 or FTS 464-5865					
16. Abstract Wind tunnel tests of propulsion-integrated aircraft models have identified inlet flow distortion as a major source of compressor airflow measurement error in turbine-powered propulsion simulators. Consequently, two Compact Multimission Aircraft Propulsion Simulator (CMAPS) units were statically tested at sea level ambient conditions to establish simulator operating performance characteristics and to calibrate the compressor airflow against an accurate bellmouth flowmeter in the presence of inlet flow distortions. The distortions were generated using various-shaped wire mesh screens placed upstream of the compressor. CMAPS operating maps and performance envelopes were obtained for inlet total pressure distortions (ratio of the difference between the maximum and minimum total pressures to the average total pressure) up to 35%, and were compared to baseline simulator operating characteristics for a uniform inlet. Deviations from CMAPS baseline performance were attributed to the coupled variation of both compressor inlet-flow distortion and Reynolds number index throughout the simulator operating envelope for each screen configuration. Four independent methods were used to determine CMAPS compressor airflow: direct compressor inlet and discharge measurements, an entering/exiting flow-balance relationship, and a correlation between the mixer pressure and the corrected compressor airflow. Of the four methods, the last yielded the least scatter in the compressor flow coefficient, approximately $\pm 3\%$ over the range of flow distortions.					
17. Key Words (Suggested by Author(s)) Wind tunnel testing Propulsion simulators Flow distortion				18. Distribution Statement Unclassified-Unlimited Subject Category - 02	
19. Security Classif. (of this report) Unclassified		20. Security Classif. (of this page) Unclassified		21. No. of Pages 194	
				22. Price A09	